A STUDY OF LONGITUDINAL COHERENT EFFECTS OF UNBUNCHED BEAMS NEAR TRANSITION IN THE FERMILAB ACCUMULATOR

BY

XIAO-QING WANG

Submitted in partial fulfillment of the
requirements of the degree of
Doctor of Philosophy in Physics
in the School of Advanced Studies of
Illinois Institute of Technology

Approved _____
Advisor

_____
Co-Advisor

Chicago, Illinois
August 1991

AA134641

ACKNOWLEDGEMENTS

This work was supported by the Universities Research Association, Inc., which is under contract with the U. S. Department of Energy. In the early years of my graduate studies at Fermilab, I had the privilege to work with Dr. John Peoples, who introduced me to the field of accelerator physics, set the direction of my research, and showed continued interest in my project. Fundamentally, it was Dr. Gerald Jackson who made this thesis a reality. During the course of my thesis research, he taught me the experimental methods, provided direction when the going was tough, and directed the writing of my thesis. His understanding, patient support, and encouragement have been a marvel to me, and I cannot thank him enough for all he has done. I am also greatly indebted to my supervisor at IIT, Professor Porter Johnson for his guidance and support during the years of my graduate studies. He has carefully read my thesis and made many invaluable comments.

I am grateful to Dr. Shao-Yuan Hsueh who has been a source of advice and friendship throughout my years at Fermilab. His insightful discussions and help on my research have benefitted me a great deal.

For his help in many different ways over the years, I would like to present my sincere gratitude to Dr. Vinod Bharadwaj. I have enjoyed his friendship while at Fermilab.

It is a great pleasure to thank all the members of the E760 collaboration and the Antiproton Source Department. Their expertise and support have always been appreciated.

Drs. James Maclachlan and Steve Stahl deserve acknowledgement for their useful discussions and help on ESME computer simulations.

My special thanks to Professor Wu-ki Tung for his guidance in my early academic years at IIT and his concern with my research project at Fermilab. Without him I would not have become an accelerator physicist.

Thanks must go to the members of the Ph.D. in Accelerator Physics Committee of the Fermi National Accelerator Laboratory for giving me the opportunity

to participate in the program. Thanks also goes to my dissertation committee members at IIT: Professors Burnstein, Johnson, Shahidehpour and Tung for their cooperation and help in clarifying various topics.

Finally I thank my parents for their understanding and support over the years, and my wife, Lili, for her help and love during the writing of this thesis.

X. Q. W.

TABLE OF CONTENTS

	Page
ACKNOWLEDGMENTS	iii
LIST OF FIGURES	vii
LIST OF TABLES	xi
ABSTRACT	xii
CHAPTER	
I. INTRODUCTION	1
1.1 Fermilab Antiproton Source Operation	2
1.2 About E760 Experiment	4
1.3 Accumulator Operation in E760	7
II. FUNDAMENTALS OF ANTIPROTON STORAGE RINGS	10
2.1 Lattice	11
2.2 Longitudinal Phase Space and RF Stacking	20
2.3 Stochastic Cooling	30
2.4 Beam Diagnostics	34
III. FERMILAB ACCUMULATOR	43
3.1 RF Cavities	44
3.2 Beam Position Monitors	49
3.3 Stochastic Cooling Systems	53
3.4 Beam Diagnostic Instruments	56
IV. ACCUMULATOR OPERATION IN E760	63
4.1 Accumulator Control System Adaptation to E760	64
4.2 Deceleration	66
4.3 Measurements of Beam Energy	78
4.4 Measurements of Beam Energy Spread	83
4.5 Deceleration History	87
V. ACCUMULATOR LONGITUDINAL IMPEDANCE	88
5.1 Longitudinal Impedance and Longitudinal Instability	89
5.2 Estimated Accumulator Impedance	97
5.3 Measurement of Accumulator Impedance	99

CHAPTER Page

VI. LONGITUDINAL INSTABILITY DURING TRANSITION CROSSING 118

6.1 Beam Momentum Blow up and Energy Loss . . . 119
6.2 Frequency Domain Measurements 122
6.3 Time Domain Measurements 131
6.4 Beam Momentum Spread in Transition Crossing 135
6.5 Transition Crossing with ARF1 shorted 136

VII. SIMULATING ACCUMULATOR TRANSITION CROSSING 151

7.1 About ESME 151
7.2 ESME Simulation of Transition Crossing 155

VIII. CONCLUSIONS 175

REFERENCES 177

LIST OF FIGURES

Figure		Page
1.1.	A Schematic View of the Fermilab Antiproton Source	3
1.2.	Schematic Layout of the Fermilab Accumulator	8
2.1.	Curved Coordinate System	12
2.2.	Trajectory of a Particle in Transverse Phase Space	16
2.3.	Accumulator Lattice for One Sextant	19
2.4.	Accumulator Beam Position at the End of A20	21
2.5.	Buckets in Longitudinal Phase Space	26
2.6.	RF Stacking in Phase Space	28
2.7.	Principle of (Horizontal) Stochastic Cooling	31
2.8.	Time Evolution of the Momentum Distribution During Stochastic Accumulation	34
2.9.	Longitudinal Spectra of Particles with Slightly Different Revolution Frequencies	36
2.10.	Single Particle Spectrum When RF is On	39
2.11.	Longitudinal Spectra of the Accumulator Beam	41
2.12.	A Sketched Transverse Spectrum of an Accumulator Beam . .	42
3.1.	A Coaxial TEM Standing Wave Resonator	44
3.2.	Configuration of an ARF1 Cavity	46
3.3.	Rough Drawing of ARF3	49
3.4.	Physical Dimensions of Circular and Rectangular BPMs . . .	50
3.5.	BPM Pickup Equivalent Circuit	51
3.6.	Locations of the Accumulator Stochastic Cooling Systems . .	54
3.7.	Schematic of the Longitudinal Schottky Detector	57
3.8.	Frequency Response of the Longitudinal Schottky Detector . .	58
3.9.	Half Cross Section of a Wall Current Monitor	59
3.10.	Accumulator Wall Current Monitor S_{21} Response	60

Figure		Page
3.11.	Shunt Load Circuit Schematic	61
4.1.	The Fermilab Accelerator Controls Computer Network	65
4.2.	Betatron Sidebands During E760 Deceleration	67
4.3.	Beam Closed Orbit Change at X:POFTT=6776 MeV/c Relative to the Initial Closed Orbit	68
4.4.	Aperture as a Function of Momentum	71
4.5.	Deceleration above Transition	74
4.6.	The Accumulator Schottky Profiles above and below Transition, as First Observed on January 8, 1988	76
4.7.	Measured γ_t as a Function of Momentum	77
5.1.	Qualitative Plot of Longitudinal Impedance	92
5.2.	Calculated Accumulator Longitudinal Impedance (Real and Imaginary Components) as a Function of Frequency	98
5.3.	A Schematic of the Beam Transfer Function for Impedance Measurement	100
5.4.	A Schematic Drawing of the Accumulator Longitudinal BTF Measurement System	103
5.5.	Longitudinal Schottky Profiles at Harmonic 126 before and after Many Frequency Scans	104
5.6.	Amplitude and Phase of the Inverse Response for a Upward and Downward Frequency Scans near $h = 2$	106
5.7.	Amplitude and Phase of the Inverse Response for a 120 Second Upward Frequency Scan near $h = 1$	108
5.8.	Beam Response Measured with 100 Hz Resolution Bandwidth	109
5.9.	Frequency Response of the ARF2 Cavity	110
5.10.	BTF Measurements at Harmonics 73 and 84	112
5.11.	Result of a Impedance Measurement with a 7.2 mA Beam	113
5.12.	Result of a Impedance Measurement with a 160 mA Beam	115
6.1.	Longitudinal Schottky Profiles at $h = 127$ before and after a Transition Crossing	120

Figure		Page
6.2.	Frequency Distribution of the Same Beam below Transition after It was Cooled Longitudinally	121
6.3.	Frequency Profiles before and after Transition Crossing with the Energy Loss Being Compensated	123
6.4.	Schottky Profiles During a Transition Crossing with the New Ramp	124
6.5.	Beam Spectrum in a Wide Frequency Range	126
6.6.	Wall Current Monitor Signals in a Transition Crossing	127
6.7.	Longitudinal Schottky Signals at $h = 127$ in the Same Transition Crossing	129
6.8.	Time Evolution of the Coherent Effect in a Non-Stop Transition Crossing	131
6.9.	Growth and Decay of the Coherent Effect	133
6.10.	Power Rise Time measured in a Step-by-Step Transition Crossing	134
6.11.	Momentum Spread as a Function of η	136
6.12.	A Schematic of ARF1 Short Layout	137
6.13.	Transition Crossing with ARF1 not Shorted	139
6.14.	Transition Crossing with ARF1 Shorted	142
6.15.	Faster Transition Crossing with ARF1 not Shorted	145
6.16.	Faster Transition Crossing with ARF1 Shorted	148
7.1.	Initial Phase Space Distribution and Energy Distribution of the Beam	157
7.2.	Illustration I of the Phase Space Motion of a Beam	159
7.3.	Illustration II of the Phase Space Motion of a Beam	161
7.4.	Time Evolution of the Phase Space Distribution	163
7.5.	Phase Space and Energy Distribution at $\eta = -1.8 \times 10^{-4}$	167
7.6.	The First Fourier component of the Beam Current as a Function of Time in Transition Crossing	170
7.7.	Simulated Beam Average Energy as a Function of η	171

Figure Page

7.8. Measured and Simulated Beam rms Energy Spread as a Function of η 171

7.9. The Fourier Component in Transition Crossing with Space Charge Added 172

7.10. The Fourier Component in Transition Crossing with $\alpha_1 \approx -2\alpha_0$ 173

LIST OF TABLES

Table		Page
1.1.	Charmonium States and Accumulator Beam Parameters	6
2.1.	Accumulator Lattice Parameters	22
3.1.	ARF1 Cavity Parameters	48
4.1.	Update Frequency of the Ramped Devices	72
4.2.	Orbit Length Measurements	82
4.3.	Results of η Measurements	85

ABSTRACT

The Fermilab Accumulator was built primarily as an 8 GeV kinetic energy antiproton storage ring. Recently it was modified for use in a medium energy experiment studying charmonium states. In the experiment, an intense antiproton beam was decelerated from the operating energy to specific energies in the charmonium region between 6.8 GeV and 3.8 GeV, and collided with protons from an internal hydrogen gas jet target. In order to decelerate the beam below 5 GeV, transition must be crossed. The method adopted for Accumulator transition crossing was to raise the value of γ_t slowly while the antiproton beam circulated in the ring unbunched. During Accumulator transition crossing with this coasting beam, longitudinal coherent instability was observed which limited the machine performance. Measurements for identifying the major source of the longitudinal instability were made with a resistive wall current monitor and a dedicated Schottky detector. Measurement results are presented and compared with the simulations. The Accumulator operation in the experiment is also recorded in this thesis, which includes deceleration of the $\bar{p}$ beam, transition crossing, and measurements of the beam energy and energy spread. In addition, since knowledge of the longitudinal impedance is important for instability studies, beam-based measurements of the Accumulator longitudinal impedance is described. The principle, the experimental setup, and measurement results are discussed.

CHAPTER I

INTRODUCTION

The Fermilab Antiproton Source Accumulator is an 8.9 GeV (total energy) antiproton storage ring which collects and stores antiprotons for operation of the Tevatron collider. Since 1987 it has been modified for use in a medium energy experiment studying charmonium states. The experiment (E760) is conducted with circulating antiproton beam of energy between 6.8 GeV and 3.8 GeV colliding with protons from an internal hydrogen gas jet target. This requires that the $\bar{p}$ beam accumulated at 8.9 GeV be decelerated to the appropriate energy.

In a synchrotron accelerator or storage ring, the acceleration of charged particles is achieved by a time-dependent radio frequency (RF) electric field generated by RF resonant cavities. The RF field also insures the stability of particles with energy deviations away from the nominal beam energy by grouping the particles into bunches equally spaced around the ring. Because particles of different momenta have different velocities and travel along different orbits, a beam with a finite momentum spread will normally have a finite revolution frequency spread. However, at a certain energy that depends upon the ring design, all particles can have the same revolution frequency. This energy is called the transition energy. At the transition energy, the lack of frequency spread inevitably produces longitudinal coherent instabilities which cause the beam momentum spread to increase and may lead to beam loss at high beam intensities. The design value of the Accumulator transition energy is 5.1 GeV. In order to perform E760 below 5 GeV, it is important to cross transition with no beam loss and as little increase in the beam momentum spread as possible.

This thesis is a study of longitudinal coherent beam instability in the Accumulator transition region, which limits the machine performance in E760 operation. The antiproton beam remains unbunched during the process of transition crossing. The thesis research includes measurements in both the time and frequency

to identify the major source of the longitudinal instability, its cure, and computer simulations for comparison with the measurement results and for better understanding of beam behavior near transition. This research is unique because until now there have been no published results on transition studies with unbunched beams. The thesis also records the Accumulator performance in E760.

The following sections of this chapter give an overview of the E760 experiment and the Accumulator operation in connection with the project. The production of antiproton beam for experimental use is the standard operation of the Antiproton Source, which is briefly described first.

1.1 Fermilab Antiproton Source Operation

The Fermilab Antiproton Source was constructed as part of the Tevatron 1 project [1] which enabled Fermilab to produce proton-antiproton collisions in the Tevatron accelerator. Antiprotons are produced when 120 GeV protons are extracted from the Main Ring at the F17 and directed onto a tungsten target in the $\bar{p}$ station. Negatively charged particles which emerge from the target with a momentum of 8.9 GeV/c are collected and transported to the Debuncher. After circulating in the Debuncher for a millisecond, only the antiprotons survive. After two seconds the antiprotons are transferred to the Accumulator, and another batch of antiprotons is injected into the Debuncher. Between Accumulator injection cycles the antiprotons are stochastically cooled and gradually a dense stack of antiprotons is built up. The layout of the extraction line, the target station, the Debuncher, and the Accumulator is shown in figure 1.1.

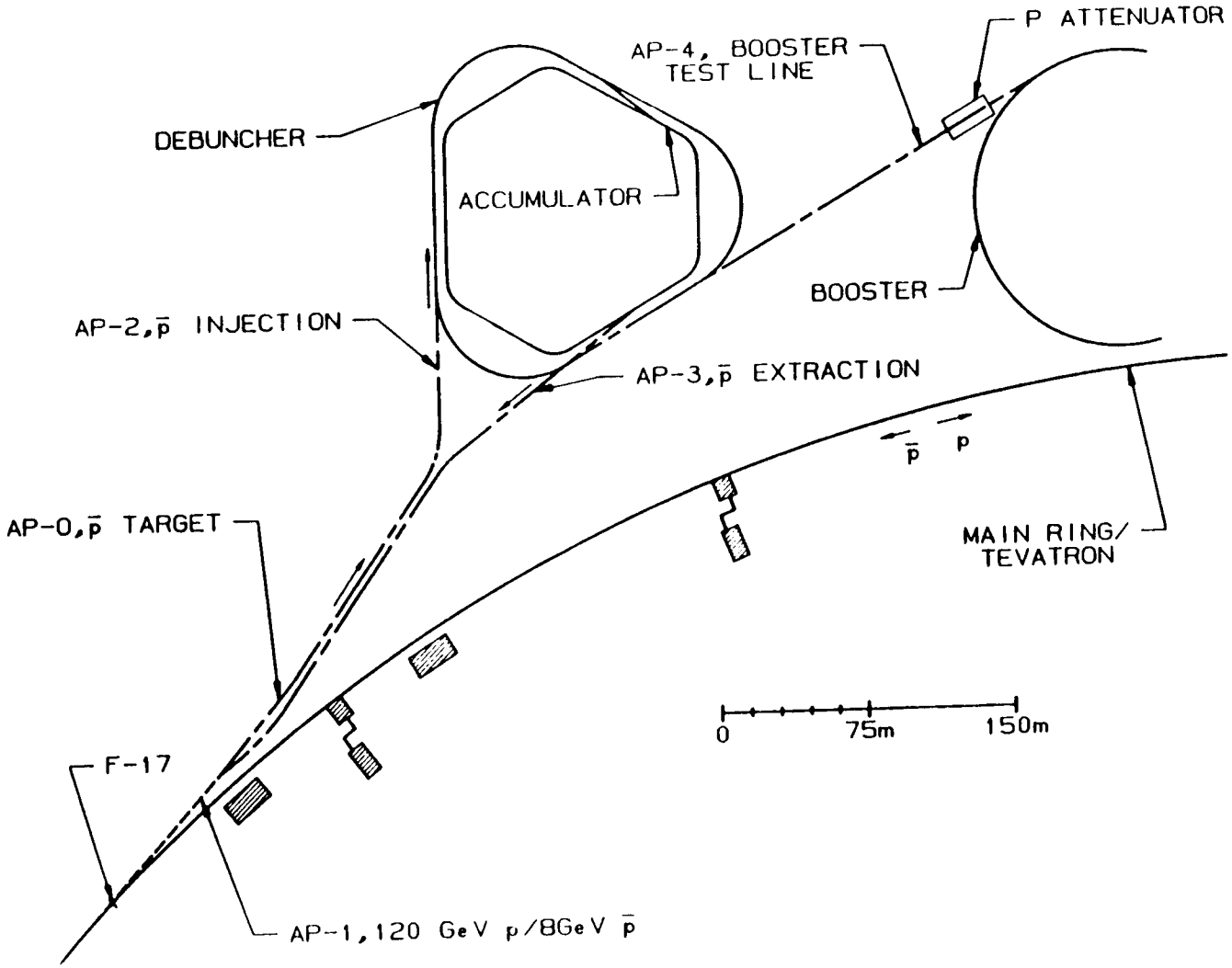

Figure 1.1. A Schematic View of the Fermilab Antiproton Source (ref. [2], p. 150).

1.2 About E760 Experiment

During the construction of the Fermilab Antiproton Source in 1981, it was realized that the Accumulator could also be used for studying medium energy antiproton interactions [2]. In March 1985, an experiment studying charmonium states from $p\bar{p}$ collisions in the Accumulator was proposed and approved as Fermilab E760 [3].

1.2.1 Physics Motivation of E760. High energy particle physics studies the constituents of matter and the laws which govern their behavior. In the current view of particle physics the fundamental constituents of matter are point-like, structureless objects of spin $\frac{1}{2}$: the quarks and leptons. Quarks undergo the strong, electromagnetic and weak interactions. They are the building blocks of the hadrons such as the proton and neutron. On the other hand, leptons—like the electron and muon—do not feel the strong force and interact only via the electromagnetic and weak force.

The current Standard Model [4,5,6] of high energy physics assumes six varieties (flavors) of quarks and six leptons. The quarks carry charges $\frac{2}{3}e$ or $-\frac{1}{3}e$ and are grouped in three generations: (u, d) (c, s) (t, b). Substantial evidence for existence of the t quark has not yet been found. Like the six leptons (e^-, ν_e) (μ^-, ν_μ) (τ^-, ν_τ), the quarks are spin $\frac{1}{2}$ fermions. In addition, quarks carry a new quantum number called "color". The requirement of color confinement, *i.e.*, no state explicitly carrying color can be observed, summarizes the fact that no free quarks have ever been found. Their properties can be inferred from the observed features of hadrons. According to the quark model, hadrons are divided into two categories: baryons, each containing three quarks, and mesons, which contain a quark and an antiquark. Heavy mesons are defined to contain at least one heavy c or b quark. Mesons consisting of two heavy quarks of the same kind are referred to as quarkonium states.

Quarkonia provide direct evidence for the strong binding force between quarks. Quantum chromodynamics (QCD) [7,8,9,10,11] is the theory of the strong

interaction of quarks, but it can be studied precisely only as a perturbation series expansion in powers of the running coupling strength $\alpha(q^2)$, where q is the 4-momentum transferred in the interaction. Since $\alpha(q^2)$ monotonically decreases with q^2, it requires large momentum transfer to get sufficiently small $\alpha(q^2)$ so that first few terms in the expansion are reasonably accurate. However, the momentum for producing the charmonium states, which are $c\bar{c}$ bound states, is in the non-perturbative region where no precise quantitative predictions can be obtained from QCD. However, in the case of bound states of heavy quarks such as c and b, the relativistic effects are expected to be small and a non-relativistic treatment should be a good approximation. The treatment is based on Schrödinger equation with a static potential. Various potential models have been developed to describe the mass spectra, decay widths, *etc*, of the heavy mesons such as J/ψ family. Some are inspired by QCD whereas the others are purely phenomenological [12,13,14,15].

Because those models are by no means a perfect description of the binding force between the quarks, it is desirable to be able to measure the masses, lifetimes, and quantum numbers of the mesons precisely. The complete and precise measurements of those parameters will provide a strong indication as to whether QCD is the right theory for the strong interaction.

1.2.2 E760 Project. The aim of E760 is to study the formation of charmonium states ($c\bar{c}$ bound states) in $p\bar{p}$ collisions. The existing information on mass, width, and decay branching ratios of charmonium states has come primarily from e^+e^- collider experiments, where only the states of the quantum numbers of the photon γ ($J^{PC} = 1^{--}$) can be directly formed as the consequence of the first order QED process: $e^+e^- \rightarrow \gamma \rightarrow c\bar{c} \rightarrow$ final states. In general, states formed in this fashion can be studied with high precision due to the fact that the precision in measurement of the state parameters depends on the knowledge of the initial state. Previously the 1^{--} states had been measured precisely, while the knowledge about other states was still uncertain and not sufficient to provide stringent test on theoretical predictions. With the $p\bar{p}$ initial state, all charmonium states can

Table 1.1. Charmonium States and Accumulator Beam Parameters

State	J^{PC}	mass [16] (GeV/c^2)	P_{beam} (GeV/c)	β
η_c	0^{-+}	2.981	3.679	0.9690
J/ψ	1^{--}	3.097	4.066	0.9744
χ_0	0^{++}	3.415	5.192	0.9844
χ_1	1^{++}	3.511	5.552	0.9860
${}^1P_1$	1^{+-}	unobs.	5.593	0.9862
χ_2	2^{++}	3.556	5.724	0.9868
η_c'	0^{-+}	3.595	5.874	0.9875
ψ'	1^{--}	3.686	6.232	0.9889
${}^1D_2$	2^{-+}	unobs.	6.742	0.9905
${}^3D_2$	2^{--}	unobs.	6.742	0.9905

be reached directly, so it is advantageous to be able to set up $p\bar{p}$ experiments for that purpose. The states of interest are listed in Table 1.1.

When studying a certain interaction process with cross section σ, the event rate R for that process(the number of events of interest per unit time) is proportional to σ. The proportionality constant is a machine dependent quantity and is called the luminosity L:

$$R = \sigma L \ . \tag{1.1}$$

As far as a high energy physics experiment is concerned, the beam energy and luminosity are the two most important machine parameters. However, since it has been difficult to design a source for $p\bar{p}$ reaction which was comparable in luminosity and energy definition to the one provided by an e^+e^- collider, that type of experiment had not been considered feasible until the emergence and use of the antiproton storage facility. Using an intense $\bar{p}$ beam produced in the antiproton storage ring, which collides with a high density H_2 gas jet target, the desired luminosity can be achieved [17]. In the Fermilab Accumulator, a luminosity of $1 \times 10^{31}\text{cm}^{-2} \cdot \text{s}^{-1}$ at the required energy can be reached with a stochastically cooled beam of 1.5×10^{11} antiprotons colliding with a H_2 gas jet with density of $\sim 1.2 \times 10^{14}\text{atoms/cm}^3$ and thickness of $\sim$ 0.9cm (cf. ref. [3], p. 15).

1.3 Accumulator Operation in E760

Figure 1.2 shows a plane view of the Fermilab Accumulator. The ring has a circumference of 474.1 meters, and its shape was chosen as the most efficient in terms of the stochastic cooling requirements.

In order to set up and run E760 in the Fermilab Accumulator, a number of operations and modification to the Accumulator need to be made. There are a number of basic issues in accelerator design that must be studied in connection with this project. The interest of the accelerator physics comes from the study of the physical phenomena in the process as well as the development of the technology for the new operating mode.

It is necessary to use stochastic cooling and stacking technique to acquire a beam of about 1.5×10^{11} $\bar{p}$'s at the normal operating momentum 8.9 GeV/c. As seen from Table 1.1, the experiment requires a momentum range from 3.7 GeV/c to 6.7 GeV/c, so the antiproton beam has to be decelerated from its normal operating energy down to the required energy. Also, it is necessary to vary the beam energy throughout that range over small increments to scan for resonances in the vicinity of a given beam energy. Therefore, there must be novel provisions for the control of magnet power supplies, as well as the RF systems to allow this variable energy operation.

During the deceleration from the normal operating energy to that required by the experiment, the transition energy must be crossed. Conventionally, the beam is accelerated (decelerated) quickly through transition to avoid substantial increase in the momentum spread of the beam. Because of the restrictions from the Accumulator RF system and magnet power supplies, the E760 deceleration can only proceed in a slow rate of 40 MeV/sec. Deceleration through transition with this rate will cause catastrophic beam loss. The transition crossing thus has to be carried out with some mechanism other than the standard one. The method adopted for the Accumulator transition crossing is as follows: while the beam is circulating unbunched in the machine at an energy near transition, the transition energy is raised to a value above the beam energy. In this process,

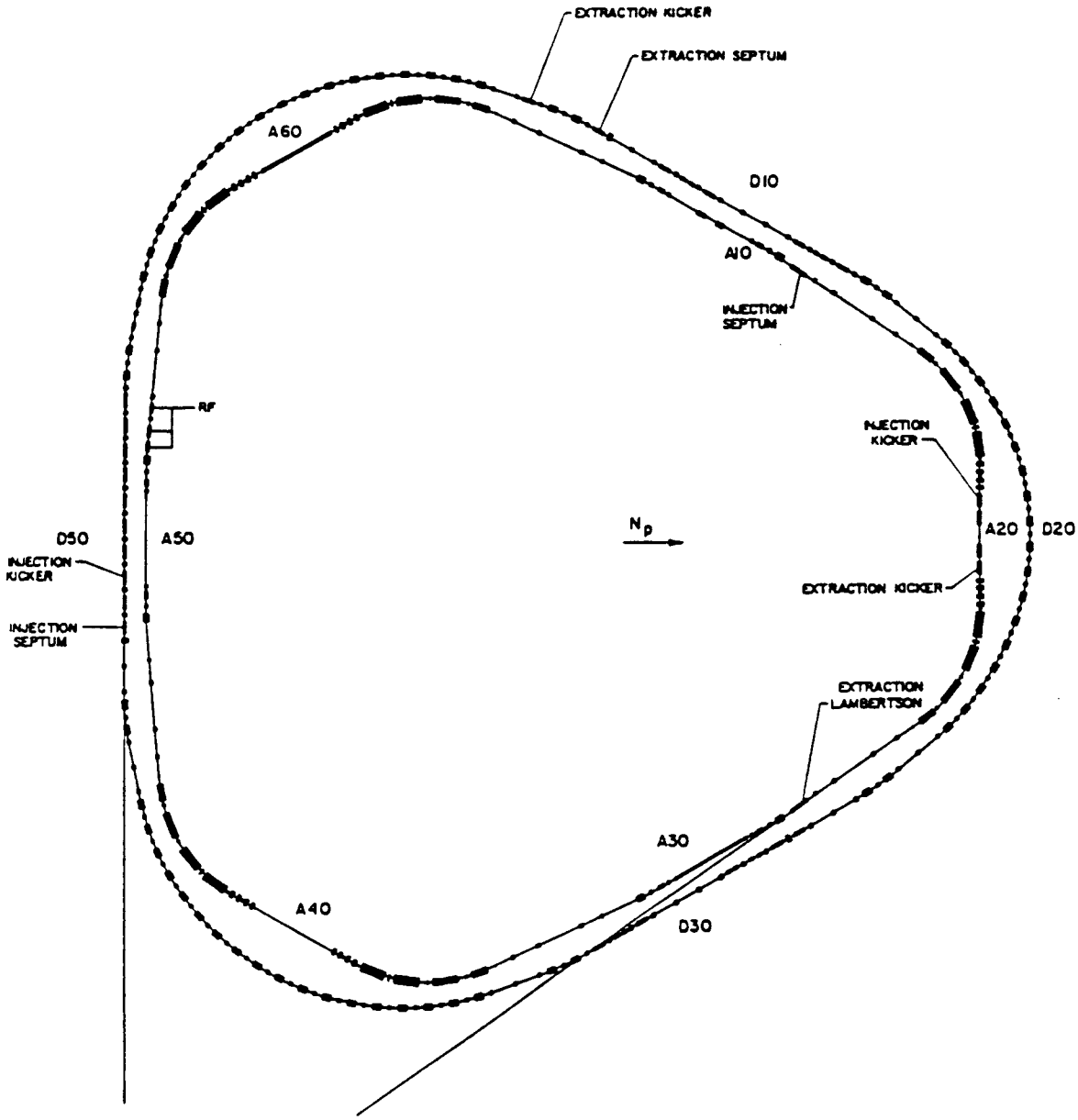

Figure 1.2. Schematic Layout of the Fermilab Accumulator. (Ref. [1], fig. 5-1.)

coherent instabilities driven by the beam self field causes the increase of the beam momentum spread and therefore limits the Accumulator performance.

When the coasting $\bar{p}$ beam collides with the gas jet, it needs to be cooled continuously to avoid an blow-up of its transverse size or momentum spread; therefore the cooling system must be modified to achieve that purpose at variable energy. Cooling is also necessary after the transition crossing.

Since the setup is, in effect, a spectroscopy experiment, the momentum spread of the beam determines, to a great extent, the mass resolution of the experiment, and the absolute accuracy of the beam momentum measurement defines the final errors on particle/resonance mass measurement. In E760, the momentum spread of the beam is measured from its revolution frequency spread, and the beam momentum is determined from the orbit length measurement done with the Accumulator beam position monitors.

CHAPTER II

FUNDAMENTALS OF ANTIPROTON STORAGE RINGS

Antiproton storage rings are machines which accumulate antiprotons produced by repeated bombardments of a high energy proton beam on a metal target to make an intense $\bar{p}$ beam for the later $p\bar{p}$ collisions. They have general features of a proton synchrotron accelerator as well as some special features required by $\bar{p}$ accumulation. The accumulated $\bar{p}$ beam in a storage ring is constrained to travel about a time-independent orbit at a constant energy. When the beam intensity is low, the interactions among the beam particles and the self-field generated by the beam interacting with its environment are negligible, and the motion of each particle is controlled only by external electromagnetic fields provided by magnets and radio frequency (RF) cavities. At high beam intensities, the motion of a particle is influenced by both the external electromagnetic field and the field induced by the beam itself.

This chapter introduces some general concepts regarding the properties of the single particle motion in a synchrotron accelerator. The coherent phenomena caused by the beam induced field in longitudinal direction will described in Chapter 5.

There are many papers and lecture notes about single particle dynamics in a synchrotron [18,19], all based on a paper by Courant and Snyder [20] in 1958.

2.1 Lattice

In a synchrotron or storage ring, almost all magnets which constrain charged particles have a symmetry plane on which the magnetic field at all points is perpendicular to the plane. This plane is called the median plane or midplane. Magnetic multipoles with midplane symmetry [21] and RF cavities play an important role in particle dynamics. The design orbit, which is a closed curve in midplane such that a particle of a certain energy can move on the curve, is determined by dipole (bending) magnets and drift spaces. The transverse motion of a charged particle, *i.e.*, the motion in the plane perpendicular to the direction of particle motion along the design orbit, is controlled principally by magnetic fields generated by magnetic multipoles. In particular, quadrupoles provide the transverse beam focusing which is essential for stability in the transverse plane. RF cavities are responsible for the stability of particle in the direction along the design orbit, which is called the longitudinal direction.

The word "lattice" in accelerator physics terminology refers to the pattern in which magnets and intervening spaces are placed to form the ring. This section discusses the motion of a charged particle in the transverse plane, and explains the design of the Accumulator lattice show the unique character of the antiproton storage ring lattice.

2.1.1 Transverse Motion. The motion of a charged particle in an electromagnetic field is described by Lorentz force equation:

$$\frac{d\mathbf{P}}{dt} = e(\mathbf{E} + \mathbf{v} \times \mathbf{B}) \ . \tag{2.1}$$

In modern synchrotrons and storage rings, the energy of a particle is high enough for the particle's velocity to be close to that of light. From the above equation it is easy to see that, because the velocity of the particle is perpendicular to the magnetic field and its value is approximately the speed of light, a bending magnetic field of one Tesla gives the same bending force as an electric field of 3×10^8 V/m. The guiding field is thus provided by the bending magnets. The curvature of the

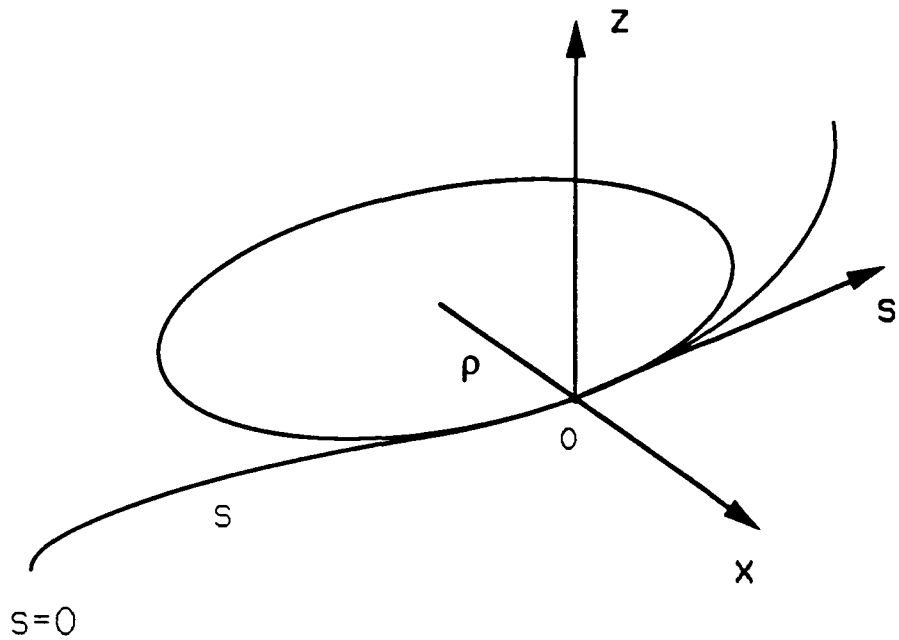

Figure 2.1. Curved Coordinate System. **s**-axis is in the tangential direction of the design orbit at a particular s, **x** and **z** are axes in the transverse plane, and ρ is the radius of curvature.

design orbit of a particle with the momentum P is related to the magnetic field by

$$\frac{1}{\rho}[m^{-1}] = 0.2998\frac{B[T]}{P[GeV/c]} \ . \tag{2.2}$$

In other words, for a particle traveling along the design orbit, its momentum is just the product of the magnetic field and the radius of curvature. This particle is referred to as the reference particle.

When a particle has the same momentum as that of the reference particle, but is not moving along the design orbit described above, it follows a different trajectory. The coordinate system shown in Figure 2.1 is usually employed to describe the transverse motion of a particle. The distance s along the reference orbit is measured from some fixed point to the point closest to the particle position, x is the displacement of the particle from the design orbit in the plane of bending (which is horizontal for the Accumulator), and z is the vertical displacement of the particle from the design orbit. The particle with transverse displacement

experiences quadrupole fields which are linearly proportional to the amount of displacement, in addition to the dipole fields. The total magnetic field near the design orbit is

$$B_x = \frac{\partial B_x}{\partial z} z \ , \qquad B_z = B_0 + \frac{\partial B_z}{\partial x} x \ , \tag{2.3}$$

where $\frac{\partial B_x}{\partial z}$ and $\frac{\partial B_z}{\partial x}$ are the vertical and horizontal field gradients respectively. For quadrupole magnets, the field gradients in the two planes are equal in magnitude and opposite in sign, and they are both constants (independent of transverse displacements). In a proton synchrotron or antiproton storage ring, the transverse displacements are small compared to the radius of curvature of the bending magnets, so are the transverse components of the particle velocity compared to its longitudinal component. Then equation (2.1) becomes

$$\begin{cases} x'' - (K - \frac{1}{\rho^2})x = 0 \\ z'' + Kz = 0 \end{cases} , \tag{2.4}$$

for the horizontal and the vertical planes respectively, where $'' = d^2/ds^2$, and K is the quadrupole focusing strength which is proportional to the field gradient and inversely proportional to the momentum of the reference particle:

$$K = \frac{e}{P} \frac{\partial B_z}{\partial x} \ . \tag{2.5}$$

From equation (2.4) it can be seen that the motion of the particle in the horizontal plane is a harmonic oscillation about the design orbit when $\frac{K<1}{\rho}$ and so is the motion in the vertical plane when $K > 0$. Machines in which K satisfies both these conditions for bounded motion in both planes can only provide weak focusing force [22] on each plane. In modern synchrotrons and storage rings quadrupole magnets produce strong focusing strength, therefore horizontal focusing and vertical focusing are not achieved at the same time. Inside a quadrupole, the curvature of the trajectory is zero ($\frac{1}{\rho=0}$) because there is no bending force applied to the particle on the design orbit. Therefore a horizontally focusing quadrupole must be vertically defocusing, and vice versa. A FODO cell which consists of a focusing

quadrupole and defocusing quadrupole with drift space between them can provide focusing force on both plane if the the quadrupole strength and the length of the drift space are properly adjusted (cf. ref. [19], p. 7).

Both equations of motion in (2.4) can be written in the general form

$$y'' + K(s)y = 0 \ , \tag{2.6}$$

which is called Hill's equation. Because the design orbit is closed, the oscillator strength K(s) has a periodicity of the design orbit circumference. It corresponds to harmonic oscillation with a variable coefficient $K(s)$. For historical reasons this transverse oscillation about the design orbit is called the betatron oscillation or betatron motion. The general solution to Hill's equation is traditionally written as

$$y(s) = \sqrt{\varepsilon_i \beta(s)} \cos(\Phi(s) - \Phi(0)) \ , \tag{2.7}$$

where the beta function $\beta(s)$ is a periodic function over the ring. It represents the variation of the betatron oscillation amplitude as the particle travels along its trajectory, and is determined by the focusing strength around the ring:

$$\frac{1}{2}\beta'' + K(s)\beta - \frac{1 + \frac{1}{4}\beta'^2}{\beta} = 0 \ , \tag{2.8}$$

ε_i is the invariant amplitude of the oscillation (independent of s). It is related to y and y' by

$$\varepsilon_i = \gamma y^2 + 2\alpha y y' + \beta y'^2 \ , \tag{2.9}$$

where α and γ are defined as

$$\alpha = -\frac{1}{2}\beta' \ , \qquad \gamma = \frac{1 + \alpha^2}{\beta} \ . \tag{2.10}$$

The variables α, β, and γ are called Twiss parameters. The phase advance around the ring is

$$\Phi(s) = \int_0^s \frac{ds'}{\beta(s')} \ . \tag{2.11}$$

For one turn, the betatron phase change $\Delta\Phi = 2\pi\nu$, where ν is called the betatron tune. The betatron tune represents the number of betatron oscillations per revolution:

$$\nu = \frac{1}{2\pi}\oint \frac{ds}{\beta(s)}\,, \tag{2.12}$$

where the integral is carried out over the circumference. Betatron tunes can be changed by changing the quadrupole strength in the ring.

The general solution to equation (2.7) can also be expressed in matrix form. The mapping from s_0 to s is given by

$$\begin{bmatrix} y(s) \\ y'(s) \end{bmatrix} = \begin{bmatrix} \sqrt{\frac{\beta}{\beta_0}}(\cos\Delta\Phi + \alpha_0 \sin\Delta\Phi) & \sqrt{\beta_0\beta}\sin\Delta\Phi \\ -\frac{(\alpha-\alpha_0)\cos\Delta\Phi+(1+\alpha\alpha_0)\sin\Delta\Phi}{\sqrt{\beta_0\beta}} & \sqrt{\frac{\beta_0}{\beta}}(\cos\Delta\Phi - \alpha\sin\Delta\Phi) \end{bmatrix} \begin{bmatrix} y(s_0) \\ y'(s_0) \end{bmatrix}. \tag{2.13}$$

The trajectory of a particle in (y, y') phase space forms an ellipse in the case of betatron oscillation, with the enclosed area $\pi\epsilon_i$. Figure 2.2 shows the phase space trajectory.

There are two concepts which are extensively used to assess the beam quality in the transverse plane and the machine operation: the emittance and aperture. The emittance is the phase space area occupied by the beam, and is frequently denoted by ϵ. The phase space area associated with the largest ellipse that the machine will accept is called the admittance or the aperture of the machine.

The above discussion has assumed that the particle undergoing betatron oscillation has no momentum error. When a particle has a momentum deviation from the reference particle, according to equation (2.2), it follows an orbit with different radius of curvature and circumference. The distortion of the closed orbit is in the plane of bending, *i.e.*, the horizontal plane. At an azimuthal position s, the displacement of the closed orbit from the design orbit per fractional momentum change is called the dispersion at that point. Since the closed orbit deviation

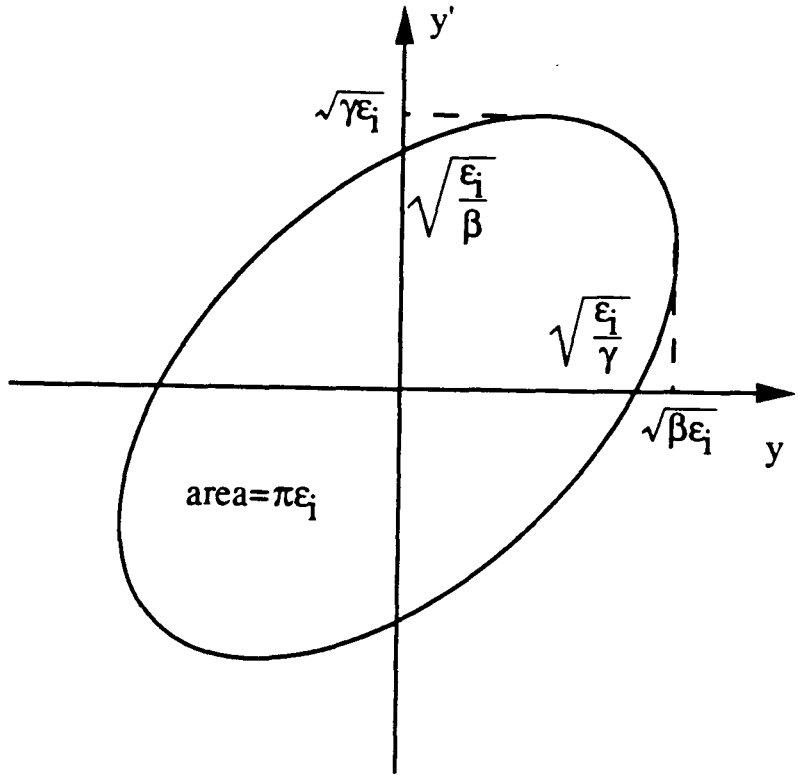

Figure 2.2. Trajectory of a Particle in Transverse Phase Space. The ellipse represents the trajectory of a particle undergoing betatron oscillation with invariant amplitude ε_i, at a location in the machine with Twiss parameters α, β, and γ.

and betatron oscillation amplitude for such particle is much smaller than the radius of curvature of the storage rings, the horizontal displacement of the particle can be written as

$$x(s) = x_\beta(s) + D(s)\frac{\Delta P}{P} , \tag{2.14}$$

where $x_\beta(s)$ is given by equation (2.7) and $D(s)$ is the dispersion function. When the horizontal betatron tune ν_x is not an integer, the dispersion function is expressed as

$$D(s) = \frac{\sqrt{\beta_x(s)}}{2\sin\pi\nu_x}\int_s^{s+C}\frac{1}{\rho}\sqrt{\beta_x(s')}\cos(\Phi(s') - \Phi(s) - \pi\nu)\,ds' \tag{2.15}$$

In a synchrotron or a storage ring, the orbits which the particles with different momenta follow are radially separated in non-zero dispersion regions ($D \neq 0$), whereas in zero dispersion regions different orbits have the same radial position.

When ν_x is an integer, the particle runs into a resonance: because all magnets are not identical, each turn the off-momentum particle experiences a bending field error. When the betatron tune is an integer this error accumulates turn by turn and leads to the betatron amplitude growth.

Momentum deviation also leads to a focusing strength error experienced by the particle. From equation (2.8) the fractional change in the beta function, due to a focusing strength error $k(s)$, can be expressed as

$$\frac{\Delta\beta(s)}{\beta(s)} = \frac{1}{2\sin 2\pi\nu}\int_s^{s+C} k(s')\beta(s')\cos 2(\Phi(s') - \Phi(s) + \pi\nu)\, ds' \tag{2.16}$$

when $\nu \neq$ half-integer. From equation (2.11) the tune shift is then obtained as

$$\Delta\nu = \frac{1}{4\pi}\oint \beta(s)k(s)\, ds\ . \tag{2.17}$$

The change in tune due to momentum is called the chromaticity by analogy with the chromatic aberrations in light optics. The chromaticity ξ is defined by

$$\Delta\nu = \xi\frac{\Delta P}{P}\ . \tag{2.18}$$

Since a quadrupole magnet always presents a focusing strength error to a particle with momentum deviation, it has the natural chromaticity

$$\xi = -\frac{1}{4\pi}\oint K(s)\beta(s)\, ds\ . \tag{2.19}$$

If the chromaticity is large, off-momentum particles will still strike the resonances even if the tunes for the reference particle are well away from them. Thus both the dispersion and the chromaticity act to define the momentum aperture of the ring.

For chromaticity compensation, a magnet that presents a gradient which is a function of momentum is needed. Sextupole magnets are normally used for this purpose. In the horizontal plane, the sextupole field is of the form

$$B_z = G_s x^2\ , \tag{2.20}$$

and the field gradient on a displaced orbit is

$$\frac{\partial B_z}{\partial x} = 2G_s D\frac{\Delta P}{P} \ . \tag{2.21}$$

The tune change due to the sextupoles in the ring is obtained from equations (2.17) and (2.21):

$$\Delta\nu = \frac{e}{2\pi P}\left[\oint \beta(s)G_s D(s)ds\right]\frac{\Delta P}{P} \ . \tag{2.22}$$

Sextupoles inevitably introduce intrinsically non-linear aberrations, and so reduce the machine's aperture [23].

2.1.2 Accumulator Lattice. The Accumulator lattice (cf. ref. [1], sec. 5.3) consists of three identical sections and has a mirror symmetry about the high dispersion straight section. The circumference of the ring is 474.13 meters. Figure 2.3 shows the lattice functions of one sextant (A10 to A20), and table 2.1 at the end of this subsection lists the detailed Accumulator parameters at the normal accumulation energy.

The unique character of the Accumulator lattice design is motivated by the requirements imposed by the stochastic cooling and RF stacking which are techniques for increasing the $\bar{p}$ beam intensity and beam density in phase space.

The requirement for high dispersion regions can be explained with equation (2.14) which is the description of the horizontal orbit of a single particle, at a fixed point s_0 in the ring:

$$x(t) = \sqrt{\varepsilon_x \beta_x(s_0)}\cos(\nu_x\omega_0 t + \phi_0) + D(s_0)\frac{\Delta P}{P} \ . \tag{2.23}$$

The first term describes the betatron oscillation, the second term accounts for the displacement caused by the momentum deviation from the central orbit. The first term changes rapidly over one revolution since the phase advance per turn ($2\pi\nu_x$) is about 13.2π in the Accumulator. The RF stacking takes place in a total of a few thousand turns, while cooling takes takes place on a time scale characterized by a few hundred thousand to a few billion turns. Thus the betatron term can be

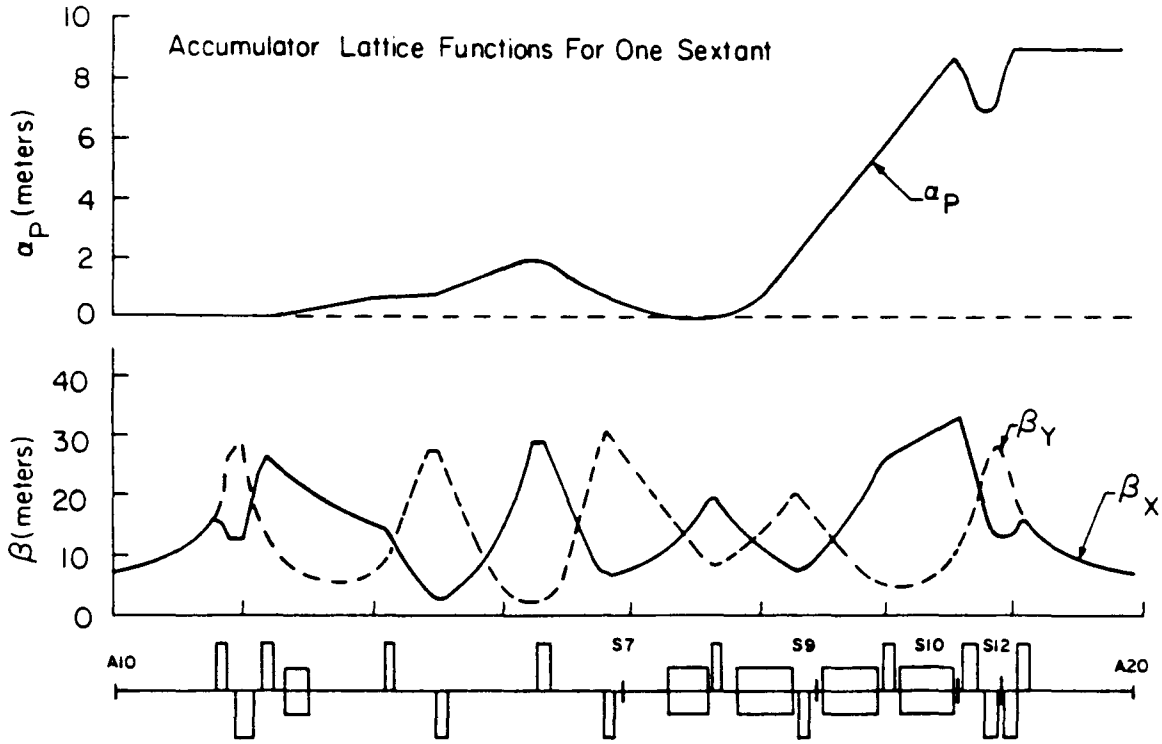

Figure 2.3. Accumulator Lattice for One Sextant (ref. [1], fig. 5-2). The sketch at the bottom shows the A10 - A20 lattice: the horizontal line represents the design orbit, the rectangles straddling the orbit line represent the dipole magnets, the bars above/below the orbit line represent the horizontally focusing/defocusing quadrupoles, and the line segments across the orbit line are used to represent the sextupoles.

approximated by its average value which is zero when studying RF stacking and momentum cooling. With the non-zero dispersion D, it is possible to move the beam horizontally within the beam pipe, by changing the momentum of the beam (RF stacking or unstacking), so that various operations do not interfere with one another. Also the momentum error of the beam can be determined by measuring the horizontal deviation of the beam orbit in a high dispersion region, provided the betatron amplitude is small there (second term is dominant). In fact this is the method of the momentum measurement used in the Accumulator momentum cooling systems. Figure 2.4 shows the horizontal beam position at the end of A20

high dispersion straight section. The relative positions of the injection, stacking, and core orbits to the central orbit at that place are 80.3 mm, 14.7 mm, and −63.3 mm ("−" means radially inward from the central orbit).

Betatron cooling and momentum correction (for momentum cooling) are performed in zero dispersion regions ($D = 0$). Also the zero dispersion region is the place for the RF cavities. Betatron coolings systems should be put in the zero dispersion region since the information there can be from the pure betatron motion. That the momentum correction should be done in the zero dispersion section can be explained with equation (2.23): in non-zero dispersion sections any sudden change in the momentum will cause a compensating change in the betatron amplitude (the position cannot change abruptly). Usually this causes the heating in betatron oscillation amplitude if D is large. In the zero dispersion region of the Accumulator the betatron cooling systems compensate for any heating caused by small values of dispersion.

2.2 Longitudinal Phase Space and RF Stacking

In a synchrotron, a particle is accelerated repetitively. The acceleration of a particle in a synchrotron is achieved by using resonant cavities, called RF cavities, which generates sinusoidal electric fields in the longitudinal direction. The time-dependent electric field produced inside RF cavities not only provides a net energy gain to the particles being accelerated, but also insures the stability of particles with energy deviation from the nominal beam energy. This is true except when the beam energy is near the transition energy, where the beam loses the stability in its longitudinal motion. In an antiproton storage ring, RF cavities are used for RF stacking to increase the beam intensity. This section describes the motion of a particle in the longitudinal phase space, the transition energy, and the RF stacking process in an antiproton storage ring.

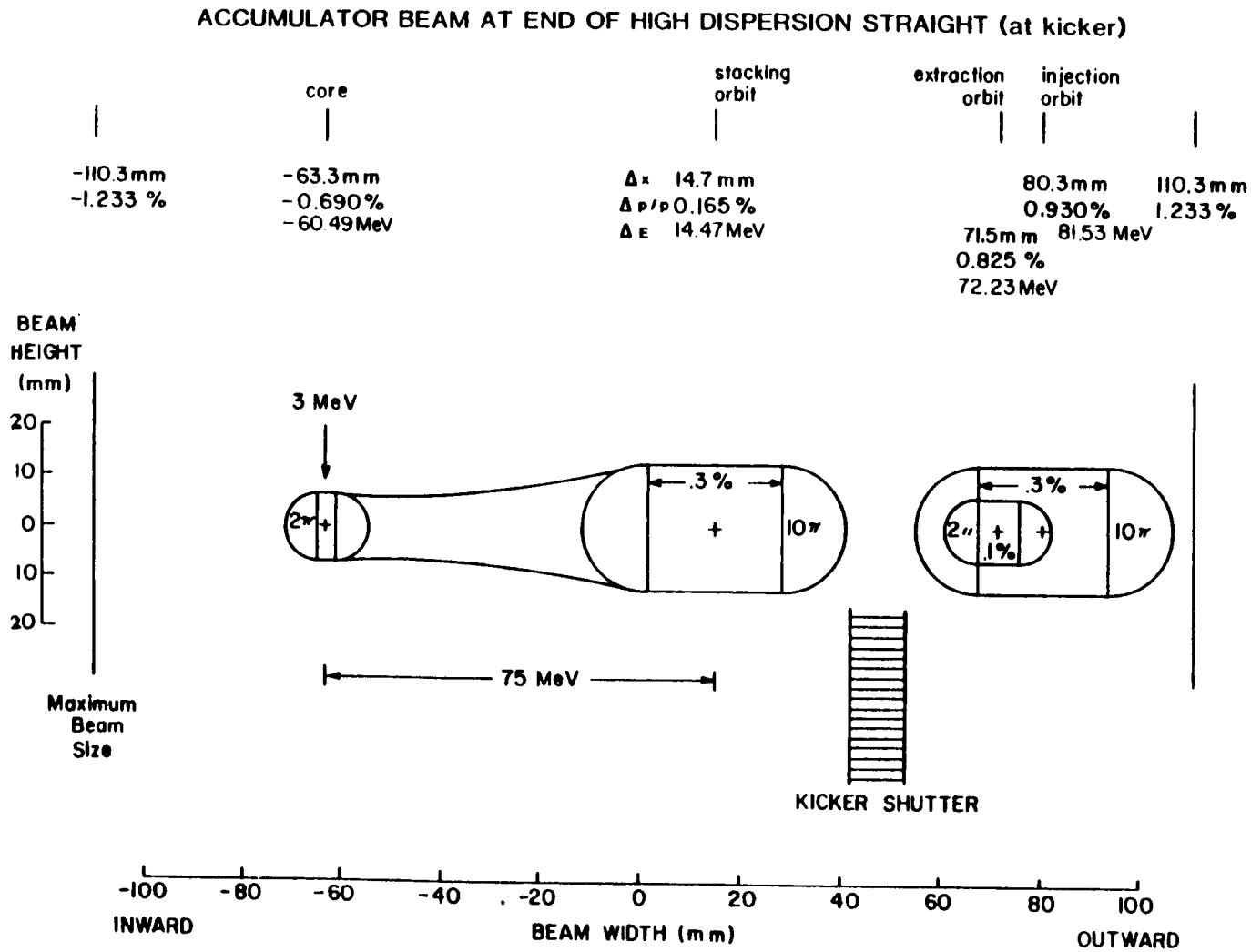

Figure 2.4. Accumulator Beam Position at the End of A20 (ref. [1], fig. 5-3).

Table 2.1. Accumulator Lattice Parameters

	Injection orbit	Stacking orbit	Central orbit	Core orbit
Kinetic energy (GeV)	8.03	7.96	7.95	7.89
$\Delta P/P$ (%)	0.930	0.165	0	-0.690
ν_x	6.616	6.611	6.611	6.614
ν_y	8.611	8.611	8.611	8.611
ξ_x	2.05	1.13	0.90	-0.22
ξ_y	0.21	0.32	0.33	0.33
γ_t	5.37	5.42	5.43	5.50
η	0.023	0.023	0.023	0.022

2.2.1 Longitudinal Motion. In a synchrotron or a storage ring, an accelerating RF cavity is operated at a frequency which is an integer multiple of the nominal revolution frequency: $\omega_{\rm rf} = h\omega_0$, where h is called the harmonic number. A particle with the nominal energy and circulates on the nominal trajectory will always experience the same RF phase, called the synchronous phase ϕ_s, when passing the RF cavity. This particle is called the synchronous particle. It will be seen in the following discussion that, if the synchronous phase is properly chosen, non-synchronous particles will oscillate about the synchronous phase, *i.e.*, a properly chosen synchronous phase leads to phase stability. In the case where there is an RF field and stable phase oscillation, the beam becomes h consecutive bunches uniformly populated around the ring. When this happens the beam is said to be "bunched". For a beam circulating in the ring with no RF field, the azimuthal distribution is uniform, and several names are applied to such a beam: unbunched beam, coasting beam, d.c. beam, and so on.

For the purpose of explaining the longitudinal motion of a particle, it is assumed that there is only one RF cavity located at a certain azimuth in the ring.

At each turn during acceleration, the phase of a non-synchronous particle relative to the synchronous phase is defined as the RF angular frequency multiplied by the time delay of the particle relative to the synchronous particle. Therefore the time delay due to a momentum error leads to the equation for the phase of the particle, and the time delay in one revolution is just the difference in the revolution period. The revolution period of a particle T is related to the circumference of the ring C and the velocity of the particle v as $T = C/v$. The fractional change in T associated with deviations in C and v is

$$\frac{\Delta T}{T_0} = \frac{\Delta C}{C} - \frac{\Delta v}{v} , \tag{2.24}$$

and, with linear approximation, it can be expressed in terms of the fractional change in momentum as

$$\frac{\Delta T}{T_0} = -\frac{\Delta f}{f_0} = \eta \frac{\Delta P}{P} , \tag{2.25}$$

where f_0 is the revolution frequency of the synchronous particle, and $\eta = \alpha_p - 1/\gamma^2$ is called the frequency slip factor. The momentum compaction α_p is defined as

$$\alpha_p = \frac{dC/C}{dP/P} . \tag{2.25}$$

It is the fractional change in the circumference per fractional change in the particle momentum, and is usually written as $1/\gamma_t^2$. When the momentum of a particle increases, so does its speed. But the circumference the particle follows also increases. For an extremely relativistic particle, gaining energy does not cause its speed to increase, but the path length for that particle increases. Therefore it takes longer for a particle of higher energy to go around a full turn. When the energy is low, the velocity change dominates. At a certain energy, the competing effects cancel. This energy is called the transition energy and is equal to $\gamma_t mc^2$, where $m = 0.938 GeV/c^2$ is the proton mass. This property is reflected through η.

The γ_t of a circular machine is determined by the dispersion:

$$\frac{1}{\gamma_t^2} = \frac{1}{C} \oint \frac{D(s)}{\rho(s)} \, ds , \tag{2.26}$$

where $D(s)$ is the dispersion function expressed in equation (2.15) and C the circumference of the ring.

Now the difference equations of motion for a particle which has completed an nth turn and received an nth kick at the RF cavity can be written as:

$$\begin{cases} \Delta E_{n+1} = \Delta E_n + eV(\sin\phi_n - \sin\phi_s) \\ \phi_{n+1} = \phi_n + 2\pi h\eta \left(\frac{\Delta E}{E_s}\right)_{n+1} \end{cases}, \tag{2.27}$$

where V is the peak RF voltage, ϕ_n is the phase in the beginning of the nth turn, ϕ_{n+1} is the phase at the end of n turn, ΔE_n and ΔE_{n+1} are the corresponding energy deviations.

In antiproton storage rings and many proton synchrotrons a large number of turns are required to change a particle's state appreciably; in other words, within one turn, the relative phase change among beam particles is negligible. Therefore for longitudinal motion turn-by-turn difference equations can be approximated by differential equations.

Let ϕ be the phase and the E be the total energy of a particle. The relative phase x and energy deviation ϵ from the synchronous particle are defined as

$$\begin{aligned} \epsilon &= E(t) - E_s(t) \\ x &= \phi(t) - \phi_s(t) \end{aligned}. \tag{2.28}$$

The equations of motion describing the longitudinal phase and energy oscillation can be written as:

$$\begin{cases} \dot{\epsilon} = \frac{\omega_s}{2\pi} eV(\sin\phi - \sin\phi_s) \\ \dot{x} = \dfrac{h\omega_s\eta}{\beta_s^2 E_s} \cdot \epsilon \end{cases}, \tag{2.29}$$

where $\beta_s = v_s/c$.

When small-amplitude motion is concerned, *i.e.*, when ϵ and x are small, equation (2.29) can be linearized as:

$$\begin{cases} \dot{\epsilon} = \frac{\omega_0}{2\pi} eV\cos\phi_s \cdot x \\ \dot{x} = \dfrac{h\omega_0\eta}{\beta_s^2 E_s} \cdot \epsilon \end{cases}. \tag{2.30}$$

The equation for x is obtained by taking the second derivative of x and substituting for $\dot{\epsilon}$ in the above equation,

$$\ddot{x} + \Omega_s^2 x = 0 \ , \tag{2.31}$$

where

$$\Omega_s = \sqrt{-\frac{h\omega_0^2 \eta e V \cos\phi_s}{2\pi\beta_s^2 E_s}} \tag{2.32}$$

In order for a particle to perform bounded oscillations around the synchronous phase when above transition ($\gamma > \gamma_t$), the factor $\cos\phi_s$ must be negative, whereas when below transition $\cos\phi_s$ must be positive. When this condition is satisfied, the stable oscillation of particle's phase and energy is called the synchrotron oscillation with Ω_s being the synchrotron frequency.

A particle undergoing synchrotron oscillations follows a closed trajectory in the (x, ϵ) phase space. For small-amplitude oscillation the trajectory is the familiar ellipse. The region in this phase space for which the motion is stable is called the "bucket", which in principle can be obtained by solving equation (2.29). For a stationary bucket ($\sin\phi_s = 0$), the bucket area has the form

$$A_{s.b.} = \frac{8\beta_s}{h\omega_s}\sqrt{\frac{heVE_s}{2\pi|\eta|}} \qquad \text{(eV·sec)} \ , \tag{2.33}$$

and the bucket height is:

$$H_{s.b.} = \frac{4\beta_s}{h}\sqrt{\frac{heVE_s}{2\pi|\eta|}} \ . \tag{2.34}$$

When $\sin\phi_s \neq 0$, the beam changes its energy. In this case the phase space description using the bucket is valid only if the energy change is slow, more precisely, the synchronous energy changes little in time $1/\Omega_s$:

$$\frac{\omega_0}{\Omega_s}\frac{eV\sin\phi_s}{E_s} \ll 1 \ . \tag{2.35}$$

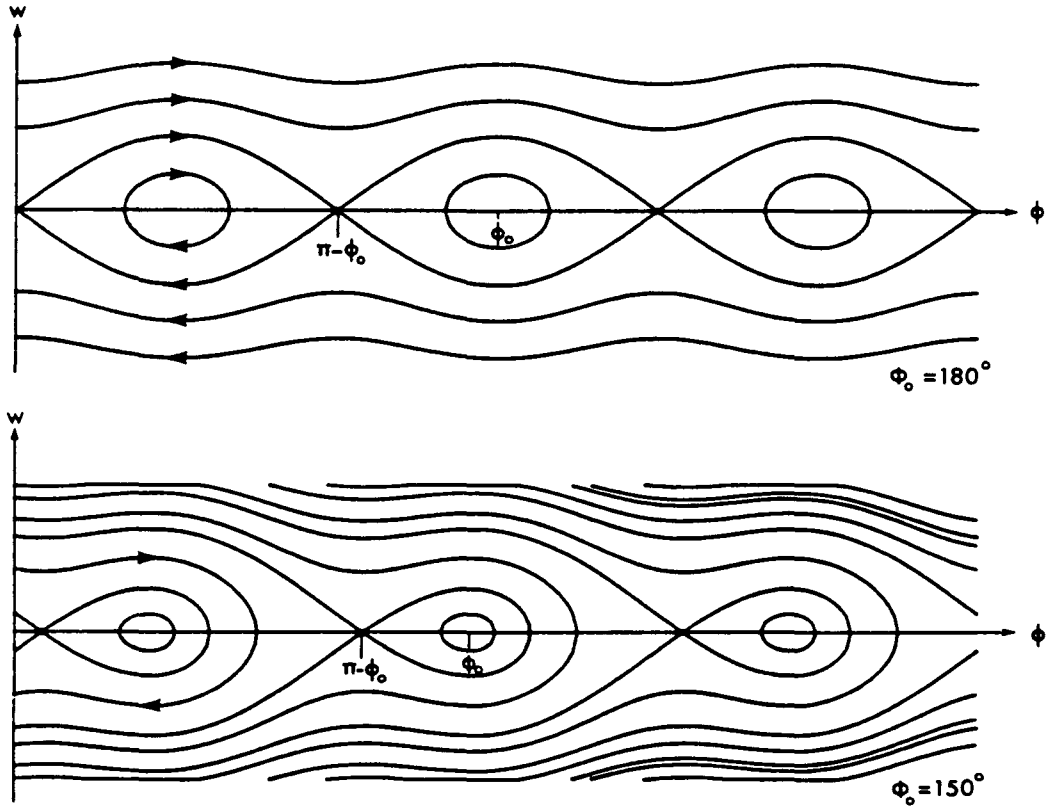

Figure 2.5. Buckets in Longitudinal Phase Space (ref [18], p. 30). The top plot shows a stationary bucket with $\phi_s = \pi$, and the bottom plot shows a moving bucket with $\phi_s = \frac{5}{6}\pi$. These buckets can provide phase stability when a beam particle is above transition.

When this condition is satisfied, the motion is said to be adiabatic. Both the shape and area of an accelerating bucket are different from those of a stationary bucket. The bucket area is $A_{s.b.}$ given by equation (2.28) multiplied by a factor less than one that depends upon $\sin\phi_s$ [24].

The area in longitudinal phase space occupied by the beam is called the longitudinal emittance of the beam. In order to accelerate a beam, the bucket area must be large enough so that all the particles are captured inside the bucket. Figures 2.5 shows a stationary bucket and a moving bucket respectively.

2.2.2 RF stacking in Accumulator. The $\bar{p}$ accumulation process in an antiproton storage ring is called stacking or RF stacking because the accumulation is done with RF manipulations. The Fermilab Accumulator is designed to receive a pulse of $\bar{p}$'s from the Debuncher every two seconds and to accumulate these pulses to make an intense antiproton beam for $p\bar{p}$ collisions in the Tevatron. In the stacking process, the injected particles are captured into RF buckets on the injection orbit. Then the buckets are accelerated toward an inner orbit (the stacking orbit) in the beam pipe. Such an acceleration is done with constant bending field, just by changing the RF frequency. As the particles approach the stacking orbit the RF voltage is reduced adiabatically and finally turned off on that orbit to minimize the dilution of the bunches. The stack tail stochastic cooling system will push the particles toward the high intensity core. Then the RF is turned on again at the injection RF frequency to capture the newly injected particles, and the process is repeated. In doing so the previously injected particles will be slightly disturbed. The energy difference between points at which the RF is switched off during successive pulses is normally chosen to be approximately the bunch area divided by 2π which corresponds to the energy width of an ideally debunched pulse. The high intensity of the core is maintained by the core cooling system. Figure 2.6 illustrates the stacking process in the longitudinal phase space.

2.2.3 Transition. An antiproton storage ring is normally operated at a fixed energy far from the transition energy. The Fermilab Accumulator is operated at 8.9 GeV total energy, its design value of γ_t is 5.43. But because the E760 experiment conducted in the Accumulator requires an antiproton beam in the energy region of 4.2 GeV to 6.8 GeV, the beam must be decelerated through the transition energy. At transition ($\eta = 0$) all particles have the same revolution period. The relative phase of each particle remains the same, so there are no synchrotron oscillations to provide phase stability at that energy. The bucket concept can no longer be used to describe the synchrotron motion because the motion is no longer adiabatic. Nevertheless the particle behavior in the vicinity of the transition energy can still be studied by making some approximations to

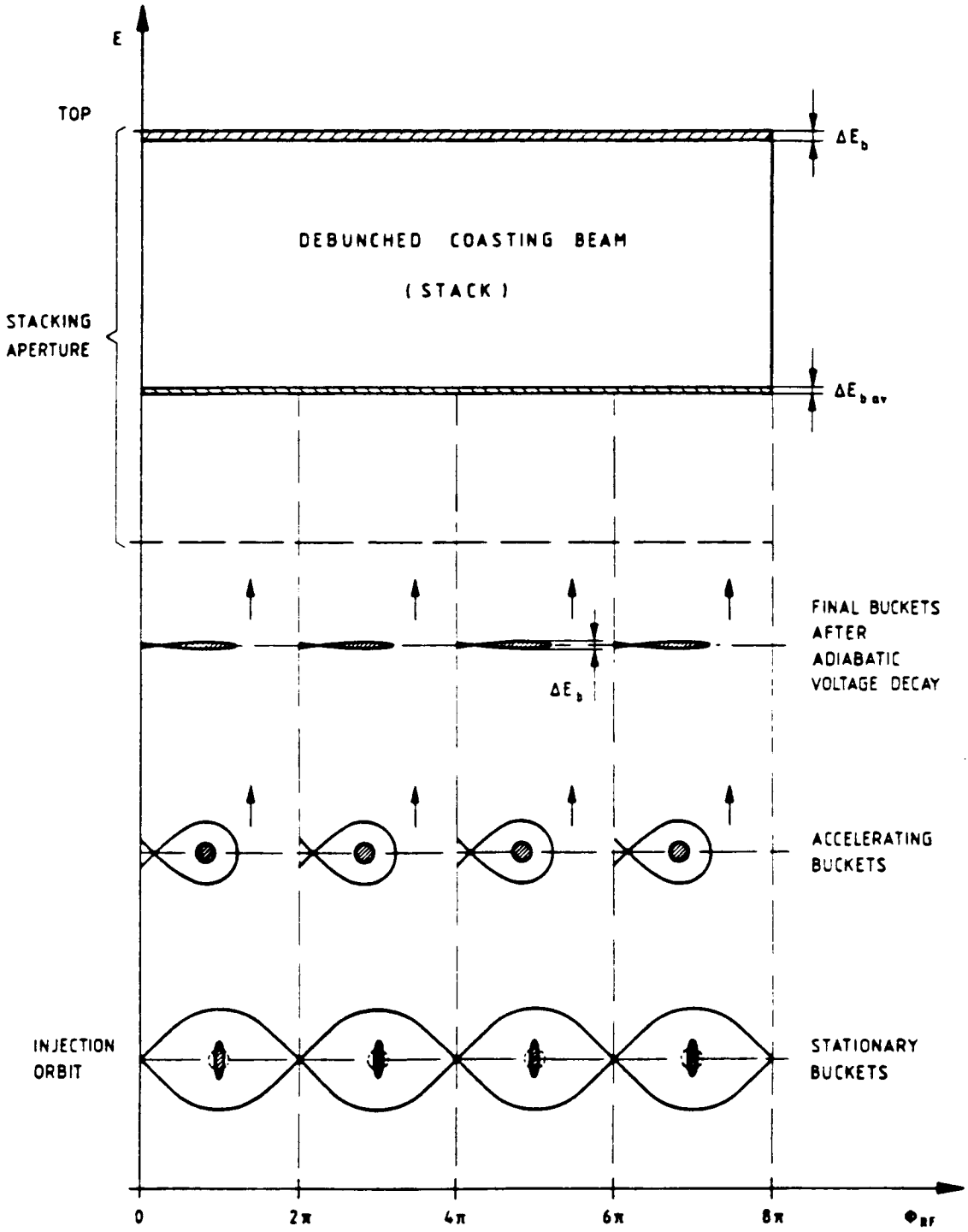

Figure 2.6. RF Stacking in Phase Space (ref. [25], p. 201). The injected beam is captured by RF on the injection orbit and moved toward the stack core. As the bunches approach the core the RF buckets are slowly (adiabatically) reduced and then turned off.

equation (2.29). The change in γ_s in the region of interest is assumed to be linear in time:

$$\gamma_s = \gamma_t + \dot{\gamma}_s t \ , \tag{2.36}$$

where t is the time measured from the transition, *i.e.*,

$$\begin{aligned} t < 0 &\quad \text{below transition;} \\ t = 0 &\quad \text{at transition;} \\ t > 0 &\quad \text{above transition.} \end{aligned} \tag{2.37}$$

Then equation (2.29) becomes

$$\ddot{x} - \frac{1}{t}\dot{x} + \xi t x = 0 \ , \tag{2.38}$$

where

$$\xi = -\frac{h\omega_s^2 eV \cos\phi_s \dot{\gamma}_s}{\pi m c^2 \gamma_t^4} \ , \tag{2.39}$$

and

$$T_c = |\xi|^{-1/3} \tag{2.40}$$

is the characteristic time during which the motion of the particle is non-adiabatic.

The solution to equation (2.38) is

$$x = |t| \left\{ \begin{matrix} A \\ A' \end{matrix} J_{\frac{2}{3}} \left(\frac{2}{3}\sqrt{|\xi t^3|} \right) + \begin{matrix} B \\ B' \end{matrix} J_{-\frac{2}{3}} \left(\frac{2}{3}\sqrt{|\xi t^3|} \right) \right\} \ . \tag{2.41}$$

If the particle arrives at transition at $t = 0$, in other words, the RF phase shift happens at the right time,

$$A = A' \ , \qquad B = B' \ . \tag{2.42}$$

The trajectory in the phase space above and below transition is the same except that the particle reverses its direction along that trajectory. If the particle arrives at the transition at the wrong time, the phase shift does not happen at $t = 0$, the solution for above and below transition must be matched at $t \neq 0$, so the

solution is no longer symmetric. Since only small amount of momentum increase is permitted when going through the transition, there is only limited tolerance on this mis-timing.

If all the particles arrive at the RF cavity at the same time at transition, each particle gets the same amount of energy increase and the momentum spread remains unchanged. In reality the particles arrive at the RF cavity at different times, each particle gets a different kick, but that does not change the particles' revolution period or their relative position among each other, and the momentum spread of the beam gets larger.

2.3 Stochastic Cooling

The stochastic cooling process has been developed to increase the phase space density of the $\bar{p}$ beam in both the transverse and longitudinal phase spaces [26]. The basic design of a stochastic cooling system consists of a pickup electrode an amplifier system, and a kicker electrode. The pickup is used to measure the position or momentum error of the particle, this error signal is amplified and sent to the kicker electrode which is used to remove the measured error. The reduction of the betatron oscillation of one particle by a pickup and a kicker is used in Figure 2.7 to show the idea of the stochastic cooling. In the simplest case, the pickup consists of two parallel plates on opposite sides of the beam. If the beam is not centered, its signal induced on one plate exceeds the signal on the other plate. The difference between the two signals is a measure of the position error. The kicker electrode in principle has a similar arrangement of plates on which a transverse electromagnetic field is created which deflect the particle. Since the pickup detects the position and the kicker corrects the angle, their spacing is chosen to correspond to a quarter of the betatron oscillation plus and integer number of half wavelengths. In reality, because a pickup has finite bandwidth W, it actually

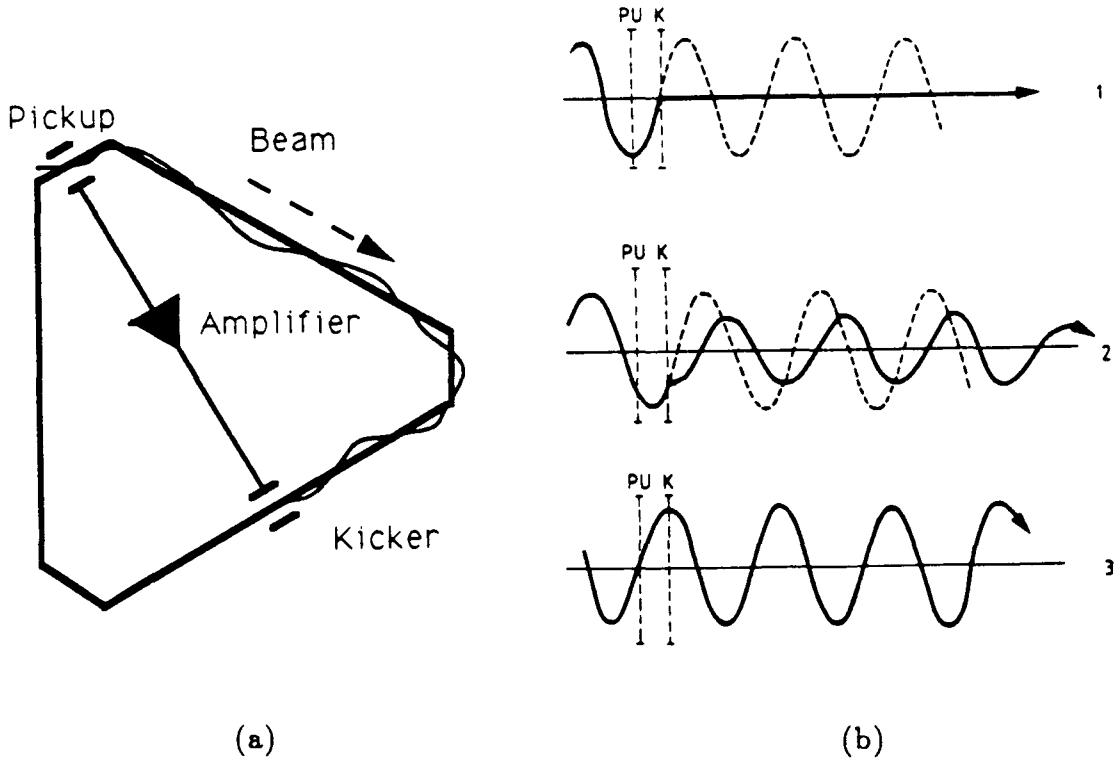

Figure 2.7. The Principle of Betatron Stochastic Cooling. (a) Basic set up. (b) The importance of betatron phase: for the kicker to completely remove the oscillation (ideal case), the pickup location should be such that the particle passes through the pickup with the maximum displacement.

measures the rms error of a group of particles, called a sample, which has the length of $T_s = \frac{1}{2W}$.†

The momentum cooling method used in the Accumulator is called the Palmer cooling (cf. ref. [26], p. 89): the pickups are placed in the A60 high dispersion straight section where the horizontal displacement caused by the betatron oscillation is negligible compared to that contributed by the momentum deviation. Thus the measurement of the momentum error is converted to the measurement of the position error. At A30 zero dispersion straight section, the particle receives a momentum "kick" which is proportional to the position error detected at A60.

---

† This is the Nyquist theorem in filtering theory.

Stochastic cooling is characterized by a cooling rate which represents how fast the rms position error gets reduced. Let

$$\Delta(x^2) = x_c^2 - x^2 \ , \tag{2.43}$$

where x_c is the corrected position. If $x_{\rm rms}^2$ is the sample variance, then the cooling rate can be written as

$$\frac{1}{\tau_{x^2}} = -f_0 \frac{\Delta(x_{\rm rms}^2)}{x_{\rm rms}^2} = \frac{2W}{N}\left[2g\left(1 - \frac{1}{\tilde{M}^2}\right) - g^2(M+U)\right] \ , \tag{2.44}$$

where g is the gain, which is proportional to the amplification (electronic gain) of the system and the number of particles in one sample, N is the total number of particles of the beam, and U the noise-to-signal ratio. Both M and $\tilde{M}$ are called the mixing factors: owing to the momentum spread and the corresponding difference in path length, particles belonging to different samples may get mixed. If it takes M turns to get a complete mixing (refreshed random sample) from the kicker to the pickup, the cooling rate would be reduced by a factor of M. The slowing down of the cooling process due to the mixing from the pickup to the kicker is represented by $\tilde{M}$, and it is proportional to M:

$$M = \alpha\tilde{M} \ , \qquad \alpha = \frac{\text{path length from PU to K}}{\text{path length from K to PU}} \ . \tag{2.45}$$

The beam path from pickup to kicker is made shorter than that from kicker to pickup. In other words, α is small.

The study of the stochastic cooling process in the frequency domain involves more details, and it is lengthy to go through the derivations. Simply speaking, since the motion of an antiproton in the ring is periodic with the revolution frequency f_0, its frequency spectrum appears as lines at nf_0 (n=0,1,2,...). A particle of different revolution frequency has the lines at different positions in the frequency domain. Thus the spectrum of the beam with frequency spread Δf_0 consists of peaks at the revolution harmonic nf_0 with the width $n\Delta f_0$, which is called the

Schottky signal and will be explained in more detail in the next section. From the pickup electrodes, the signal containing the information of the frequency distribution of the beam is amplified and filtered in the path to the kickers, then kicker electrodes correct the desired frequency components.

From the analysis in the frequency domain the expression of M for momentum cooling can be obtained, which shows that the cooling should be conducted at an energy far enough from the transition energy in order to have a sufficient cooling rate:

$$M = \frac{f_0 \beta^2 E \bar{\psi}(E)}{W N |\eta|} \ln\left(\frac{f_{max}}{f_{min}}\right) , \tag{2.46}$$

where f_{max} and f_{min} are the upper and the lower limit of the cooling system respectively, and $\bar{\psi}(E)$ is the average particle density (number/eV). For betatron cooling, a factor of 0.5 should be multiplied to the RHS of the above expression.

Besides the cooling rate, the momentum distribution of the beam during the stochastic cooling process is of more interest since it contains information about peak density, density in the tail of the energy distribution, asymmetry, and so on. The Fokker-Planck equation describes the evolution of the beam profile:

$$\frac{\partial \psi}{\partial t} = \frac{\partial}{\partial E}\left(-F\psi + D\frac{\partial \psi}{\partial E}\right) \tag{2.47}$$

where F is the coefficient of the cooling term and D is coefficient of the heating term. The heating comes from the thermal noise of the circuit, heating due to other particles, and other sources (cf. ref. [1], p. 5-12). A derivation and discussion of this equation is given by D.Möhl, *et al.*(cf. ref. [26], pp. 91-93). The time evolution of the stack in the Accumulator is shown in figure 2.8 to demonstrate the momentum distribution during the $\bar{p}$ accumulation.

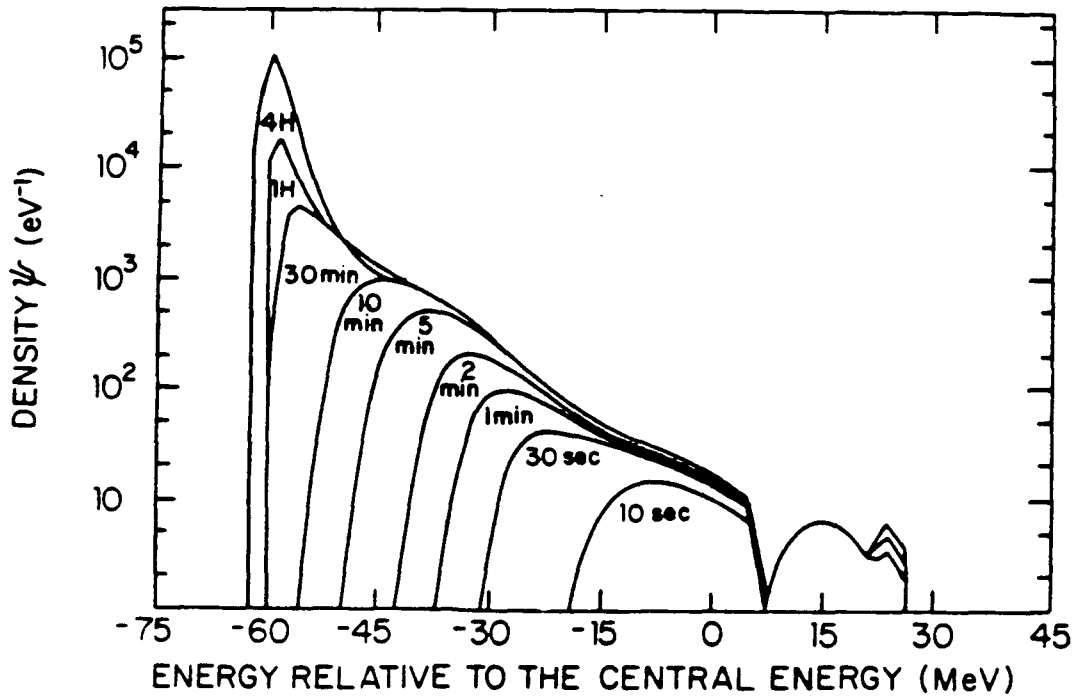

Figure 2.8. Time Evolution of the Momentum Distribution During Stochastic Accumulation(ref. [1], fig. 5-16). The small round hump on the right side is the newly injected beam, the small pit on its right is the portion of previously injected pulse displaced by RF stacking.

2.4 Beam Diagnostics

Knowledge of beam behavior in an accelerator comes from observations with beam diagnostic instruments. Some information about the transverse and longitudinal conditions of the beam can be obtained by observing the frequency spectra of the beam with specialized pickup detectors and spectrum analyzers. During the Accumulator deceleration process measurements of the beam revolution frequency, the betatron tunes, and the synchrotron frequency are all based on these beam observation principles. In this section only the longitudinal spectrum of a coasting beam is derived. A lecture note by R. Siemann [27] gives detailed descriptions about both the transverse and longitudinal spectra of a bunched beam and here only the results are given. The particle is assumed to be a proton or an antiproton

with negligible synchrotron radiation – the electromagnetic radiation produced by a charged particle moving with relativistic speed along a curved trajectory. The detector is assumed to have a uniform response over all frequencies, *i.e.*, an infinite bandwidth, and the details of the instruments will be described in the next chapter.

Mathematically a time domain function is related to its frequency spectrum by the Fourier transform. The Fourier transform of a time domain function $f(t)$ is defined as

$$F(\omega) = \int_{-\infty}^{+\infty} f(t)e^{-j\omega t}\, dt \ , \tag{2.48}$$

where $j = \sqrt{-1}$ and ω is the angular frequency variable. The inverse Fourier transform is

$$f(t) = \frac{1}{2\pi}\int_{-\infty}^{+\infty} F(\omega)e^{j\omega t}\, dt \ . \tag{2.49}$$

The angular frequency ω is a convenient variable in the Fourier transform, whereas a spectrum analyzer reads out the frequency $f = \omega/2\pi$ which is a convenient quantity when discussing measurements. In the following discussion the word "frequency" depends on the context. There is another difference between the mathematical formulae and the measurements that should be emphasized: when doing the Fourier transform the complex number form or the phasor representation is used for convenience, which gives negative frequency components in the spectrum. It should be noted that physical quantities represented by these phasors are the projections onto the real axis. In other words, a negative frequency appearing in the Fourier transform are always observed as a positive frequency with the same absolute value. Therefore the negative frequency components should be folded to the positive frequency side to get the real spectrum measured with a spectrum analyzer.

When there is no RF, a particle circulates in a machine with a constant revolution frequency ω_0, and the current measured by a detector at some azimuth θ is

$$i(t) = q \sum_{n=-\infty}^{\infty} \delta\left(t - nT_0 - \frac{\theta}{\omega_0}\right) \ , \tag{2.50}$$

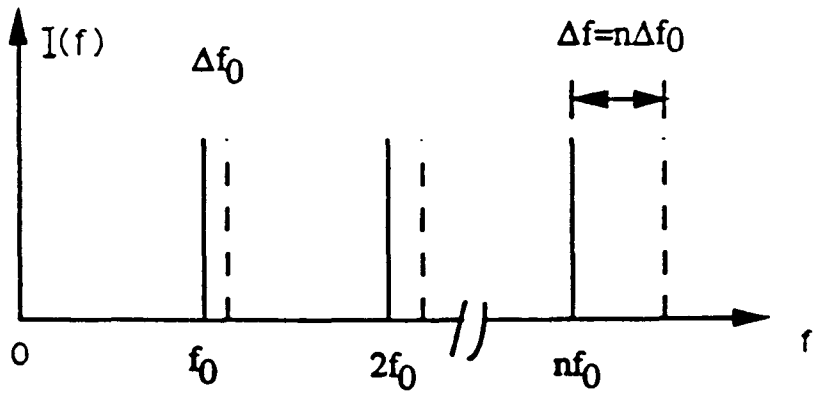

Figure 2.9. Longitudinal Spectra of Two Particles. The two particles have slightly different revolution frequencies.

where $T_0 = 2\pi/\omega_0$ is the revolution period of the particle. With the Fourier transform, the frequency spectrum of the current is found to be

$$I(\omega) = q\omega_0 \sum_{n=-\infty}^{\infty} e^{-jn\theta}\delta(\omega - n\omega_0) \ . \tag{2.51}$$

It is a series of spectral lines, represented by δ-functions, with equal height at $n\omega_0$. As mentioned before, folding the negative frequency side to the positive side gives the physical spectrum measured by a spectrum analyzer. The measured spectrum contains lines with an interval of the revolution frequency. All the a.c. components ($n \neq 0$) have the same amplitude and are twice as high as the d.c. component ($n = 0$).

If there is another particle which has a slightly different momentum from that of the first one, it then has different revolution frequency. Its spectrum is a set of lines appearing at different positions from the first set. The frequency difference at a revolution harmonic n is the difference in their revolution frequencies multiplied by that harmonic number. Figure 2.9 shows the two frequency line sets. Therefore by measuring the frequency difference at a revolution harmonic and knowing η the momentum difference can be obtained.

For a beam circulating in a machine, the situation is not that simple. Consider a group of particles with the same energy, and therefore the same revolution frequency. If these particles are assumed to be uniformly distributed in the azimuthal direction, the amplitude of the spectral line at the nth revolution harmonic is that of a single particle integrated over θ

$$I_n(\omega) = \frac{N'q}{2\pi}\delta(\omega - n\omega_0)\int_0^{2\pi} e^{-jn\theta}\, d\theta \ , \tag{2.52}$$

where N' is the number of particles having the same energy. The integral over θ is zero when $n \neq 0$, which means that no frequency or momentum measurement can be made. This is because the particles around the ring have different time delays, which is reflected by the phase angle in expression (2.51) for a single particle spectrum. If the particles are uniformly distributed around the ring, their effects on the detector cancel exactly. In reality, the beam comprises a finite number of particles. If the motions of these particles are not correlated, the cancellation cannot be exact. The calculation of the beam spectrum is the same as other statistical calculations. The particles in the beam are a finite sample drawn from the uniform distribution, and the actual beam distribution has fluctuations from the parent distribution. An equivalent way of stating the beam spectrum calculation method is that the initial phase distribution of the beam particles is assumed to be random. The current spectrum then comes from the beam fluctuation noise.

The charge density for N' particles with the same momentum is

$$\rho(\theta) = q\sum_{i=1}^{N'} \delta(\theta - \theta_i) \ . \tag{2.53}$$

The current is obtained by substituting this expression for the charge density into equation (2.51) and performing the integral over θ. The result for the nth revolution harmonic is

$$I_n(\omega) = I_n\delta(\omega - n\omega_0) \ , \tag{2.54}$$

where

$$I_n = q\omega_0 \sum_{i=1}^{N'} e^{-jn\theta_i} \tag{2.55}$$

is the amplitude of the beam current spectrum at the frequency $\omega = n\omega_0$ for a given set of N' particles. However, due to the randomness of the initial phase of each particle, the meaningful quantities are the mean and rms values of I_n, which are determined by averaging over all samples of N' particles.

The mean value of the current is

$$< I_n >= q\omega_0 \left\langle \sum_{i=1}^{N'} e^{-jn\theta_i} \right\rangle = 0 \ , \tag{2.56}$$

where <> stand for ensemble averaging. The square of the rms current is

$$\begin{aligned} < I_n^2 > &= \frac{1}{2} < I_n I_n^* > \\ &= \frac{q^2\omega_0^2}{2} \sum_{i=1}^{N'} \sum_{k=1}^{N'} e^{-jn(\theta_i - \theta_k)} \ . \end{aligned} \tag{2.57}$$

When averaged, the phase factor is equal to zero for $i \neq k$ and equal to one for $i = k$. Then the above expression becomes

$$< I_n^2 >= \frac{q^2\omega_0^2 N'}{2} \ , \tag{2.58}$$

which shows that the rms value of the current is proportional to the square root of the total number of the particles. Because the spectral line at the negative frequency side must be folded to the positive frequency side in order to give the physical spectrum of the beam measured by the spectrum analyzer, a factor of two should be multiplied to the rms current obtained from the above expression. We get

$$\sqrt{< I_n^2 >} = q\omega_0\sqrt{2N'} \ . \tag{2.59}$$

The above calculations show that, even though the average current value is zero, fluctuation or the noise of the particles generates a signal on the detector. The

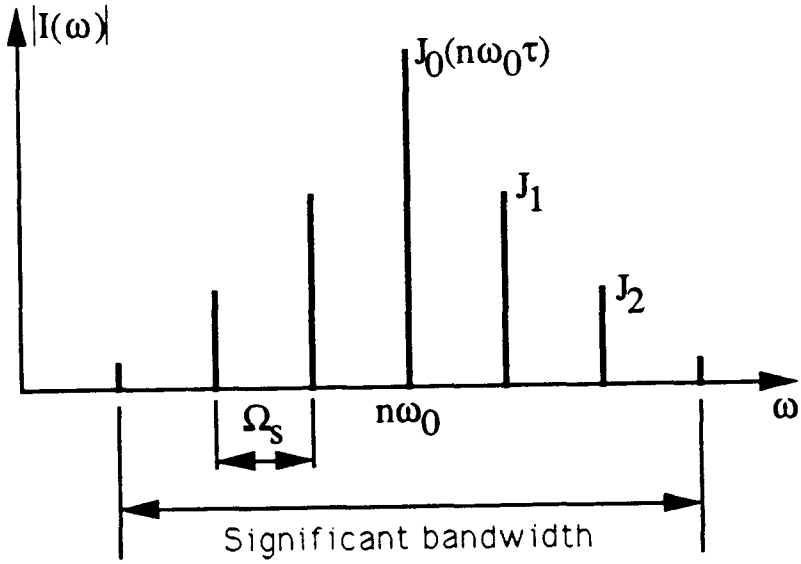

Figure 2.10. Single Particle Spectrum When RF is On.

amplitude of the signal is proportional to the square root of the number of the particles. This signal is called the Schottky signal or Schottky noise, because the noise from the beam is the signal perceived by the detector.

Because of Schottky noise, it is possible to measure the frequency spread of the beam. The momentum spread of the beam then can be obtained if the value of η is known.

When the beam is bunched, the particles inside the RF bucket perform synchrotron oscillations. The revolution frequency of a beam particle is then modulated by the synchrotron frequency. It is the same phenomenon as frequency modulation (FM) in radio engineering. Similar to a FM wave, a particle undergoing a synchrotron oscillation has a frequency spectrum that consists of lines at revolution harmonic and series of lines called, synchrotron sidebands, with interval of the synchrotron frequency. The height of a synchrotron sideband is given by Bessel's function. Figure 2.10 shows such a spectrum.

In the multiple particle case, the synchrotron sidebands are observed only because the beam has a finite number of particles and the synchrotron motions of these particles are uncorrelated. The incoherent synchrotron sideband signals

are also called the Schottky signals. It should be emphasized that signals of a bunched beam at revolution harmonics are coherent, unlike a coasting beam, because of the periodic beam structure produced by the RF. Signals from a coasting beam and a bunched beam in the Accumulator are shown in figure 2.11 as examples of the beam longitudinal spectra. Both of them are measured around a frequency corresponding to the 126th revolution harmonic of the beam at 8.9 GeV. In figure 2.11(b) the beam is bunched at the 84th harmonic with the 53 MHz RF system called ARF1.

In the transverse plane, the measured quantity is the dipole moment which is the product of the beam current and rms displacement from the center of the detector. At the location of the detector, if the closed orbit of the beam is off the center of the detector, the frequency spectrum of the beam will contain peaks at every revolution harmonic, and the synchrotron sideband may appear also if the beam is bunched. The betatron oscillations of the beam contribute to the spectrum the betatron sidebands appearing at frequencies $\omega = |m \pm \nu|\omega_0$, where m is an integer and ν is the betatron tune. The betatron tune can be written in an explicit form as the sum of an integer Q and a decimal q, *i.e.*, $\nu = Q + q$, and the frequencies at which the betatron sidebands appear are

$$\omega = |m \pm Q|\omega_0 \pm q\omega_0 = n\omega_0 \pm q\omega_0 \ , \tag{2.60}$$

where $n = |m \pm Q|$ and must be greater than one when the minus sign in front of q is taken. The above expression shows that, in the spectrum a betatron sideband is separated from its adjacent revolution harmonics by either $q\omega_0$ or $(1-q)\omega_0$. It can also be seen from the above discussion that only the fractional part of the betatron tunes is able to be measured, but the integer part of the tunes is known values and is not that important. Figure 2.12 shows a sketched transverse spectrum of an Accumulator beam.

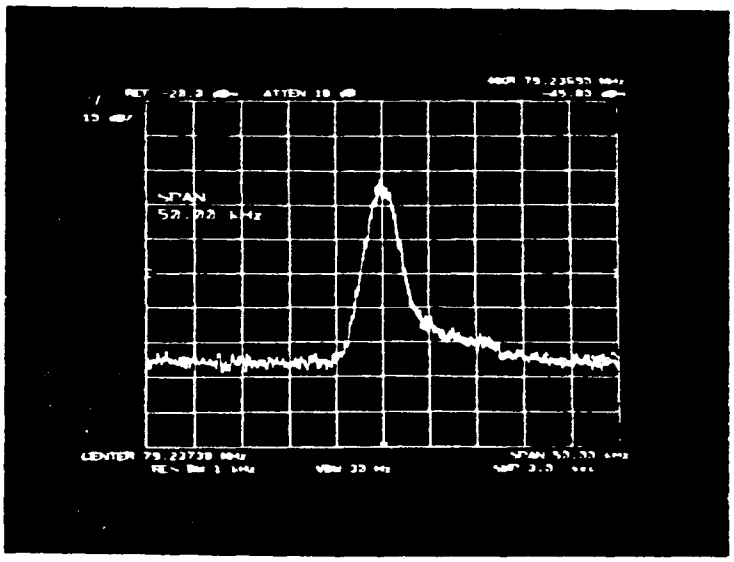

(a)

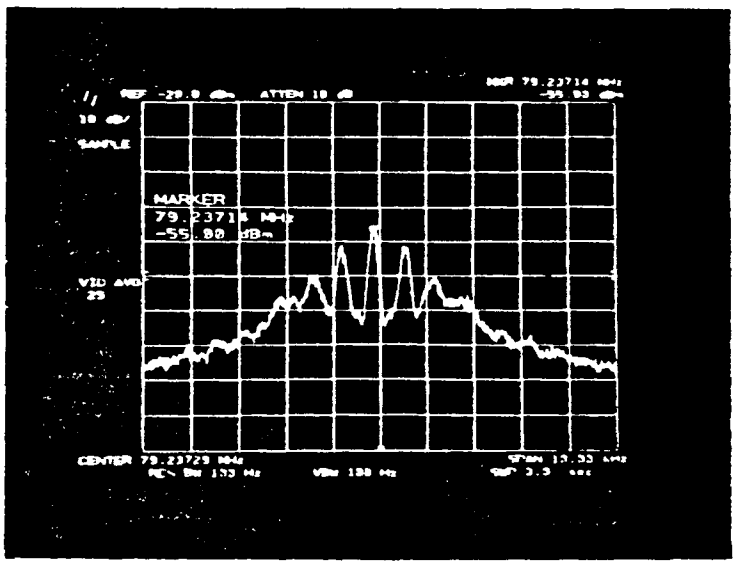

(b)

Figure 2.11. Accumulator Beam Longitudinal Spectra. They are measured around 79 MHz (h=126 at 8.9 GeV) with the Accumulator longitudinal Schottky detector. (a)The Schottky signal of an unbunched beam gives the frequency distribution of the beam. (b)The Schottky signal for a bunched beam. The central peak is the 126th revolution, and peaks on both sides are the synchrotron sidebands.

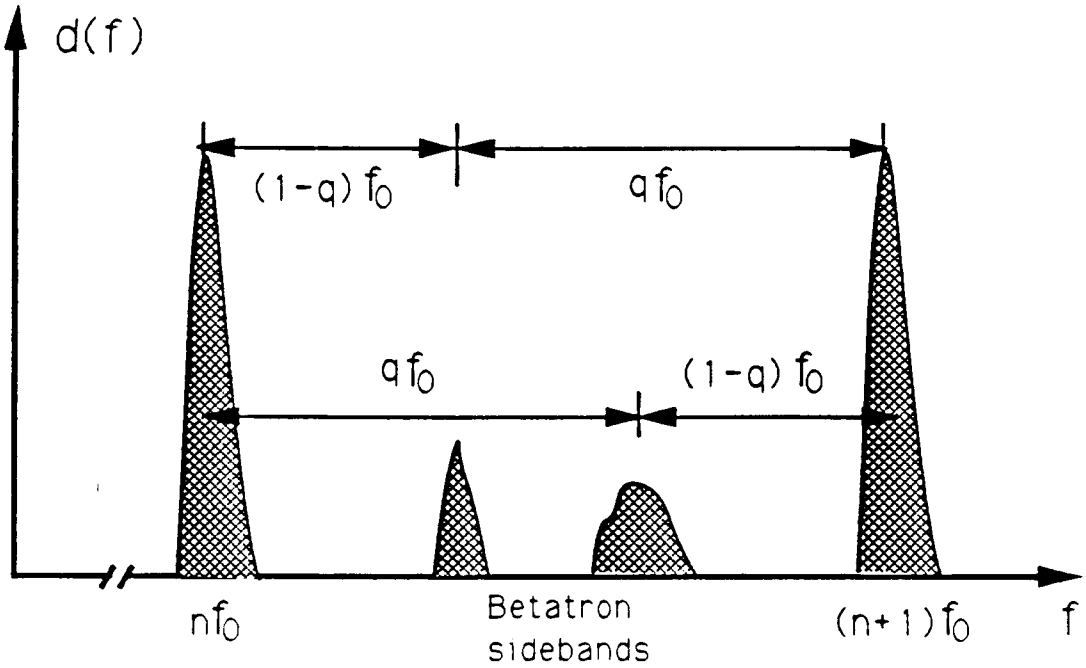

Figure 2.12. A Sketched Transverse Spectrum of an Accumulator Beam. The fractional part of the betatron tune, q, is approximately 0.611 in the Accumulator.

CHAPTER III

FERMILAB ACCUMULATOR

The Accumulator is operated at a kinetic energy of 8 GeV. The circumference of of the ring is 474.1 meters, and a particle traveling along the design orbit has a revolution period of 1.6 micro-seconds. This makes $1mA$ beam current in the machine correspond to 10^{10} particles. It is designed to receive a pulse of $\bar{p}$'s from the Debuncher every two seconds and to accumulate these pulses to make an intense antiproton beam for the later $p\bar{p}$ collisions in the Tevatron. This is achieved by using RF stacking and stochastic cooling techniques. In the accumulation process the injected pulse is captured in the injection orbit and moved toward the stacking orbit. As it approaches the stacking orbit, the RF voltage is reduced adiabatically and finally turned off on that orbit to get the minimum dilution of the bunches and minimal disturbance to the existing stack. The stack-tail cooling system will push the particles toward the high intensity core. The high intensity of the core is maintained by the core cooling systems.

During running of E760, a stacked antiproton beam is decelerated from its normal energy to different energies in the charmonium state region in the central orbit. Deceleration of the beam is carried out by an Accumulator RF system. Success of the deceleration relies on the measurements and corrections of the machine and beam parameters. Such measurements are done with the Accumulator beam diagnostic instruments such as the beam position monitors (BPMs) and the Schottky detectors. The beam needs to be stochastically cooled when colliding with the gas jet. This chapter is an overview of the Accumulator instrumentation. More details can be found in the references given in the chapter.

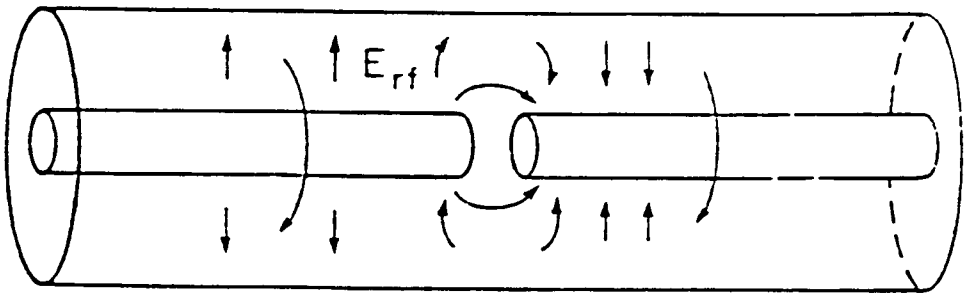

Figure 3.1. A Coaxial TEM Standing Wave Resonator (ref. [28], p. 569). It illustrates the working principle of the ARF1 and ARF3 cavities. At resonance, the maximum voltage occurs at the open end (accelerating gap) and the maximum current occurs at the shorted end.

3.1 RF Cavities

There are three RF systems in the Accumulator, named ARF1, ARF2 and ARF3 respectively. The main RF system ARF1 was built for $\bar{p}$ stacking. Its resonant frequency is at 52.8 MHz, which is close to the 84th revolution harmonic. ARF2 is a broadband cavity which is used to produce a suppressed bucket for $\bar{p}$ extraction. The newly built ARF3 system, resonating at 1.26 MHz or the second harmonic, is of high power and wide dynamic range so that it can be used for a variety of beam acceleration and capture tasks. In this section only the structures of ARF1 and ARF3 cavities are described because ARF3 was used to decelerate the $\bar{p}$ beam in E760 operation, and it was found that the longitudinal instability during the Accumulator transition crossing is mostly attributed to ARF1.

In general, RF cavities used in a circular proton accelerator are standing wave resonators which provide the required longitudinal phase space area and change the proton energy at some specific rate. In practice, instead of having simple cylindrical pill-box cavity structures, the RF cavities are designed to have the beam pipe and its accelerating gap enclosed by a shorted coaxial structure [29]. The inner conductor of the coaxial structure may be larger than the beam pipe and need not be of the same material. Such a structure is operated in a transverse electromagnetic (TEM) standing wave mode and presents resonance properties which are the same as that of a parallel RLC circuit (antiresonant circuit), when

the length of the coaxial transmission line is one quarter wavelength of the TEM wave. Figure 3.1 shows the configuration of a TEM standing wave RF cavity structure to illustrate the working principle of the ARF1 and ARF3 cavities. Each half of the structure has the characteristics of a quarter-wave TEM resonator slightly foreshortened by a capacitance at the high voltage end. This capacitance is introduced to account for the concentration of electric field, due to additional structures, such as a ceramic vacuum seal with field limiting corona rolls, in the gap region. It reduces the physical length of the transmission line. The two mirror images will be operated in push-pull mode, *i.e.*, 180° out of phase, with the two gaps combined into one in the middle, and gap voltage of twice as much. This coaxial transmission line type of design has several advantages over a simple cylindrical cavity, such as the short transit time across the gap, the intensive electromagnetic field in the gap region ready to be delivered to the beam, and the smaller physical dimension in the longitudinal direction.

ARF1 consists of two cavities: ARF1-1 and ARF1-2. They together provide peak RF voltage of 50 kV. Figure 3.2 is a side-view schematic of the configuration of one-half of a ARF1 cavity. The cavity is made of copper. The diameter and the total length of the outer shell are 36″ and 71.9″ respectively. The inner conductor has a 6″ diameter with an accelerating gap 6.75″ in width at the center sealed by ceramic. The intermediate cylinder has a length of 52.6″ and diameter of 19.14″.

This structure is virtually the same as the above example except that here the two shorted ends have been folded to meet each other. In other words, each half is a folded quarter-wave transmission line slightly foreshortened at the high voltage end. The cavity wall and the outer surface of the intermediate cylinder form a part of the transmission line while the inner surface of the intermediate cylinder and the vacuum pipe form the other part of the transmission line. This is to reduce the total length of the cavity. In addition, the characteristic impedance of the coaxial structure is tapered from a small value (37 ohms) near the high current end to a larger value (69 ohms) near the high voltage end. This makes coupling to a relatively low impedance RF power source convenient while allowing

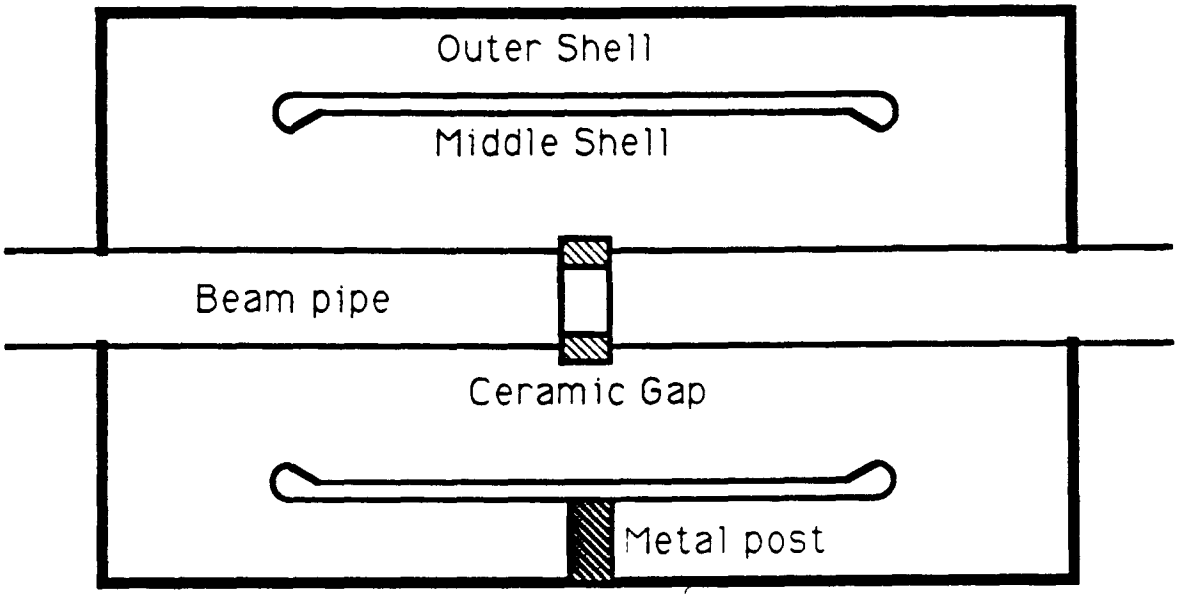

Figure 3.2. Configuration of an ARF1 cavity.

development of very high gap voltages. Because the two power amplifiers which drive the cavity are operating 180° out of phase, *i.e.*, in push-pull mode, the currents at the low impedance end are exactly opposite, and a real metallic short is not needed. There is a metal post at the low impedance end to support the intermediate cylinder, because the electric field there is zero, and putting in such a post does not change the field distribution in the cavity.

Performance of an RF cavity is usually assessed by the quality factor Q and the shunt resistance $R_{\rm sh}$ [30]. The quality factor of a cavity is defined to be

$$Q = \frac{\omega W}{P}\,, \tag{3.1}$$

where W is the total electromagnetic energy stored in the cavity and P is the power absorbed by the structure, when the system is at resonance with the resonant circular frequency ω. The shunt resistance $R_{\rm sh}$ is the resistance presented by the structure to the beam current in the accelerator when at resonance. It can be

thought of as the effective resistance for dissipation of all of the power lost in the structure when the gap voltage V_{gap} appears across it. Its definition is

$$R_{\text{sh}} = \frac{V_{\text{gap}} \cdot V_{\text{gap}}^*}{2P} \ . \tag{3.2}$$

From the above definition, it is easy to get another interpretation for R_{sh}: it accounts for the amount of input power needed to produce the required gap voltage. Obviously Q and R_{sh} vary as the situation of power loss inside the cavity changes. It is R_{sh}/Q that merely depends on the cavity geometry.

For a cavity structure like ARF1, the quantity R_{sh}/Q can be analytically calculated. Such a calculation is straight forward (cf. ref. [29], pp. 18-19). The result shows that $R_{\text{sh}}/Q = 148$ for an ARF1 cavity. Numerical calculation with SUPERFISH, a three-dimensional cavity calculation program developed at Los Alamos National Laboratory, gives a result of $R_{\text{sh}}/Q = 164$. The two results agree within 10%.

The quality factor of a ARF1 cavity would be of order 10^4 if the ohmic loss along the coaxial line were the only loss inside the cavity. It is desirable to make ARF1 a low Q (broadband) cavity because of its purpose for $\bar{\text{p}}$ stacking and Z/n stability requirement of 850Ω or less.† To extract energy out of ARF1 and therefore lower its Q, four disks are put at relatively high voltage locations and four loops at high current locations. Some power in the cavity can be coupled to 50Ω resistors with those capacitive and inductive couplers and dissipated. Table 3.1 gives the Q value and shunt resistance of the ARF1 cavities, where the Q values are from

† Details about the longitudinal instability will be given in chapter 5. Simply speaking, the impedance of the ring at a revolution harmonic divided by the harmonic number must not exceed some value in order for the beam to remain stable.

Table 3.1 ARF1 cavity parameters.

	Q	R_{sh} ($k\Omega$)
ARF1-1	161	26.4
ARF1-2	191	31.3

measurements of the cavity frequency response, and the shunt resistance values are from SUPERFISH results for R_{sh}/Q [31].

The 1.26MHz ARF3 system is the RF system used in E760 deceleration. It has been modified to have improved cavity tuning range and increased voltage capability in order to provide sufficient bucket area over a wide frequency range [32].

The ARF3 cavity is also formed by two shorted coaxial structures placed face to face, as shown in figure 3.3. Its main housing is a $1/2''$ thick aluminum cylinder that is $66''$ long and $28''$ in diameter. The vacuum chamber which also serves as the inner conductor of the coaxial section is a $4''$ diameter stainless steel tube with a $4''$ diameter by $2''$ long ceramic gap in the center of the chamber. For each half of the cavity, an assembly of 15 ferrites fills the space between the inner and outer conductor to reduce the resonance frequency.

Each half of the cavity uses input coupling capacitors of 500 pF, gap shunt fixed capacitors of 1400 pF plus a 250 pF variable which foreshorten the structure so that it resonates at 1.26 MHz. The shunt resistance of the cavity is designed to be 1500Ω to meet the Z/n stability requirement. There are some 50Ω deQing loads coupled to the cavity through 400 pF load coupling capacitors. Details about the low level RF amplitude and phase control is also described in reference [32].

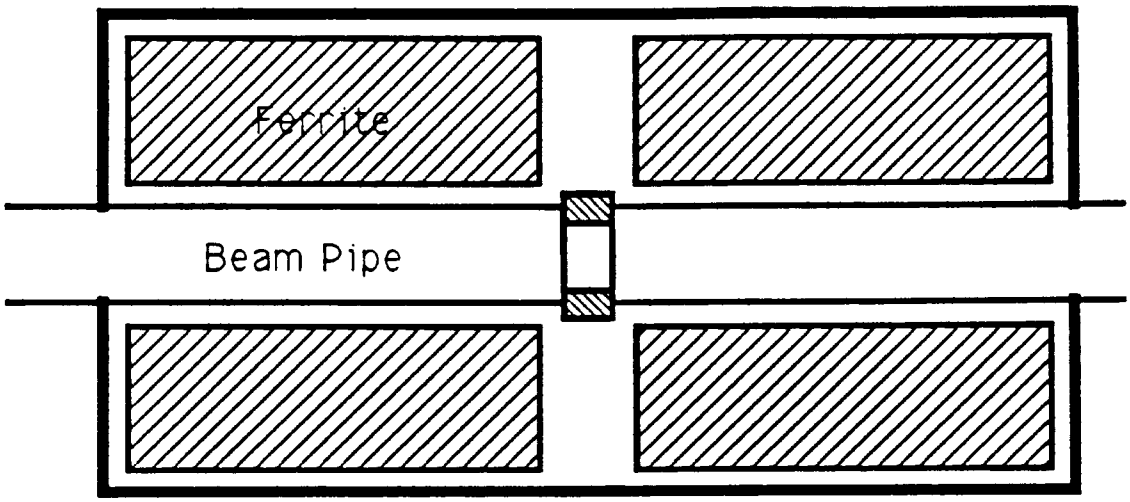

Figure 3.3. Rough drawing of ARF3.

3.2 Beam Position Monitors

The Accumulator beam position monitor (BPM) system [33] is designed to provide single turn beam position information for beam intensities greater than 1×10^9 particles, and multi-turn (closed orbit) information for beam intensities greater than 1×10^7 particles, both with sub-millimeter resolution. The measurements are processed by a high frequency (53 MHz) system which relies on 53 MHz signals produced by the bunched beam.

There are 90 pickups in the Accumulator system. In general there is one pickup at each quadrupole (with horizontal pickups at focusing quadrupoles and vertical pickups at defocusing quadrupoles). This results in more than five position measurements per plane per betatron wavelength in each ring. The pickups themselves are either diagonally cut cylinders or rectangles, depending on location, with signals capacitively coupled from the beam. To maximize signal levels the pickups cover the full azimuth and their capacitance to ground has been minimized. The pickups are bidirectional to accommodate beams circulating in either direction.

There are two varieties of the pickups used in the Accumulator BPM systems. The circular pickups are used in the low dispersion regions and the rectangular

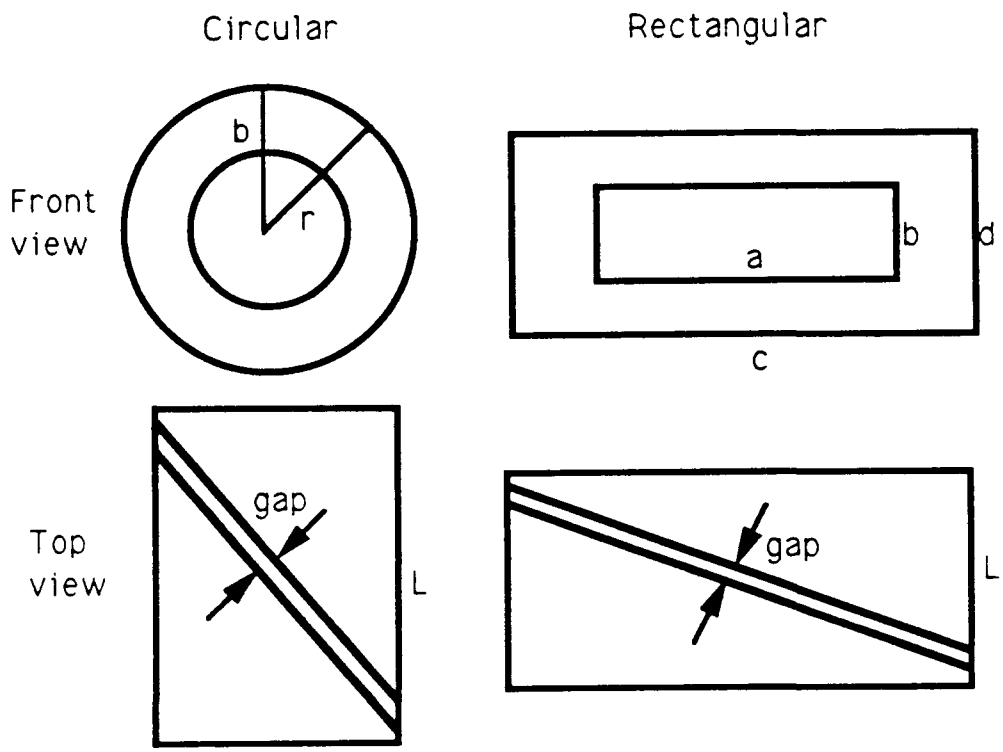

Figure 3.4. physical dimensions of circular and rectangular BPMs.

ones in the high dispersion regions. Figure 3.4 shows the geometry of both types of the pickups.

For both types of pickups it can be shown that with the given geometry the difference signal from the two plates is a linear function of the beam displacement (transverse beam position) [34].

Since the length of the pickup is chosen to be much shorter than the wavelength corresponding to the operating frequency (53 MHz), the field induced on each plate is quasi-static and the pickup can be represented with a conventional lumped circuit when calculating the pickup response. The circuit is formed by capacitors and terminating resistors, as shown in figure 3.5. Each plate and ground form a capacitor, this capacitor is in parallel with the termination resistor. When

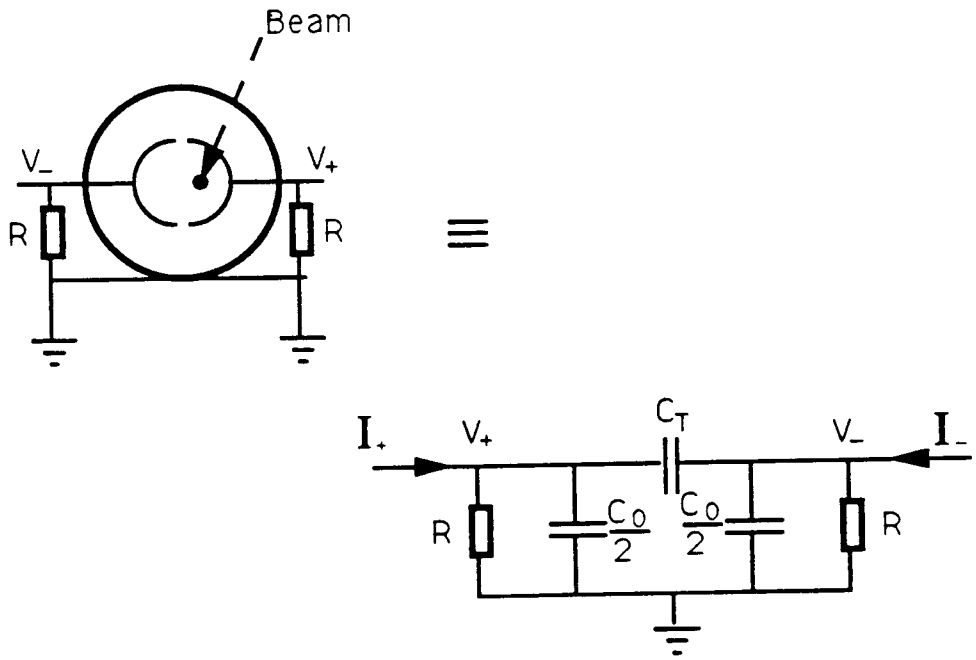

Figure 3.5. BPM pickup equivalent circuit. It is valid when the length of the pickup is much shorter than the wavelength corresponding to the operating frequency. The capacitance between each plate and ground is $C_0/2$, the coupling capacitance between the two plates is C_T when calculating the difference signal voltage. Each plate is terminated with a resistor R.

calculating the difference response, the coupling between the two plates is taken into account and represented by a coupling capacitance.

The sum and difference output voltages are then given by

$$V_\Sigma = \frac{Rn\theta I_n}{1 + \frac{j\omega RC_0}{2}}, \qquad V_\Delta = \frac{Rn\theta I_n}{1 + \frac{j\omega R(C_0+4C_T)}{2}} \left(\frac{x}{a}\right), \tag{3.3}$$

where C_0 is the capacitance of the entire pickup to ground, R the resistance of each electrode to ground, n is the revolution harmonic, I_n is the Fourier component of the rms component of the beam current at that harmonic, a is the apparent aperture of the pickup, θ is the ratio of the length of pickup to the mean radius of the ring, and C_T is the coupling capacitance between the plates. Measurement of the prototype pickup shows that $C_0 = 75$pf and $C_T = 11$pf.

From the above expression it can been seen that as a function of the terminating resistance R, signal levels are maximized with $\omega RC_0 \gg 1$, which is the

range chosen for the pickup. Then the beam position is derived from the ratio of the sum to difference signal as

$$\frac{x}{r} = \beta \frac{V_\Delta}{V_\Sigma} , \tag{3.4}$$

where β is the sensitivity: and $2r$ is the physical full width of the pickup, and β is the pickup sensitivity. From the prototype measurement, it is found that $\beta = 1.95$.

The precision of the position measurement depends on the noise associated with the sum and difference signals. If V_N is the rms noise voltage, the rms deviation of the measured position x is given by

$$\sigma_x = \frac{\beta r V_N}{V_\Sigma} . \tag{3.5}$$

There are two primary sources of noise in the BPM system. They are thermal noise generated in the terminating resistance on the plates, and the amplifier noise generated in the preamplifier. The gain of the preamplifier is sufficient for the contribution to the noise from the elements downstream to be negligible. Because the resistor R and the plate capacitance $C_0/2$ are in parallel connection, the contribution from the resistor thermal noise is given by

$$V_N^2 = \frac{4kTR\Delta f}{1 + \left(\frac{\omega R C_0}{2}\right)^2} , \tag{3.6}$$

where Δf is the bandwidth and $kT = 4 \times 10^{-21}$ Joules at 300K. This noise source is negligible compared with the preamplifier noise. The noise level of the preamplifier designed for the BPM system has been measured to be

$$V_N = 2 \times 10^{-9} \sqrt{\Delta f(\mathrm{Hz})} \ (\mathrm{Volts}) . \tag{3.7}$$

It can be seen that the noise level is proportional to the square root of the bandwidth. Calculation shows that in all cases (coasting beam, bunched beam, beam with gap, *etc.*) V_Σ is inversely proportional to C_0/L; therefore to enhance the signal-to-noise ratio, efforts have been made to reduce the capacitance/length and design a narrow bandwidth system. For multi-turn measurements the bandwidth is chosen simply to cover the frequency spread of the beam, caused by its momentum spread, at 53 MHz.

3.3 Stochastic Cooling Systems

There are six specific cooling systems in the Accumulator. The stack-tail momentum cooling system and betatron cooling systems have bandwidths of 1-2 GHz.† The core momentum and betatron cooling systems were upgraded from 2-4 GHz to 4-8 GHz in 1989 for faster cooling rates at the core [35]. The locations of the Accumulator cooling systems are shown in figure 3.6. All kicker assemblies have been located remotely from the pickup electrodes to minimize coupling and feedback.

In the Accumulator, quarter-wave loop pickups are adopted for the 1-2 GHz and former 2-4 GHz stochastic cooling systems. The loop pickup is a segment of transmission line of well-defined characteristic impedance on which the image currents of the beam can be induced. As similar to the beam position pickups described in Section 3.2, when the induced signals extracted from each plate are combined, the output voltage is proportional to the beam image current, whereas the difference signal from the two plates is proportional to the beam image current times the transverse displacement. As the beam moves away from the pickup, the voltage induced on each plate decreases exponentially. In the 1989 upgrade of the core cooling systems, 2-4 GHz pickups were replaced by newly designed 4-8 GHz quarter wavelength pickups. The 4-8 GHz pickup has a smaller physical size, and the portion of the beam at the edges of the core aperture cannot produce enough voltage on such a pickup because of the exponential decay of the pickup sensitivity. Therefore in the new 4-8 GHz systems two pickups are placed side by side to cover the core aperture.

The antiprotons are injected at an energy 80 MeV greater than the energy of the central orbit. The harmonic 84 RF system (ARF1) decelerates the beam to the stacking orbit which is 15 MeV greater than the energy of the central orbit. As the beam approaches the stacking orbit, the RF voltage is adiabatically reduced.

---

† 1-2 GHz means that the pickup response has a maximum at 1.5 GHz, and 3dB points below the maximum at 1 and 2 GHz. The same for the others.

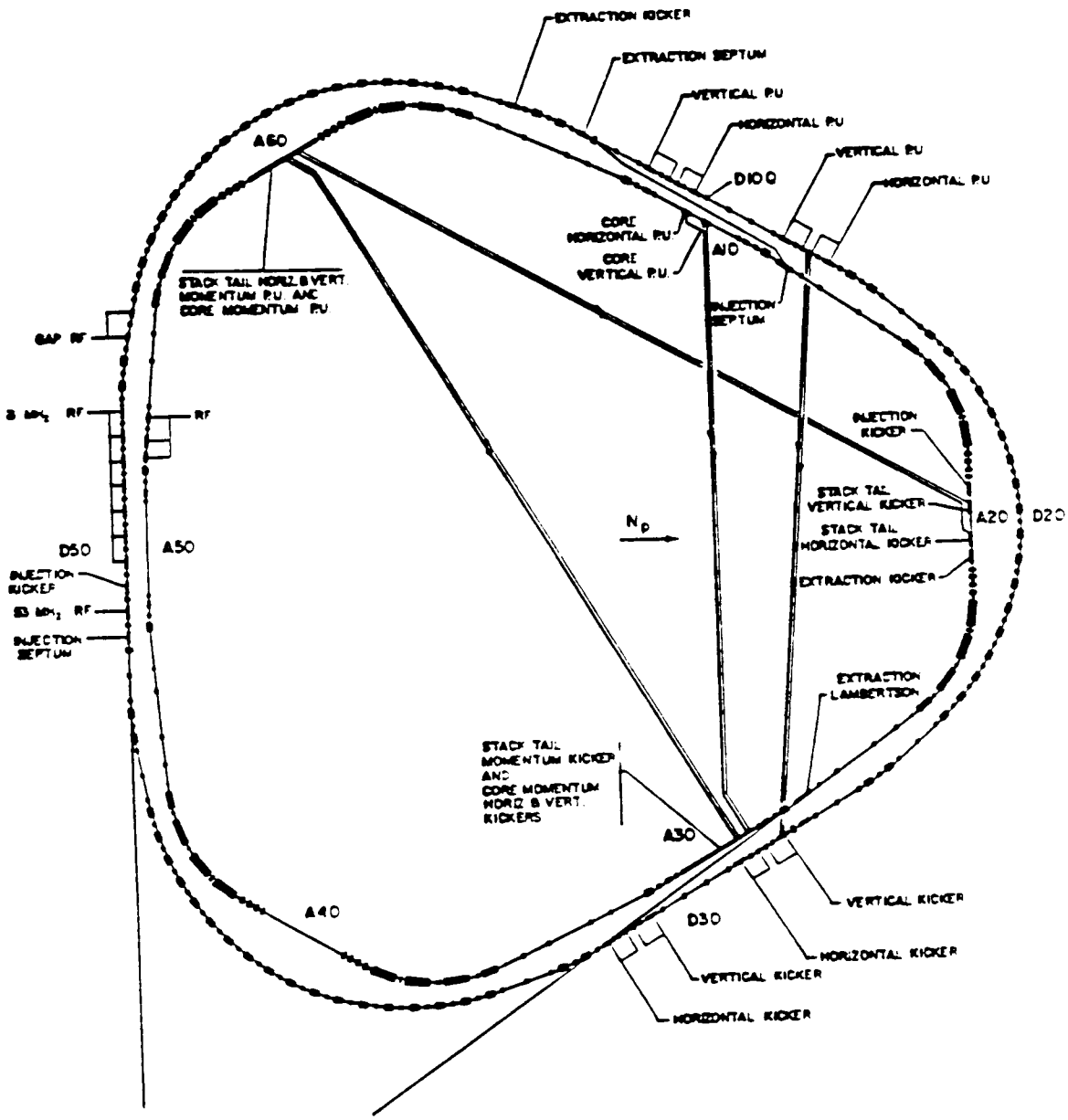

Figure 3.6. Locations of the Accumulator Stochastic Cooling Systems (ref. [1], fig. 5-33). In the stack-tail systems, there are 160 pickups and 160 kickers for the momentum cooling system, and the betatron cooling systems use 32 pickups among those 160 momentum pickups. In the 4-8 GHz core betatron cooling systems, both horizontal and vertical betatron pickup and kicker arrays contain 64 electrodes each, the momentum pickup array contains 128 electrodes and the kicker array consists of 256 electrodes.

This process takes about 0.2 second. After the batch is deposited on the stacking orbit, the stack-tail cooling system is turned on. Since the stacking orbit is radially inward from the stack-tail pickups, the voltage induced on the upper and lower pickups by a single antiproton decreases exponentially as the antiproton moves away from the pickup. If the average value of the displacement of N_s antiprotons sampled by the pickups is x(s), the induced voltage is

$$V = \sum_{i=1}^{N_s} k e^{-\pi D \Delta E_i / h \beta^2 \bar{E}}, \tag{3.8}$$

where h is the vertical separation of the pickup plates, k is the proportionality coefficient, and ΔE is the energy difference relative to the value at the center of the stack-tail pickup. The above expression shows that the closer the antiprotons are to the stack-tail pickups, the greater their contribution is to the signal. Therefore, the batch most recently injected has much greater contribution to the signal than that from the previous ones, which may have formed a dense core, even though the intensity of the core is much greater than that of the injected batch. As a result, there is little interference between stack-tail and core pickups.

For the Accumulator, the value of $|\eta|$ and the maximum harmonic number n at which order the Schottky band is observed for cooling are chosen such that with the energy difference ΔE between the high extreme of the stacking orbit and the low energy extreme of the core orbit,

$$\left| n\eta \frac{\Delta E}{\beta^2 \bar{E}} \right| < 1 \ , \tag{3.9}$$

in other words, the frequency spectrum of a particle on the stacking orbit does not overlap that of a particle on the core orbit. Therefore, there is a one-to-one correspondence between frequency and energy within the nth Schottky band. When the stack-tail correction signal is amplified and applied to the stack-tail kickers in the zero dispersion of sector A30, all the particles passing through the kickers experience this signal whether they are on the stacking orbit or on the

core orbit. But a particle responds significantly only to the signals which have the same frequencies as its revolution harmonic. As a result, the signals from the core do not interfere with the stack-tail and vice versa.

Since the $\bar{p}$ beam is decelerated on the central orbit during E760 running, a new set of momentum cooling electrodes, which is the same as the core momentum cooling system, has been installed. Computer stable delays have been installed to permit cooling at any desired energy. In the core momentum cooling system two sets of 4-8 GHz pickup-pairs placed in the A60 high dispersion short straight section. One set is centered 30 MeV above the core energy and the other is centered 30 MeV below the core energy. The momentum error signal is obtained by subtracting the signals from the two sets of pickups. The signal is then applied to the kickers in the A30 zero dispersion region for momentum corrections. The horizontal and vertical coolings on the central orbit are carried out by the core betatron cooling systems. The core betatron cooling pickups are located in the A10 zero dispersion region, and the kickers are in the A30 zero dispersion region. The betatron phase advance between pickup and kicker is about $2\frac{3}{4} \times 2\pi$ in both transverse planes.

Technical details in the Accumulator cooling system design are given in reference [1], sections 5.9-5.11.

3.4 Beam Diagnostic Instruments

During the process of the Accumulator transition crossing, two detectors have primarily been used in the study of the beam behaviour in the longitudinal direction. The frequency distribution of a coasting beam is obtained with a longitudinal Schottky detector, and longitudinal coherent effects can be observed with a broadband device called a wall current monitor.

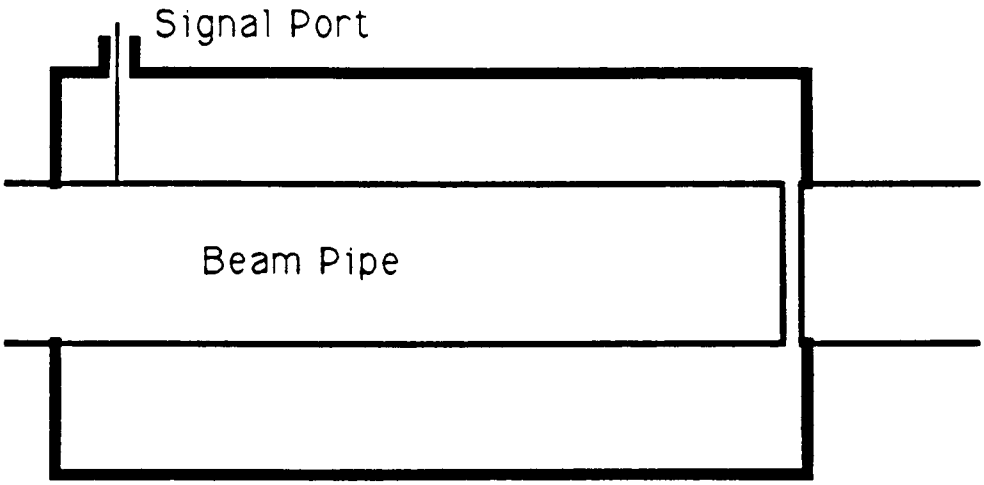

Figure 3.7. Schematic of the longitudinal Schottky detector.

3.4.1 Schottky Detector. The Schottky signal is incoherent, and therefore small in amplitude. In order to detect such a small signal, the Schottky detector must be a low noise or high gain device. The Accumulator longitudinal Schottky detector, located in the A10 low dispersion straight section, is designed to be of coaxial structure shorted at one end. Its length is made such that it is a quarter wave length device resonating at 79.3 MHz, half way in between the two adjacent ARF1 harmonics. This frequency is chosen to prevent large coherent signals at RF harmonics from being picked up by the detector, which leads to saturation of downstream electronics.

Figure 3.7 shows the physical dimensions of the Accumulator longitudinal Schottky detector, which is made of stainless steel. The detector is a low Q device due to large skin losses in the steel. Simple calculations indicate that the unloaded Q of the device is about 320. Near the high current end, there is a port from which a small fraction of the signal is magnetically coupled out by a conducting wire to a 50Ω load. This results in a slightly lower loaded Q. At resonance, the output impedance of the detector comes from the skin loss. This small impedance makes the detector a low noise device.

The frequency response of the Accumulator longitudinal detector is shown in figure 3.8.

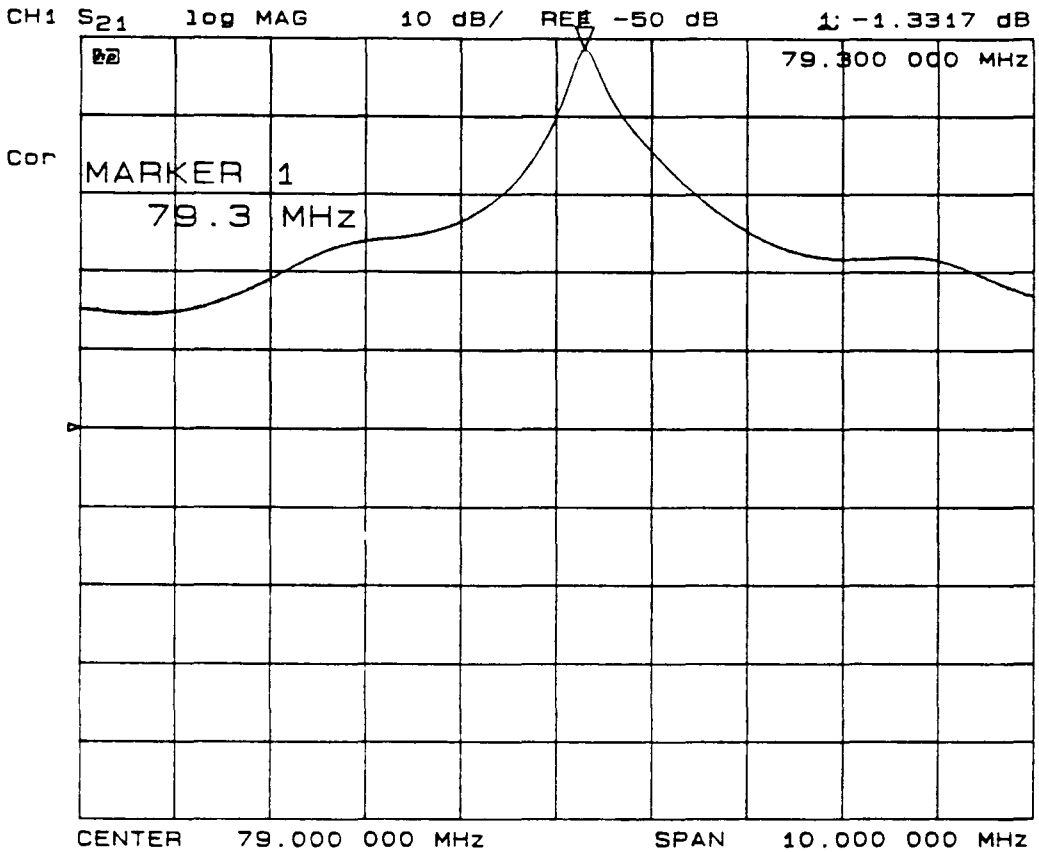

Figure 3.8. Frequency response of the longitudinal Schottky detector.

3.4.2 Wall Current Monitor. A wall current monitor [36], also called a resistive wall monitor, is a device that measures the beam current with flat amplitude response over a large frequency range, *i.e.*, a broadband beam current detector.

Figure 3.9 shows schematically half the cross section of the Accumulator wall current monitor installed in the beam pipe.

The beam pipe is cut and a resistor with known resistance is put across the gap. The ceramic seal allows the resistor and the magnetic material to reside outside the vacuum. The cavity shield prevents any external noise from entering the system and provide a needed d.c. path for the monitor for beam instability reasons.

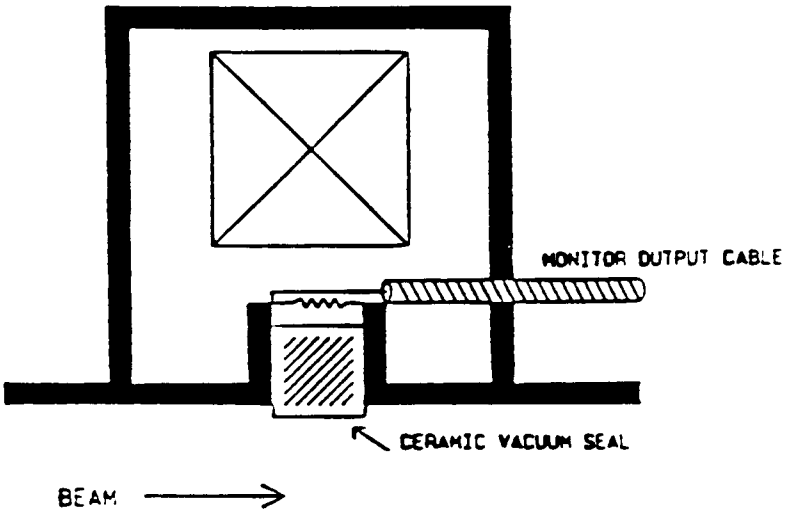

Figure 3.9. Half cross section of a wall current monitor.

The beam current spectral component at a specific frequency, except d.c. current, can be obtained by measuring the voltage across the resistor. The d.c. beam current cannot be detected because the beam pipe is shorted by the cavity shield and the voltage across the resistor is zero. At low frequencies such that the skin depth is greater than the thickness of the beam pipe, the magnetic component of the wave penetrates the metallic walls of the beam pipe and the magnetic core. The magnetic core, the cavity wall, and the resistor form a transformer with a single turn secondary loop. As the beam passes through the detector, it induces current in the secondary loop and therefore voltage across the resistor. When the frequencies are so high that the skin depth is smaller than the thickness of the beam pipe, fields appear within the beam pipe but not outside it. Outside the beam pipe, the field generated by the beam is cancelled exactly by the field generated by its image current, which is equal in magnitude and opposite in direction, in the beam pipe. The voltage across the resistor is the image current multiplied by the resistance. This is the reason that the device is call the wall current monitor. Usually the working principle of a wall current monitor is introduced intuitively as follows: the beam in the beam pipe induces an equal and opposite image current

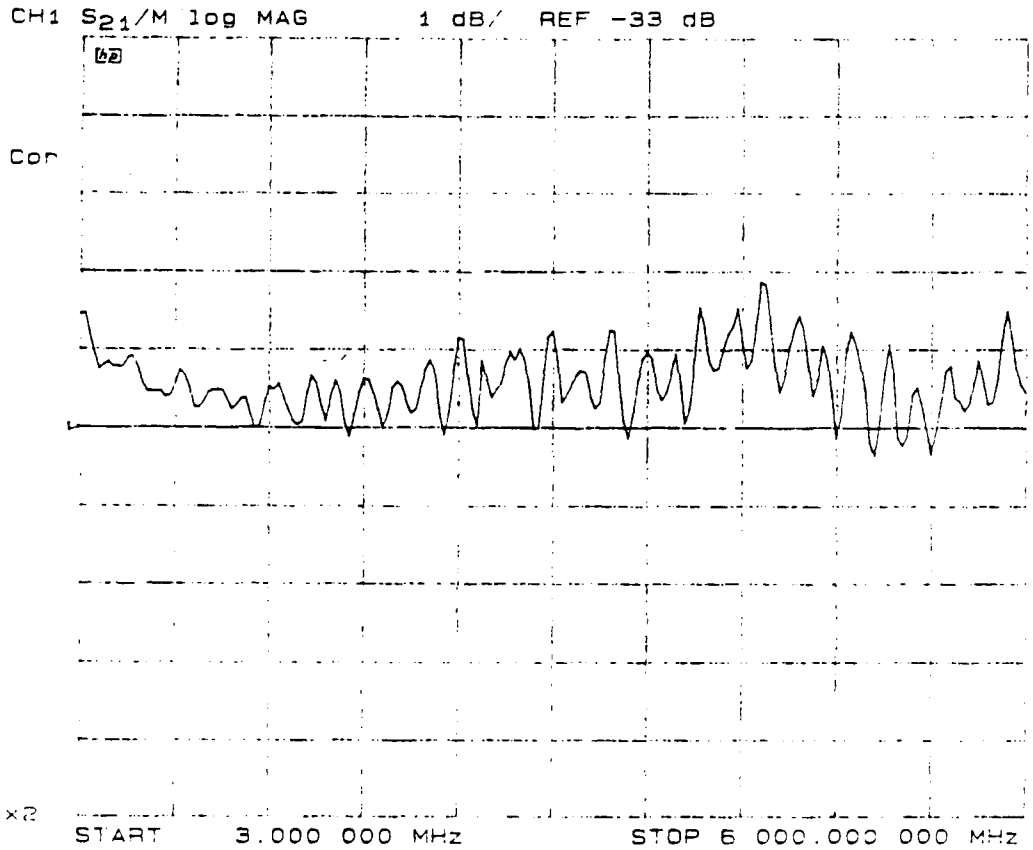

Figure 3.10. Accumulator wall current monitor S_{21} response.

in the beam pipe. When the beam pipe is cut and the resistive material is put into the gap, a voltage is generated across the resistance as the image current flows through it. This description is identical to that the low frequency transformer forces a current equal and opposite to the beam current through the resistor, only a change in point of view. A transformer has the response of a high pass filter with a 3dB point below the maximum at a frequency determined by the time constant of the transformer. A low frequency transformer is one with the 3dB point frequency much lower than the frequency of concern.

The wall current monitor was designed such that, over a wide frequency range (3 kHz to 6 GHz), a large and constant fraction of the wall current flows through the intended resistance because the detector is required to have a flat response. The value of the gap resistance is determined in the following way: the gap and

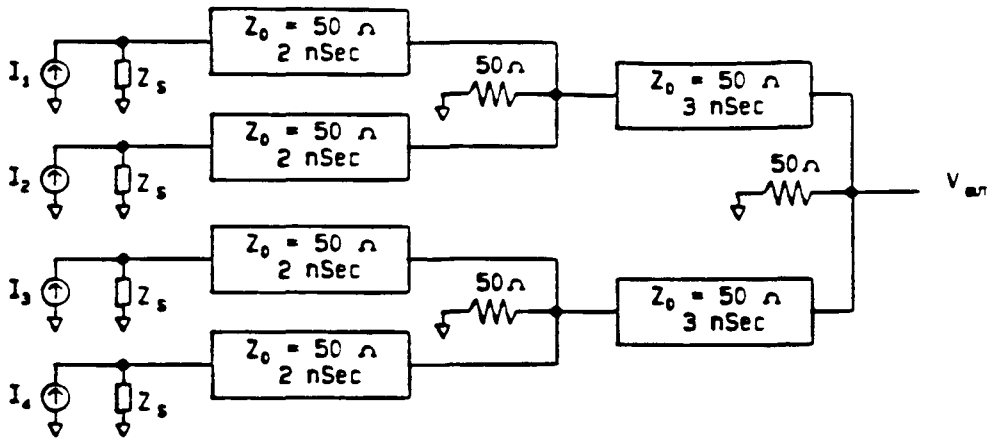

Figure 3.11. Shunt loaded circuit schematic.

the ceramic is modeled to form a radial transmission line through which currents from the inside of the beam tube must flow to reach the resistor, and the resistor must terminate this line properly for a frequency independent response. This resistance is found to be 1.4 Ohms. The resonant property exhibited by the cavity housing limits the bandwidth of the detector. To eliminate this effect, different types of magnetic material are put together in the cavity to make the resonant frequencies high enough to be outside the frequency range of the detector. With the Accumulator wall current monitor design, the cavity shield presents a broadband impedance of between 10 and 20 Ohms up to multi-gigaHertz frequencies, which leads to a shunting effect of about 10%. In addition, at very high frequencies, the resistor across the gap exhibits resonant property which also limits the bandwidth. For this reason eighty 120 Ohm RF chip resistors are evenly spaced around the circumference. These resistors are used because they exhibit very high self-resonant frequencies, and therefore act as constant resistors over the frequency range of concern. Test of the Accumulator wall current monitor shows that its response is flat over the frequency range of 3 kHz to 6 GHz. Figure 3.10 gives its S_{21} response from 3 MHz to 3 GHz.

In order to eliminate the sensitivity of the detector to the radial position of the beam, the wall current flowing through the resistors is extracted from four

points at 90° intervals around the gap. The signals are combined with the shunt loaded circuit shown in figure 3.11. The circuit is not back terminated, therefore any observation device connected to it must have 50Ω input impedance to provide proper forward termination.

CHAPTER IV

ACCUMULATOR OPERATION IN E760

Conducting the E760 experiment in the Accumulator requires deceleration of an intense $\bar{p}$ beam from its normal stacking energy of 8.9 GeV to specific energies in the charmonium state region in order to perform energy scans across the resonances. Deceleration is managed by PAUX, a PDP-11 front end computer dedicated to this purpose. A computer program changes the settings of the various ramped devices according to interpolation of an input file (ramp table). To decelerate the beam below 5 GeV, the transition energy must be crossed. The method adopted for transition crossing in the Accumulator is to raise the value of γ_t while the beam is circulating unbunched in the ring. This operation provides an opportunity for studying coherent beam phenomena near transition.

Precise knowledge of the average energy and energy spread of the beam is required for width measurements of the charmonium resonances. During scans the beam is continually cooled in both longitudinal and transverse directions, which is essential to the success of the experiment. The transverse cooling systems counteract the beam emittance growth arising from the beam repeatedly traversing the gas jet. The momentum cooling serves two purposes: it compensates for the beam energy loss due to the beam particles ionizing the hydrogen gas molecules at each traversal and it narrows the beam energy spread to below 1 MeV.

This chapter describes the operational aspects of the E760 deceleration in the Accumulator, including construction of ramp tables, software for deceleration control, deceleration process and transition crossing, and beam energy measurement.

4.1 Accumulator Control System Adaptation To E760

The Accumulator control system is part of the Fermilab Accelerator Control System [37] which is designed as a distributed computer based system. A schematic overview of the Fermilab Accelerator Control System is shown in Figure 4.1.

The top row shows seventeen PDP-11/34 computers which support the accelerator operator consoles on a one-to-one basis. Most human intervention is accomplished through application programs running on those computers. The three VAX-11/785's shown in the next two levels serve as a central database repository for routine and scaling information, as a central message switching facility between the network buses, as an additional computation facility for larger calculations and simulations (may be done on FPS-164), and as a development platform for ongoing work. In the next level are the front end PDP-11's, which serve as an interface between the operator consoles and the CAMAC modules and microprocessor based systems which control the accelerator.

Normally in the Fermilab control system magnet ramps are generated by dedicated microprocessors. Ramp tables are downloaded by application programs running on the console computer. Then by using timing and scaling signals sent to these microprocessors, ramps are generated at a 720 Hz update rate.

However, since the Accumulator was designed as a fixed energy machine, it was instrumented with DAC's and digital output directly on the front end's serial CAMAC link rather than with the more expensive microprocessor based ramp modules (CAMAC 165 module). Reinstrumenting the Accumulator with ramp modules to accomplish deceleration for E760 would be rather expensive and be disruptive to the ongoing Collider program. However, because of the large inductance of the Accumulator power supplies and magnets, deceleration could only proceed slowly over a period of several minutes. Most devices would need to be updated only at $\sim$ 1 Hz rate while a few would need a 60 Hz rate. Also, the Serial CAMAC crate controller used in the Fermilab Control System has the capability of a second link being attached with the appropriate hardware arbitration. Two computers can therefore hook up to the same CAMAC crates. Thus, a second

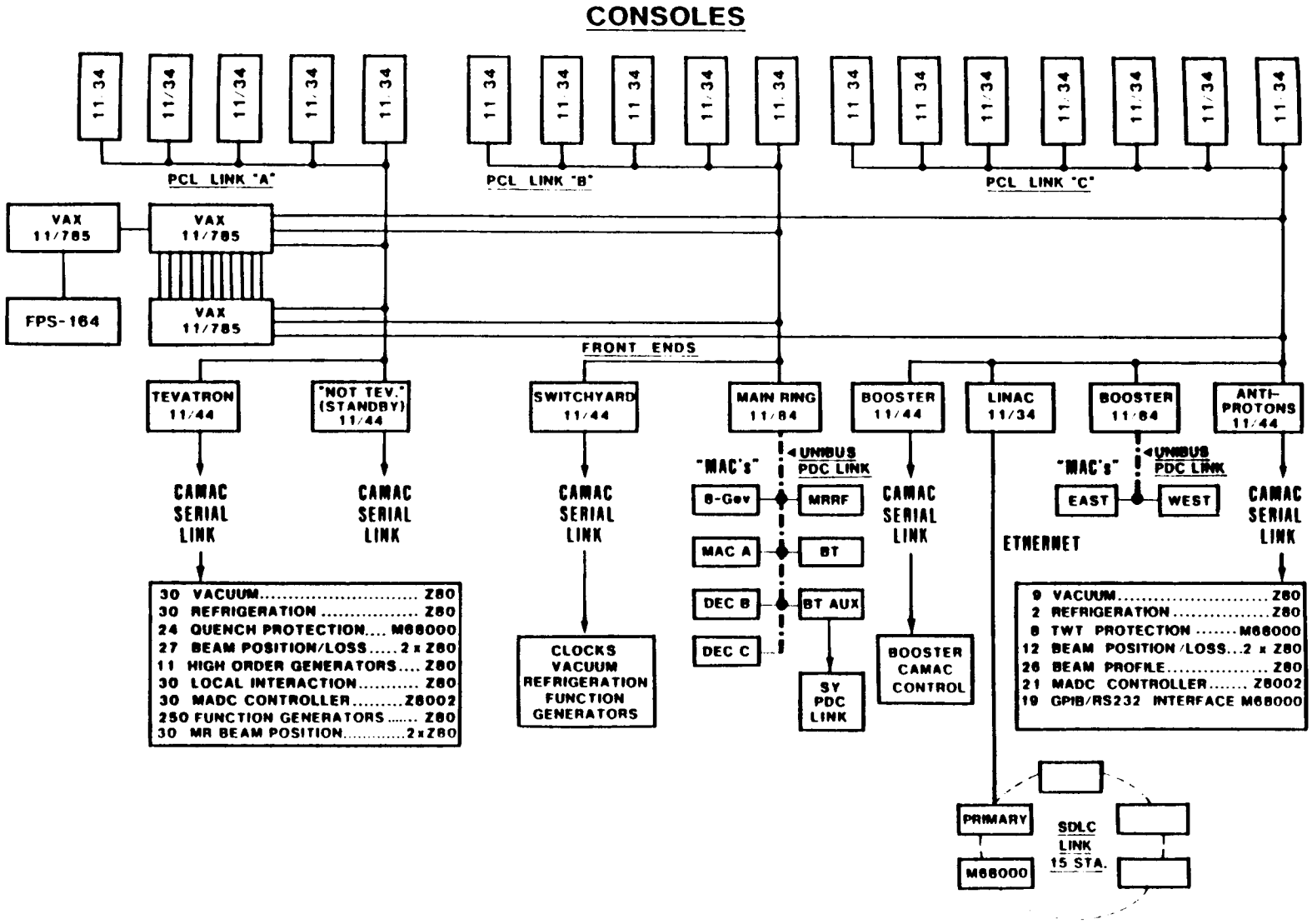

Figure 4.1. The Fermilab accelerator controls computer network (ref. [37], p. 9).

auxiliary front end PDP-11 (PAUX) was installed, whose sole purpose is to ramp all the devices of the Accumulator during deceleration. The antiproton front end is left unchanged while the new auxiliary front end is connected to the second port of the relevant CAMAC crates.

4.2 Deceleration

Special control software and different ramp tables are required for deceleration above, below, and across transition. In this section, work on the ramp table construction and software development [38] is presented before a description of the deceleration process.

4.2.1 The Ramp Tables. To implement deceleration *via* software control it was necessary to generate smooth ramp tables for about ninety devices in the Accumulator. Those devices included the main dipole bus, three quadrupole busses, two quadrupole shunts, four sextupole busses, two skew quadrupoles, and more than sixty trim elements. Two reasons prevented construction of a realistic ramp table by calculation: that the magnetic field measurements which had been done were not detailed enough at low energies, and differing time constants on different buses. The ramp tables were therefore constructed empirically.

The ramp table was first formed by taking the 8 GeV working point and extrapolating the energy to zero. The energy difference between two adjacent ramp points was approximately 40 MeV. At each ramp point the horizontal and vertical tunes were measured and, if necessary, corrected until they agreed with the desired values. Tune correction for each plane could be made independently by changing the settings of the quadrupole busses simultaneously in a certain proportion. Figure 4.2 shows the horizontal and vertical sidebands of a beam after tune corrections have been made. The new settings for the relevant devices at that point were saved into the ramp tables. At some energies the closed orbit was measured and compared with the stored 8 GeV orbit, and corrections were made to minimize the orbit change. Figure 4.3 shows a closed orbit change in

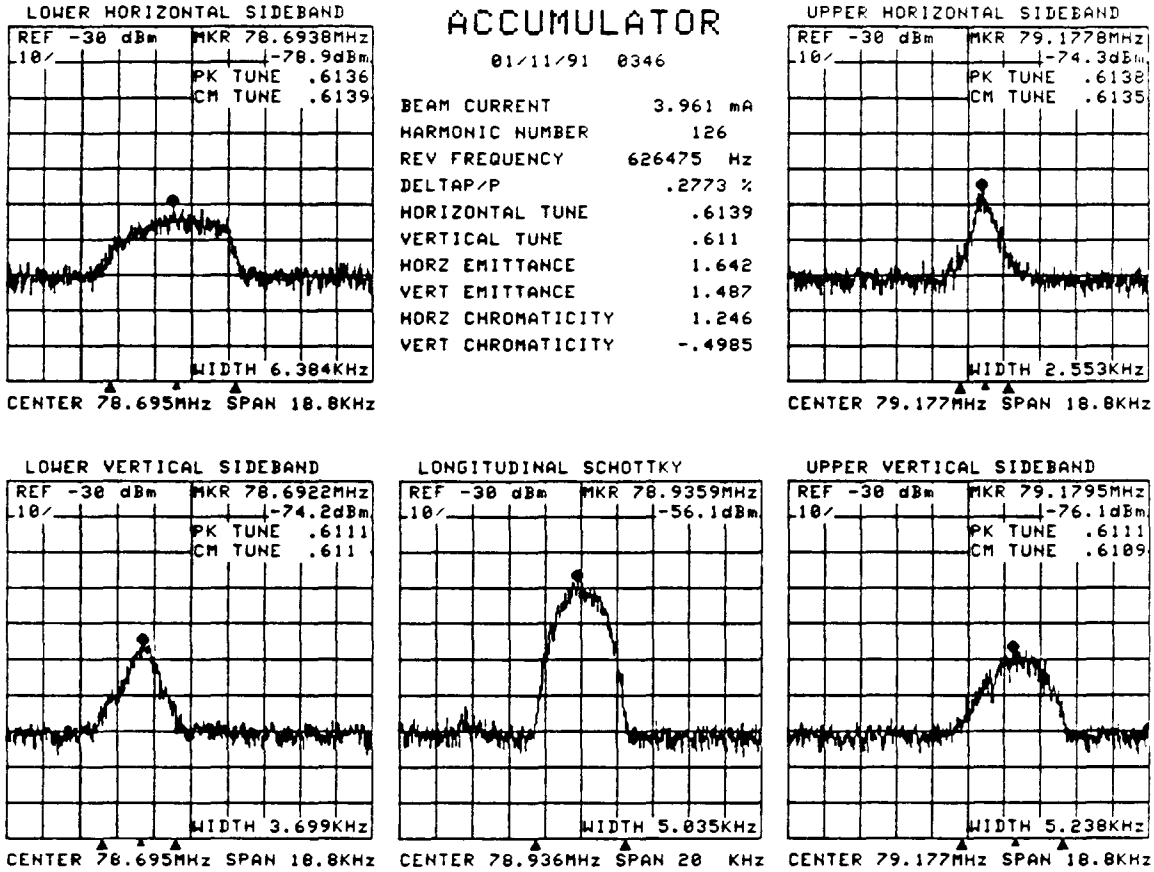

Figure 4.2. Betatron Sidebands During E760 Deceleration. The upper and lower betatron sidebands are displayed by a tune measurement program after tune corrections have been made at a generic momentum X:POFTT=6774 MeV/c. Tunes are held constant at $\nu_h = 6.614$ and $\nu_v = 8.611$ throughout the deceleration. The chromaticity values given by the program are calculated from the widths of the upper and lower sidebands, and are not reliable.

the deceleration process. Other accelerator parameters which were measured and corrected at some ramp points were the horizontal and vertical chromaticities, and the dispersion in the zero dispersion straight sections. The ramp tables were updated with the new settings each time the correction was made. The transverse apertures were measured to check the adequacy of the closed orbit. Three different ramp tables were made for deceleration above transition, transition crossing, and deceleration below transition respectively.

This procedure of constructing ramp tables required large number of iterations before a working ramp table was made. The result of this work is illustrated

ACCUMULATOR CLOSED ORBIT (HORIZONTAL)

A:R1LLFS 52.792 A:R3HLFB 258.8615
A:IBEAM 4.57
CO Date/Time: 12/18/90 0628:43
AVG OVER 20 FRAMES (20 20 20 20 20 20) FILE 168 HAS BEEN SUBTRACTED
Deltap/p = .0001

BEAM POSITIONS (mm)

A1Q1	-.67	A2Q14	1.21	A3Q1	.67	A4Q14	-1.2	A5Q1	0	A6Q14	2.41
A1Q3	-.34	A2Q11	1.21	A3Q3	.67	A4Q11	0	A5Q3	-.33	A6Q11	2.42
A1Q4	-1.49	A2Q10	1.2	A3Q4	-.33	A4Q10	0	A5Q4	-.66	A6Q10	1.21
A1Q6	-3.03	A2Q8	-2.5	A3Q6	-4.01	A4Q8	2.7	A5Q6	-1.67	A6Q8	-3.32
A1Q8	3.46	A2Q6	3.66	A3Q8	-3.99	A4Q6	-.33	A5Q8	3.05	A6Q6	-.34
A1Q10	1.2	A2Q4	3.53	A3Q10	1.21	A4Q4	0	A5Q10	0	A6Q4	-1.34
A1Q11	0	A2Q3	.34	A3Q11	0	A4Q3	-.33	A5Q11	0	A6Q3	-1.66
A1Q14	-1.2	A2Q1	.33	A3Q14	1.21	A4Q1	-.33	A5Q14	0	A6Q1	-1.34

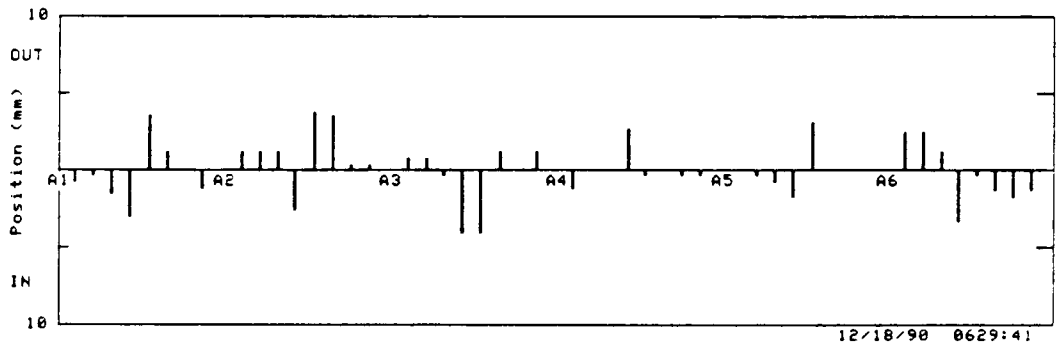

(a) Horizontal beam positions.

Figure 4.3. Beam Closed Orbit Change at X:POFTT=6774 MeV/c Relative to the Initial Closed Orbit.

ACCUMULATOR CLOSED ORBIT (VERTICAL)

A:R1LLFS 52.792 A:R3HLFB 258.8615
A:IBEAM 4.57
CO Date/Time: 12/18/90 0628:43
AVG OVER 20 FRAMES (20 20 20 20 20 20) FILE 16B HAS BEEN SUBTRACTED

BEAM POSITIONS (mm)

A1Q1	-.67	NO PU	NO MUX	A3Q1	-.33	NO PU	NO MUX	A5Q1	-.67	NO PU	NO MUX
A1Q2	-.67	A2Q14	-.54	A3Q2	-.33	A4Q14	.71	A5Q2	-1	A6Q14	-.36
A1Q5	0	A2Q13	-1.07	A3Q5	-.67	A4Q13	.72	A5Q5	.33	A6Q13	0
A1Q7	1.32	A2Q9	-.66	A3Q7	1	A4Q9	-2	A5Q7	.33	A6Q9	.67
A1Q9	0	A2Q7	1	A3Q9	-1.99	A4Q7	.34	A5Q9	-.33	A6Q7	.67
A1Q13	.71	A2Q5	.34	A3Q13	1.24	A4Q5	-.33	A5Q13	-.18	A6Q5	-1
A1Q14	.35	A2Q2	0	A3Q14	.71	A4Q2	0	A5Q14	-.18	A6Q2	-.34
NO PU	NO MUX	A2Q1	0	NO PU	NO MUX	A4Q1	0	NO PU	NO MUX	A6Q1	-.33

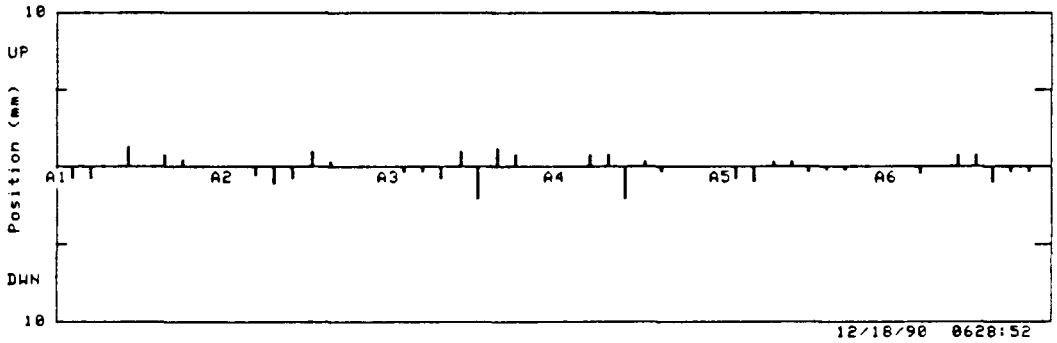

(b) Vertical beam positions.

Figure 4.3. (continued)

in figure 4.4, which shows the aperture as a function of momentum. The tunes were held constant at $\nu_h = 6.614$ and $\nu_v = 8.611$ at an accuracy of about 0.003. Chromaticities were approximately zero throughout the ramp.

The deceleration rate is limited by the amount of RF voltage available and large time constants on the main busses. The latter limits the rate at which the currents for the dipoles and large quadrupoles can be changed. The standard deceleration rate is 20 MeV/sec. When deceleration proceeds, the computer program changes the setting of each ramped device at a certain frequency called the update frequency, by interpolating the two adjacent points in the ramp table. The update frequencies for the various devices are given in Table 4.1. Even though magnets leave saturation during deceleration, the dipole and large quadrupole magnets are well into saturation at the design energy. Therefore, their busses need a higher update frequency to maintain precise control of the Accumulator lattice parameters. The natural time constants of the power supplies filter the steps generated by the digital ramp. The RF frequency is synthesized from a 10 MHz reference oscillator and is therefore extremely agile. The discontinuities in the ramp caused by the 60 Hz update frequency are digitally filtered to smaller steps at a 20 kHz rate by a dedicated 68000 microcomputer in a VME crate. The filter time constant is chosen to be approximately equal to the step response time constant of the dipole bus. The RF voltage can be ramped but is usually left constant.

4.2.2 Special Software. The following computer programs were developed especially for the Accumulator deceleration and energy scans:

1. Ramp Program to update the power supplies based on the input ramp tables. The ramp program must operate simultaneously with the standard control system, which has access to the same hardware through the same CAMAC interface.
2. Ramp Editor to create and modify the ramp tables. The program supports polynomial extrapolation and interpolation of the tables to allow rapid ramp generation. Individual ramp points may be edited by hand. The

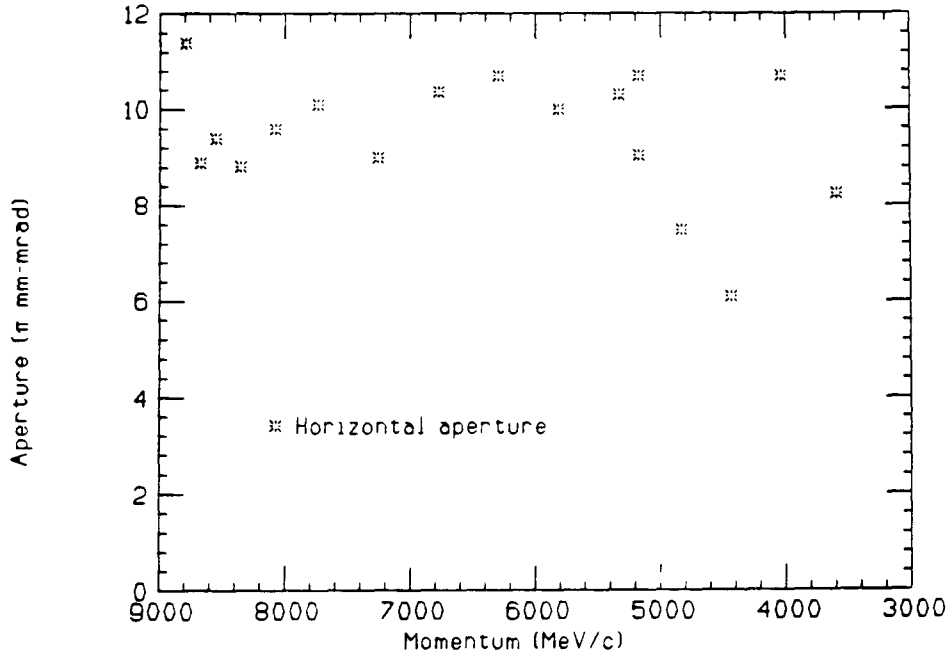

(a) Horizontal aperture.

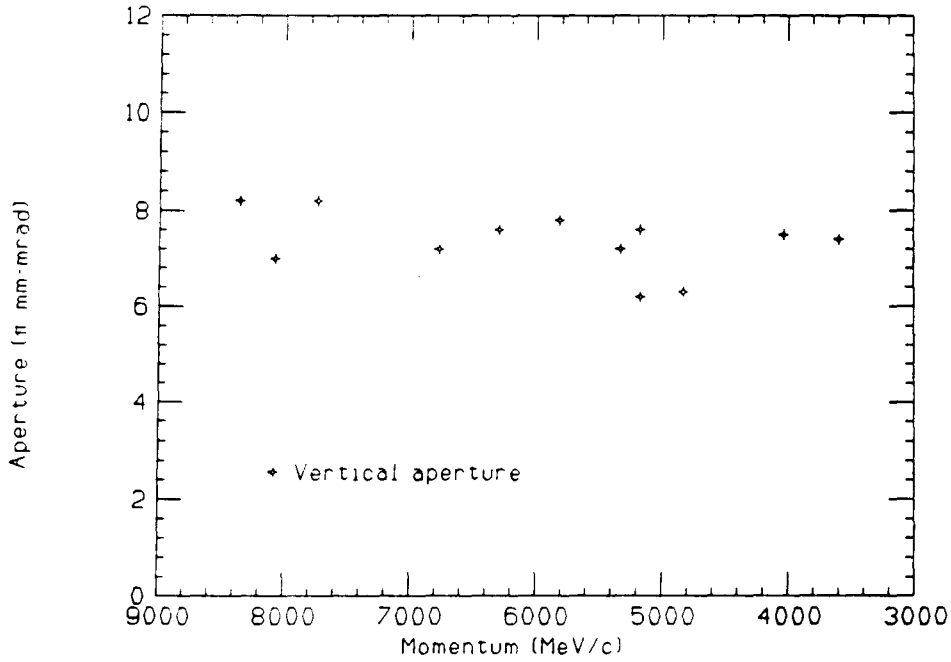

(b) Vertical aperture.

Figure 4.4. Aperture as a Function of Momentum. Decrease in the horizontal aperture around 5 GeV/c is due to transition crossing.

Table 4.1. Update Frequencies of the Ramped Devices

Device type	Quantity	Update frequency (Hz)
Frequency	1	60
Dipole Bus	1	60
Quadrupoles	4	60
RF voltage	1	60
Sextupoles	5	7.5
Skew quads	2	7.5
Octupoles	2	7.5
Horz. trims	8	0.5
Vert. trims	24	0.5
Dipole shunts	30	0.5
Damper timing	4	0.5

ramp editor can also propagate small changes at a given point to different points in the ramp.

3. A Deceleration Sequencer to automate the deceleration process. The sequencer can be programmed to perform arbitrary sequences of the following operations automatically: 1) RF manipulations including capture, deposit, and moving of the beam, 2) cooling operations including turning the system on and off and setting the timing based on the revolution frequency, and 3) magnet ramping when a "start" and "stop" energy is given.
4. A Fast Data Logger to record the sequence of events in the deceleration. This information is usually uninteresting, but can be crucial to understanding subtle failure modes.
5. An Energy Scanning program for automatic or manual change of the beam energy in very fine steps (as small as 178 keV). The stochastic cooling is monitored and the timing delays are automatically controlled. At 5 minute intervals various beam parameters are measured, a closed orbit measurement is taken, and the beam energy and width are calculated. These data are sent to the experimental data acquisition system *via* CAMAC link.

6. An Orbit Length and Beam Energy program that calculates the beam orbit length from the BPM radial positions. The program interpolates to find the orbit at the points between the beam monitor pickups.

4.2.3 Deceleration above Transition. The stacked $\bar{p}$ beam at the core orbit has already been cooled. It can be continuously cooled as long as necessary to facilitate adiabatic capture by the ARF3 system for deceleration. The beam is then moved to the central orbit, and the control of the RF system is taken over by PAUX, which executes a deceleration procedure to the desired energy or to just above transition, whichever is greater.

Beams of over 20 mA of antiprotons have been routinely decelerated to above transition with almost 100% efficiency. Figure 4.5 shows the beam current and the RF voltage in the deceleration of a $\bar{p}$ beam of 18 mA.

4.2.4 Transition Crossing. The design value of the Accumulator transition energy is 5.1 GeV, which corresponds to a transition gamma $\gamma_t = 5.43$. Transition crossing is necessary for deceleration below 5 GeV. When a beam in a circular accelerator is near the transition energy, the RF voltage can provide little phase stability. The less time the beam stays in that region the smaller its momentum spread blow-up will be. The conventional method for transition crossing is by swift acceleration of the beam across the transition region. However the Accumulator deceleration is as slow as 40 MeV/sec, and this rate is not fast enough for crossing transition without major disruption of the bunches. Therefore an alternative method for transition crossing is adopted in the deceleration operation. In this technique, the beam is debunched at an energy slightly above transition, γ_t is then raised to a value such that the beam energy is below transition, and the beam is recaptured.

Change of γ_t is achieved by changing the dispersion function $D(s)$ around the ring, which has been explained in chapter 2. The large aperture quadrupoles, to which the tunes are not sensitive, primarily determine the dispersion in the high dispersion sections. γ_t is raised by increasing the setting for the large quadrupole

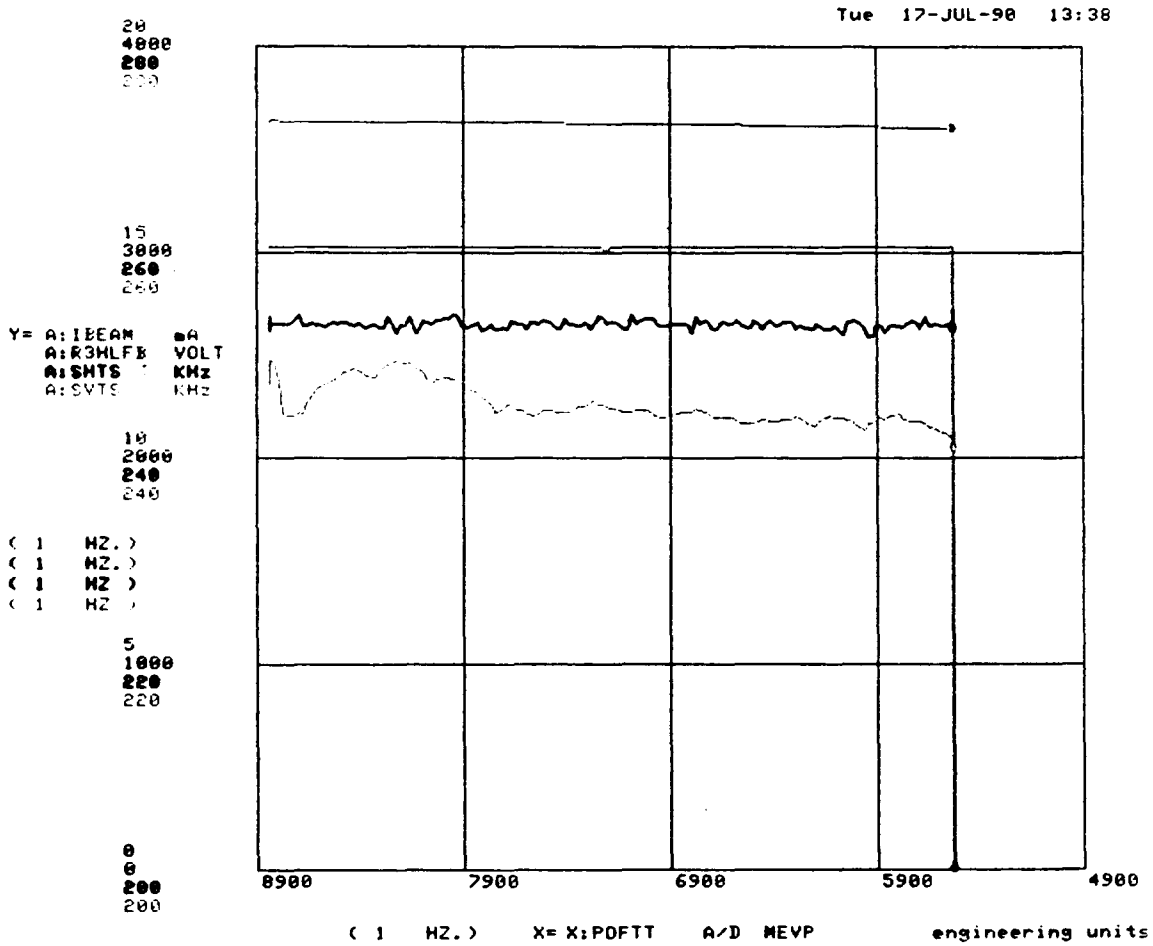

Figure 4.5. Deceleration above Transition. The top trace shows the d.c. beam current which is initially 18mA. The next trace shows the constant ARF3 voltage of about 3 kV during deceleration. The beam is debunched at X:POFTT=5174 MeV/c, so the RF voltage drops instantaneously at that momentum.

bus current while leaving the dipole field unchanged. Meanwhile, settings of the other quadrupole busses are adjusted to keep the tunes constant in the γ_t crossing process. Because of these quadrupole current changes, the actual dispersion in the zero dispersion sections becomes negative. This fact reduces the momentum aperture of the ring and therefore limits the amount of γ_t change.

Two ramp tables for transition crossing were made in the 1990 run. In the first one, called the old ramp, γ_t was raised from 5.5 to 6.1 when the beam gamma was $\gamma = 5.647$, *i.e.*, η was changed from 0.001 to -0.004. Afterwards another ramp table, called the new ramp, was made where $|\eta|$ was about the same before and after transition crossing. γ_t was raised from 5.15 to 6.1, which made the initial and final values of η 0.006 and -0.004 respectively. Measurements of γ_t and γ will be described in this chapter. Both tables had 24 ramp points. Each step normally took 0.5 second, but could be made five times faster if required.

Transition crossing is observed using the longitudinal Schottky signal. From the familiar formula

$$\frac{\Delta f}{f} = -\eta \frac{\Delta P}{P} , \tag{4.1}$$

it is easy to see that, above transition, the higher frequency side of the profile corresponds to the lower momentum side in the beam momentum distribution. When the beam is below transition, the opposite correlation is observed. Figure 4.6 shows the longitudinal Schottky profiles before and after the first successful transition crossing on January 8, 1988.

During the process of transition crossing, a large increase in the momentum spread of the beam was observed. The largest amount of beam which could be decelerated across transition without loss was found to be about 10 mA. Measurements were made to discover the source for this momentum blow up, which will be presented in the next chapter.

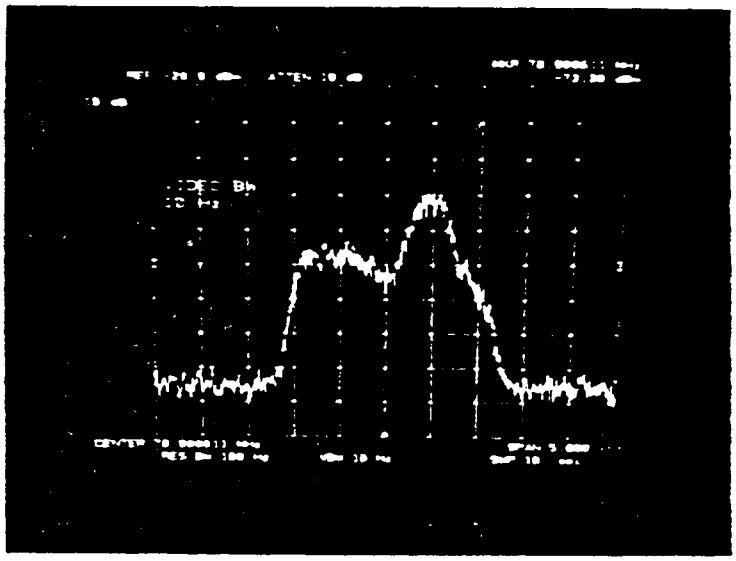

(a) Above transition.

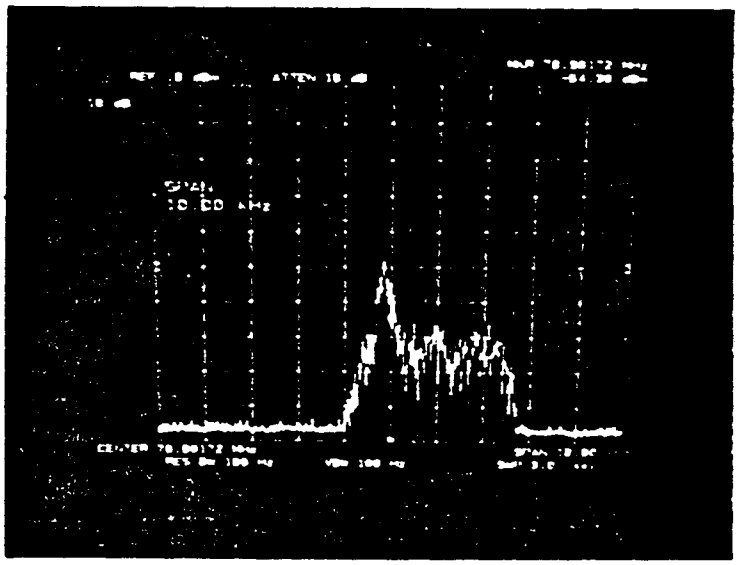

(b) Below transition.

Figure 4.6. The Accumulator Longitudinal Schottky Profiles above and below Transition, as first observed on January 8, 1988. The "shoulder" changed side when the beam was across transition. There was 2 mA of protons in the machine before γ_t crossing. Beam loss in the process was not recorded.

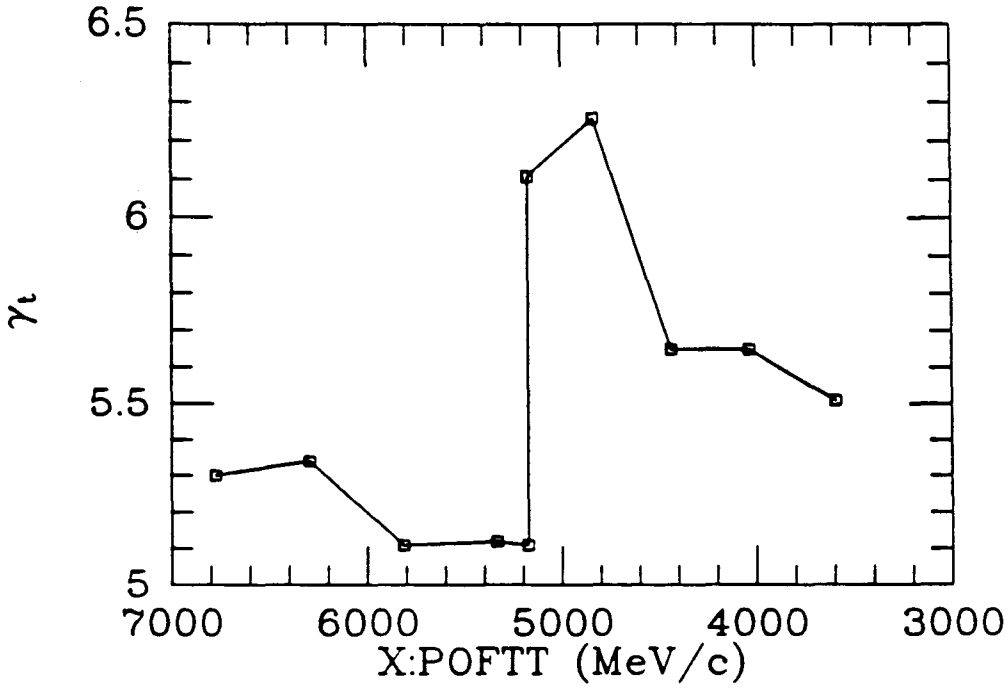

Figure 4.7. Measured γ_t as a Function of Momentum.

4.2.5 Deceleration below Transition.

In order to resume deceleration after transition crossing, the beam must be cooled both longitudinally and transversely before adiabatic capture by ARF3. The ramp table for deceleration below transition was constructed such that, as the deceleration proceeds, γ_t is gradually returned from 6.1 back to its design value of 5.43. In other words, the lattice is gradually put back to its normal state. This makes the dispersion in the zero dispersion sections zero again, and therefore increases the momentum aperture of the ring. In addition, as the beam is decelerated away from transition, η increases, and the RF bucket area becomes smaller constant RF voltage. The decrease in γ_t makes η increase more slowly than it would for a constant γ_t. This leads to a bigger bucket area for deceleration below transition. Figure 4.7 shows the measured γ_t as a function of momentum during deceleration.

4.3 Measurements of Beam Energy

Knowledge of the average energy and the energy spread of the beam is essential in determining the mass and width of a charmonium resonance. At the same time precise measurements of the beam energy and the orbit length leads to a more accurate value of η, which is necessary for understanding beam behavior during transition crossing. Discussions in this section and in the next section are based on a paper by the members of the E760 collaboration [39].

In principle the beam energy can be calculated if the orbit length and the revolution frequency of the beam are known. The revolution frequency of the beam can be measured precisely from the Schottky spectrum with a spectrum analyzer. While the length of the central orbit was determined by surveying technique, the measurement is not precise enough for a better J/ψ mass measurement. Instead, the length of the central orbit is determined by observing the J/ψ whose mass is well known and width is very narrow. The beam is decelerated down to J/ψ, and the orbit length at that point is obtained from the J/ψ energy and the revolution frequency. This horizontal orbit at the J/ψ is referred to as the reference orbit. The orbit is then controlled to be the same as the reference orbit at any other resonances so that the orbit length is a known value.

4.3.1 Frequency Measurement. Both average beam energy and beam spread are calculated from the measurement of the beam revolution frequency spectrum. The beam energy is determined by measuring the velocity of the beam. The beam velocity is given by:

$$c\beta = fL = f(L_0 + \Delta L) \tag{4.2}$$

where $c\beta$ is the beam velocity in the laboratory frame, f is the revolution frequency of the particles in the beam, L is the orbit circumference which differs from the reference orbit L_0 by ΔL.

The energy spread of the beam is derived from the revolution frequency spectrum of the beam by

$$\frac{\Delta P}{P} = -\frac{1}{\eta}\frac{\Delta f}{f} , \tag{4.3}$$

where $\eta = 1/\gamma_t^2 - 1/\gamma^2$.

The beam revolution frequency spectrum is measured from the longitudinal Schottky signal of the beam current. The Schottky signal is detected by the Accumulator longitudinal Schottky detector which is connected to a *HP* 8568B spectrum analyzer. The frequency profile given by the spectrum analyzer every 3 to 5 minutes is then read out and saved on tape.

4.3.2 The Orbit Length Measurement. The reference orbit is determined by decelerating the beam to the excitation energy of the J/ψ resonance at 4065.7 MeV/c beam momentum, slowly scanning the beam energy in small increments of 0.5 MeV as the resonance is approached, and measuring the J/ψ production cross section to determine where the resonance peak occurs. At the resonance peak the beam revolution frequency f_0 is measured. Since the J/ψ is very narrow (0.068 MeV) and its mass is well known (3096.9 $\pm$ 0.1 MeV), the reference orbit length can be determined to as high a precision as 2 mm. The reference length at the peak of the J/ψ resonance is given by

$$\begin{aligned} L_0 &= \frac{c\beta_0}{f_0} \\ &= \frac{cM_\Psi}{f_0\left(M_\Psi^2 - 2m_p^2\right)}\sqrt{M_\Psi^2 - 4m_p^2} , \end{aligned} \tag{4.4}$$

where f_0 is the revolution frequency of the beam at the J/ψ beam energy, m_p is the proton mass, and M_Ψ is the mass of the J/ψ.

The primary difficulty in the determination of the beam energy is the measurement of the orbit length change ΔL between the reference orbit and the current orbit of interest. The measurement of ΔL is facilitated by 48 horizontal beam position monitors (BPM's) distributed throughout the Accumulator at horizontally focusing quadrupole locations. The BPM's measure the horizontal position of the

beam. One digital bit of the BPM readout, averaged over 20 samples, varies from 0.3 mm to 1.2 mm depending on the location of the BPM. The BPM readout at the energy of interest is compared to the BPM readout that was recorded at the reference energy. The resulting difference orbit is used to calculate ΔL.

The orbit length change, expressed in terms of the difference in horizontal position between the reference orbit and the current orbit is given to the fist order by (cf. ref. [20], p. 42)

$$\Delta L = \int_0^{L_0} \frac{\Delta x(s)}{\rho(s)}\, ds \ , \tag{4.5}$$

where

$$\rho(s) = \frac{P}{eB(s)} \tag{4.6}$$

is the radius of curvature of the reference orbit at position s, s is the path length along the reference orbit, and $\Delta x(s)$ is the horizontal displacement from the reference orbit at position s. The second and higher order terms not appearing in equation (4.5) turn out to be completely negligible (10^{-8}). Since $B(s)$ is large only in the dipole magnets, the effects due to quadrupoles, sextupoles, and trim dipoles can be neglected. Thus, to a good approximation, the integral of equation (4.5) can be replaced by a sum that includes only the contribution from the main bending dipole magnets,

$$\Delta L = \sum_{i=1}^{N_{\text{dipole}}} \frac{\Delta x_i}{\rho} \Delta s_i \ , \tag{4.7}$$

where Δx_i is the horizontal displacement from the reference orbit at the ith dipole, ρ is the radius of curvature which is 17.464 m for all main dipoles, and Δs_i is the effective length of the ith dipole.

Equation (4.7) requires that Δx be known at the center of each dipole magnet. They are extracted from the analysis of the BPM data. Since the Δx's are not measured at the center of the dipoles, a method of extrapolating to the center of the dipole is needed. The displacement Δx_i is expressed in terms of horizontal

displacement readout on two or three nearby BPMs. The thin lens approximation† is used to track Δx through the quadrupoles.

It is desired to keep the same orbit at all resonances. The first thing to do is to fix the radial position of the beam. This is accomplished by fixing the momentum cooling pickup in the AP20 high dispersion region at a fixed position and maintaining constant cooling gain to compensate for the average ionization loss of the $\bar{p}$ beam traversing the gas jet. Secondly, all the magnets should be ramped proportionally to the beam momentum. This is not accomplished for the entire energy range in which the experiment is interested. But for each scan across a narrow resonance, this can be assumed to be true. The magnitude of this error can be calculated from [40]

$$\sqrt{\langle \delta x_i^2 \rangle} = \frac{\sqrt{N\beta_i < \beta >}}{2\sqrt{2}\sin(\pi\nu)}(\delta\theta)_{\rm rms} \ , \tag{4.8}$$

where δx_i is the closed orbit distortion at location i produced by N random kicks $(\delta\theta)_{\rm rms}$ around the ring. It is assumed that $(\delta\theta)_{\rm rms}/\theta$ is about 10^{-5} because it corresponds to the level to which the dipole bus is regulated. With all these numbers, δx_i is found to be about 1.4×10^{-4} m. This corresponds to an error in orbit length of $\Delta L = 0.12$ mm.

For each scan of a narrow resonance, as long as the two conditions mentioned above are satisfied the orbit length variation (to the degree of accuracy described above) can be ignored. The total width measurement is independent of the orbit length measurement. On the other hand, the resonance mass measurement does depend on the orbit length measurement because it cannot be assumed that the orbit does not vary over the energy range from the J/ψ to the current resonance of interest.

---

† A quadrupole focuses a charged particle with a certain focal length, like an optical lens. "Thin lens" means that the physical length of the quadrupole is much shorter than its focal length.

Table 4.2. Orbit Length Measurements

Run Number	Average dL (mm)	$\sigma(dL)$ (mm)
748	0.29	0.24
749	0.31	0.18
752	0.99	0.25
753	1.09	0.27
756	0.61	0.28
757	0.58	0.26
760	0.0	0.36
	-0.91	0.06
761	-0.69	0.16
764	0.22	0.25
765	0.22	0.22
768	-0.61	0.28
769	-0.71	0.24

The error in the orbit length measurement is estimated from one Ψ' scan during which the cooling pickup position and the cooling gain were believed to be kept constant throughout the scan. Since the orbit length variation is negligible, any variation measured by the BPM is an estimation of the measurement error. The orbit length measured by the BPMs is listed in table 4.2 from which a conclusion can be drawn that the error in the orbit length measurement is ± 1 mm.

The error in the center-of-mass energy is given by

$$\Delta E_{\rm cm} = \frac{m_p^2 \beta^2 \gamma^3}{M_r} \left[\frac{dL}{L} + \frac{df}{f} \right] , \tag{4.9}$$

where M_r is the resonance mass. The error is dominated by the uncertainty in the orbit length measurement because $df/f = 3 \times 10^{-7}$, but $dL/L = 2 \times 10^{-6}$. The effect of a given error in the orbit length measurement becomes worse with increasing energy. At the J/ψ energy $\delta E = \pm 0.050$ MeV, and at the Ψ' energy $\delta E = \pm 0.150$ MeV.

4.4 Measurements of Beam Energy Spread

To obtain the energy spread of the beam, the value of η at that energy must be known. The methods used to determine η are described in this section.

4.4.1 Double Scan. The beam energy spectrum is measured by measuring the beam frequency spectrum. It is important to know dE/df in order to relate beam frequency spread to beam energy spread. A scheme known as "double scan" was used to measure dE/df.

In a normal scan the beam energy is changed in steps to scan the resonance. In each step the magnet settings are changed in proportion to the energy change to keep the beam on the central orbit. In a double scan,the resonance is scanned twice, once with the beam on a "central orbit" and the other time on a "side orbit". The side orbit is radially displaced away from the central orbit. The frequency difference between the two orbits is about one σ_f of the beam frequency spread. If the energy difference between the two orbits are known, dE/df is readily calculated. Because the peak of the resonance defines the energy uniquely, it can be used as a marker for the measurement of the energy difference between the two orbits. For each central and side orbit pair with the same magnet settings,

$$E_s - E_c = \frac{dE}{df}(f_s - f_c) \ . \tag{4.10}$$

Let f_1 and f_2 be the revolution frequencies of the beam on the central and side orbit respectively at the resonance peak. Let f_3 be the frequency of the beam on the central orbit corresponding to f_2, *i.e.*, f_3 and f_2 form a pair. From the above equation,

$$E_2 - E_3 = \frac{dE}{df}(f_2 - f_3) \ . \tag{4.11}$$

Between the first and third orbit,

$$E_1 - E_3 = \beta\gamma^3 m_p(\beta_1 - \beta_3) = \beta^2\gamma^3 m_p \left(\frac{f_1 - f_3}{f_3}\right) \ . \tag{4.12}$$

Because E_1 and E_2 are equal, from equations (4.11) and (4.12),

$$\frac{dE}{df} = \beta^2\gamma^3 m_p \left[\frac{f_1 - f_3}{f_3(f_2 - f_3)}\right] . \tag{4.13}$$

Then a expression for η is

$$\eta = \frac{f_2 - f_3}{\gamma^2(f_1 - f_3)} . \tag{4.14}$$

The derivation of equation (4.14) assumes that the length of the first orbit and the third orbit is exactly the same. Because the beam position at the high dispersion region is fixed by the position of the momentum cooling pickup, this assumption is good if the orbit distortion introduced by the random kicks of the magnetic elements around the ring can be ignored. The contribution of the random kicks was estimated to be 0.12 mm in last section. Thus the difference between the two orbit lengths can be ignored.

It can be seen from equations (4.13) and (4.14) that dE/df and η can be measured accurately by this method because it depends only on the frequency measurement. The parameters in those equations (β and γ) are known accurately because resonance masses of J/ψ and Ψ' are known accurately. For the narrow states J/ψ and Ψ', double scans were performed beside the normal scans. For wider states χ_1 and χ_2 only single scans were done. For these states, η was measured by measuring the synchrotron frequency and γ_t of the machine.

4.4.2 Determination of η From f_s Measurements. In this method the beam is bunched at h=2. When the RF signal is on, the synchrotron frequency of a particle undergoing the synchrotron oscillation is related to η by

$$f_s^2 = -\frac{eV f_{\rm rf}^2 \eta \cos\phi_s}{2\pi h \beta^2 E_s} , \tag{4.15}$$

where every quantity has been explained in chapter 2. When the beam is not being accelerated or decelerated, the absolute value of η can be expressed in terms of f_s as

$$|\eta| = 2\pi h \frac{f_s^2}{f_{\rm rf}^2}\beta^2 \left(\frac{E_s}{eV}\right) . \tag{4.16}$$

There are several measurements which must be made in order to evaluate η. The energy of the beam is known to better than 1×10^{-4}. The RF frequency is known to 1×10^{-7}. For the beam energies of interest to us, the synchrotron frequency typically varies between several Hertz when near transition to several tens of Hertz. The measurement of the synchrotron frequency is made by Fourier decomposing the signal from a gap monitor with the use of the *HP*3652A dynamic spectrum analyzer with milli-Hertz resolution. In this spectrum the synchrotron motion of the beam appears as a series of sidebands near the revolution frequency of the beam. By measuring the frequency difference of many synchrotron frequency harmonics, typically eight to twelve, the synchrotron frequency can be measured to better the 1%.

The primary uncertainty in the determination of η from this technique is due to the uncertainty in the measurement of the RF voltage. The most accurate measurement of the RF voltage utilizes a bolometric RF power meter. Besides, distortion of the RF wave due to other resonant modes changes the synchronous phase and synchrotron frequency of the beam. In order to take this effect into account when determining η, the harmonic content of the RF voltage is measured by a spectrum analyzer. The relative amplitudes of these components are measured to be more than two orders of magnitude lower than the power at $h = 2$. The phases of these harmonics are not known (it is the power that is measured) and therefore a correction to the power meter measurement cannot be calculated. Estimates with the actual power spectrum of the RF voltage show that, with the worst possible phase relationship among those frequency components, the change in the synchrotron frequency is less than 0.5%.† In other words the distortion in the RF wave is negligible. The power meter is calibrated at the J/ψ energy using equation (4.15). η used in the voltage calibration is obtained from double scan at J/ψ. This introduces a 5% error in the measurement. The uncertainty in the RF voltage actually seen by the beam introduces another 5% error. The

† M. Church, private communication.

Table 4.3. Results of η Measurements [40]

States	η (γ_t)	η (f_s)	η (double scan)
J/ψ	−0.0186	−0.0185	−0.0182
χ_1	0.0046	0.0053	-
χ_2	0.0064	0.0068	-
ψ'	0.0109	0.0105	0.0094

overall uncertainty in the estimate of η from this method is approximately 10%. The measurement of η at various energies is tabulated in table 4.3.

4.4.3 Determination of η From γ_t Measurements. If the RF is off and only the magnetic field strength of the main bending dipoles is changed, the beam revolution frequency and orbit length will change in a way such that the beam momentum remains constant. The relationship between the change in magnetic field strength dB and the change in revolution frequency df is given by

$$\frac{dB}{B} = \gamma_t^2 \frac{df}{f} \ . \tag{4.17}$$

Thus there is a power law relationship between B and f in this special case (no change in beam energy), and γ_t can be estimated by measuring the slope of a graph of B versus f.

The measurement of B is performed by reading out a NMR probe located in a main dipole magnet which is not part of the Accumulator lattice but is powered by the same electrical bus which supplies all the other main dipoles. The revolution frequency is the center of the longitudinal Schottky spectrum as measured with a spectrum analyzer. Once γ_t is obtained, with the known η value of the beam η can be calculated.

There are several difficulties in measuring η using this technique. A small error in the determination of γ_t gives rise to a large error in η, as can be seen by taking differentials on both sides of the formula defining η:

$$\frac{d\eta}{\eta} = \left[\frac{2}{\left(\frac{\gamma_t}{\gamma}\right)^2 - 1}\right] \frac{d\gamma_t}{\gamma_t} \,. \tag{4.18}$$

As γ approaches γ_t the fractional error in η becomes large without bound. At the J/ψ the quantity in the square brackets is -5.37, at the Ψ' is is 4.57. The measurement of B is subject to unknown uncertainties. The dipole magnet containing the NMR probe is not affected by shunt corrections that are applied to the other main dipoles in the lattice. Thus the NMR does not see exactly the same field as is seen by the beam. There are two effects that change γ_t as we change the B field. First, the lattice changes since the quadrupoles do not change as the dipole field is changed. This effect contributes about 4% error. Second, the second order term in γ_t contributes about 2% error. In addition, there is the systematic uncertainty due to misalignment of quadrupoles and sextupoles. Table 4.3 lists the results of η measurements at various energies.

4.5 Deceleration History

Deceleration in E760 was first attempted in September 1987 with a proton beam. ARF1 was used for deceleration during 1987-1988 fixed target run. By January 1988 the proton beam of 3.9 mA had been decelerated through the transition energy with 3.2 mA remaining in the machine. In April 1988 deceleration down to the transition was achieved with 87% efficiency for a beam of 11 mA. After a long collider run, deceleration work resumed in August 1989 when a proton beam was decelerated with 100% efficiency to momentum of 4 GeV/c. In March 1990, the first antiproton beam of 11 mA was successfully decelerated to that momentum. Since 1989, deceleration has been carried out with the newly improved ARF3 system.

CHAPTER V

ACCUMULATOR LONGITUDINAL IMPEDANCE

Coherent instabilities are very important collective phenomena since they damage the beam quality when the beam current is above the instability threshold. Collective phenomena are effects caused by the presence of a large number of particles in the beam, while coherent effects in particular require definite phase relationship among the beam particles. Coherent effects make a high intensity beam behave differently from the dynamics of a single particle, which is entirely determined by the guide field.

The origin of the coherent effects is the electromagnetic field created by the beam itself. This self-field, in which the beam moves, depends strongly on the electromagnetic properties and the geometry of the environment. When the beam intensity is large enough, the effects become sizeable and cannot be neglected. In other words, the motion of a particle in such an intense beam is strongly influenced by the beam-generated field. Longitudinal coherent instability occurs if a small deviation from the nominal distribution of particles in longitudinal position and energy creates self-fields which increase this initial deviation.

The longitudinal impedance is an important machine parameter which gathers all the properties of the longitudinal self-field of a beam. The instability threshold depends on the impedance of the ring. In the process of the Accumulator transition crossing, beam momentum blow up caused by longitudinal coherent instability is observed. Identifying the source of the instability relies on knowledge of the Accumulator longitudinal impedance. This chapter first introduces the concept of the longitudinal impedance and explains its role in determining the instability threshold of a machine, and then shows the estimated Accumulator longitudinal impedance. Finally, measurement of the Accumulator impedance with an unbunched beam is described.

5.1 Longitudinal Impedance and Longitudinal Instability

Longitudinal coherent effects build up because the beam particles interact with each other via wake fields, which are time-varying longitudinal electric fields generated by the charge of the beam. Impedance is an important frequency domain quantity which is related to the wake field through the Fourier transform. It determines the beam induced voltage at a specific frequency produced by the a.c. component of the beam current with that frequency.

In principle, wake fields can be determined by solving Maxwell's equations with proper boundary conditions. However, it is a difficult task (even in the frequency domain) when taking into account the numerous details of a vacuum chamber with a large number of cross section changes, pickup electrodes, kickers, septum magnets, bellows, and so on. In studying coherent effects, impedance is introduced to parameterize the effects of wake fields. Wake fields, impedances, and coherent effects are very important topics in modern accelerator physics, and there are many dedicated articles. A general introduction to wake fields and impedance concepts is given in an article by P. Wilson (cf. ref. [30], sec. 3), and an article by A. Chao [41] gives a review of basic analytic approaches to instability calculations. This section only gives a brief description about the longitudinal impedance and longitudinal instability to provided an overall picture on the subject. Discussion of longitudinal instability is limited to the unbunched beam case which directly relates to the stability problems in the Accumulator transition crossing process.

5.1.1 Wake Fields and Impedances. When a charged particle moves in free space at a velocity v close to the velocity of light c, in the laboratory frame the electromagnetic field carried by the particle is Lorentz contracted into a thin disk perpendicular to the particle's direction of motion with an angular spread of of order of $1/\gamma$, where $\gamma = [1 - v^2/c^2]^{-1/2}$. Thus a second charged particle moving behind the first one on the same or on a parallel path, at the same velocity $v \approx c$, will not be subjected to any forces from the fields produced by the leading charge. The situation is different if the two particles are moving in the vicinity

of metallic objects or other boundary discontinuities. The trailing particle still will not experience the direct fields in the wave front moving with the leading charge. This wave can, however, scatter from the boundary discontinuities, and this scattered radiation will be able to reach the trailing particle and exert forces parallel and perpendicular to its direction of motion. These scattered waves are termed wake fields. Let q be the charge of the leading particle and e be that of the trailing particle. In the longitudinal direction the force acting on e is proportional to q and can be expressed as

$$F_L = -eqW_L(s) \ , \tag{5.1}$$

where W_L is called the wake function. It describes the response of the vacuum chamber environment to a delta function beam, and is mathematically equivalent to a Green's function: the force acting on a slice of a real beam at azimuth s is given by

$$\int_{-\infty}^{s} W_L(s - s')\lambda(s')ds' \tag{5.2}$$

where $\lambda(s')$ represents the charge density. The boundaries of the integral are set such that only charges before s contribute to the force due to causality.

In a circular accelerator, because the motion of a particle is periodic and many physical phenomena manifest themselves through one or more spectral lines, it is natural and often convenient to do beam dynamics in the frequency domain. Time and frequency domain quantities are related by the Fourier transform. In the frequency domain, the beam current is decomposed into the Fourier components which are of sinusoidal form. The contribution of each a.c. component of the beam to the wake field can be studied separately by considering the response of the environment to a modulated beam current of the form

$$I_0(s, \omega) = \hat{I}_0 e^{j(\omega t - ks)} \ . \tag{5.3}$$

For a coasting beam, ω can only be a multiple of the revolution frequency ω_0, *i.e.*, $\omega = n\omega_0$.

With the above current the longitudinal wake field at position s is the sum of wakes produced by all the charges that have passed at previous times:

$$\begin{aligned} E_L(s,\omega) &= \int_0^\infty \frac{ds'}{c} I_0(s+s',\omega) W_L(s') \\ &= I_0(s,\omega) \int_{-\infty}^\infty \frac{ds'}{c} e^{-j\omega s'/c} W_L(s') \ . \end{aligned} \tag{5.4}$$

A retarding voltage over the path of length ℓ which contains the wake field can be defined by writing $V(s,\omega) = -\ell E_L(s,\omega)$. Then the voltage is related to the current by

$$V(s,\omega) = -Z_L(\omega) I_0(s,\omega) \ , \tag{5.5}$$

where

$$Z_L(\omega) = \ell \int_{-\infty}^\infty \frac{ds'}{c} e^{-j\omega s'/c} W_L(s') \tag{5.6}$$

is called the longitudinal impedance and is related to the wake function through the Fourier transform. Impedance in the frequency domain and wake function in the time domain are two complementary descriptions of the same physics.

In general, for a circular accelerator there are four major sources of the longitudinal impedance. In the following discussion the impedance will be expressed in the form of Z_L/n instead of Z_L, where n is the harmonic number. As will be seen in next section about longitudinal instability that it is Z_L/n that directly relates to beam stability problems.

Smooth beam pipes produce two effects: a capacitive or space charge effect and a resistive wall effect. The space charge effect results from the fact that a beam will produce a longitudinal electric field. Since the vacuum pipe is at ground, the potential will vary along the beam if a density modulation is present. The potential is proportional to charge, and the longitudinal electric field which is the negative gradient of this potential is therefore 90° out of phase with the beam current. In other words, the effect is capacitive. The charge induced on the walls of the beam chamber will follow the propagation of the beam modulation. The

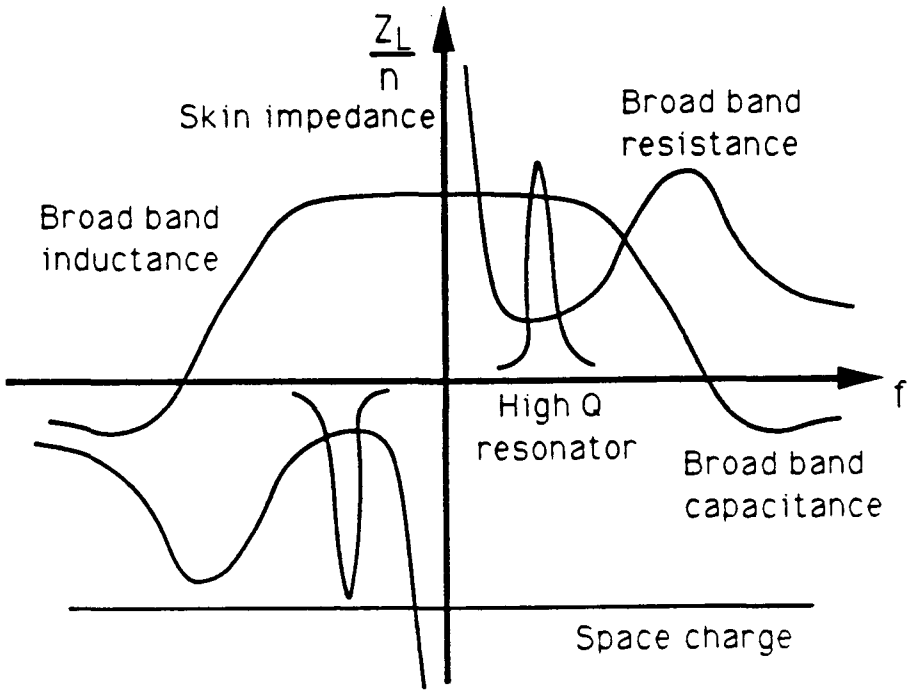

Figure 5.1. Qualitative Plot of Longitudinal Impedance.

space charge component of Z_L/n is independent of frequency and is very large for low β particles:

$$\left(\frac{Z_L}{n}\right)_{\text{s.c.}} = -j\frac{Z_0 g}{2\beta\gamma^2}\ , \tag{5.7}$$

where $Z_0 = \mu_0 c = 377\Omega$, and $g = 1 + 2\ln(b/a)$ is the geometric factor with a and b being the radii of the uniform round beam and beam pipe respectively.

If the walls have non-zero resistance, at frequencies where the skin depth is small, the "resistance" actually consists of equal parts of resistance and inductance:

$$\left(\frac{Z_L}{n}\right)_{\text{r.w.}} = (1+j)\frac{Z_0\beta\delta_0}{2b\sqrt{n}}\ , \tag{5.8}$$

where $\delta_0 = 2/\sqrt{\mu_0\omega_0\sigma}$ is the skin depth at the revolution frequency ω_0.

Contribution to the longitudinal impedance also comes from the parasitic resonators corresponding the unwanted resonances such as higher order longitudinal modes in RF cavities. These are narrow band ($Q \gtrsim 10$) resonators.

Finally, numerous incidental cross section variations produce a longitudinal impedance which can be accounted for by the so called broad-band model. The impedance of a single transition is inductive and it rises approximately linearly with frequency up to the cut-off frequency of the smaller pipe. At cut-off, the impedance drops precipitously and becomes mostly real. Therefore this impedance can be modeled with a $Q = 1$ (broad band) resonator centered around the cut-off frequency of the pipe. The impedance for a cavity with quality factor $Q = 1$, shunt resistance R_s, and resonance frequency being the cut-off frequency ω_c is

$$(Z_L)_{\text{b.b.}} = \frac{R_s}{1 + j\left(\frac{\omega}{\omega_r} - \frac{\omega_r}{\omega}\right)} \ . \tag{5.9}$$

As is expected, at low frequencies $\omega \ll \omega_c$ the impedance is inductive and depends linearly on the frequency, when the frequency increases it becomes more and more resistive.

A qualitative plot of longitudinal impedance is given in figure 5.1, in which properties of the four major impedance sources are sketched.

5.1.2 Longitudinal Instability. Longitudinal instability of a coasting beam can be visualized as self-bunching by the beam induced voltage. Quantitatively, this instability can be understood with the aid of the Vlasov equation which describes the evolution of the particle density distribution in the longitudinal phase space.

The longitudinal phase space is formed by θ, which is the azimuthal position of the particle, and its canonical conjugate variable

$$J = 2\pi \int_{E_0}^{E} \frac{dE}{\omega} \ , \tag{5.10}$$

where E_0 is the energy in the center of the distribution, or some design energy of interest. Let $\Psi(t,\, \theta,\, J)$ be the density distribution in phase space. Liouville's theorem states that this phase space density does not change with time:

$$\frac{d\Psi(t,\, \theta,\, J)}{dt} = 0 \ . \tag{5.11}$$

Usually the beam contains only a small relative energy spread and an even smaller frequency spread, thus the variable J can be approximated by $\omega_0\epsilon = \omega_0(E - E_0)$, where ω_0 is the revolution frequency corresponding to E_0. The above equation can be explicitly expressed as:

$$\frac{\partial\Psi(t,\ \theta,\ \epsilon)}{\partial t} + \omega\frac{\partial\Psi(t,\ \theta,\ \epsilon)}{\partial\theta} + \dot{\epsilon}\frac{\partial\Psi(t,\ \theta,\ \epsilon)}{\partial\epsilon} = 0 \tag{5.12}$$

which is the Vlasov equation. The time derivative of the relative energy, $\dot{\epsilon}$, is caused by the coherent self-field of the beam and can be expressed in terms of the beam induced voltage V_s as

$$\dot{\epsilon} = \frac{e\omega_0 V_s}{2\pi}\ . \tag{5.13}$$

The phase density $\Psi(t,\ \theta,\ \epsilon)$ is normalized such that it is related to the total number of beam particles N and the beam line density $\lambda(\theta)$ by

$$\int_0^{2\pi}\int_{-\infty}^{\infty}\Psi(t,\ \theta,\ \epsilon)d\epsilon d\theta = N \tag{5.14}$$

and

$$\int_{-\infty}^{\infty}\Psi(t,\ \theta,\ \epsilon)d\epsilon = \lambda(\theta)\ . \tag{5.15}$$

For a small initial deviation from the nominal stationary distribution, the solution to the Vlasov equation can be assumed to have the form

$$\Psi(t,\ \theta,\ \epsilon) = \Psi_0(\epsilon) + \Psi_1(\epsilon)e^{j(\Omega t - n\theta)} \tag{5.16}$$

with

$$\Psi_1 \ll \Psi_0\ , \tag{5.17}$$

and the Vlasov equation can be linearized as

$$\frac{\partial\Psi_1(t,\ \theta,\ \epsilon)}{\partial t} + \omega\frac{\partial\Psi_1(t,\ \theta,\ \epsilon)}{\partial\theta} + \dot{\epsilon}\frac{\partial\Psi_0(\epsilon)}{\partial\epsilon} = 0\ . \tag{5.18}$$

The perturbation which is added on top of the stationary distribution assumes a prebunching of the beam with n wavelengths around the ring. In other words, only the nth Fourier component of the beam is taken into account. The corresponding a.c. component of the beam, I_n, is related to Ψ_1 by

$$I_n = e\omega_0 \int_{-\infty}^{\infty} \Psi_1(\epsilon) d\epsilon \ . \tag{5.19}$$

The circular frequency with which this perturbation propagates is not exactly $n\omega_0$. Beam induced fields cause a slight coherent frequency shift $\Delta\omega$ which is defined to be

$$\Delta\omega = \Omega - n\omega_0 \tag{5.20}$$

with $\Delta\omega$ being a complex number. With the phasor notation adopted in this section, the perturbation will grow exponentially with time if $\mathrm{Im}(\Delta\omega) < 0$. Provided the coherent frequency shift is much smaller than the beam revolution frequency, in other words if the growth time of the perturbation is much longer than the revolution period, the two adjacent harmonics cannot couple and it is correct to assume (5.16) to be the form of the solution to the Vlasov equation.

Substituting equation (5.13) into the linearized Vlasov equation, the perturbation $\Psi_1(\epsilon)$ leads to the expression [42]

$$I_n e^{j(\Omega t - n\theta)} = -\frac{j e^2 \omega_0^3 |\eta| V_s}{2\pi\beta^2 E_0} \int \frac{\frac{dg_0(\omega)}{d\omega}}{\Omega - n\omega} d\omega \ . \tag{5.21}$$

Inside the integral, $\Psi_0(\epsilon)$ has been replaced by the corresponding frequency distribution function $g_0(\omega)$ which can be obtained from the longitudinal Schottky signal. Other quantities are self-explanatory. The complex path integral can be split into a principal value and a residue [43]:

$$\int \frac{\frac{dg_0(\omega)}{d\omega}}{\Omega - n\omega} d\omega = \mathcal{P}.\mathcal{V}. \int \frac{\frac{dg_0(\omega)}{d\omega}}{\Omega - n\omega} d\omega + j\frac{\pi}{n}\frac{dg_0}{d\omega}\Big|_{\omega=\Omega/n} \ . \tag{5.22}$$

Equation (5.21) eventually describes the beam self-bunching effects. The beam induced voltage V_s is related to the a.c. component of the beam current I_n by

$$V_s = -Z_L I_n e^{j(\Omega t - n\theta)} \ . \tag{5.23}$$

When the beam is far from transition, $\eta \neq 0$, and this voltage will cause the revolution frequency of the particle, and therefore phase space distribution $g_0(\omega)$, to change. This modified I_n in turn changes the strength of the self-field, V_s. It is a process of mutual influence of the beam distribution and the beam generated field. Equilibrium or stability is achieved if V_s is such that in equation (5.21) the right hand side is less than or equal to the left hand side when the coherent frequency shift is $\Delta\omega = 0$. The process is called the decoherence. This condition is usually expressed as a condition on Z_L/n which is the measure of the self-field strength for a given beam current:

$$\left|\frac{Z_L}{n}\right| \leq F\frac{\beta^2 E|\eta|(\Delta p/p)^2}{eI_0} \ . \tag{5.24}$$

This is the well known Keil-Schnell criterion [44]. In the inequality, the form factor F depends on the frequency distribution of the beam and is of order one, I_0 is the d.c. current of the beam, and $\Delta p/p$ is the FWHM momentum spread of the beam. Qualitatively the Keil-Schnell criterion can be thought of as an upper limit for the amplitude of the beam induced voltage causing the self-bunching of the beam: the bucket area must never contains enough charge to generate an equal or greater bucket area.

At the normal operating energy of the Accumulator, with the stack parameters $E = 8.84\text{GeV}$, $|\eta| = 0.02$, $\Delta p/p = 0.0007$, and $I_0 = 0.1\text{A}$, the stability criterion is

$$\left|\frac{Z_L}{n}\right| \leq 850\ \Omega \ . \tag{5.25}$$

The calculated result of the Accumulator impedance fits within this limit, as will be shown in the next section.

However, beam cannot maintain stability when it is near transition. In the transition region, because of small η, all particles have the same revolution frequency to the first order, despite their energy differences. A particle, driven by the coherent field, remains the same azimuthal position relative to other particles in the beam no matter whether it gains or losses energy. In other words, the line structure of the beam and therefore the beam generated field remain the same at each revolution. Decoherence is completely lost, *i.e.*, some particles at certain azimuthal positions keep gaining energy while the other particles keep losing energy. This leads to a disruption of the beam.

5.2 Estimated Accumulator Impedance

For each type of device in the Accumulator, longitudinal impedances have been calculated in an internal $\bar{p}$ memo [45]. Calculations include those for smooth beam pipes, transitions between pipe sizes, cavity structures such as bellows, *etc.*, injection and extraction kickers, strip-line pickups, stochastic cooling pickups and kickers, BPM electrodes, and damper electrodes. The newly installed 4-8 GHz stochastic cooling system was not included in that note.

The result shows that the longitudinal impedance of the Accumulator is mainly generated by the resonant objects ARF3, ARF1, and the longitudinal Schottky detector. The plot of Z_L/n versus frequency given in figure 5.2 shows prominent resonances at 1.2 MHz, 53 MHz, and 79 MHz. Higher modes of the ARF1 cavities occur at 130 MHz and 250 MHz. Broad band cavities, stochastic cooling, and space charge contributes a broad background impedance at these resonant frequencies.

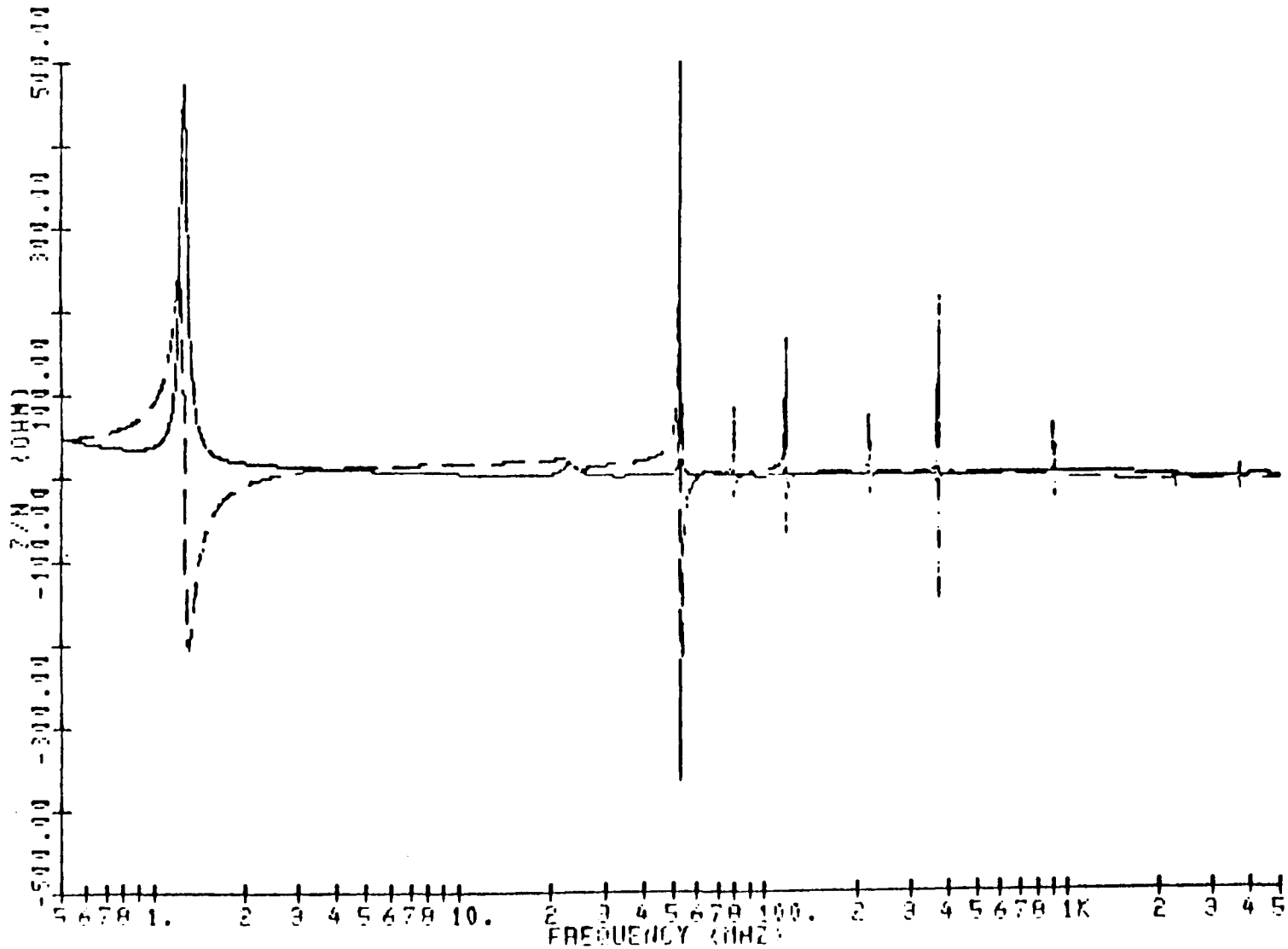

Figure 5.2. Calculated Accumulator Longitudinal Impedance (Real and Imaginary Components) as a Function of Frequency (ref. [45], fig. 7).

5.3 Measurement of Accumulator Impedance

An experiment was set up to measure the Accumulator longitudinal impedance as a function of frequency. The measurements were done by perturbing a coasting beam longitudinally. The sinusoidal excitation voltage generated by a RF cavity causes current modulation to the beam. In the absence of the longitudinal impedance, the amplitude of the modulated current and its phase relative to the excitation is determined by the frequency distribution of the beam. The effect of the longitudinal impedance is that the modulated current produces another voltage at the same frequency as the excitation, which changes the amplitude and phase of the modulated current. The longitudinal impedance is obtained by measuring the current modulation generated by the external RF voltage.

5.3.1 Beam Transfer Function. A small RF voltage applied to the beam causes the current modulation. The beam response or the beam transfer function (BTF) is defined as the ratio of this current modulation to the excitation voltage. The beam response can be derived using the Vlasov equation, and the derivation is very similar to that of the longitudinal instability threshold. In the presence of an external excitation, the time derivative of the relative energy, $\dot{\epsilon}$, is caused the vectorial addition of the beam-induced voltage V_s and the excitation voltage V_e, and can be written as

$$\dot{\epsilon} = \frac{e\omega_0}{2\pi}(V_s + V_e) \ , \tag{5.26}$$

where the beam-induced voltage V_s is given in equation (5.22), and the excitation voltage V_e can be written as

$$V_e(t) = V_0 e^{j\Omega t} \tag{5.27}$$

if the RF cavity is assumed to be located at $\theta = 0$. The a.c. beam current measured by a current detector at a azimuth θ_p satisfies the following equation:

$$I_n e^{j(\Omega t - n\theta_p)} = -\frac{je^2\omega_0^3\eta\left(V_0 - I_n Z_L e^{-jn\theta_p}\right)e^{j\Omega t}}{2\pi\beta^2 E_0}\int\frac{\frac{dg_0(\omega)}{d\omega}}{\Omega - n\omega}d\omega \ , \tag{5.28}$$

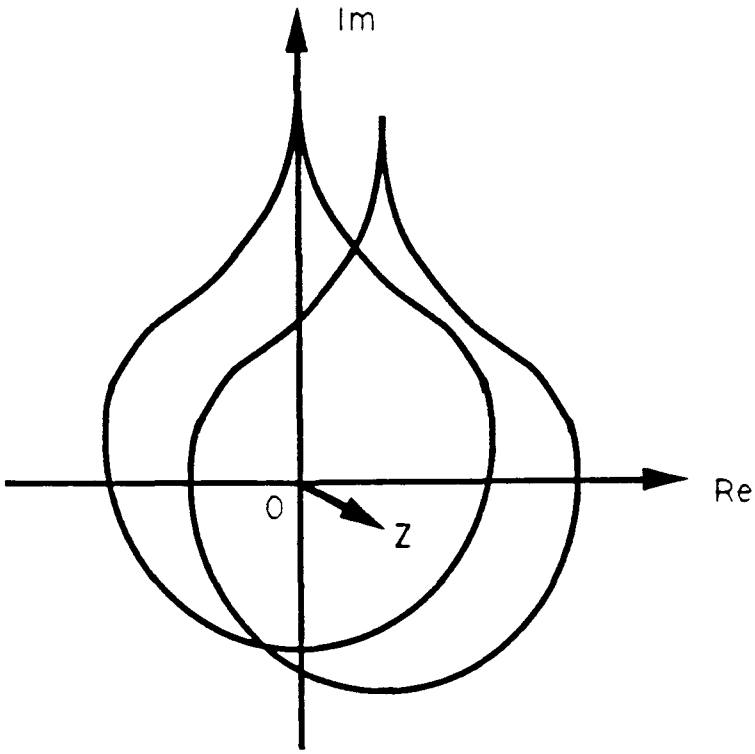

Figure 5.3. A Schematic of the Beam Transfer Function for Impedance Measurement. The impedance causes a displacement of the inverse response calculated from the beam frequency distribution. The vectorial difference of the two diagrams gives the impedance.

which is very similar to equation (5.21) except the additional term for the external voltage.

From equation (5.27), when the current detector is at the same location as the kicker ($\theta_p = 0$), the beam transfer function can be obtained as

$$\frac{1}{\mathcal{R}(\Omega)} \equiv \frac{V_0}{I_n} = \left[\frac{jeI_0\omega_0^2|\eta|}{2\pi\beta^2 E_0} \int \frac{\frac{dg_0(\omega)}{d\omega}}{\Omega - n\omega} d\omega \right]^{-1} + Z_L(\Omega) \ , \tag{5.29}$$

where $1/\mathcal{R}(\Omega)$ stands for the inverse response at a frequency Ω, I_0 is the d.c. beam current, E_0 is the central beam energy, and $\eta = 1/\gamma_t^2 - 1/\gamma^2$. The frequency distribution $g_0(\omega)$ can be obtained from the longitudinal Schottky signal, and therefore the integral on the RHS of the above equation can be computed numerically. It can be seen that in the absence of the impedance the inverse response is determined by the frequency distribution, and the effect of the impedance is to shift

that inverse response. Since the beam only has a small frequency spread around the revolution frequency, a beam response can only be measured near revolution harmonics when $\Omega \sim n\omega_0$, where n is a revolution harmonic, in other words, Ω/n has to fall within the beam frequency spectrum to get a significant response (cf. ref. [43], p. 3). For a scan of the excitation frequency from one side of the frequency distribution to the other at a revolution harmonic, the inverse response for each excitation frequency can be plotted on a complex plane. A sample plot is shown in figure 5.3. Because the range of the excitation frequency scan is much smaller than the revolution frequency, it is reasonable to assume that the impedance is a constant in the range of the frequency scan. Therefore the impedance causes a displacement of the inverse response diagram, and the impedance can be obtained by averaging differences.

When the detector is not at the same location as the kicker, the phase delay of the beam from the kicker to the detector causes a rotation of the inverse response diagram. The connecting cables in the experiment also add additional phase delays. These effects must be taken into account to get the correct results.

To summarize the principle of this beam-based impedance measurement: the beam transfer function is measured when performing an excitation frequency scan through the frequency distribution at a revolution harmonic, the inverse response without the impedance is computed with the measured frequency distribution, and the difference of the two gives the value of the impedance at that revolution harmonic.

5.3.2 Experiment Setup. To measure the impedance in a wide frequency range, a broadband RF kicker is required. In the Accumulator impedance measurements, a broadband RF system called ARF2 was used to excite the beam, and the resultant beam current modulation was measured with the 3kHz - 6GHz Accumulator wall current monitor. A Hewlett-Packard 3577A network analyzer was used to generate the external RF signal applied to the beam, measure the current modulation, and calculate the inverse response. The frequency distribution of the beam was measured using a Hewlett-Packard 8568B spectrum analyzer connected to the Accumulator longitudinal Schottky pickup.

Figure 5.4 shows the schematic setup for the measurements. The experiment was done in the Pbar Source Control Room (AP10 building) which is above the A10 zero dispersion region of the ring. The signal generated by the HP3577A network analyzer is split into two: one is for exciting the beam and the other provides the reference voltage for the beam response calculation. The excitation signal is amplified by a 55dB, 250kHz - 150MHz power amplifier and sent to ARF2 which is located in the A50 zero dispersion region. The current modulation signal detected by the wall current monitor in the A10 zero dispersion region is amplified by a 20dB, 20kHz - 2GHz SONOMA amplifier and sent to an input port of the network analyzer. The network analyzer calculates the beam response by taking the ratio of the wall current monitor signal to the reference voltage. With this setup, the distance between the kicker and detector is about one third of the machine circumference.

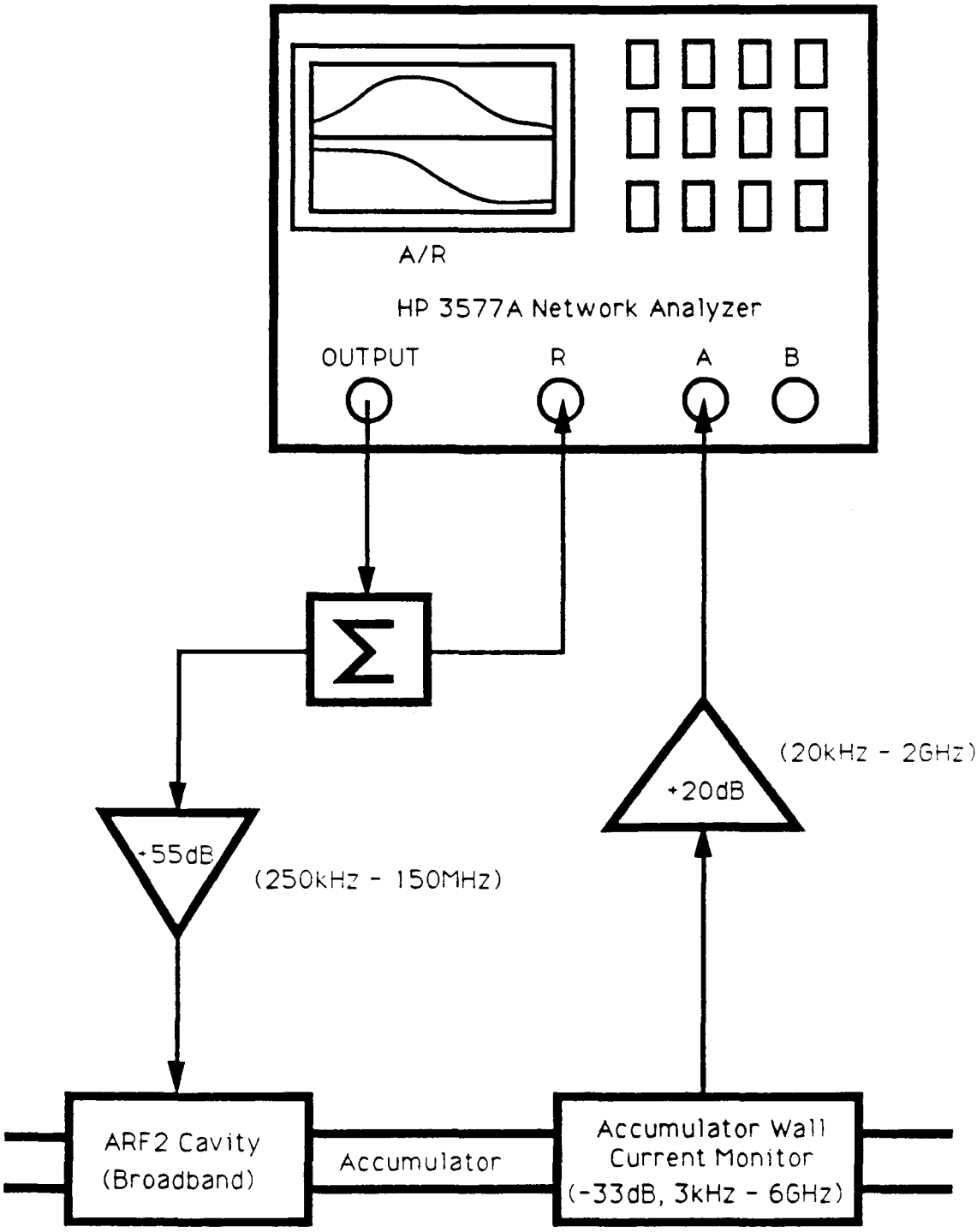

Figure 5.4. A Schematic Drawing of the Accumulator Longitudinal BTF Measurement System. The broadband kicker ARF2 is located in the A50 zero dispersion region, and the Accumulator wall current monitor is in the A10 zero dispersion region.

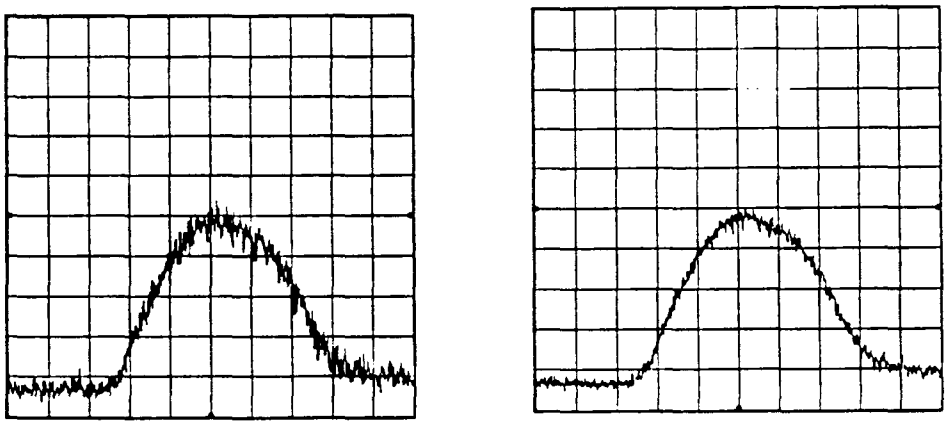

Figure 5.5. Longitudinal Schottky Profiles at Harmonic 126 before and after Many Frequency Scans. The two displays have the same center frequency (78.797765 MHz), frequency span (2 kHz), and vertical scale.The frequency widths taken at points 6dB down from the peak are approximately 400Hz.

5.3.3 Measurement Procedure and Results. The Accumulator BTF measurements were done with beams at 8.9 GeV. In order to obtain correct measurement results, several experimental parameters, which include the amplitude of the network analyzer signal, the frequency sweep time, and the resolution bandwidth of the network analyzer receiver, need to be determined. In addition, the frequency dependence of the ARF2 cavity response needs to be measured for impedance calculation.

The derivation of the beam response given in this section assumes that it is a linear response, *i.e.*, the current modulation of the beam is proportional to the external excitation. This requires that the disturbance to the beam must be small. In the Accumulator BTF measurement experiment, the amplitude of the RF signal generated by the network analyzer at a fixed frequency was gradually increased from −49dBm (minimum) to find the signal range for a linear response. This was done at frequencies corresponding to revolution harmonics $n = 1, 2, 3, 5, 84$. It was found that, up to −15dBm, the beam response is linear. When the amplitude

of the signal exceeded −12dBm, saturation of the +55dB power amplifier caused distortion of the excitation wave. Figure 5.5 shows a result of the beam frequency distribution measurements before and after many frequency sweeps, indicating that the disturbance is negligible.

The resolution bandwidth of the network analyzer receiver can be viewed as the bandwidth of a bandpass filter. The bandwidth of this bandpass filter is determined by a quality factor Q. A smaller resolution bandwidth leads to a more accurate measurement of the BTF, with a longer measurement time due to the fact that a resonant system with a higher Q has a longer filling time†. But on the other hand, in measuring the BTF the sweep time should be kept short in order not to disturb the beam significantly. To find the proper combination of sweep time and resolution bandwidth, frequency sweeps in different directions and with different sweep times were tried for a fixed resolution bandwidth. It was found that, with a small resolution bandwidth of 1Hz, the beam response had a significant frequency shift for upward and downward frequency scans. Such a measurement is shown in figure 5.6; the sweep time is 20 seconds in this example. Increasing the sweep time from 20 seconds to 40 seconds reduced this frequency shift. This indicated that the frequency shift was due to the long filling time of the bandpass filter. Further increase in the sweep time to 120 seconds caused distortion of the beam frequency distribution, as shown in figure 5.7. When the resolution frequency was greater than 10Hz, the difference in the beam response to upward and downward scans became negligible, even for scans as fast as two seconds. Figure 5.8 shows a measurement result.

The inverse response measured by the network analyzer only gives a relative BTF. It must be multiplied by a scale factor before comparing with the calculated inverse response to get the impedance. For this reason, the frequency dependence of the ARF2 cavity was measured in a frequency range up to 200 MHz with a −30dBm excitation signal. Its response is shown in figure 5.9.

---

† *The filling time for a resonant system is the time it takes for the voltage to decay to 1/e of its peak value.*

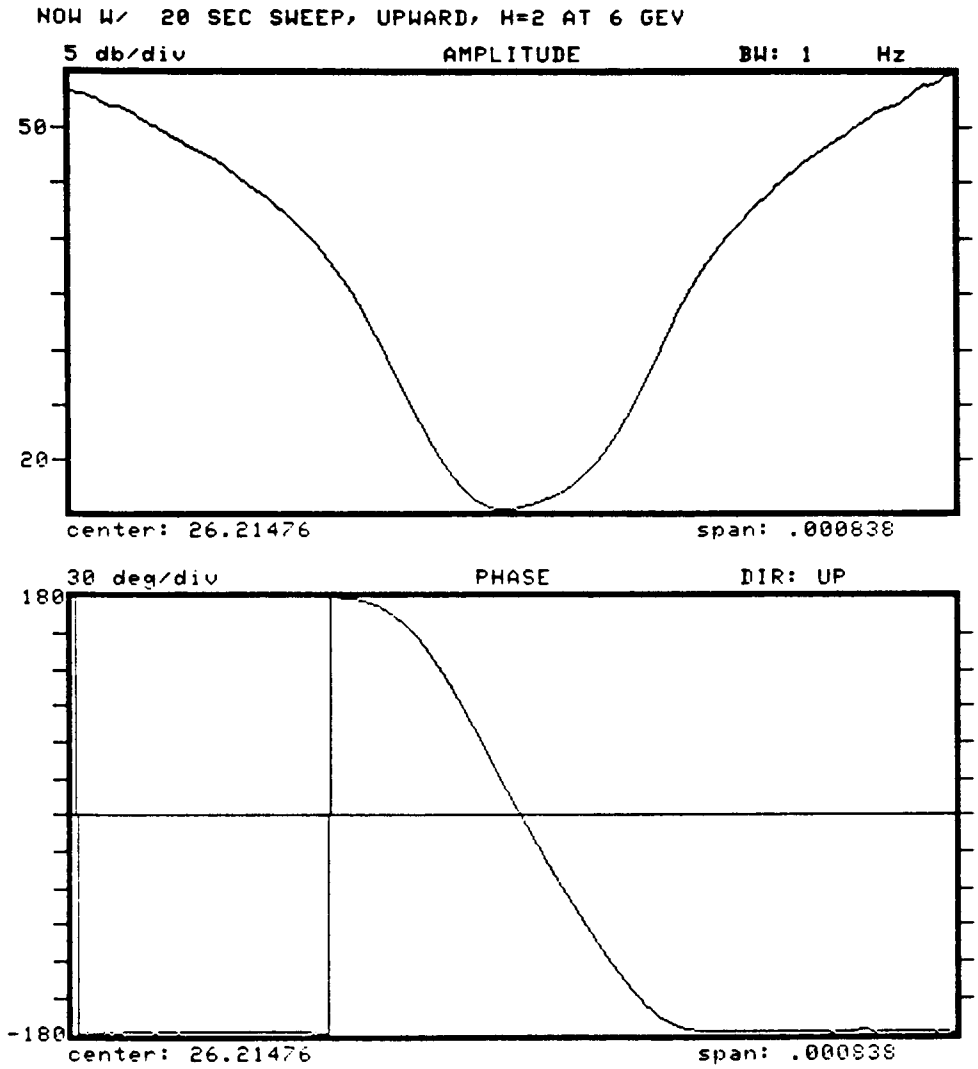

Figure 5.6. Amplitude and Phase of the Inverse Response for a Upward and Downward frequency scans near $h = 2$. The sweep time is 20 seconds. The values of the center frequency and frequency span are invalid.

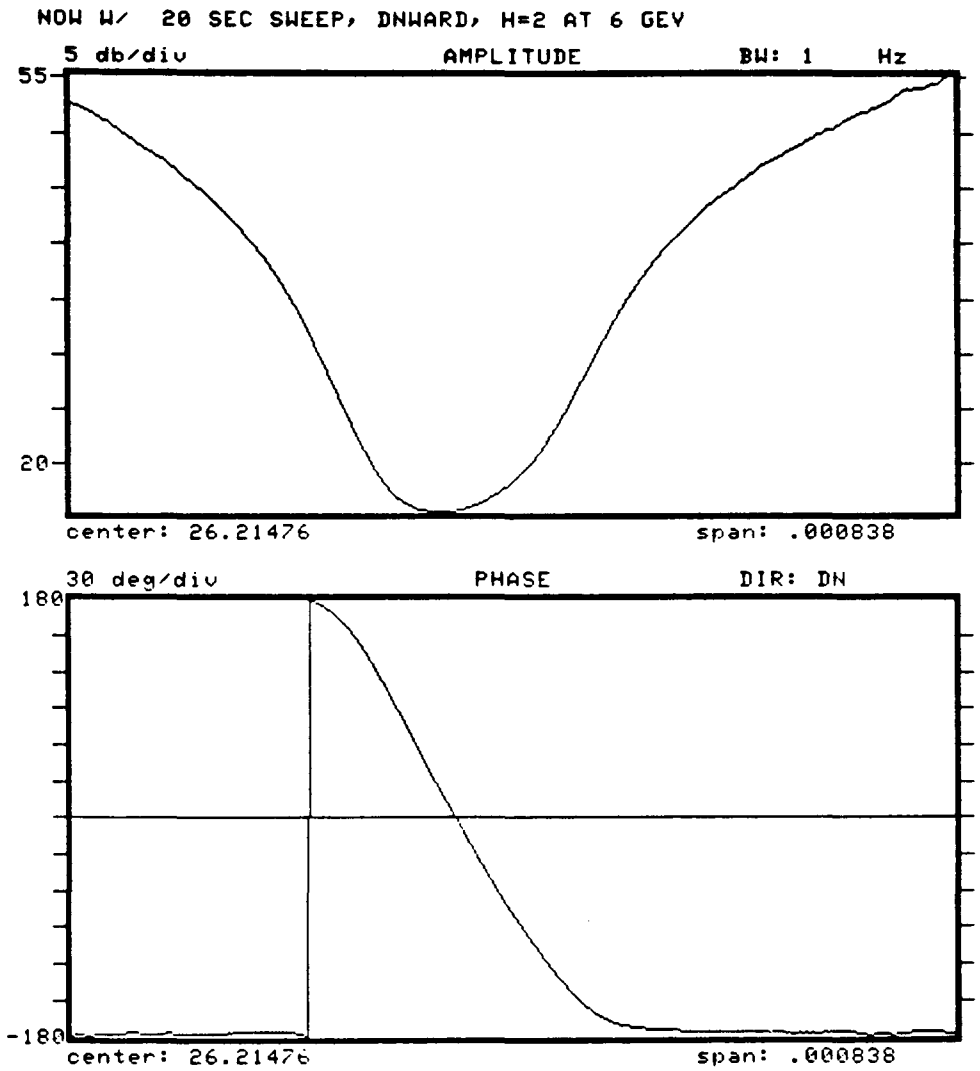

Figure 5.6. (continued)

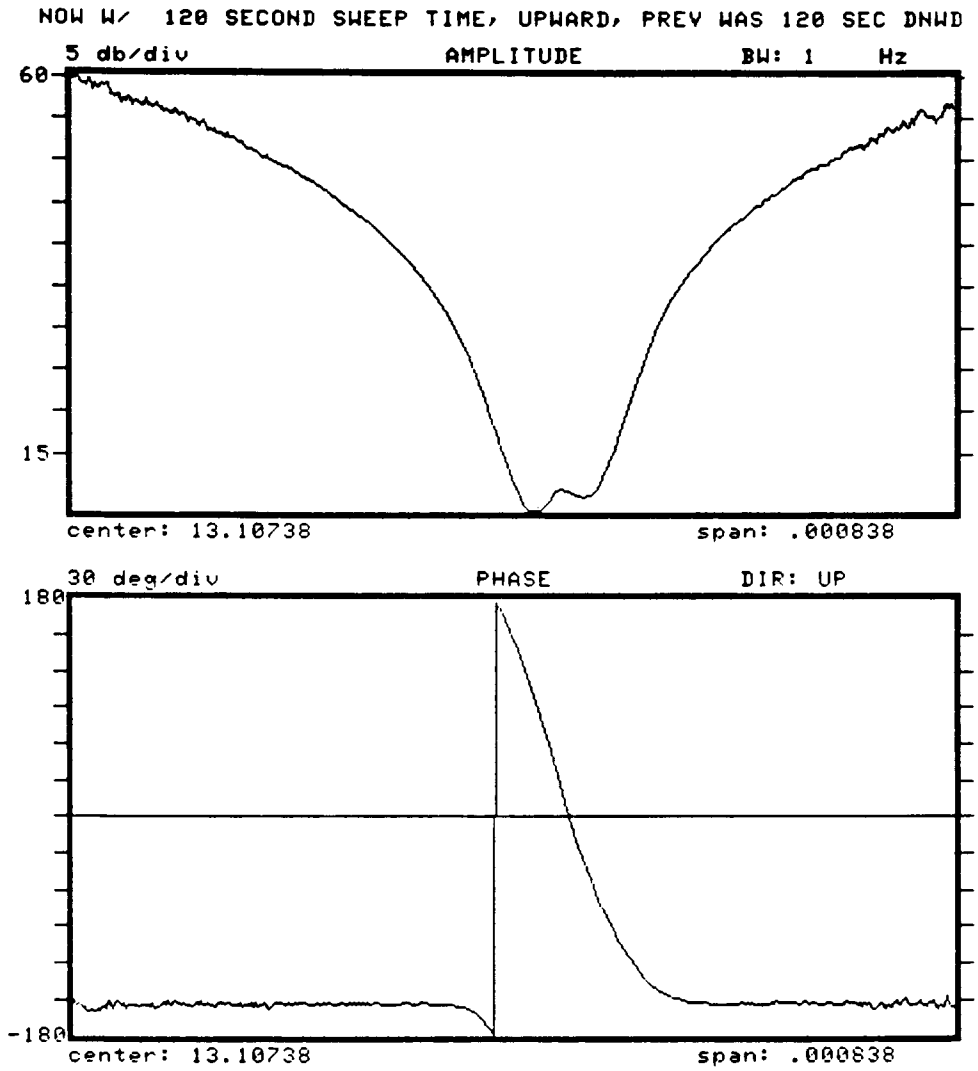

Figure 5.7. Amplitude and Phase of the Inverse Response to a 120 Second Upward Frequency Scan near $h = 1$. The values of the center frequency and frequency span are invalid.

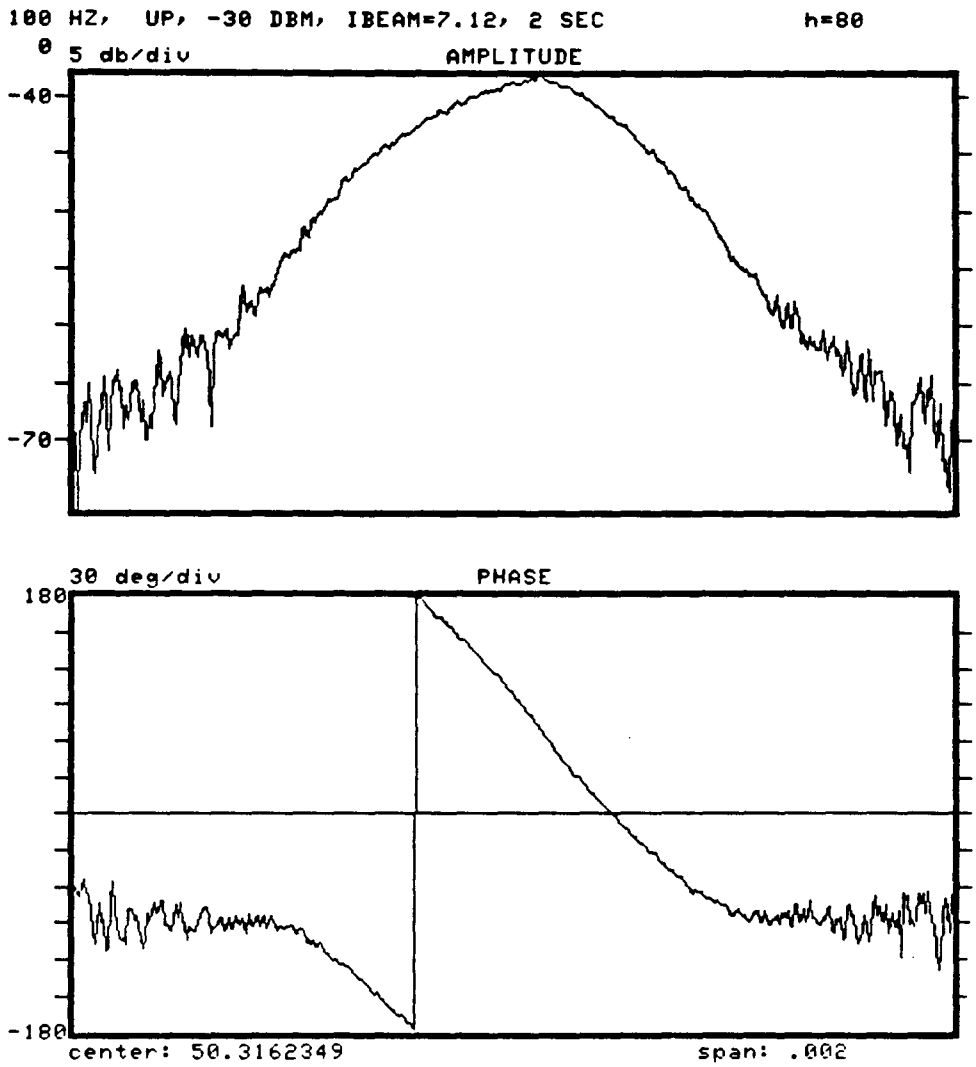

Figure 5.8. Beam Response Measured with 100Hz Resolution Bandwidth.

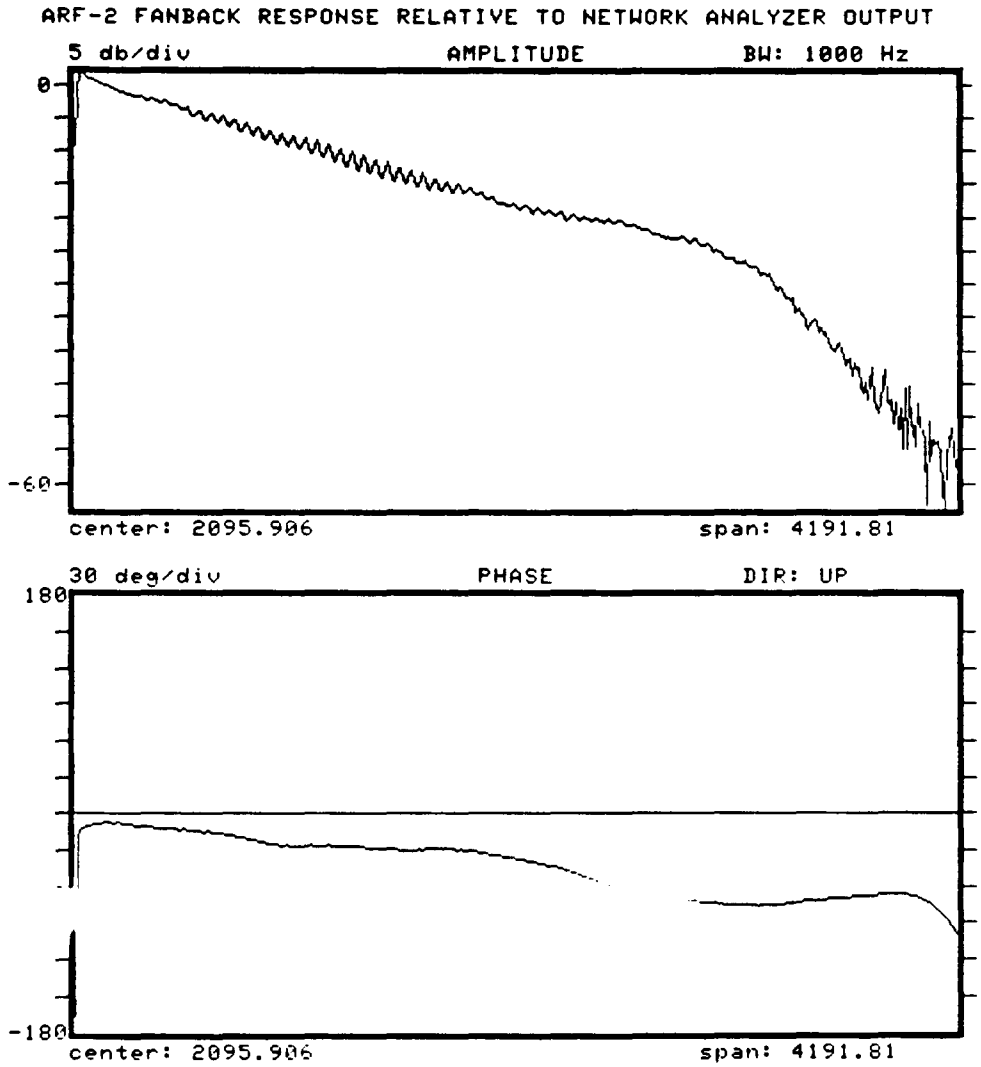

Figure 5.9. Frequency Response of the ARF2 Cavity. The frequency range is from 0 Hz to 200 MHz.

The Accumulator BTF measurements were performed in a frequency range from 6MHz to 200 MHz, and with different beam intensities. Figure 5.10 shows the inverse response at $h = 73$ and $h = 84$. The diagrams have been rotated to remove the additional phase delay introduced primarily by the cable length, and the separation of the kicker and detector. The responses of the RF kicker and power amplifiers also contribute to the phase delay. Simple calculations show that, for a frequency increase of one revolution harmonic, the additional phase delay due to the cable length and the different detector location from the kicker is about 360°. The measured inverse responses at different revolution harmonics have approximately the same orientation in the complex plane.

Data analysis has been done to calculate the impedance at each revolution harmonic. Figures 5.11 and 5.12 show the results for $h = 84$. Those measurements were done with beams of 7.2mA and 161mA respectively. The beam frequency distribution measured from the Schottky signal cannot be used directly for evaluating the integral in equation (5.29), because it is a incoherent signal which is very noisy. In figure 5.11, the measured frequency profile is smoothed using data smoothing techniques. In figure 5.12, the measured frequency profile is fitted with a Gaussian distribution multiplied by a sum of Hermite polynomials (cf. ref. [46], p. 407). In both cases, the scale factor for the measured BTF is obtained from calibration of the ARF2 cavity and the wall current monitor, and taking the nominal values of the power amplifiers, which have not been calibrated. Because a 1dB error in the voltage calibration will result in a 10% error in the scale factor, its measurement must be precise in order to get an accurate value.

Because the ARF1 cavities have a resonant frequency near the 84th harmonic, the large impedance of ARF1 ($\sim 60k\Omega$) should cause a shift of the inverse response along the real axis in the complex plane. As is shown in figures 5.11 and 5.12, the measured response did not show the shift as expected. The reason for this is unknown. It has been suspected that the resonant frequency of ARF1 was between the two adjacent revolution harmonics, either between 83 and 84 or between 84 and 85. With $Q = 200$, the magnitude of the impedance dropped more than one half of

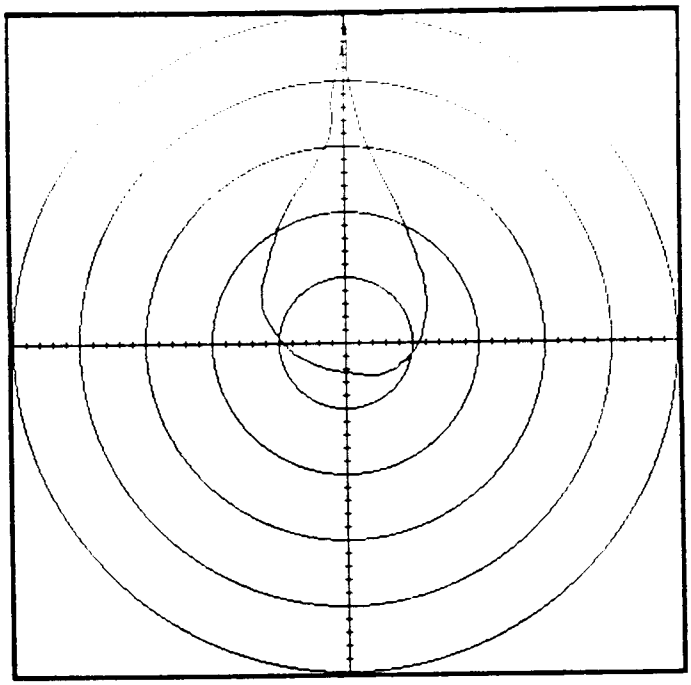

(a) $h = 73$.

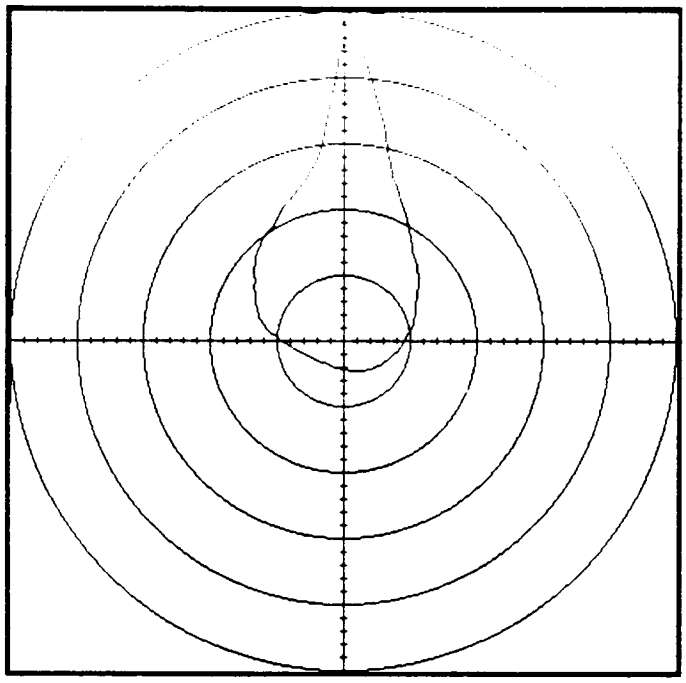

(b) $h = 84$.

Figure 5.10. BTF Measurements at Harmonics 73 and 84. Since the ARF1 cavities have a resonant frequency near harmonic 84, a significant amount of shift along the real axis is expected for the inverse beam response at that harmonic. However, no noticeable response shift due to longitudinal impedance is evident.

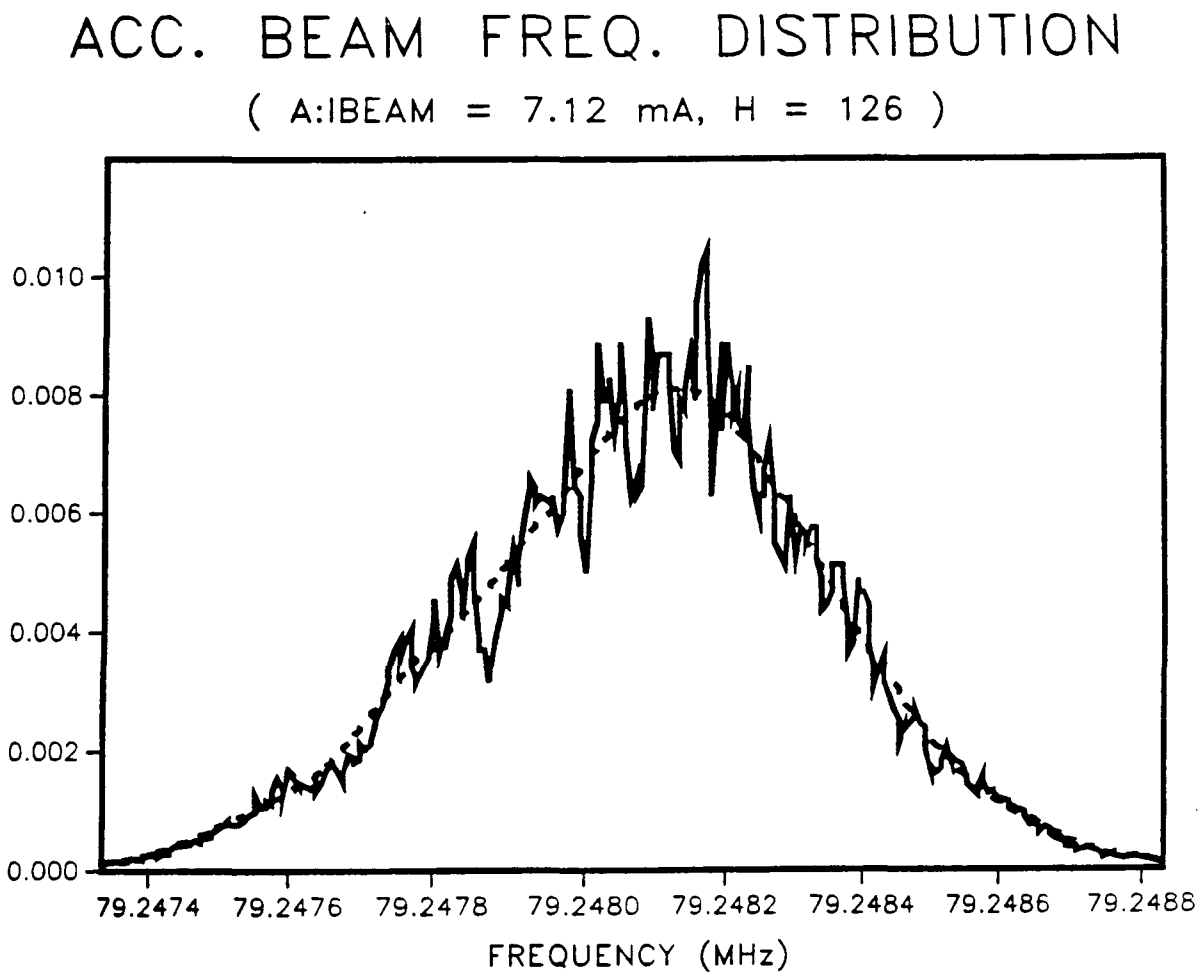

(a) Measured and smoothed beam frequency distribution at $h = 126$.

Figure 5.11. Result of a Impedance Measurement with a 7.2mA Beam. In (b), the solid line is the measured inverse response, and the dashed line is the calculated inverse response. The smoothed frequency distribution has been used for integral evaluation. The measured inverse response has been enlarged by 20%.

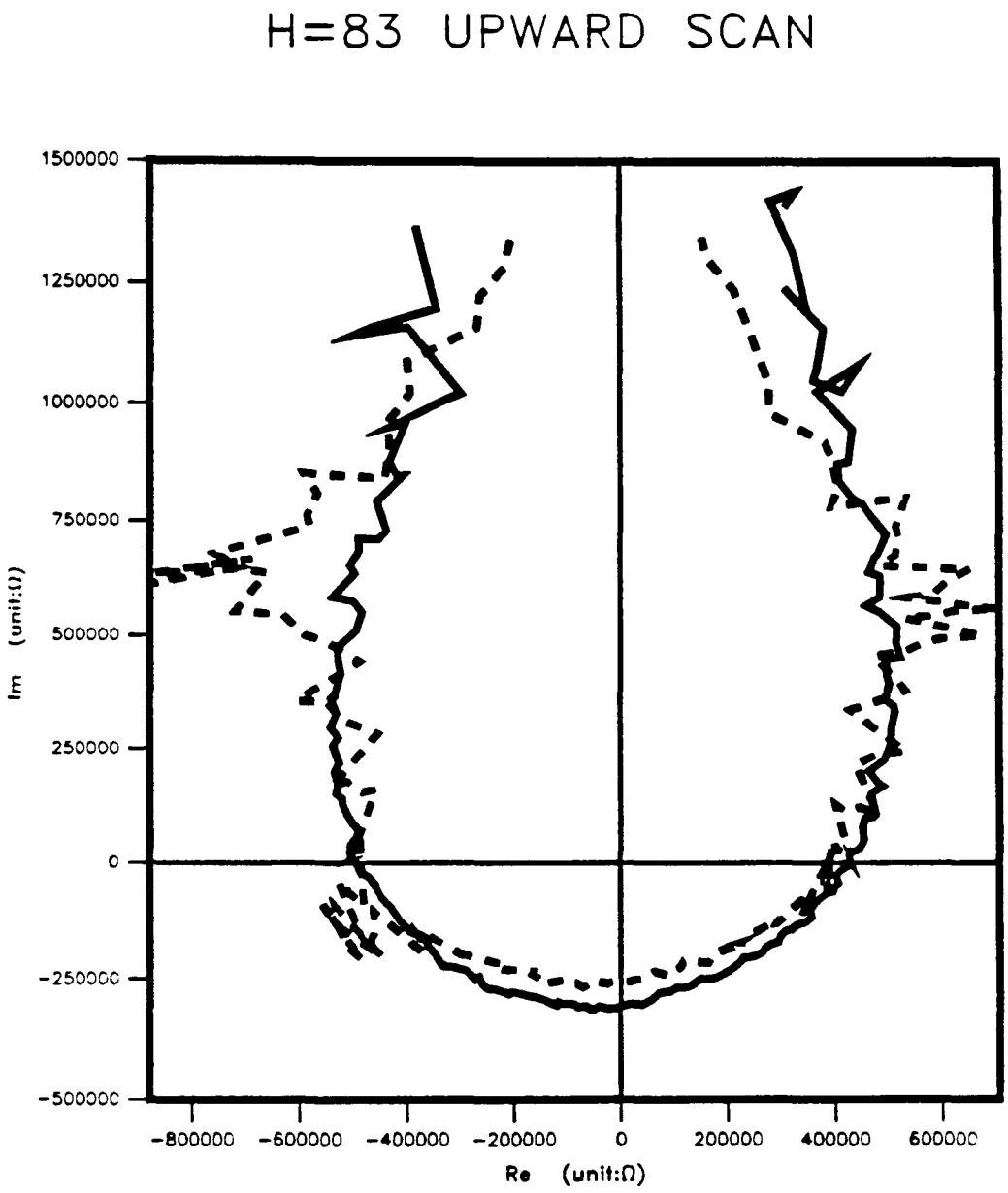

(b) Inverse response in the complex plane for impedance calculation at $h = 84$.

Figure 5.11. (continued)

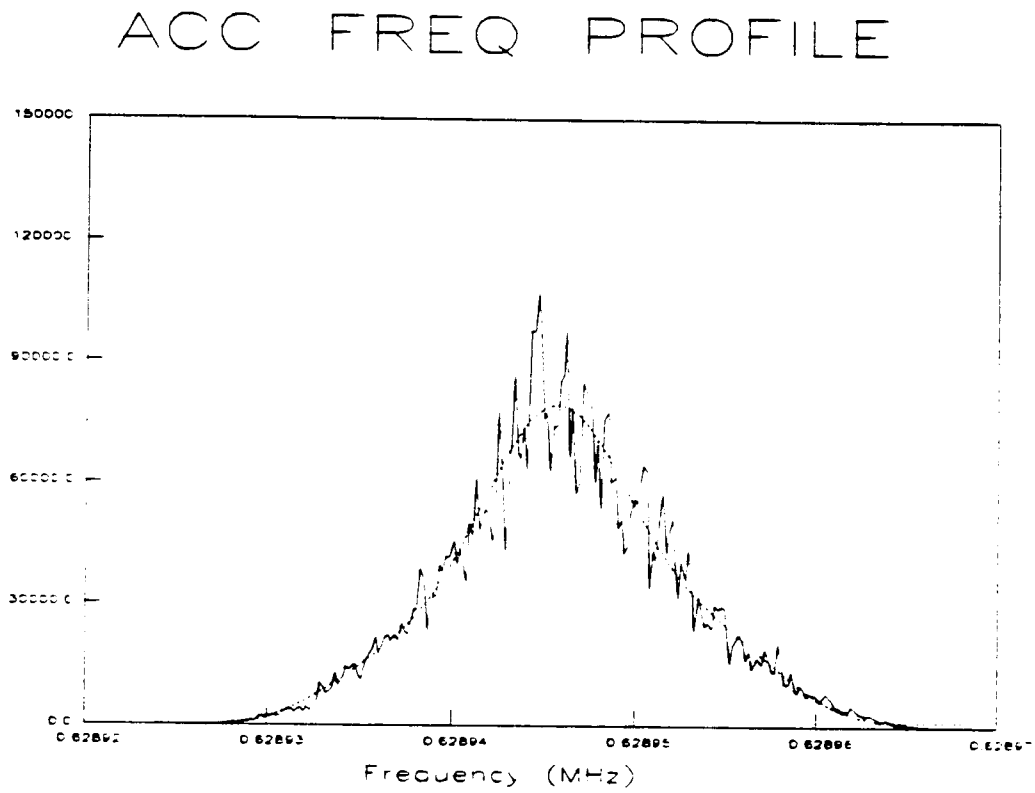

(a) Measured and fitted beam frequency distribution at $h = 126$.

Figure 5.12. Result of a Impedance Measurement with a 160mA Beam. In (a) the measured frequency distribution is fitted with nine terms. In (b), the solid line is the measured inverse response, and the dashed line is the calculated inverse response. The fitted frequency distribution has been used for integral evaluation. The measured inverse response has been enlarged by 12%.

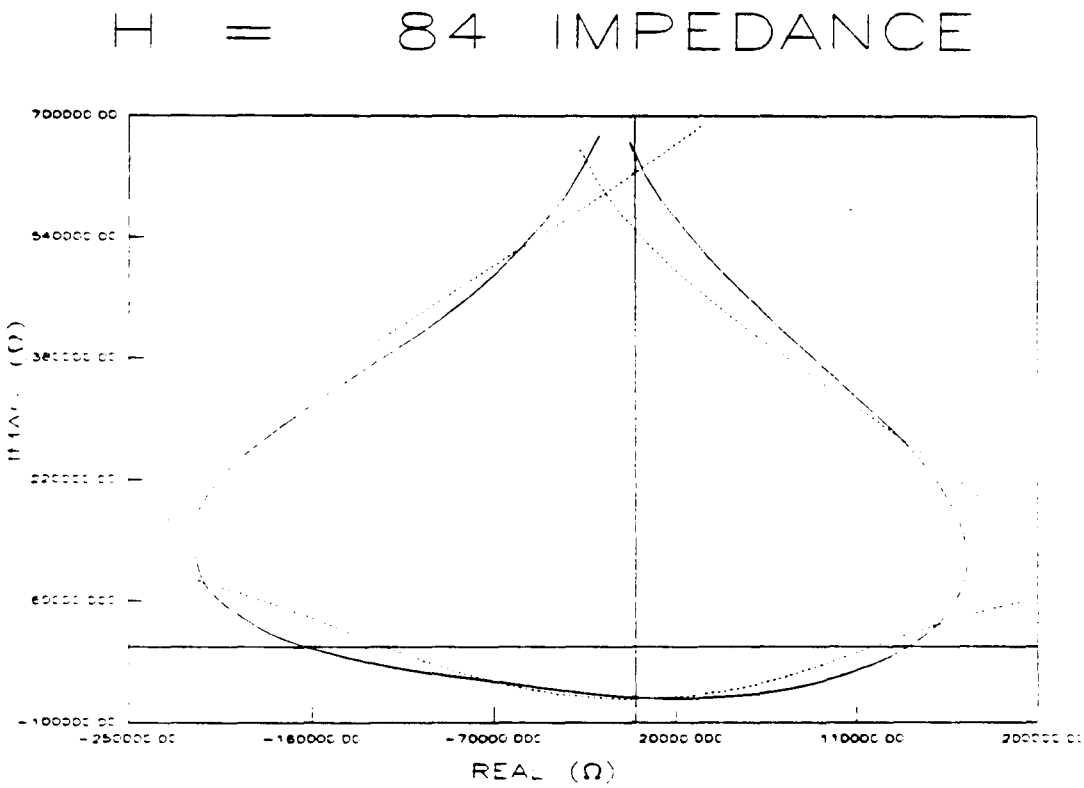

(b) Inverse response in the complex plane for impedance calculation at $h = 84$.

Figure 5.12. (continued)

its peak value at the nearest revolution harmonic, and the beam current of several milliamp was too small to perceive that impedance (figure 5.11). With more than 10 times of the beam intensity (160 mA) and two times of the momentum spread, the effect of response shift due to an impedance should be more evident since the magnitude of the calculated inverse response is proportional to the square of the momentum spread and inversely proportional to the beam current. But still no response shift is evident (figure 5.12). In all other data, no impedance is found either.

However, in a recent experiment for measuring the Tevatron impedance using the same method, a significant response shift was observed at the resonant frequency of the tevatron RF cavities [47]. More detailed measurement and data analysis have yet to be done to confirm the principle of this measurement method.

CHAPTER VI

LONGTUDINAL INSTABILITY DURING TRANSITION CROSSING

From luminosity considerations in E760, it is desired to decelerate the largest $\bar{p}$ beams possible into the charmonium energy region. Longitudinal instability was observed during the Accumulator transition crossings, which imposed a critical limit on the amount of $\bar{p}$ beam that could be decelerated below transition. The instability caused beam momentum blow up as well as beam intensity loss when the beam current was above 10 mA. Therefore, it is important to study the origin and properties of this longitudinal instability in order to improve the transition crossing efficiency when the beam current exceeds 10mA. From an accelerator physics viewpoint, the Accumulator transition crossing provides an unique opportunity for studying the effects of longitudinal instabilities on a coasting beam near the transition energy.

Studies were done at E760 transition crossings during a period from July to early September 1990. The total number of transition crossings during that period was six. As has been explained in chapter 4, there were two ramp tables for transition crossing, one (the old ramp) raised γ_t from 5.50 to 6.10 and the other (the new ramp) raised γ_t from 5.15 to 6.10. Each table had 24 ramp points, and each step normally took 0.5 second. The values of γ_t before and after the crossing process were measured by changing the current of the main dipole bus and measuring the corresponding revolution frequency of the beam. Measurements in the transition region were made either with the old ramp or the new ramp, depending on the E760 experiment plan for each transition crossing.

6.1 Beam Momentum Blow Up and Energy Loss

The momentum spread of the beam, $\frac{\Delta P}{P}$, was obtained by measuring the frequency spread $\frac{\Delta f}{f}$ from the longitudinal Schottky signal and using the relationship

$$\frac{\Delta P}{P} = -\frac{1}{\eta}\frac{\Delta f}{f}, \tag{6.1}$$

where $\eta = 1/\gamma_t^2 - 1/\gamma^2$. Since the initial and final values of γ_t were known, and the value of γ for the beam could be obtained from the beam energy which had been precisely calibrated, the corresponding η values could be calculated. Figure 6.1 shows the longitudinal frequency distributions of the beam at $h = 126$ before and after transition crossing in one study. The initial and final values of η were -1.48×10^{-3} and 4.68×10^{-3} respectively, the total energy of the beam was 5286.1 MeV, and the beam had been cooled longitudinally before the crossing process. The frequency profiles were measured with the Accumulator longitudinal Schottky detector. The frequency spread was defined to be its 10dB width when being used to calculate the beam momentum spread. It was found that the momentum spread of the beam was 0.25% before transition crossing, and 0.82% after the process.

The average energy loss of the same beam in the transition crossing process was obtained making use of the fact that the momentum cooling pickups would always center the beam between the cooling pickups. After the crossing process, the beam was cooled again longitudinally. It was found that the cooling resulted in a central frequency increase of 1.36 kHz. From equation (6.1), this frequency increase corresponded to an energy increase of 19 MeV. With the assumption that the cooling pickups would keep the beam on the same orbit, the beam after being cooled below transition should have the same energy as that above transition. In this way, the average energy loss during the Accumulator transition crossing process was found to be 19 MeV. When using RF to increase the beam energy before transition crossing, the peak of the beam frequency distribution remained

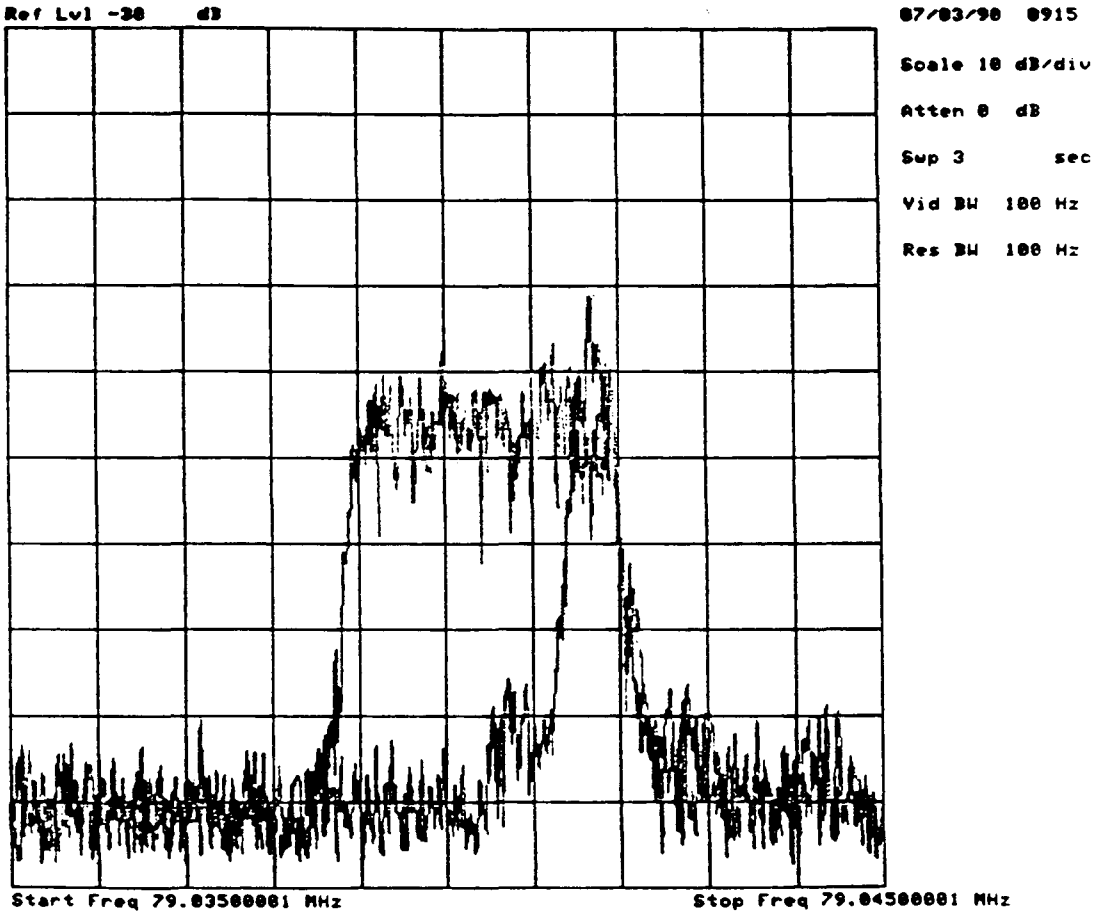

Figure 6.1. Longitudinal Schottky Profiles at $h = 126$ before and after a Transition Crossing. The narrow profile shows the frequency distribution of the beam before transition crossing when the beam is above transition, and the wide one shows the frequency distribution after the crossing process.

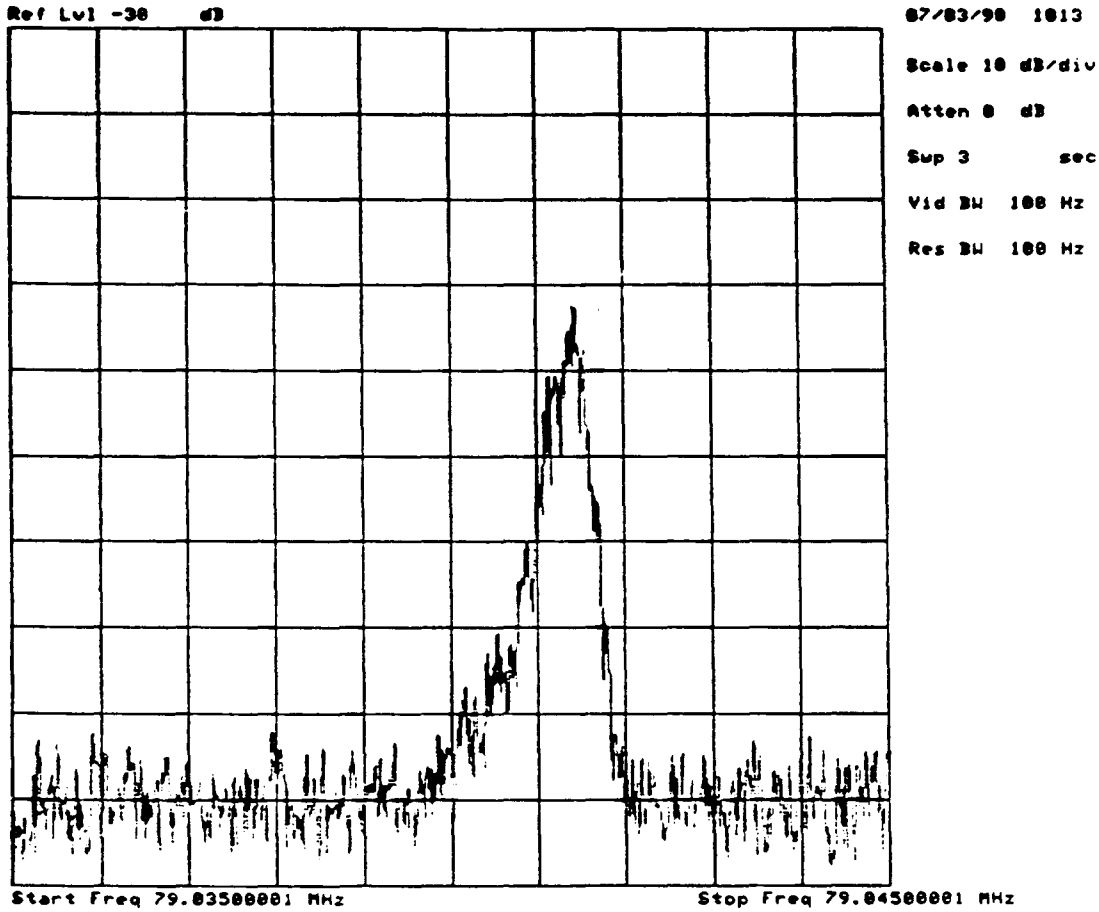

Figure 6.2. Frequency Distribution of the Same Beam below Transition after It was Cooled Longitudinally.

unchanged in the process, indicating that the average energy loss had been compensated. Figure 6.3 shows the result.

Since the closed orbit of the beam was different from the design orbit (which was the one that passed through the centers of all quadrupoles and the higher order multipole magnets), changing the quadrupole bus settings for transition crossing also distorted the closed orbit. This would result in a revolution frequency shift of the beam. But this effect was found to be negligible.†

As was shown in section 4.4, a small error in the γ_t measurement gives rise a large error in η, especially when the measurement is done near transition, according to the expression

$$\frac{d\eta}{\eta} = \left[\frac{2}{\left(\frac{\gamma_t}{\gamma}\right)^2 - 1}\right] \frac{d\gamma_t}{\gamma_t} . \tag{6.2}$$

At the starting and ending points of transition crossing, the uncertainty in determining η is about 40%. Therefore, the beam width and average energy loss measurements which rely on knowledge of η are not accurate.

6.2 Frequency Domain Measurements

In another set of studies, γ_t was raised step by step from its initial value to its final value, and the longitudinal frequency spectrum of the beam was studied to identify the major source of the longitudinal instability during transition crossing. The broadband wall current monitor was used to observe the beam coherent effect in a wide range. The longitudinal Schottky pickup was also used to measure the Schottky profile at each crossing step. Each detector was connected to a HP8568B spectrum analyzer on which signals were displayed. Signals from the wall current monitor was amplified by a 20dB, 20kHz - 2GHz amplifier before being sent to the spectrum analyzer.

---

† S. Y. Hsueh, private communication.

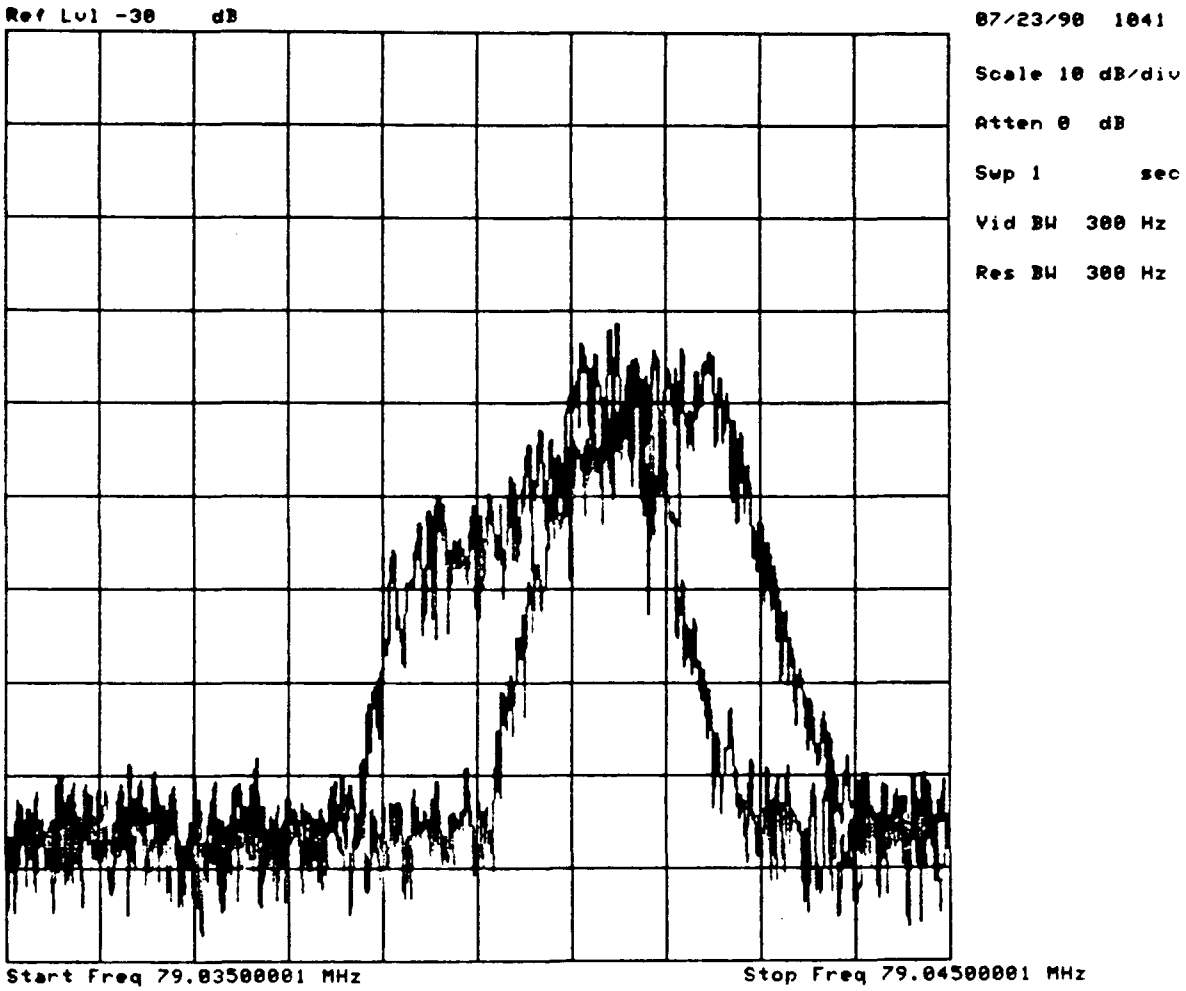

Figure 6.3. Frequency Profiles before and after Transition Crossing with the Energy loss being Compensated.

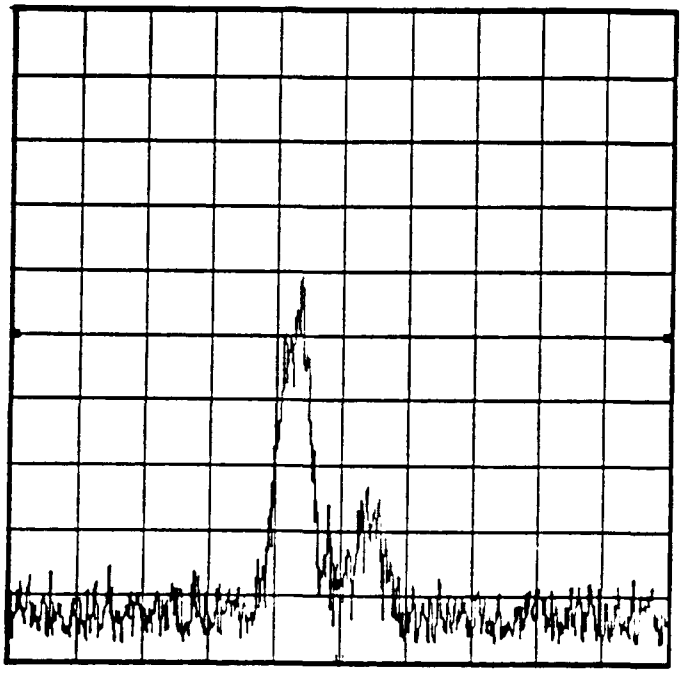

(a) At the crossing step 14.

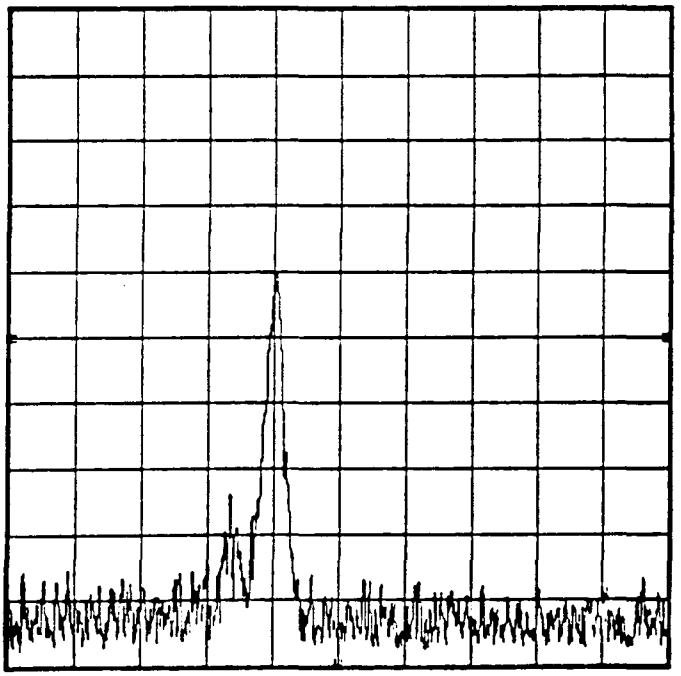

(b) At the crossing step 15.

Figure 6.4. Schottky Profiles During a Transition Crossing with the New Ramp.

In one such study using the new ramp table for transition crossing, it was found that transition crossing occurred between crossing steps 14 and 15. Figure 6.4 shows the Schottky profiles at those two steps. In figure 6.4 the small hump next to the major part of the beam frequency distribution switched sides, which clearly indicated that the beam was on one side of the transition at step 14 and on the other side at step 15.

In the frequency domain studies, the beam was stochastically cooled before each transition crossing. It was observed that as the beam approached transition, coherent lines appeared at frequencies which were integer multiples of 53 MHz. Figure 6.5 shows the beam spectrum displayed on the spectrum analyzer. The beam intensity was 5.7mA. The spectrum analyzer was set in the MAX HOLD mode‡ for displaying the positions and peak height of the coherent lines. This indicated that the beam had a coherent structure with a periodicity of 53 MHz. A more precise measurement in a narrower frequency range around 53 MHz showed that the fundamental coherent line appeared at at 52.9 MHz, and the closer the beam was to transition, the bigger the peak height of the coherent line. Some results of the wall current monitor measurements are show in figure 6.6. Meanwhile, as shown in figure 6.7, a sharp peak was observed to rise from the longitudinal Schottky profile, indicating the bunching effect of the beam. Simple calculations showed that the fundamental frequency at which the coherent line appeared, 52.9 MHz, was the 85th revolution harmonic of the beam and was very close to the resonant frequency of the ARF1 cavity. These observations provided a clear evidence that the large shunt resistance of ARF1 was the major source of the longitudinal beam instability in the transition crossing process. In other words, the beam induced voltage in ARF1 caused self-bunching of the beam in transition crossing.

---

‡ In the MAX HOLD mode, the spectrum analyzer compares the newly measured value at a specific frequency with the stored value at the same frequency. Whichever is greater becomes the new stored value and is displayed on the screen.

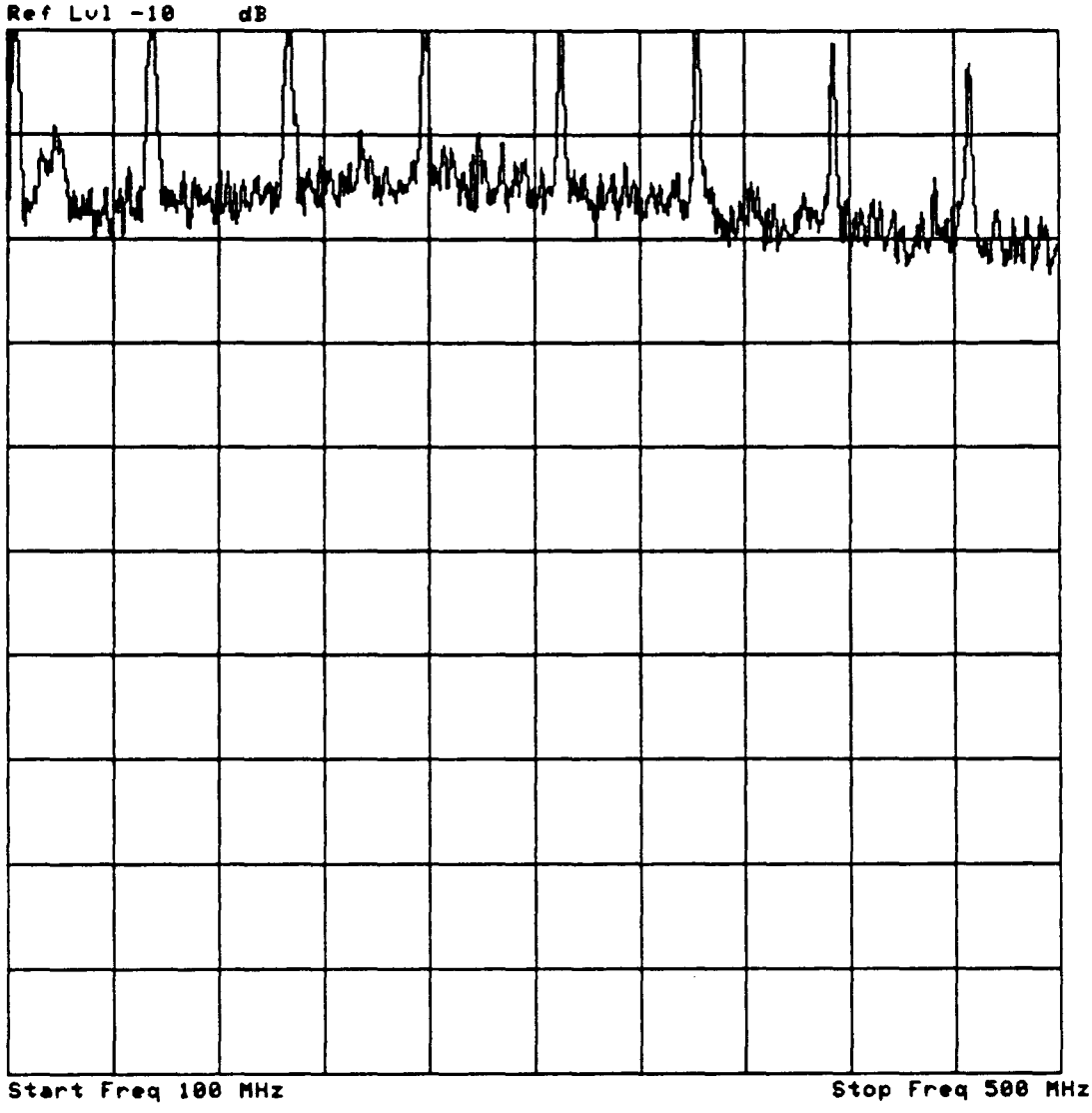

Figure 6.5. Beam Spectrum in a Wide Frequency Range.

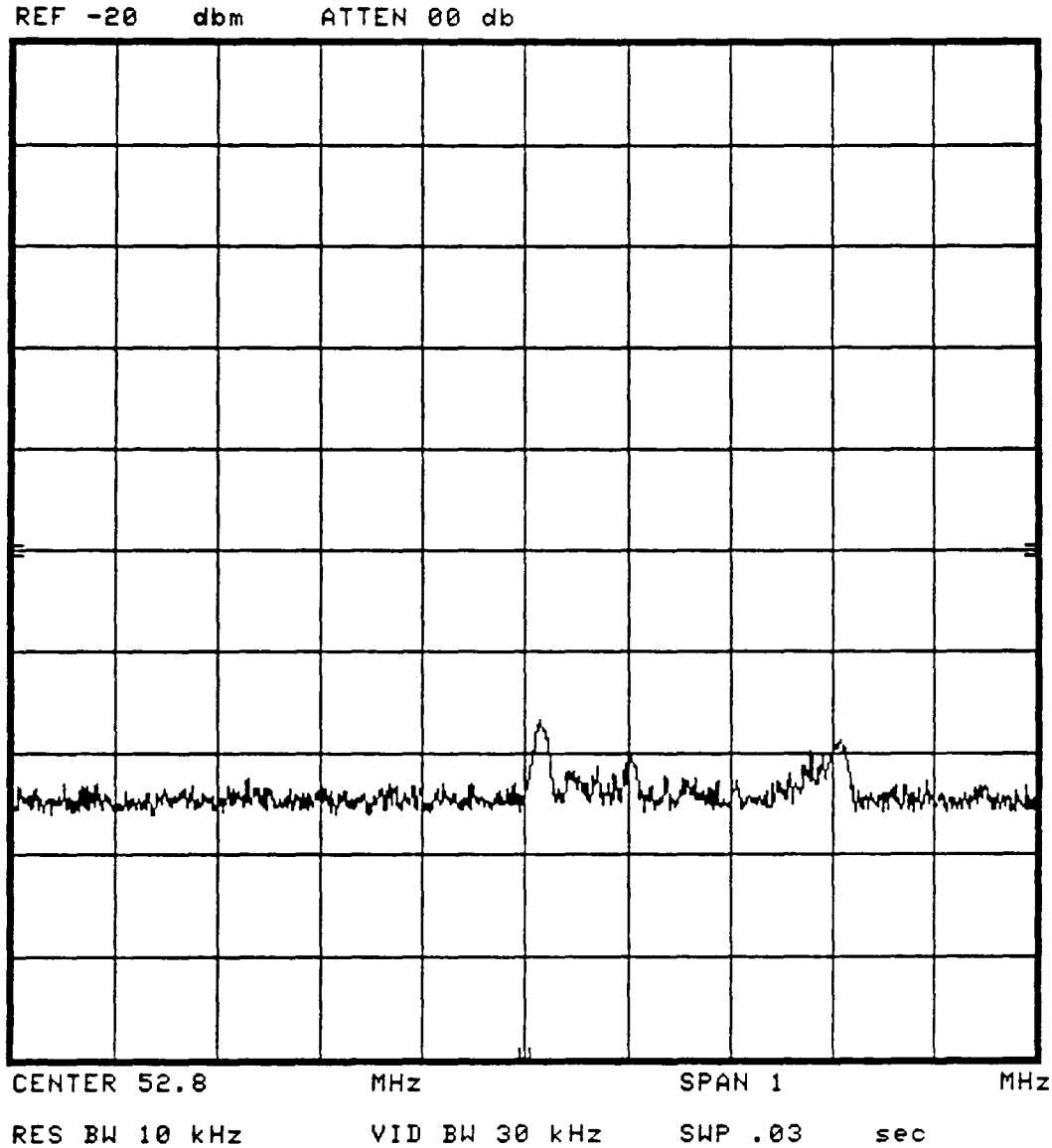

(a) Before transition crossing.

Figure 6.6. Wall Current Monitor Signals in a Transition Crossing. The spectrum analyzer was set in the MAX HOLD mode. The small humps in (a) were due to the noise of some unknown sources and were irrelevant to the measurements.

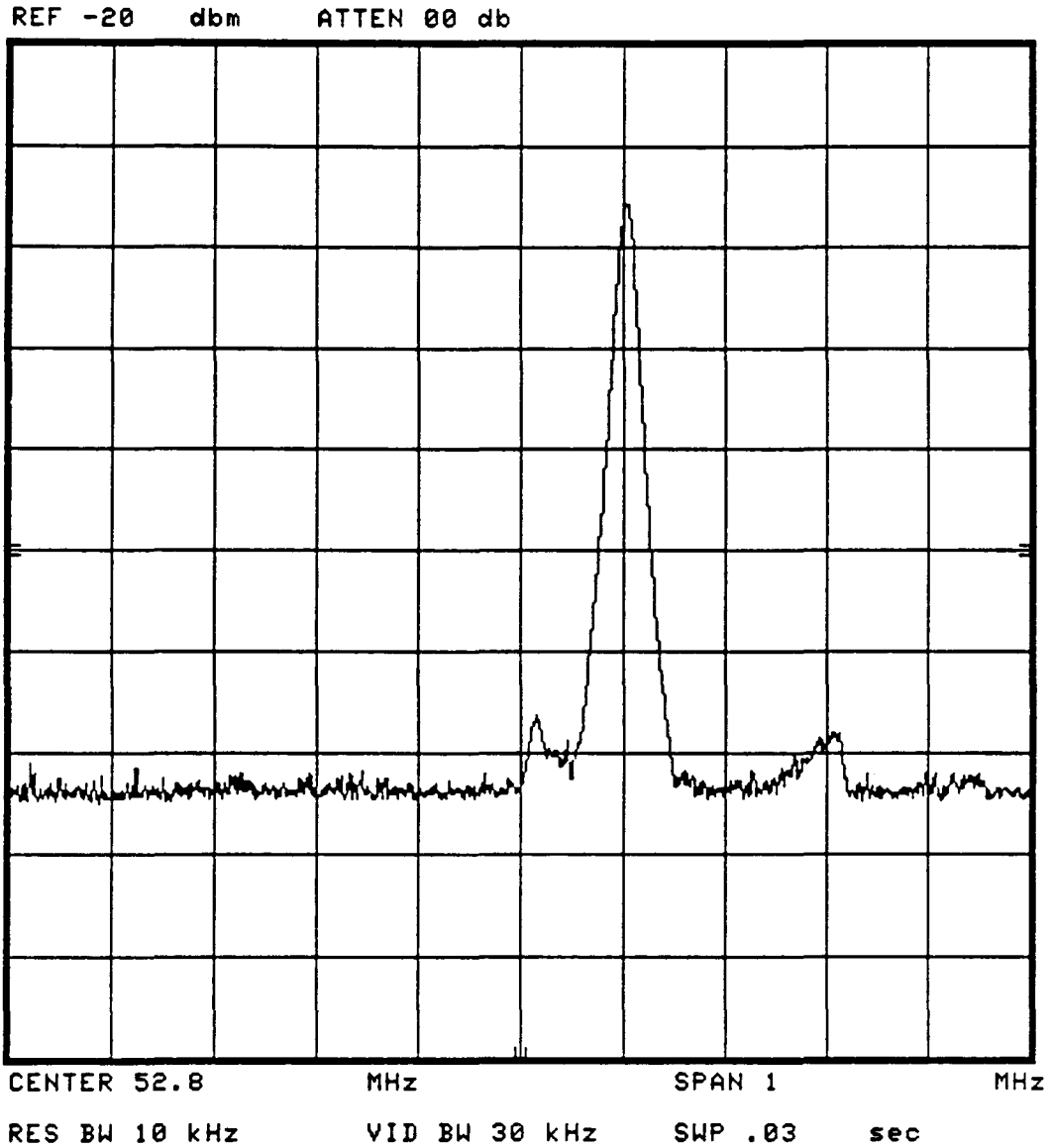

(b) At the end of step 14.

Figure 6.6. (continued)

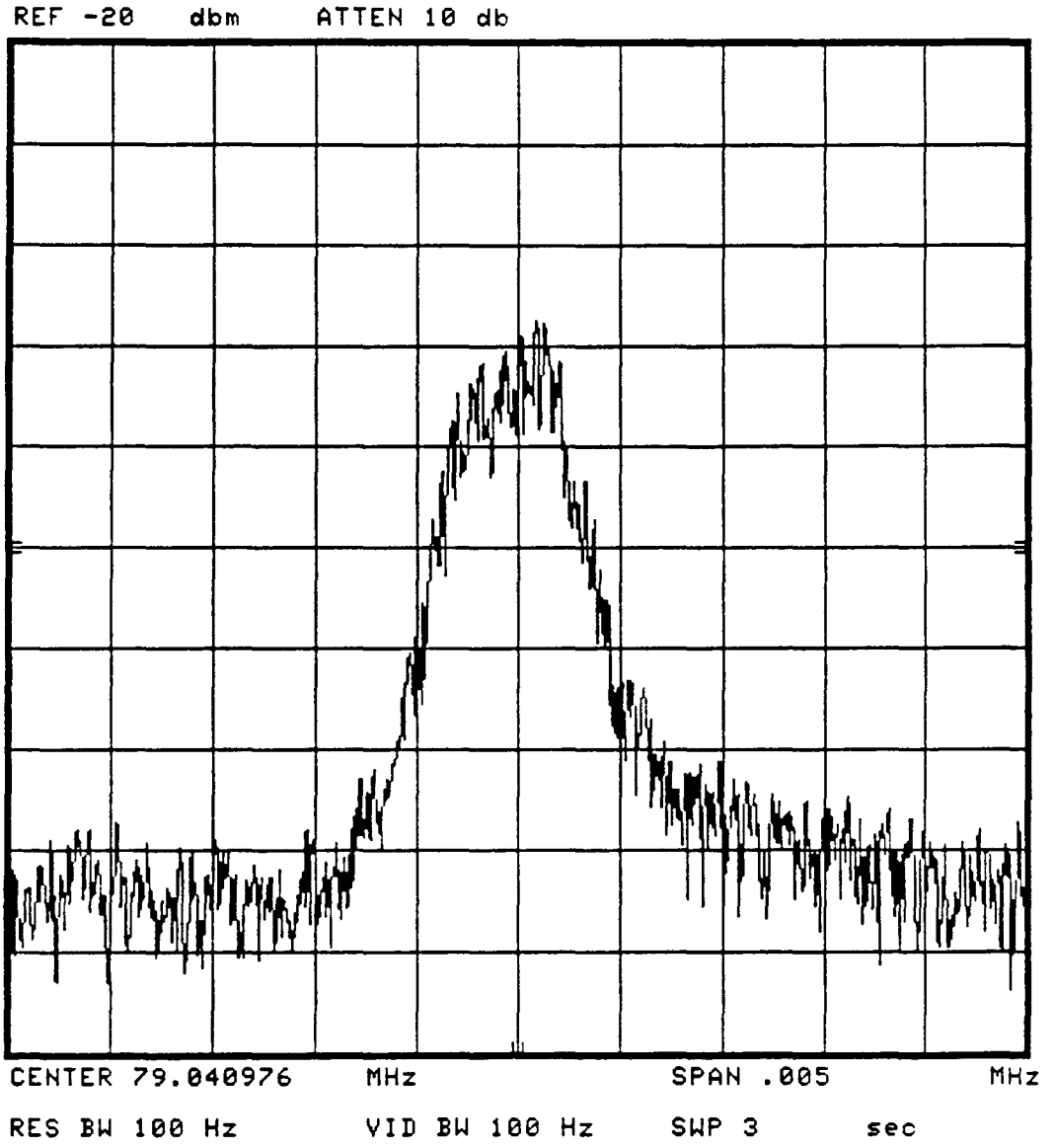

(a) Before the crossing process.

Figure 6.7. Longitudinal Schottky Signals at h=127 in the Same Transition Crossing.

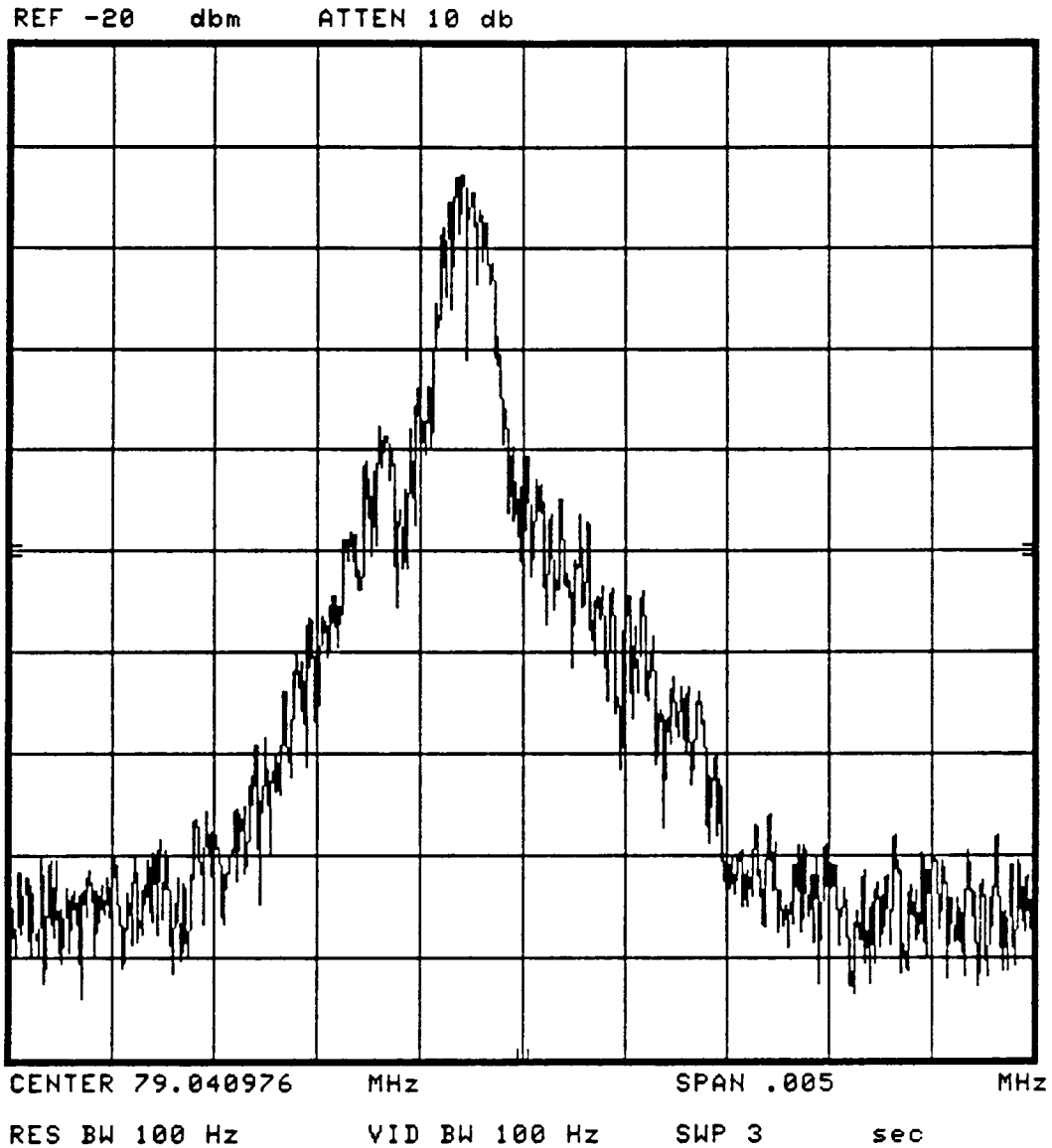

(b) Between steps 14 and 15.

Figure 6.7. (continued)

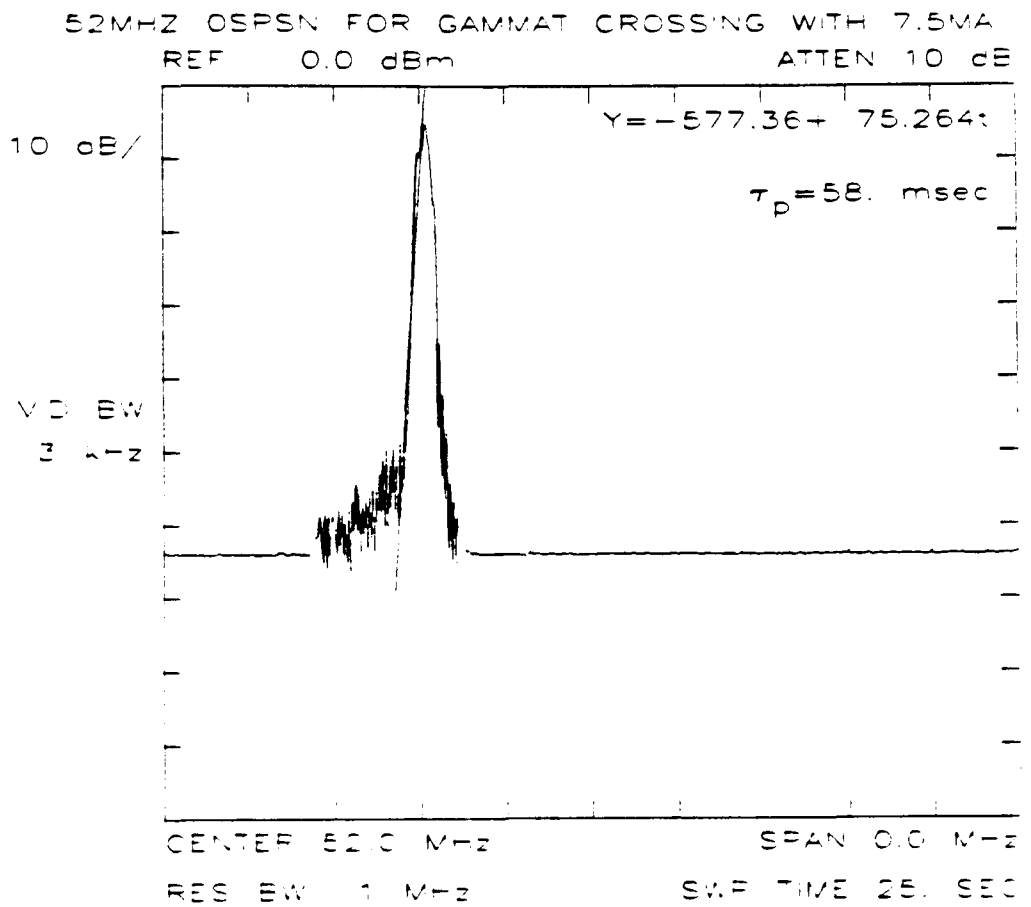

Figure 6.8. Time Evolution of the Coherent Effect in a Non-stop Transition Crossing.

6.3 Time Domain Measurements

When a spectrum analyzer is set to have zero frequency span about a certain center frequency, it measures the total power of the input signal in a frequency range about that center frequency as a function of time. The frequency range is determined by the resolution bandwidth of the spectrum analyzer. In the transition studies, the time evolution of the longitudinal instability of the beam was measured by using the wall current monitor and setting the spectrum analyzer at a center frequency near the ARF1 resonant frequency with zero span. In a time domain measurement shown in figure 6.8, a non-stop transition crossing was done with an antiproton beam of 7.5mA. the center frequency and resolution frequency of the spectrum analyzer were set to be 52.0 MHz and 1 MHz respectively to

measure the total power of the coherent signal in the frequency range. This center frequency was chosen before the frequency at which the coherent line appeared was precisely measured. Since the average revolution frequency of the beam near transition was approximately 625 kHz, the resolution bandwidth of 1 MHz was set to make certain that at least one revolution harmonic was covered. As figure 6.8 showed, above the noise floor the coherent signal started with a fuzzy and slow increase followed by a sharp rise when the beam crossed transition. This could be explained as follows: the beam induced voltage in the ARF1 cavities caused self-bunching of the beam and so a periodic coherent structure (h=85), and on the other hand the magnitude of this voltage depended on the beam coherent structure at the resonant frequency of the cavity. It was a process of mutual influence. The coherent structure produced by the beam-induced voltage was smeared provided the frequency spread of the beam was large enough, and the voltage was consequently reduced. In this way the beam remained stable. This process repeated as the beam approached transition, except that the momentum spread would increase if the frequency spread was too small to stabilize the beam. But the small signal amplitudes and fast decoherence processes in the early part of transition crossing suggested that the frequency spread of the beam was large enough for decoherence without a significant increase in the momentum spread. At transition, no decoherence occurred due to lack of the frequency spread, which caused the continuous rise of the coherent signal.

Note that in figure 6.9 the vertical scale is logarithmic. A linear growth in the picture represents an exponential growth in the linear scale. For exponential growth, the rise time is defined to be the time it takes for the amplitude (or power) of a signal to reach e times its initial value. The rise time of the coherent effect for that crossing process can be obtained by making a linear least-square fit to the rising edge of the signal. It is found that the rise time for the power of the signal is 36 msec. This value should be multiplied by two to get the rise time for the amplitude.

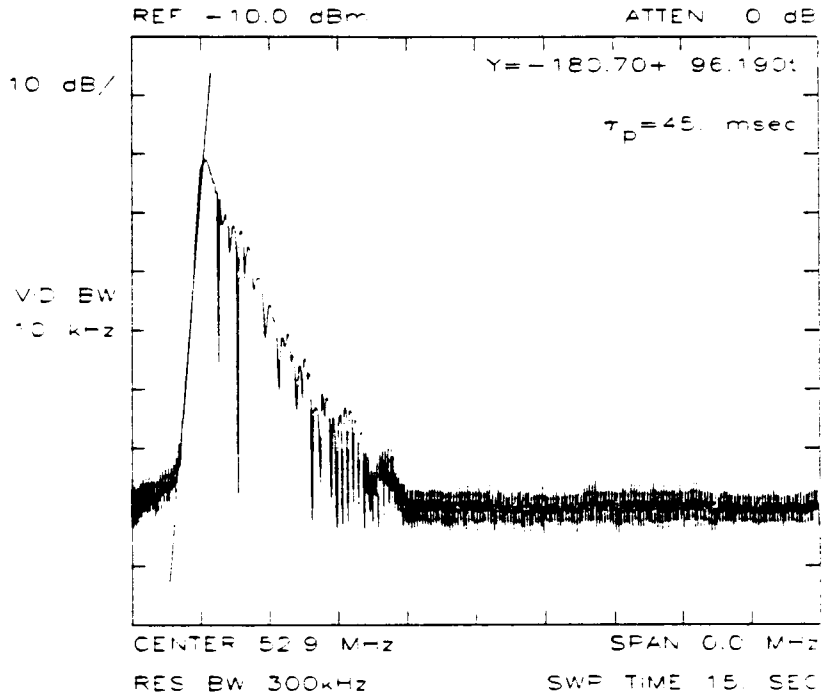

(a)The measurement taken at $\eta = 7 \times 10^{-4}$.

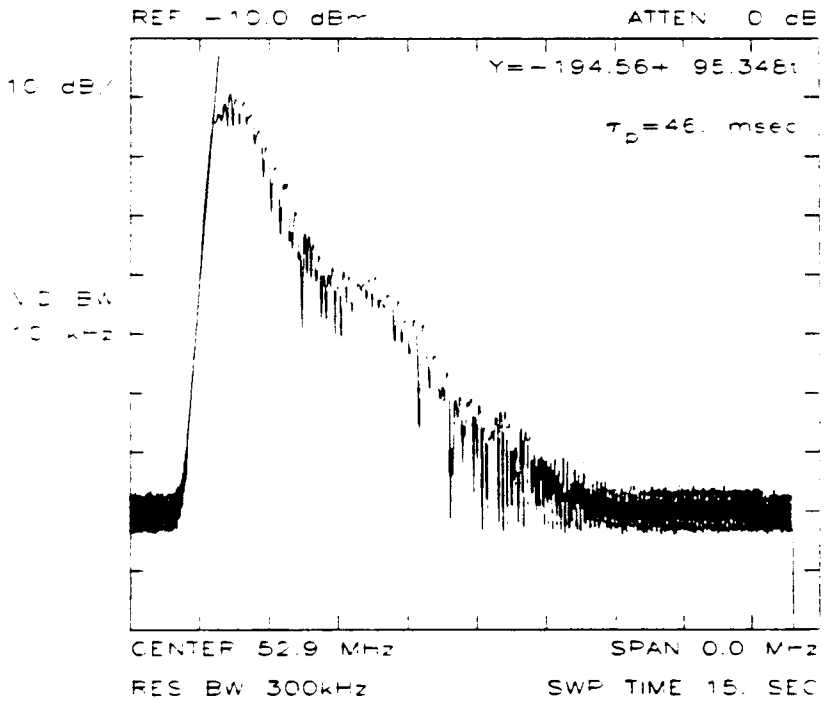

(b)The measurement taken at $\eta = 1 \times 10^{-4}$.

Figure 6.9. Growth and Decay of the Coherent Effect. The value of γ_t was raised by one step using the old ramp. Transition was crossed between the steps six and seven when the old ramp was used. Measurement was done with a $\bar{p}$ beam of 4.33mA. It showed that decoherence took longer when the beam actually crossed transition.

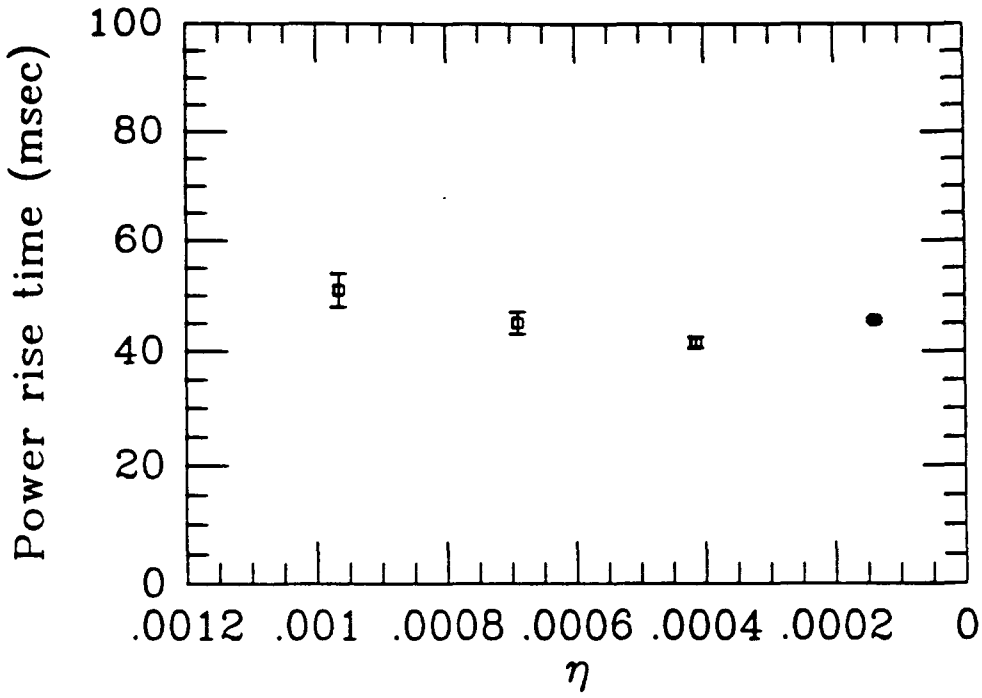

Figure 6.10. Power Rise Time Measured in a Step-by-step Transition Crossing.

The time domain measurements were also done with a beam of 4.33mA when γ_t was changed step by step. In the study, the center frequency of the spectrum analyzer was set to 52.9 MHz and its resolution bandwidth was set to 300 kHz. With these settings, the total power of the 85th revolution harmonic of the beam would be measured. Two such measurements is shown in figure 6.9. The beginning of the sharp rising edge corresponded to the time the magnets started ramping. The measurement showed that the coherent effect decayed gradually after ramping of the devices had stopped. As explained in the last paragraph, this decoherence was caused by the beam structure change. In figure 6.9 the notches that appeared in the process of decoherence were due to the overlap of the modulations as the phase space distribution sheared, just like sudden debunching.

Figure 6.10 shows the power rise time as a function of η in the same measurements, in which η is calculated assuming that γ_t changes linearly, and the error comes from the linear least-square fitting. It can be seen that there is no appreciable drop in the rise time as the beam approaches transition. The measurements

also show that, when $\eta \gtrsim 1 \times 10^4$, the decoherence process takes approximately the same amount of time, whereas when the beam actually crosses transition, this process takes longer time. This fact also indicates that, when the beam is far enough from transition, decoherence is achieved without significant increase in the beam momentum spread. The beam momentum blow-up happens primarily when it crosses transition. This is proved by both the measurements of the beam momentum spread and computer simulations. The measured momentum spread of the beam in transition crossing will be shown in the next section, and the result of computer simulation will be given in the next chapter.

6.4 Beam Momentum Spread in Transition Crossing

It is standard for the momentum spread of the beam to be obtained by measuring the frequency spread from the longitudinal Schottky signal. In the transition crossing process, this method was used to measure the momentum spread of the beam when the beam was far enough from transition, in other words, when the coherent effect was negligible and the frequency spread was truly caused by the momentum spread of the beam. A plot of the momentum spread of the beam as a function of η in a certain transition crossing process is given in figure 6.11. These measurements were done on September 2, 1990. The frequency spread of the beam is defined to be its rms width. The dominant systematic error comes from the uncertainty in determining η, which is at least 40% according to equation (4.18). The error bars shown in the plot represent the errors in measuring the rms frequency spread, which is determined by the resolution bandwidth. The plot shows that the beam momentum blow-up occurs at the moment of transition crossing.

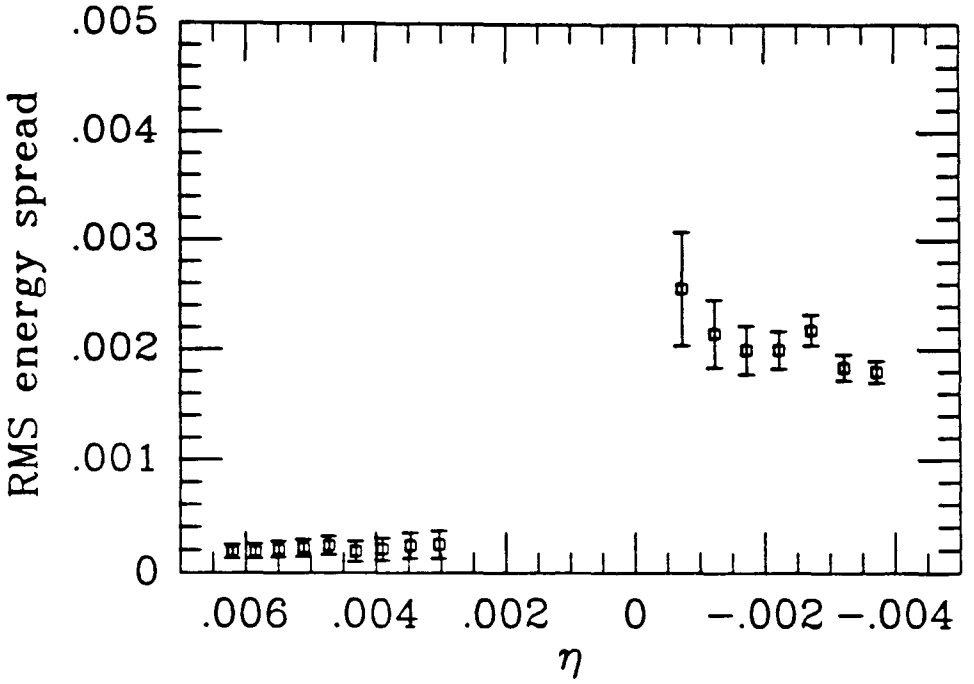

Figure 6.11. Momentum Spread as a Function of η.

6.5 Transition Crossing with ARF1 Shorted

Transition studies were also done on December 20, 1990 with the RF cavities shorted. The purpose was to remove the identified major source of the longitudinal instability by making the shunt impedance of ARF1 zero. The short of the ARF1 cavity is a metal sleeve that can be slid in to short the accelerating gap. Figure 6.12 shows a schematic of the ARF1 short. In this experiment, the beam was not cooled before transition crossing.

Before shorting ARF1, transition was done with a beam of 4.25mA to verify the existence of the coherent effect. Figure 6.13 shows the Schottky signal and the resistive wall monitor signal. The shift of the average frequency of the beam was about 600 Hz. In a transition crossing with 3.75mA beam and with ARF1 shorted, it was found that the height of the coherent peak at 52.9 MHz decreased at least 50dB, as shown in figure 6.14. There was no appreciable disruption to the frequency distribution. The shift of the average frequency of the beam was reduced by a factor of two, so was the rms frequency spread. With both ARF1

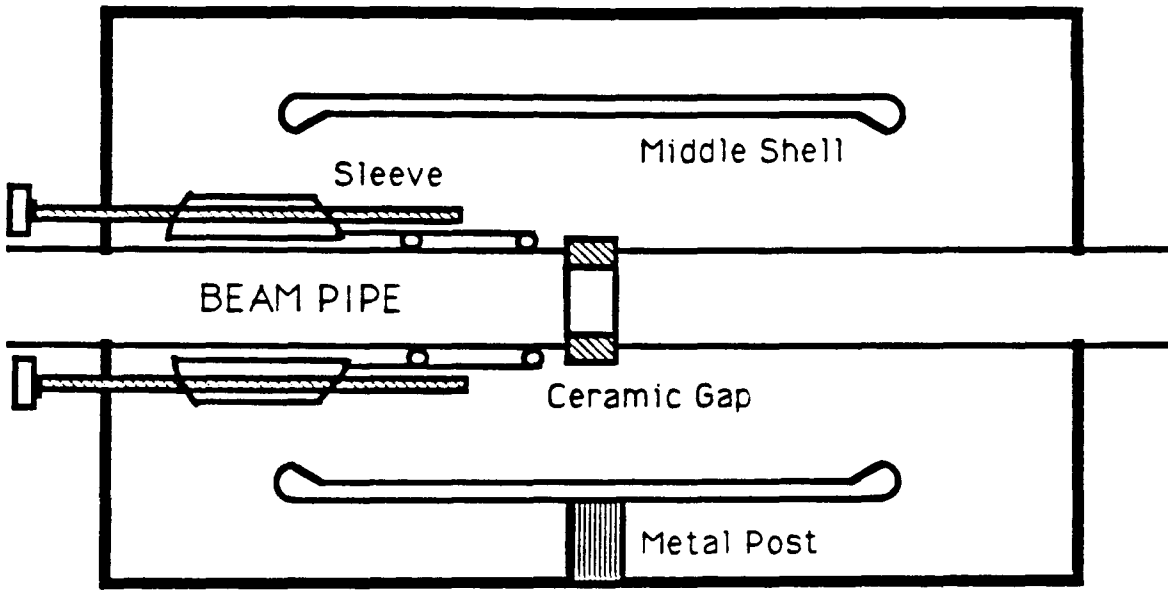

Figure 6.12. A Schematic of ARF1 Short Layout.

and ARF3 shorted, the observation was the same, indicating that ARF3 had little effect on the beam during transition crossing. As a matter of fact, throughout the experiment, the wall current monitor measurements around 53 MHz never showed coherent lines with an interval of 1.2 MHz, as was the case when the beam was bunched with ARF3. Afterwards, a faster transition crossing with 4.1mA beam was made with ARF1 not shorted. The crossing process was made six times as fast as the normal one. The coherent signal completely disappeared above the noise floor, as shown in figure 6.15. The Schottky signal display showed an undisrupted frequency distribution after transition crossing. With ARF1 shorted, this fast ramp was used for a transition crossing with a beam of 5.5mA. As expected, no coherent signal was observed during the process. Figure 6.15 shows the results. Calculations from the frequency spread of the beam showed that there was no momentum blow up in those crossing processes with ARF1 shorted or with the fast ramp. Even though the value of η was not accurately obtained in the calculations, this conclusion could still be confirmed by the fact that, as the Schottky signals showed, the shape of the beam momentum distribution after transition crossing

was not distorted, whereas momentum blow up caused by coherent instabilities was accompanied by a change in the momentum profile.

From these observations it can be seen that either shorting the cavity or speeding up the crossing process has greatly reduced the coherent instability, and therefore the momentum blow-up of the beam during transition crossing. It is also found that, independent of the speed of transition crossing, a shift of about 300Hz in the average frequency was always observed when ARF1 was shorted. This frequency shift may be caused by some other sources of instability which have not been found, but more likely it is due to the change of the bending force before and after transition crossing. Simple calculations show that 1.5mm change in the orbit length can cause this amount of frequency shift. If this frequency shift is taken into account in calculating the energy loss in the crossing process, as in section 6.1, the result gives a value of about 14 MeV. However, the energy measurement near transition is rough due to the large uncertainty in termining η, and the result is still subjected to about 40% uncertainty.

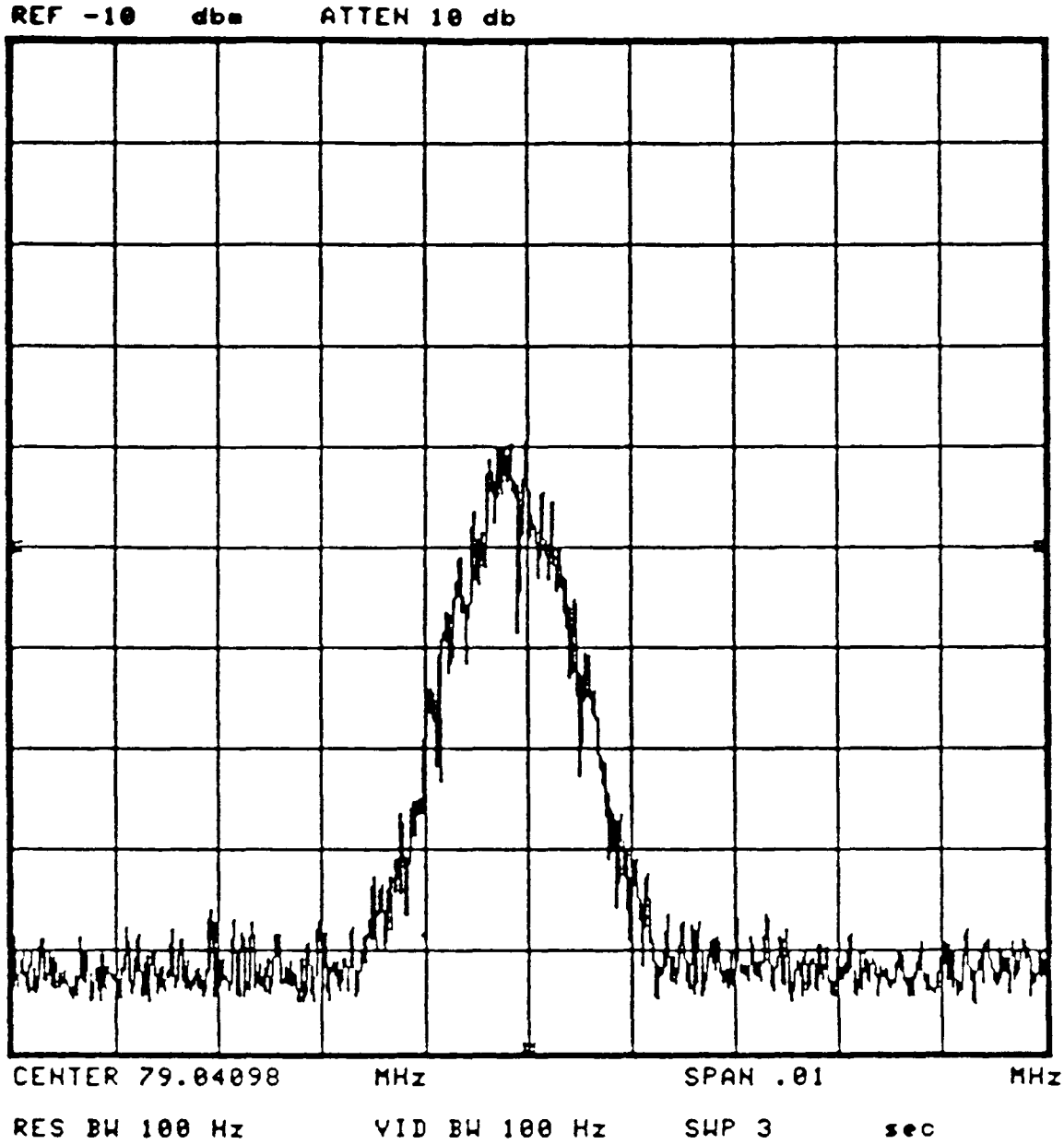

(a) Schottky Signal before transition crossing.

Figure 6.13. Transition Crossing with ARF1 not Shorted. The normal ramp table was used for this crossing with a beam of 4.25mA. The spectrum analyzer for displaying the resistive wall monitor signal was set in the MAX HOLD mode.

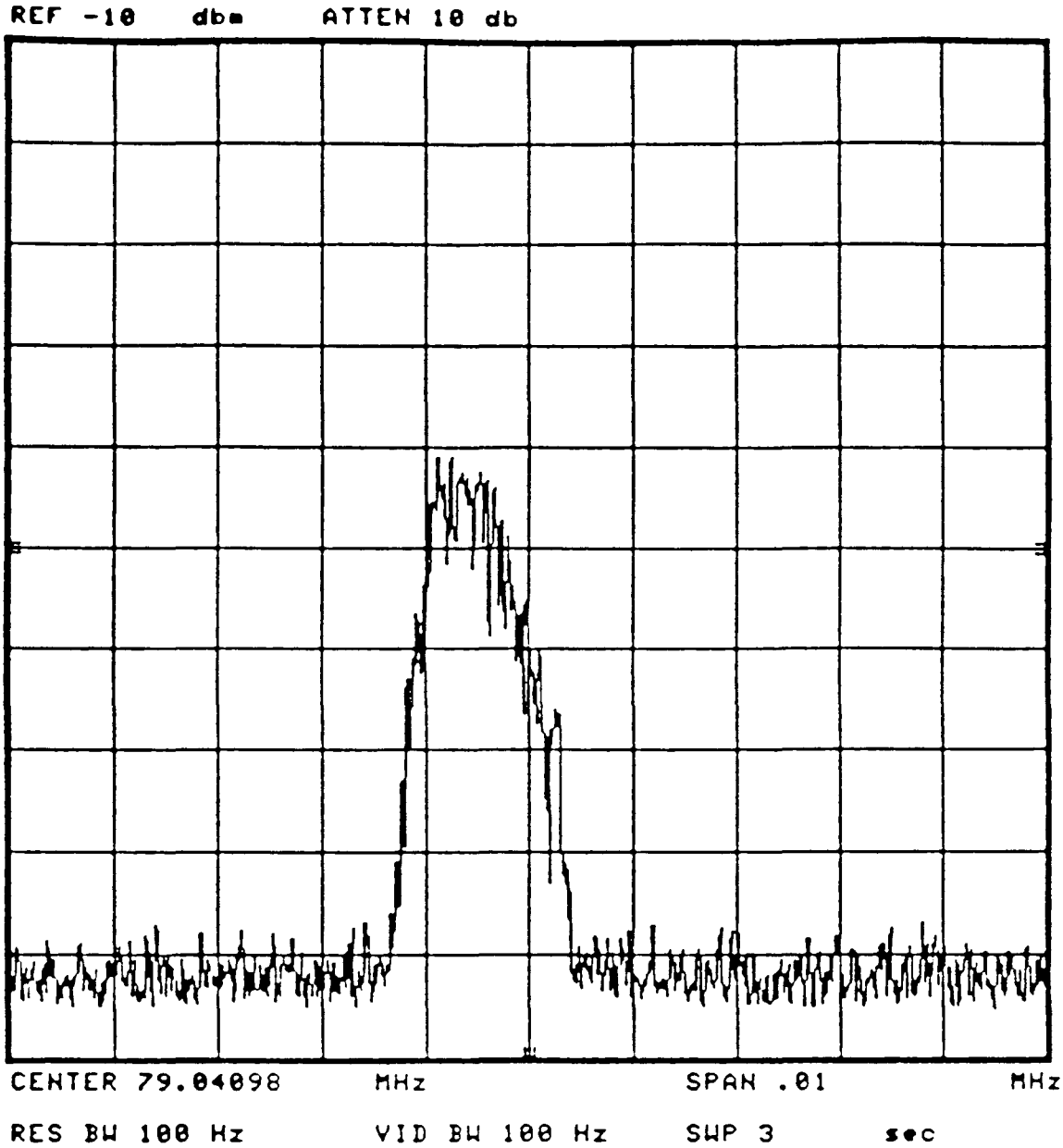

(b) Schottky Signal after transition crossing.

Figure 6.13. (continued)

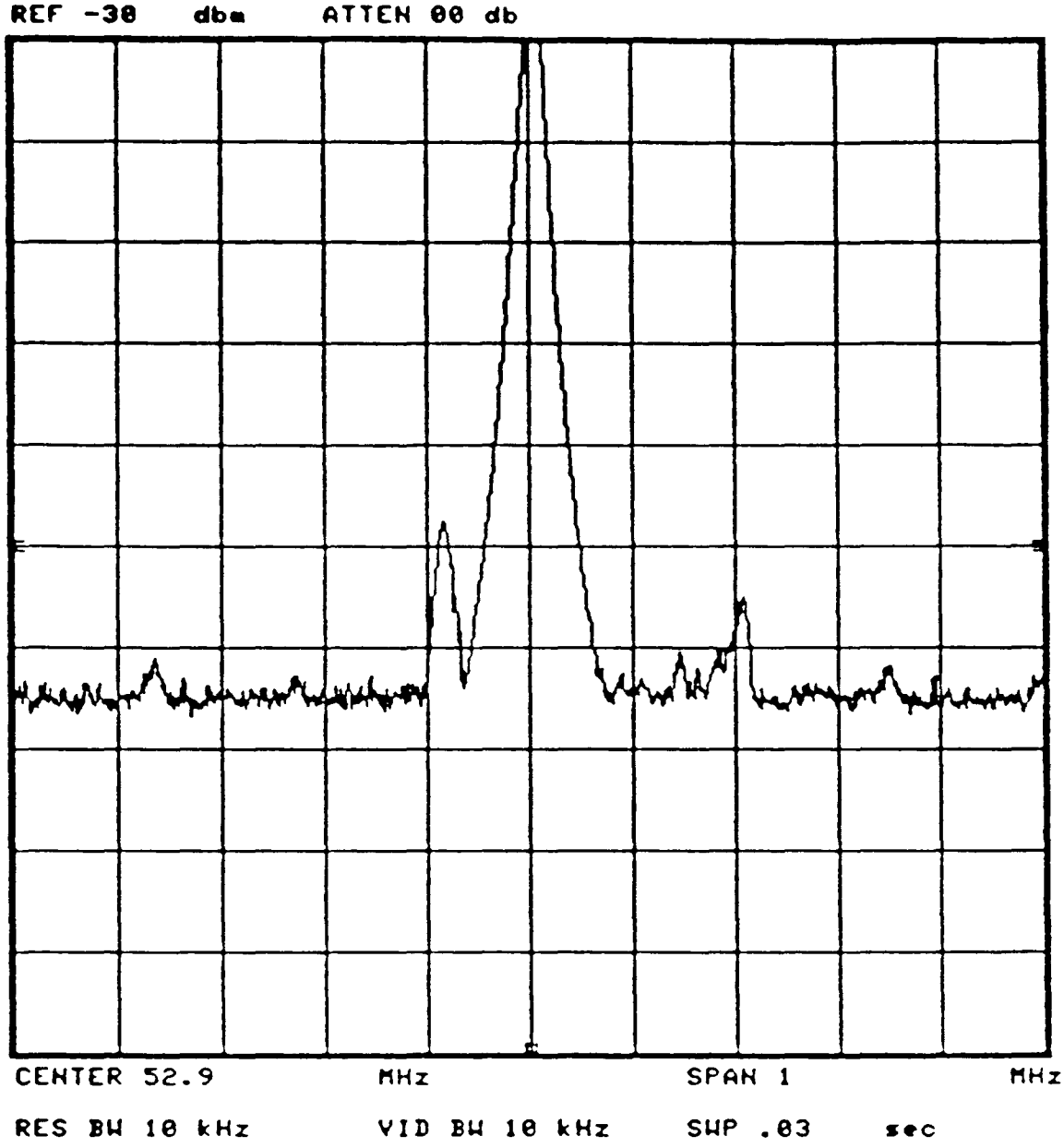

(c) Wall current monitor signal.

Figure 6.13. (continued)

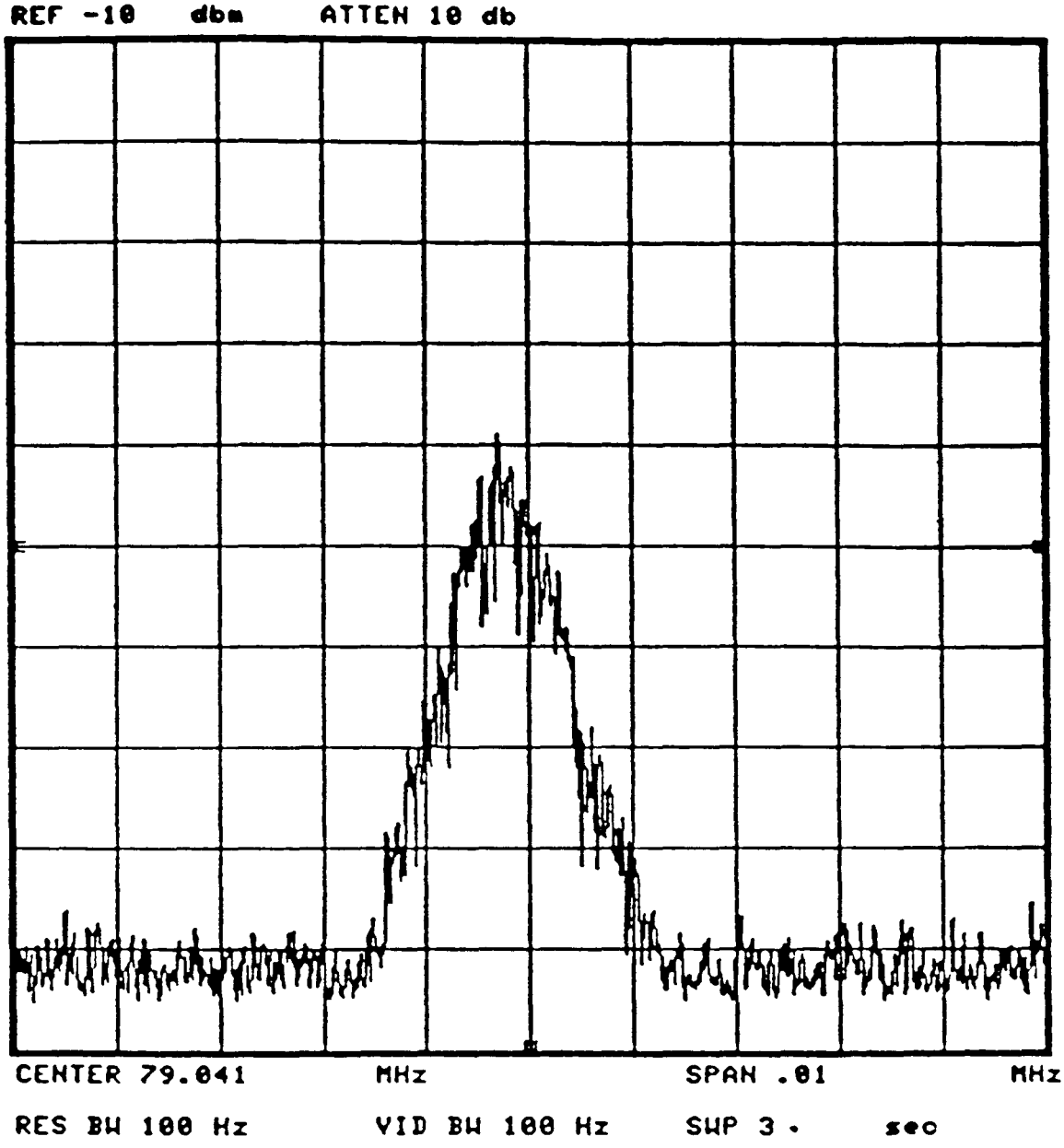

(a) Schottky Signal before transition crossing.

Figure 6.14. Transition Crossing with ARF1 Shorted. The normal ramp table was used for this crossing with a beam of 3.75mA.

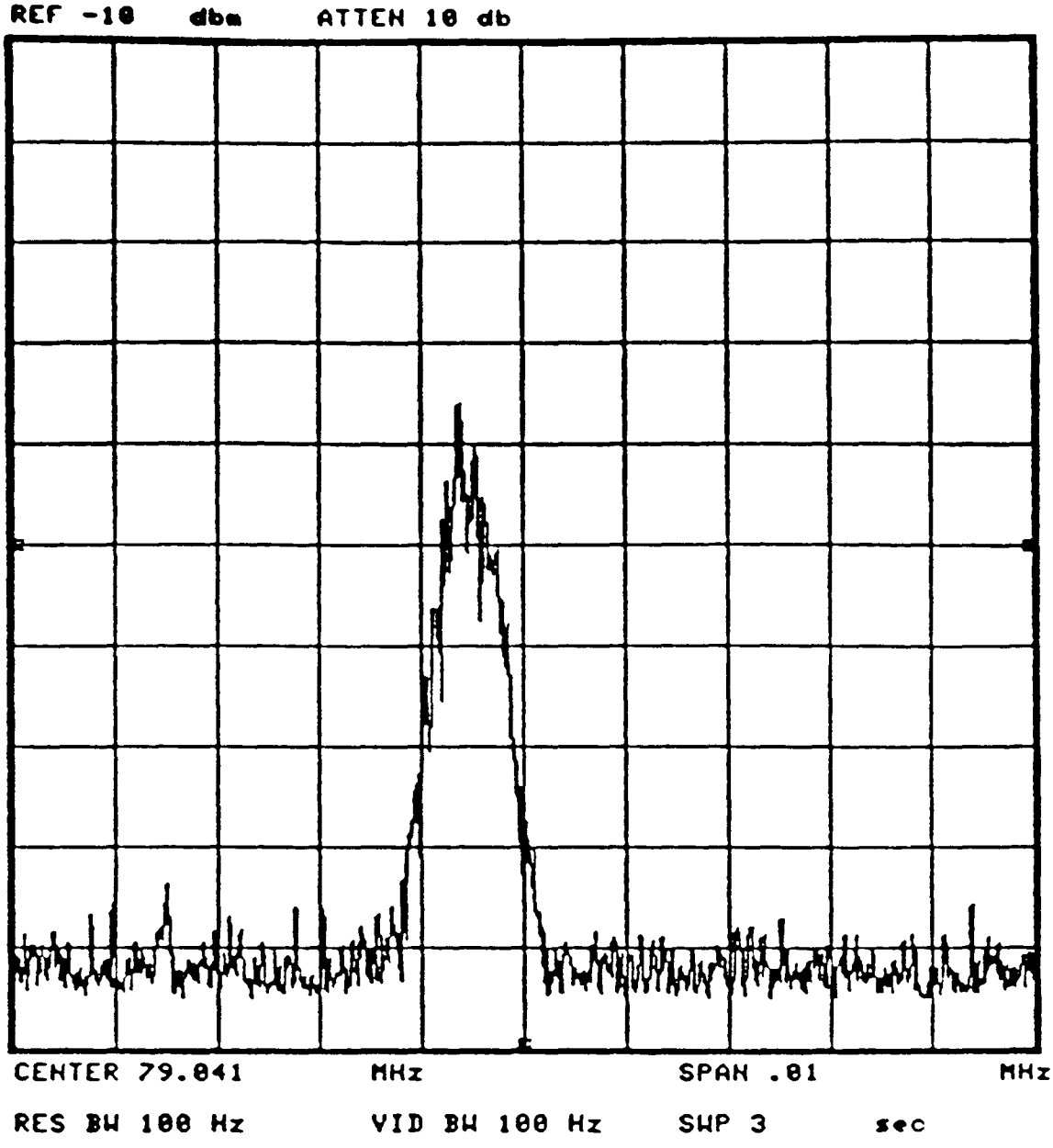

(b) Schottky Signal after transition crossing.

Figure 6.14. (continued)

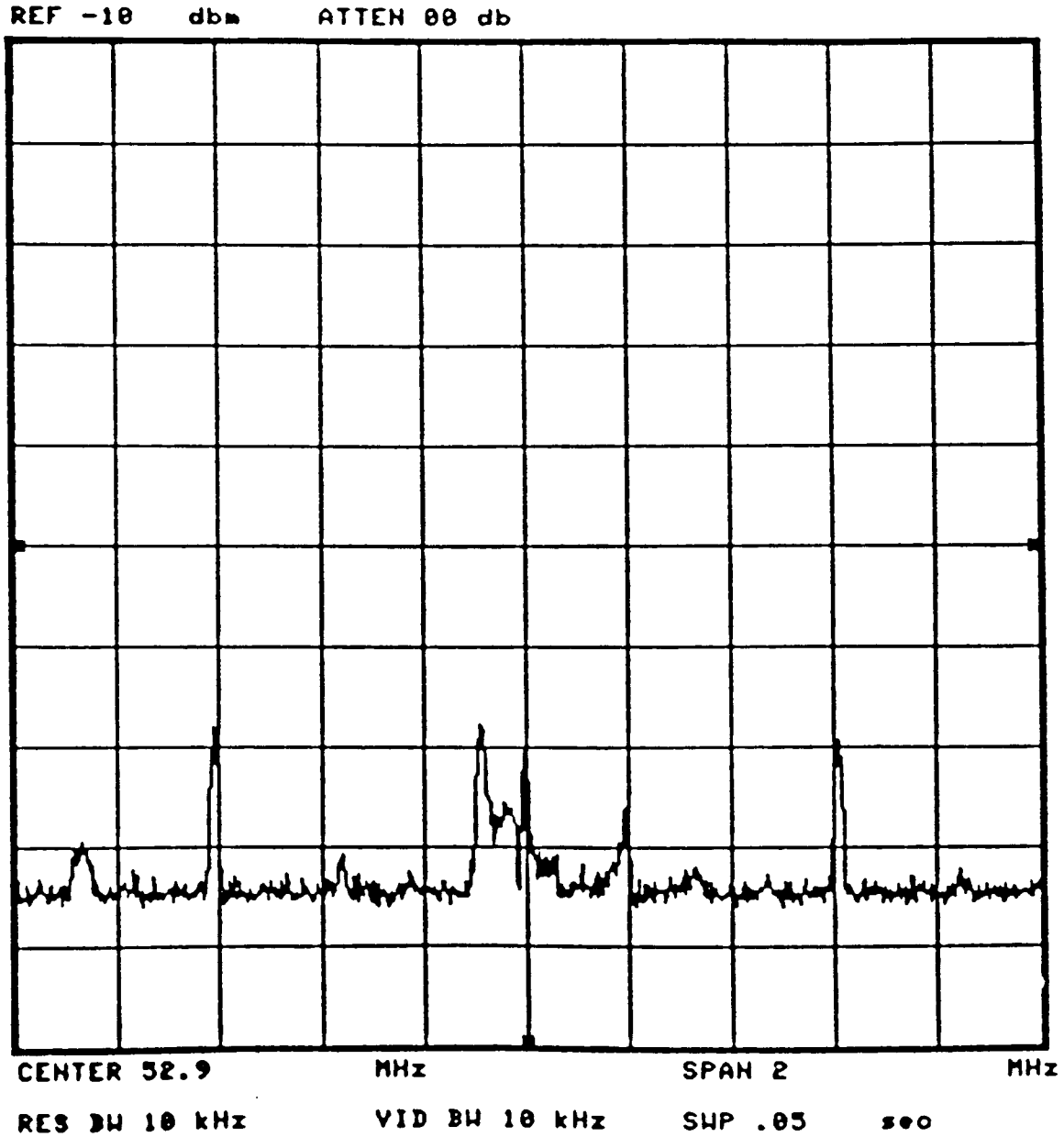

(c)Wall current monitor signal.

Figure 6.14. (continued)

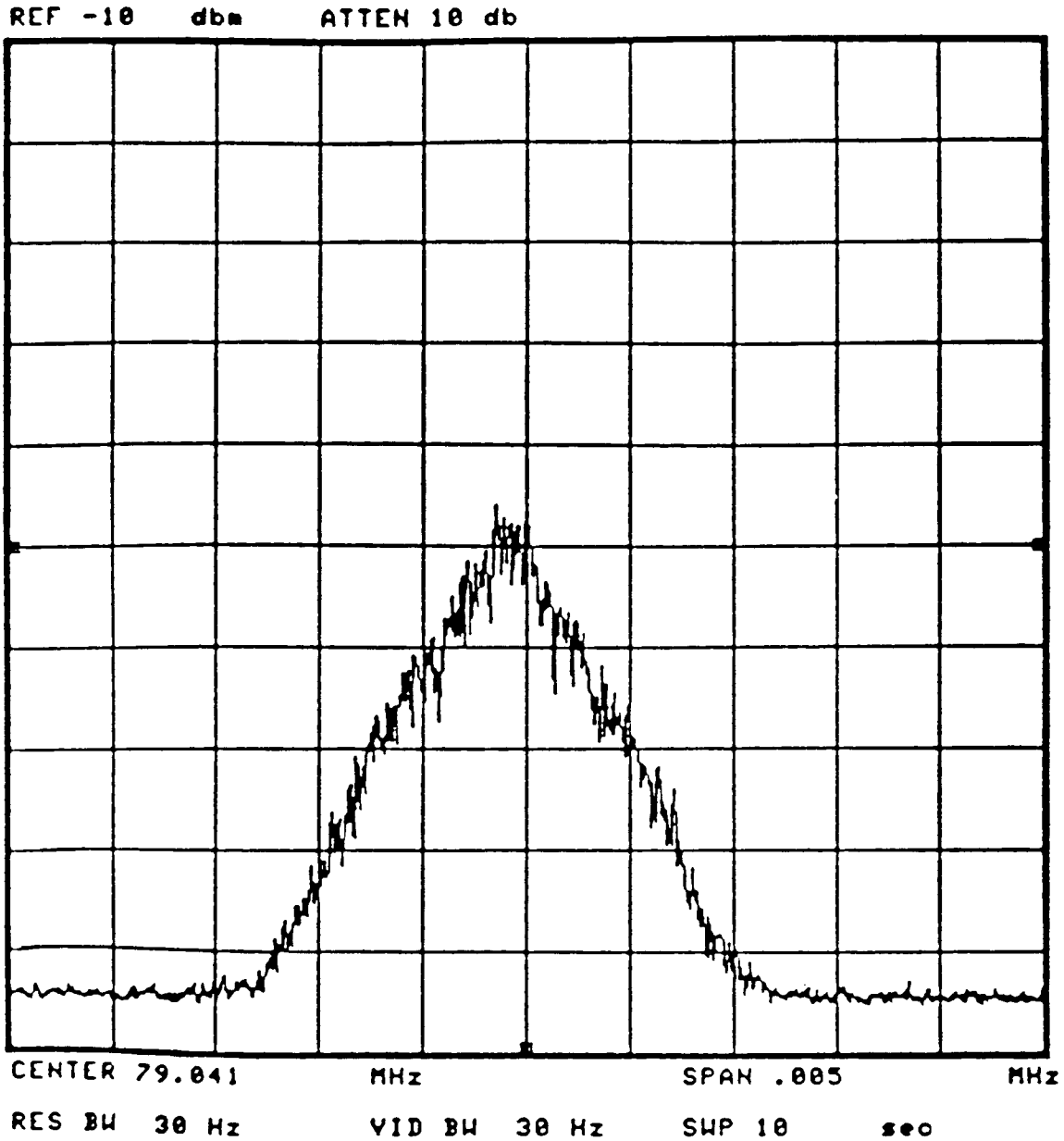

(a) Schottky Signal before transition crossing.

Figure 6.15. Faster Transition Crossing with ARF1 not Shorted. The ramp table was made such that the crossing process was six times as fast. The beam intensity was 4.1mA.

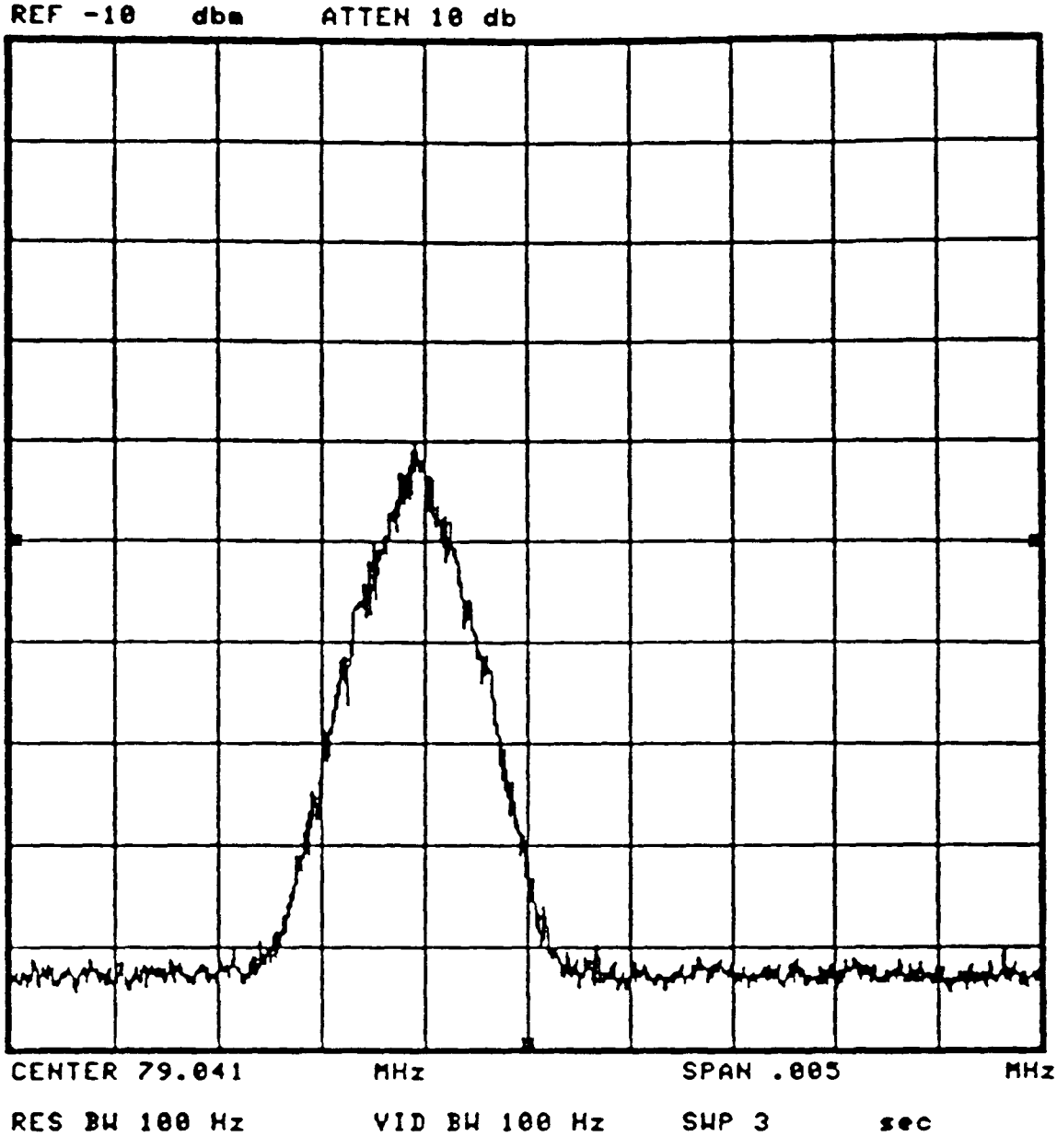

(b) Schottky Signal after transition crossing.

Figure 6.15. (continued)

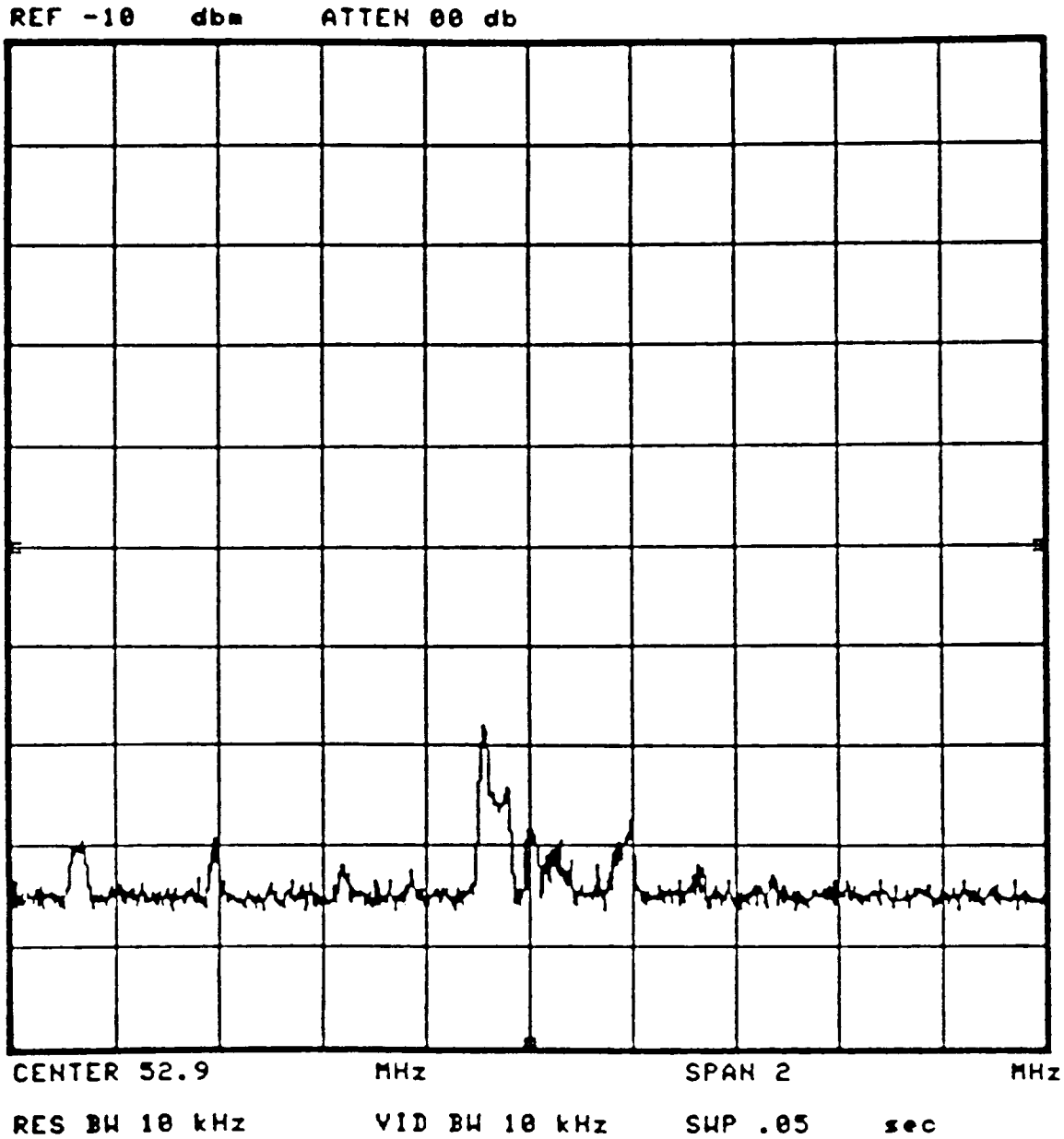

(c)Wall current monitor signal.

Figure 6.15. (continued)

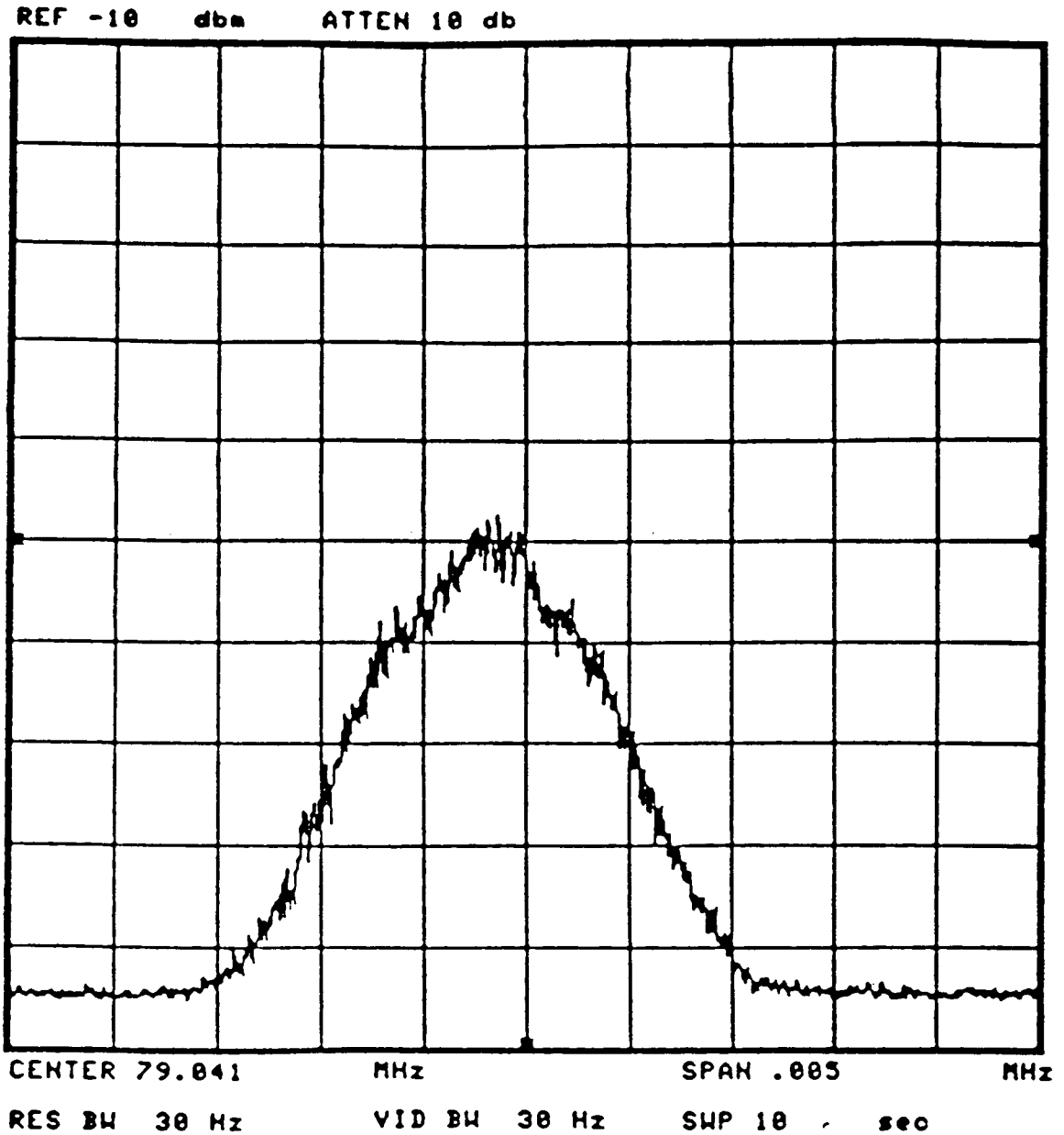

(a) Schottky Signal before transition crossing.

Figure 6.16. Faster Transition Crossing with ARF1 Shorted. The fast ramp table was used for this crossing with a beam of 5.5mA.

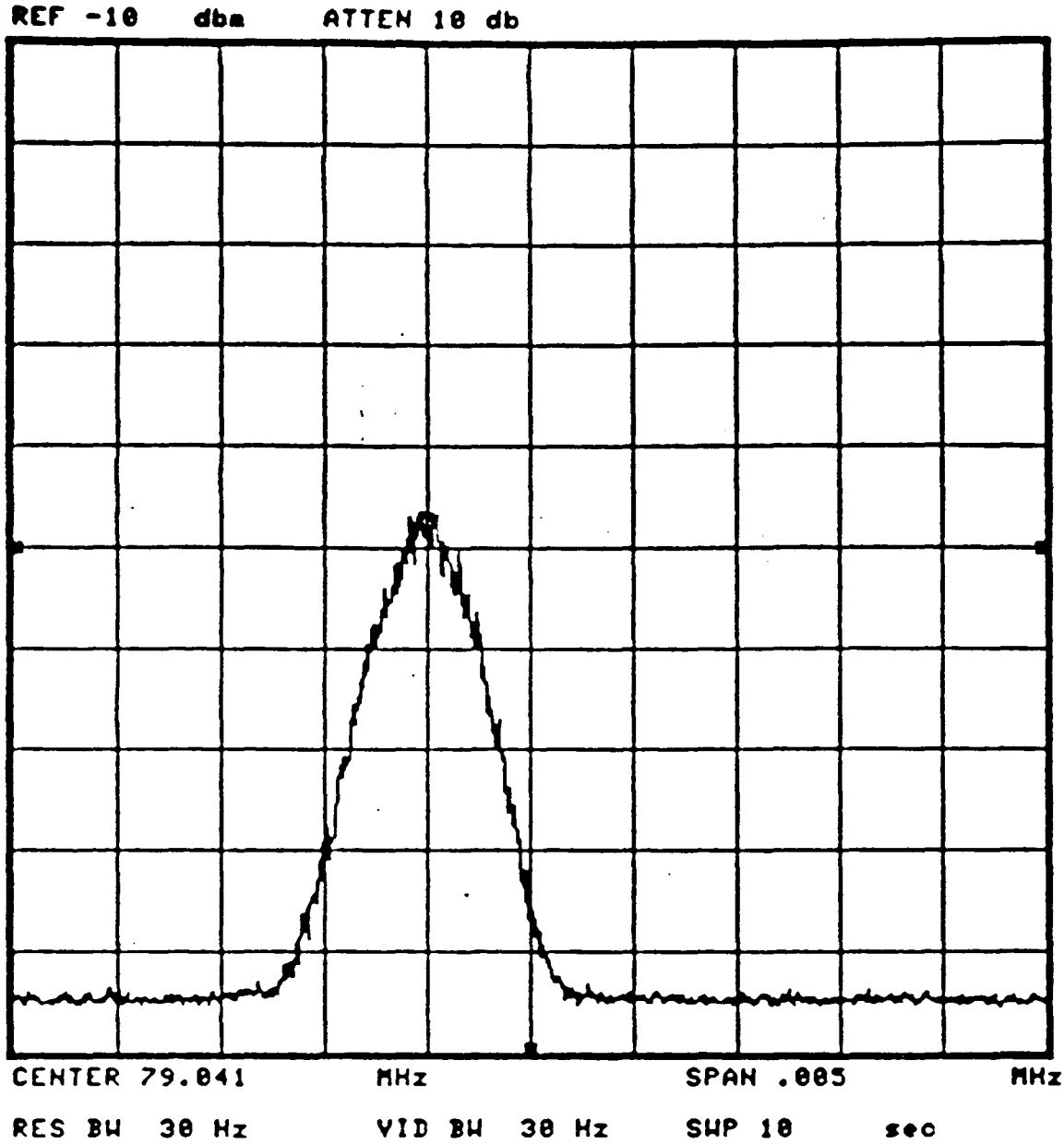

(b) Schottky Signal after transition crossing.

Figure 6.16. (continued)

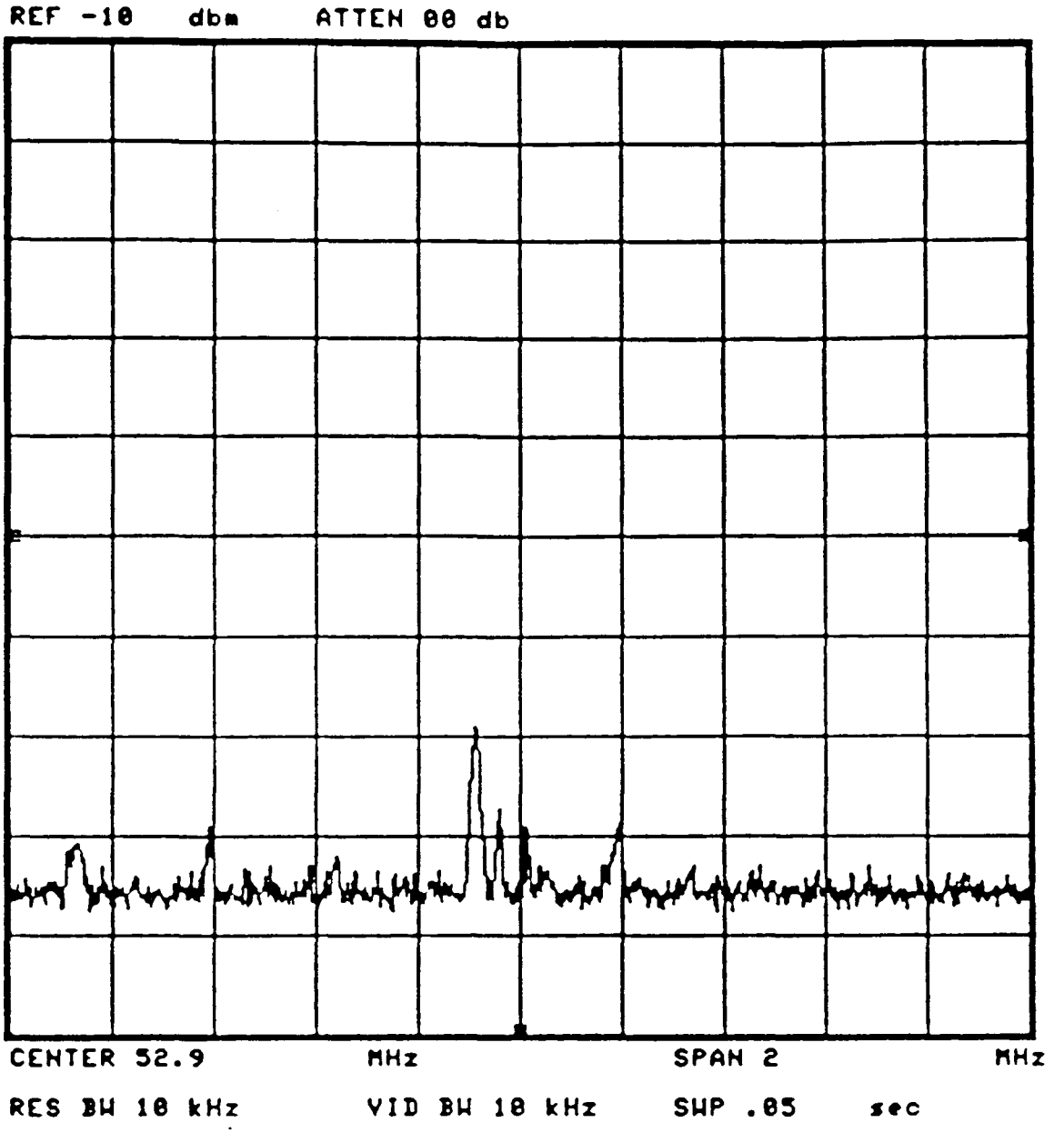

(c) Wall current monitor signal.

Figure 6.16. (continued)

CHAPTER VII

SIMULATION OF ACCUMULATOR TRANSITION CROSSING

A computer tracking program called ESME [48] has been used to simulate the Accumulator transition crossing process in longitudinal phase space. Simulation helps the development of an understanding of the details of the process and confirm the measurement results. Some ESME simulation results will be presented in this chapter.

7.1 About ESME

ESME is a computer program written to calculate the evolution of a distribution of particles in longitudinal phase space. It generates a requested initial distribution of particles and tracks the distribution turn-by-turn by iterating a map corresponding to the single particle equations of motion. Collective effects can also be studied by including beam-induced forces on each individual particle in the distribution. This section outlines the features of ESME relevant to the simulation of the Accumulator transition crossing. More details can be found in the ESME user's guide (ref. [48]).

7.1.1 Coordinate System. The basic coordinates used in ESME are the azimuth of the particles and the difference of their energy from the synchronous energy at the time when the RF passes through its synchronous phase. The azimuth is measured with respect to a location where the rf voltage is applied, and is in the range

$$-180^\circ \leq \theta_{i,n} \leq 180^\circ \ , \tag{7.1}$$

where i is the particle index and n is the turn number. The sense of θ is clockwise positive, but the beam travels in the $-\theta$ direction, or counterclockwise. In a beam with h identical bunches, typically a well behaved bunch will be centered near

$\theta = 0 \bmod 180/h$, therefore ESME calculates for a single bunch with periodic boundaries set at $\theta = \pm 180°/h$ for calculation efficiency. The unit for energy is MeV; the unit for azimuth is radian for calculations but degree for input and output. The basic time unit of the difference equation is the turn number, but all input specification of parameter time dependence is in seconds.

7.1.2 Difference Equations. The difference equations used in ESME for tracking the single particle motion are given as

$$\theta_{i,n} = \left[\frac{\tau_{s,n-1}}{\tau_{s,n}} \theta_{i,n-1} + 2\pi \frac{\tau_{i,n}}{\tau_{s,n}} - \pi \right]_{\mathrm{mod}(2\pi)} + \pi \tag{7.2}$$

and

$$E_{i,n} = E_{i,n-1} + eV(\varphi_{s,n} + h\theta_{i,n}) - eV(\varphi_{s,n}) \ , \tag{7.3}$$

where $E_{i,n}$ is the energy of the ith particle relative to the synchronous energy at the end of the nth turn, $\varphi_{s,n}$ is the synchronous RF phase in the nth turn, and $\tau_{s,n}$ and $\tau_{i,n}$ are the revolution periods of the synchronous particle during the nth turn and that of the ith particle respectively. Equations (7.2) and (7.3) give the change in the azimuth and energy of the ith particle during the nth turn of the synchronous particle.

In a circular accelerator or a storage ring, the revolution period of a particle is determined by its velocity and path length. In ESME, the velocity of each particle in the distribution may be calculated exactly at each turn from its energy. Due to the non-linearity of the lattice, when a particle has a momentum deviation from the synchronous particle, the change in its path length can be expressed as

$$\frac{\Delta C}{C_0} = \alpha_0 \frac{\Delta P}{P_0} + \alpha_1 \left(\frac{\Delta P}{P_0} \right)^2 + \cdots \ , \tag{7.4}$$

where C_0 and P_0 are the orbit length and momentum of the synchronous particle respectively, α_0 leads to the familiar γ_t, and α_1 gives the lowest order non-linear

dependence of the path length on momentum. For a particle with a certain momentum deviation from the synchronous particle, ESME calculates the change in its path length with the input parameters α_0, α_1, α_2, and α_3. In this way of calculating the velocity and path length of a particle, the relation between the revolution period of the synchronous particle $\tau_{s,n}$ and that of the ith particle is treated precisely in ESME. This feature is very important when the synchronous energy is close to the transition energy.

7.1.3 Collective Effects. Effects of beam-generated fields on an individual particle are manifested as an additional accelerating or decelerating voltage acting on the particle during each turn. This voltage is related to the beam current through the impedance. Since the impedance of a machine is frequency dependent and the beam current is not a pure harmonic a.c. current, ESME finds the frequency spectrum of the beam current using the fast Fourier transform (FFT) and calculates the voltage generated by each component.

In the phasor representation, a beam current with a fundamental frequency $\Omega = h\omega_0$ (for example, a beam with h identical bunches) can be expressed with its frequency spectrum as [49]

$$I_b(\Omega t) = \frac{Ne\omega_0}{2\pi} \sum_m \Lambda_m e^{j(-m\Omega t+\varphi_m)} , \tag{7.5}$$

where N is the total number of particles in the beam and ω_0 is the revolution frequency of the synchronous particle. Each current component multiplied by the longitudinal impedance evaluated at that frequency gives the beam-induced voltage. The longitudinal impedance Z_L evaluated at frequency $m\Omega$ is denoted as the phasor $Z_m e^{j\chi_m}$. The beam-induced voltage is applied to each particle at the time the synchronous particle is at the gap. The voltage depends on the relative phase between the particle and the current. The phase of the synchronous particle

is zero. Thus, the energy increment for the ith particle on the nth turn due to the beam-induced voltage is

$$eV_{i,n}^{b} = \frac{Ne^2\omega_0}{2\pi} \sum_m \Lambda_m Z_m e^{j(m\phi_{i,n}+\varphi_{m,n}+\chi_m)} , \tag{7.6}$$

where $\phi_{i,n} = h\theta_{i,n}$ is the phase of the ith particle relative to the synchronous particle.

ESME calculates the beam-induced voltages from space charge, wall impedance, and resonant cavities. The space charge calculation assumes a constant geometric factor relating average beam radius and average beam pipe radius. The wall impedance is characterized by an arbitrary table of real and imaginary components of the impedance versus frequency. A resonant object is characterized by resonant frequency, the quality factor, and shunt resistance.

The line density of a beam comes from the *theta*-projection of its phase space distribution. In ESME, the line density is calculated numerically by binning the θ-projection of the phase space distribution. The current spectrum can be obtained by a FFT of the bin occupation numbers. The choice of the bin width which determines the highest frequency component of the beam current spectrum involves both numerical and physical considerations. Too few bins will result in a poor representation of the line density. On the other hand, many bins will produce a good representation of the line density only if there are a sufficient number of particles in each bin, which requires a large number of particles in the simulation. In other words, tracking a sufficient number of particles to give an adequate representation of the beam may consume a large amount of computing time. In general, choices of the bin number and the total number of particles depend on the problem of interest and the computing resources. [50]

7.2 ESME Simulation of Transition Crossing

As has been seen in section 7.1.3, it is impractical for ESME to simulate coherent beam effects with impedance sources in a wide frequency range. Fortunately, it was found in the Accumulator transition crossing that the impedance of ARF1 was the major cause of the beam longitudinal instability in that process. Therefore, simulations can done with ARF1 being the only resonant object responsible for the longitudinal coherent effect.

7.2.1 Binning. In the Accumulator transition crossing, the 85th revolution harmonic is the closest one to the resonant frequency of ARF1. This means that the beam-induced voltage in ARF1 produces a periodic beam structure with a fundamental frequency of about 53 MHz which is 85 times of the revolution frequency. Therefore to simulate the effect of ARF1 on the beam, calculations are restricted to $-180°/85 \leq \theta \leq 180°/85$ with periodic boundary conditions. In doing so, the Fourier series of the beam current consists of components at harmonics of 53 MHz. The initial distribution of the beam is generated such that it is Gaussian in energy and randomly uniform in azimuth. It is reasonable to assume that about ten terms in the beam current spectrum will lead to a good simulation result, since the impedance only drives the beam at the first harmonic of 53 MHz. In the simulation, the total number of bins is chosen to be 16 which will give eight terms in the current spectrum. The total number of particles used for the simulation is 10000, which results in about 625 particles in each bin and therefore about 4% statistical fluctuation. Because the Accumulator transition crossing is a long process taking at least about 10^6 revolutions, simulation is time-consuming. The total number of particles of 10000 is what can be reasonably afforded for simulation.

7.2.2 Simulation Results. In the simulation, the beam and lattice parameters are taken from the transition measurements made on September 2, 1990 with the new crossing ramp table: the beam current is 4.5mA, the rms energy width of the beam is approximately 1 MeV, and the initial value of η is -0.0062. ARF1 is modeled to have a resonant frequency at 52.9 MHz, a quality factor of 200, and a shunt resistance of 60 $k\Omega$. The effects of space charge and non-linear dependence of path length on momentum are ignored at first. Figure 7.1 shows the phase space and energy distributions of the beam before the transition crossing process.

According to the simulation, in the process of transition crossing, there is no real bunching of the beam due to the ARF1 impedance in the usual sense, *i.e.*, bunching when an external RF voltage is present. The motion of the beam particles in longitudinal phase space can be illustrated with figures 7.2 and 7.3 in which the simulation is done for a different beam. The beam-induced voltage in the ARF1 cavity changes the beam distribution such that there is a coherent structure with the frequency of 53 MHz. But the frequency spread of the beam causes changes in the relative azimuthal positions of the beam particles and therefore smears that coherent structure. Because the impedance is almost purely resistive, the amplitude of the coherent structure is proportional to the beam-induced voltage. Therefore, to show the amplitude of the coherent structure, these figures present the energy loss per particle per turn, which is the negative beam-induced voltage, as a function of azimuth.

Simulation of the Accumulator transition crossing shows that dramatic change in the beam distribution in longitudinal phase space occurs when η is about 10^{-4}. Significant increase in the beam energy spread is required in the transition region for counteracting the coherent instability. Time evolution of the beam distribution in phase space near transition is shown in figure 7.4. Beam gets stabilized when the absolute value of η exceeds 10^{-4} on the other side of the transition. The phase space distribution and energy distribution of the beam at $\eta = -1.8 \times 10^{-4}$ is shown in figure 7.5.

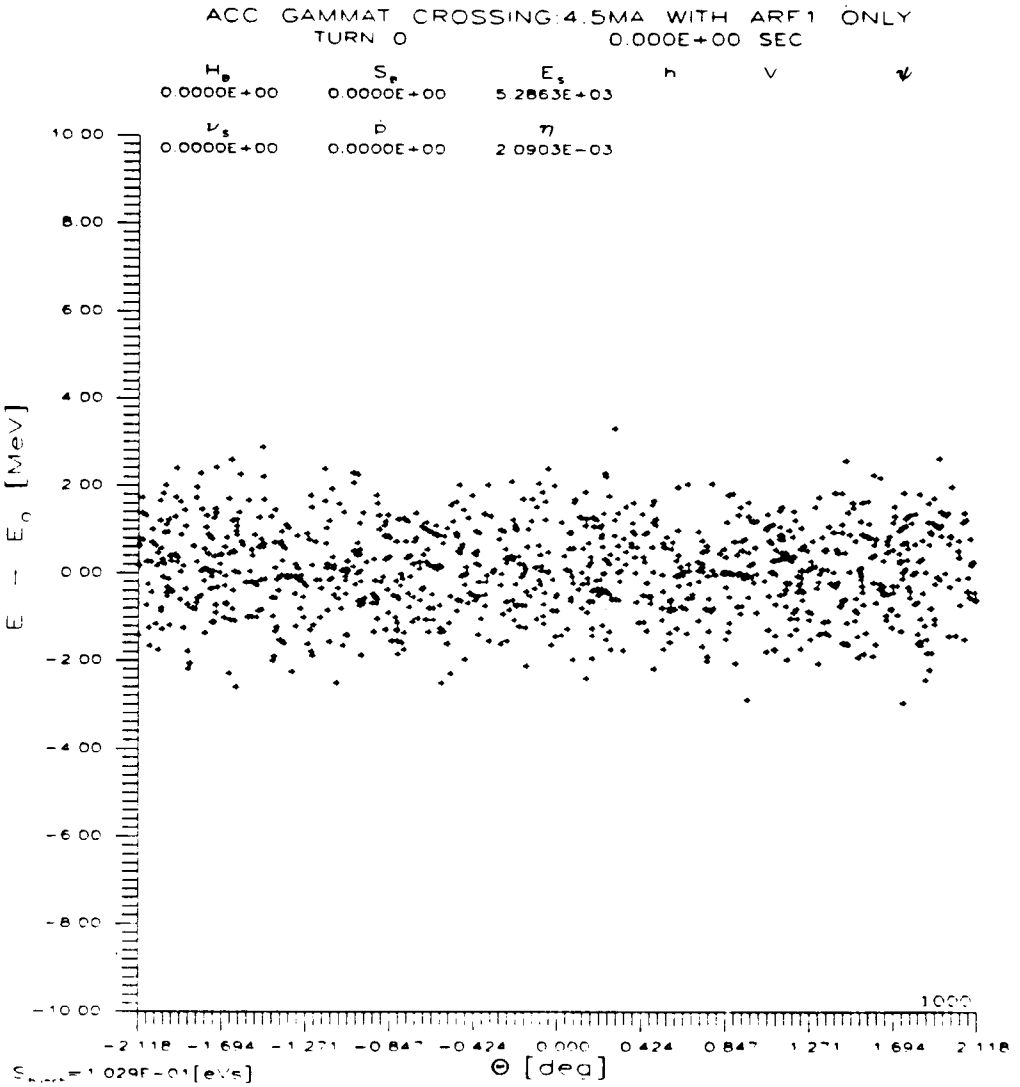

(a) Phase space distribution.

Figure 7.1. Initial Phase Space Distribution and Energy Distribution of the Beam. The latter is the E-projection of the former. The total number of particles used for simulation is 10000, but only one tenth of that number is plotted in longitudinal phase space.

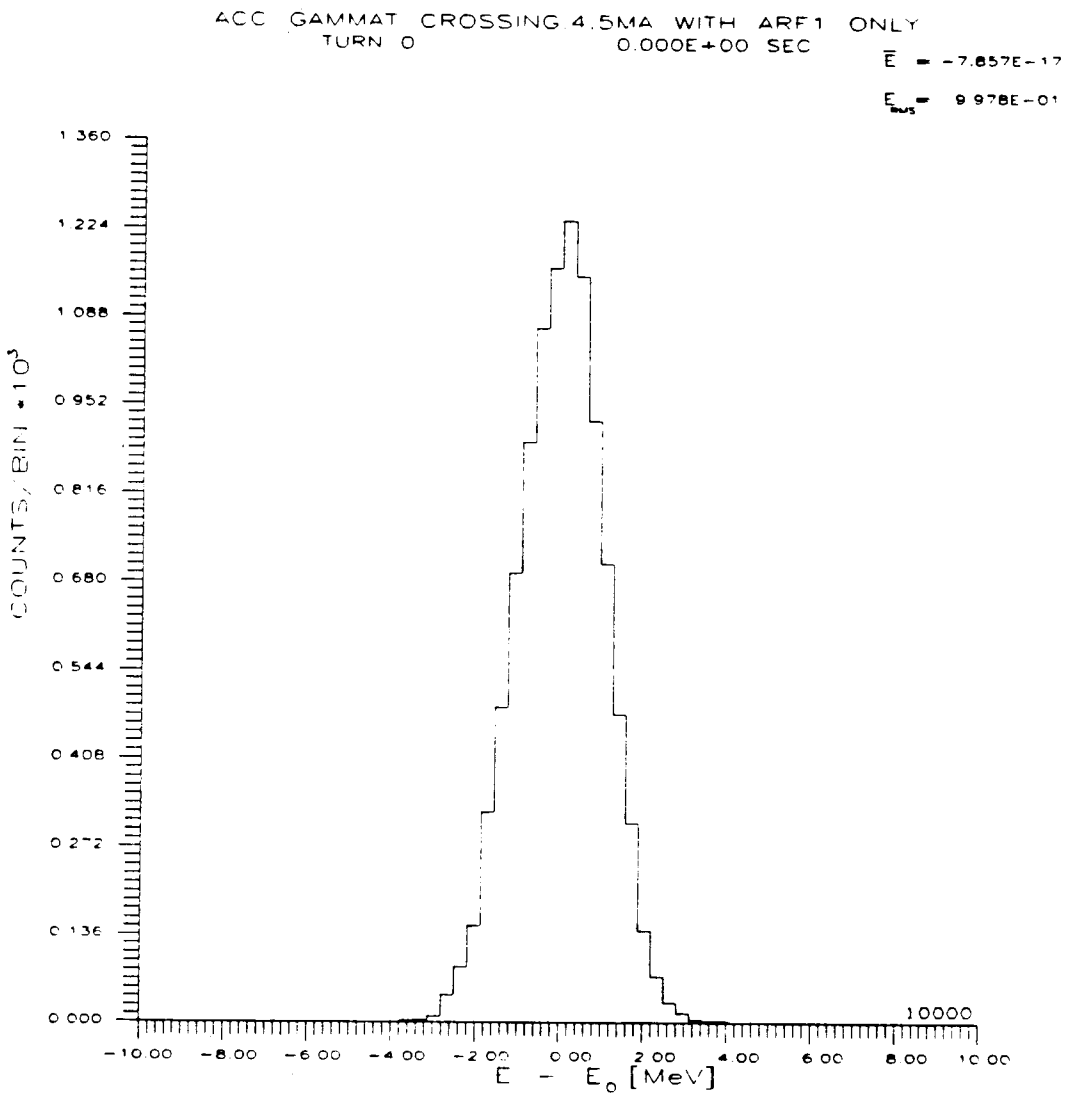

(b) Energy distribution.

Figure 7.1. (continued)

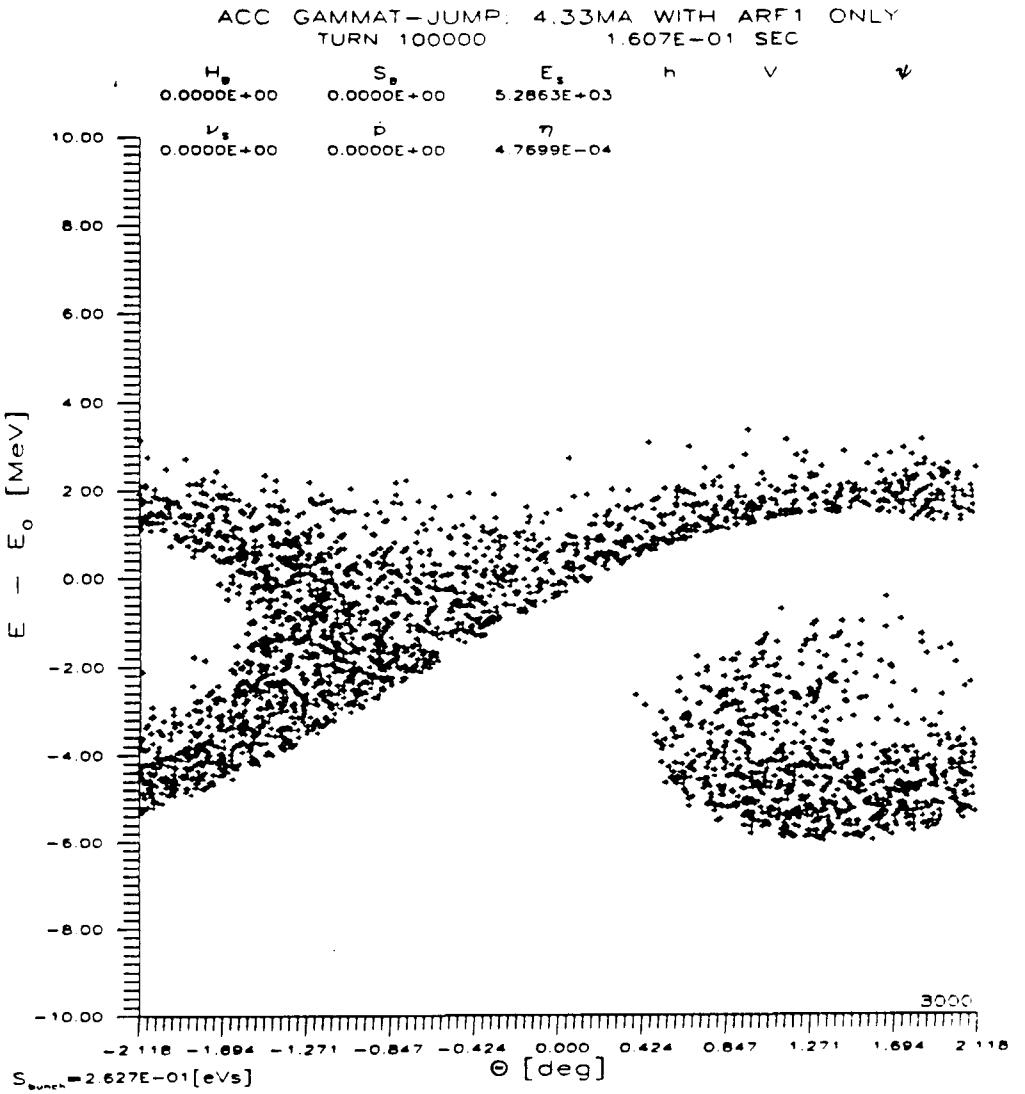

(a) Phase space distribution.

Figure 7.2. Illustration I of the Phase Space Motion of a Beam. The beam is initially Gaussian in energy and randomly uniform in azimuth. The coherent structure is produced by the beam-induced voltage in ARF1.

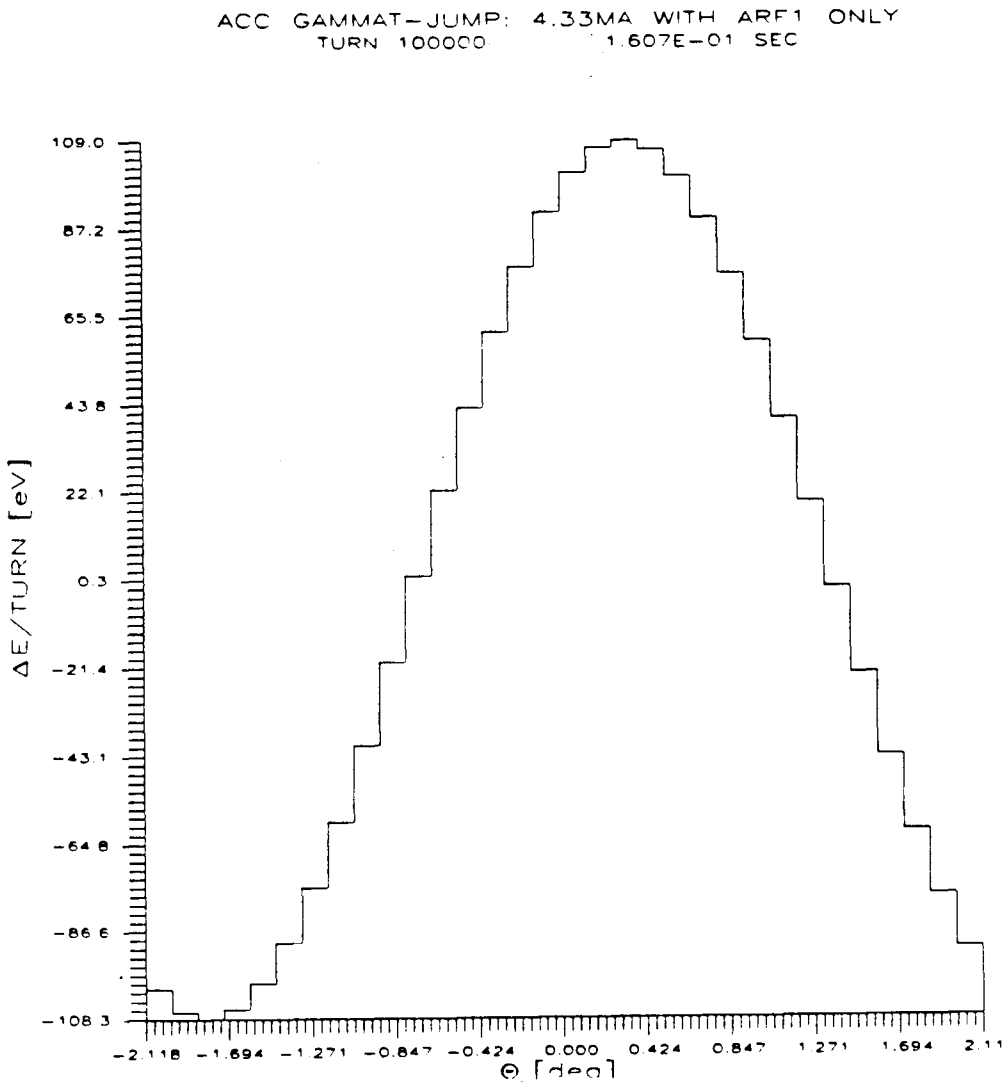

(b) Energy loss per particle per turn as a function of azimuth.

Figure 7.2. (continued)

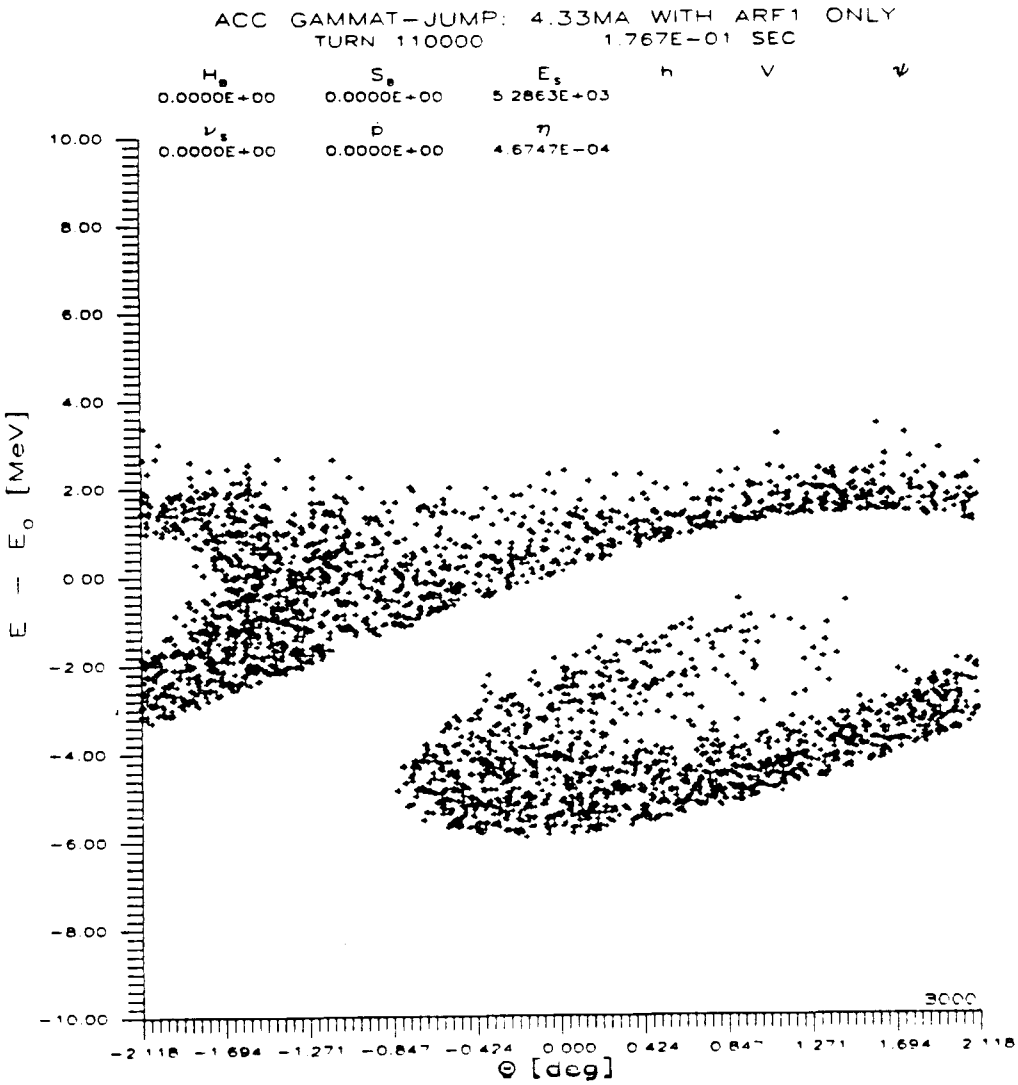

(a) Phase space distribution.

Figure 7.3. Illustration II of the Phase Space Motion of a Beam. Some time later, the coherent structure is reduced due to the frequency spread of the beam. Since the amplitude of the a.c. beam component at 53 MHz is proportional to the peak value of the beam energy loss per turn, it can be seen that the coherent structure is reduced by comparing (b) with figure 7.2(b).

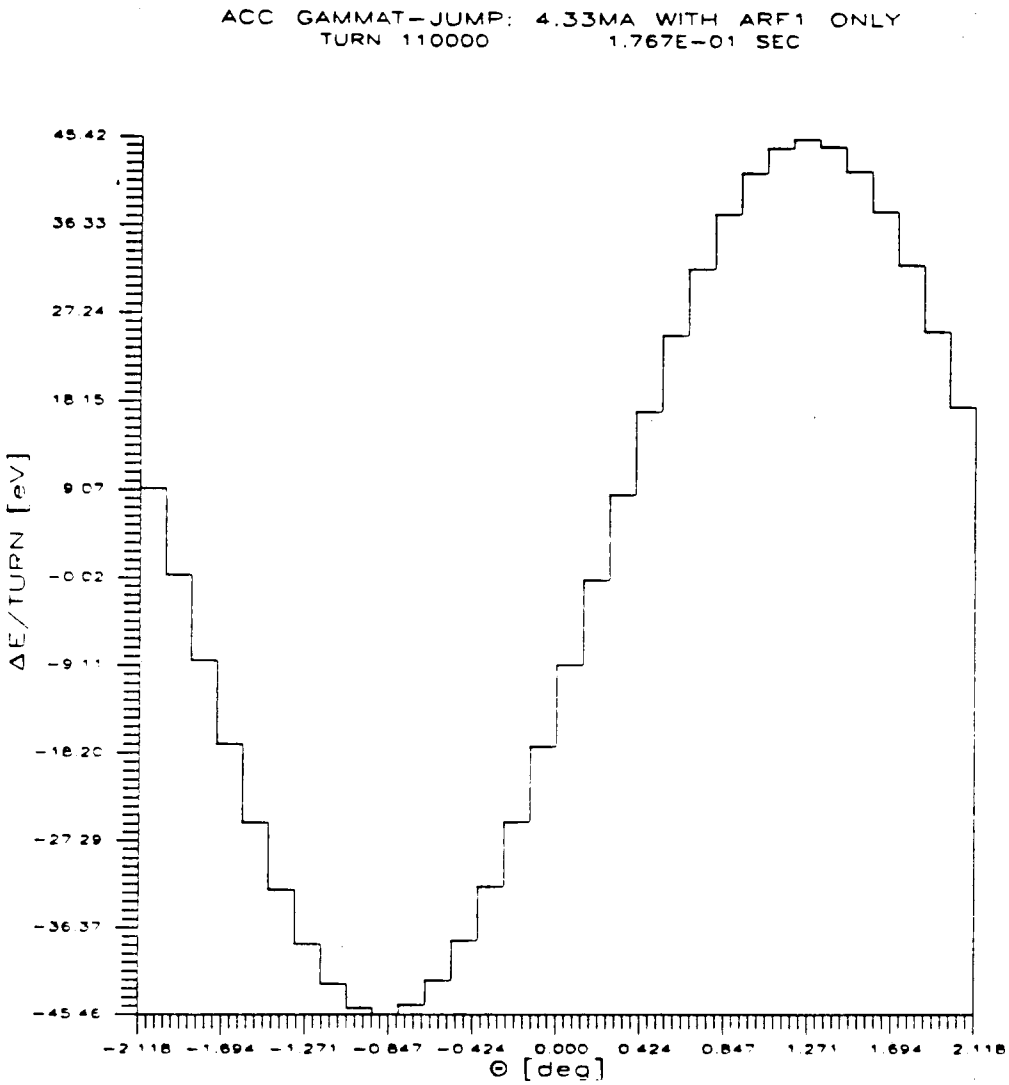

(b) Energy loss per particle per turn as a function of azimuth.

Figure 7.3. (continued)

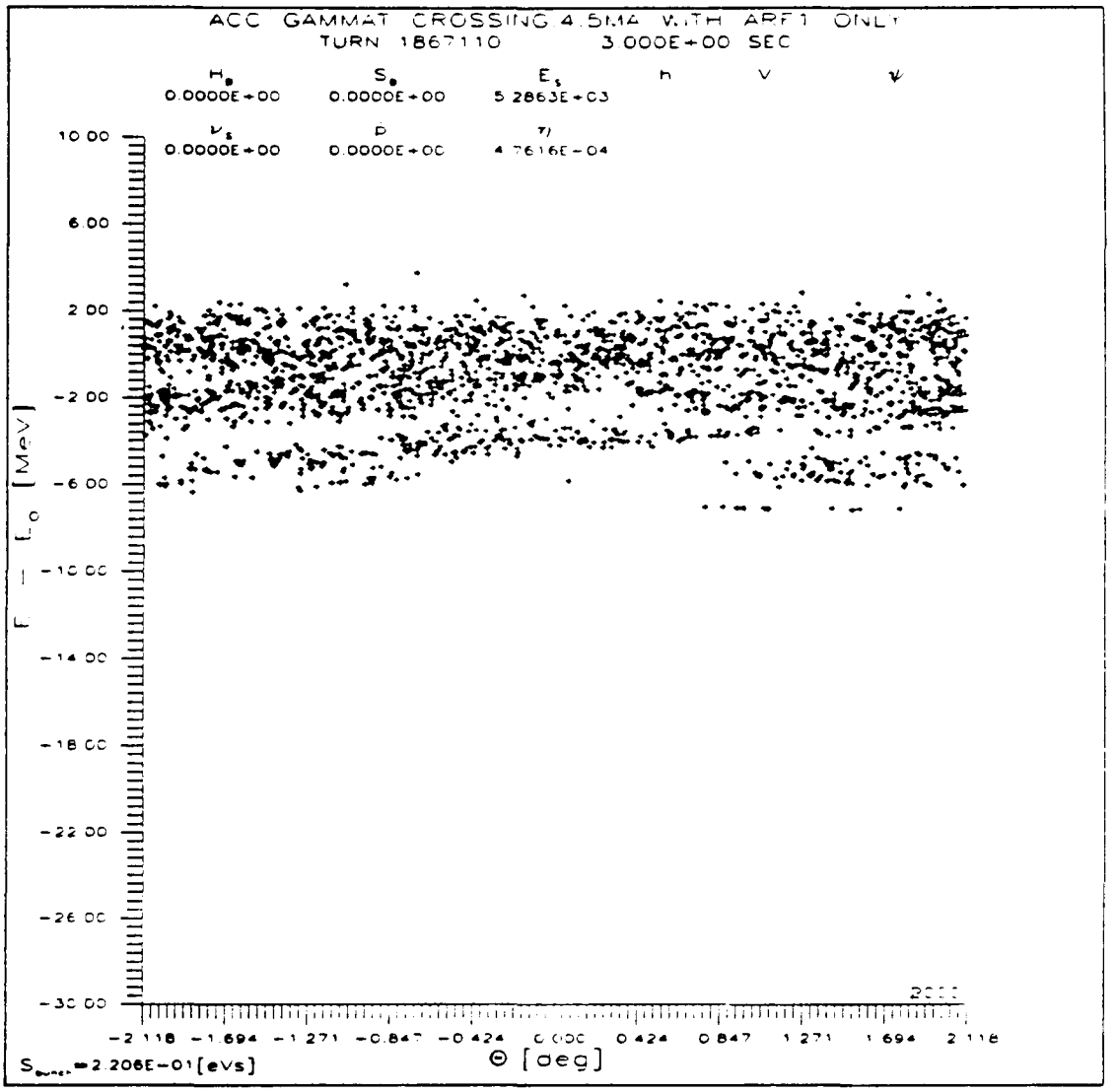

(a) Phase space distribution at $\eta = 4.8 \times 10^{-4}$.

Figure 7.4. Time evolution of the phase space distribution.

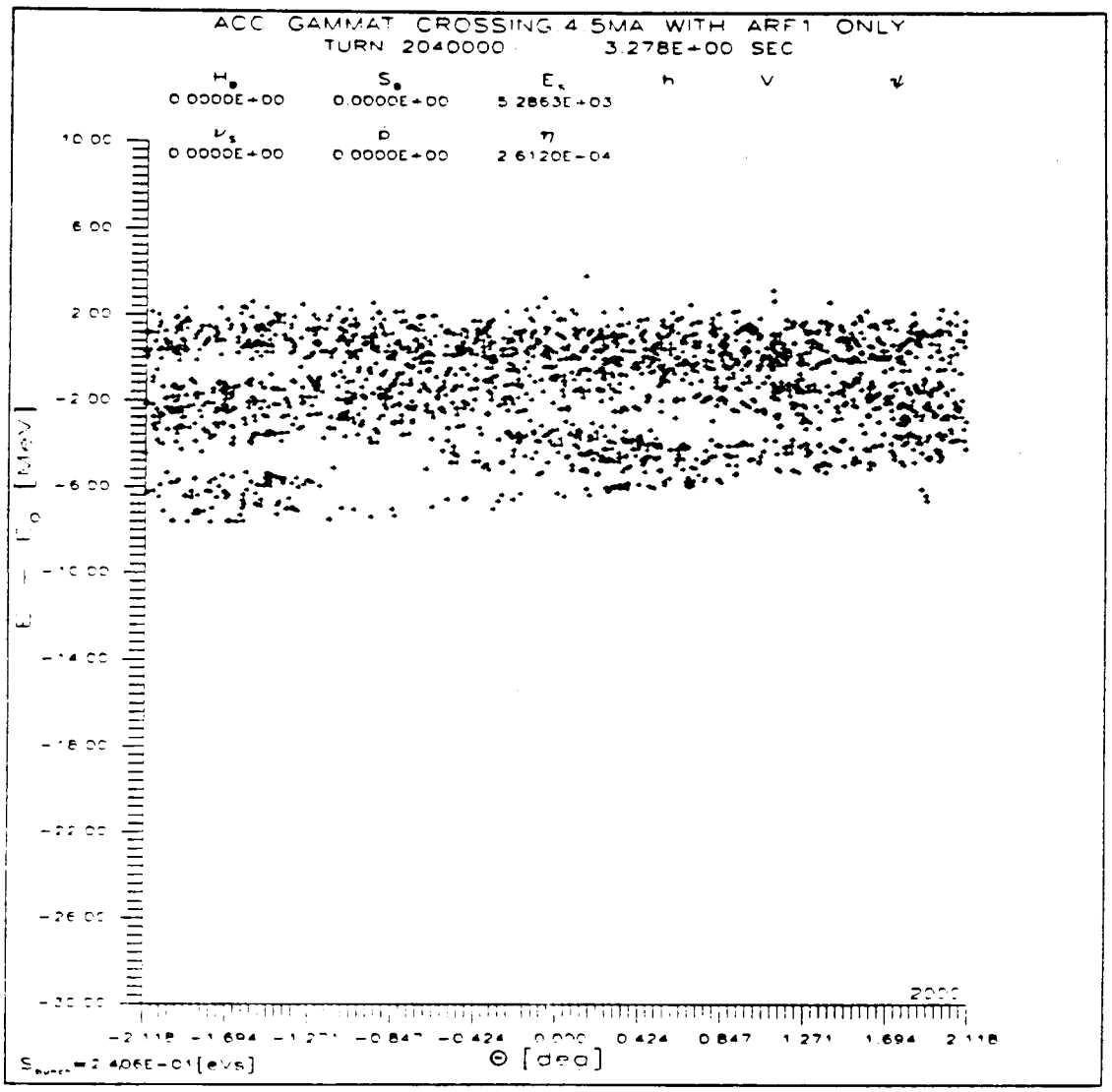

(b) Phase space distribution at $\eta = 2.6 \times 10^{-4}$.

Figure 7.4. (continued)

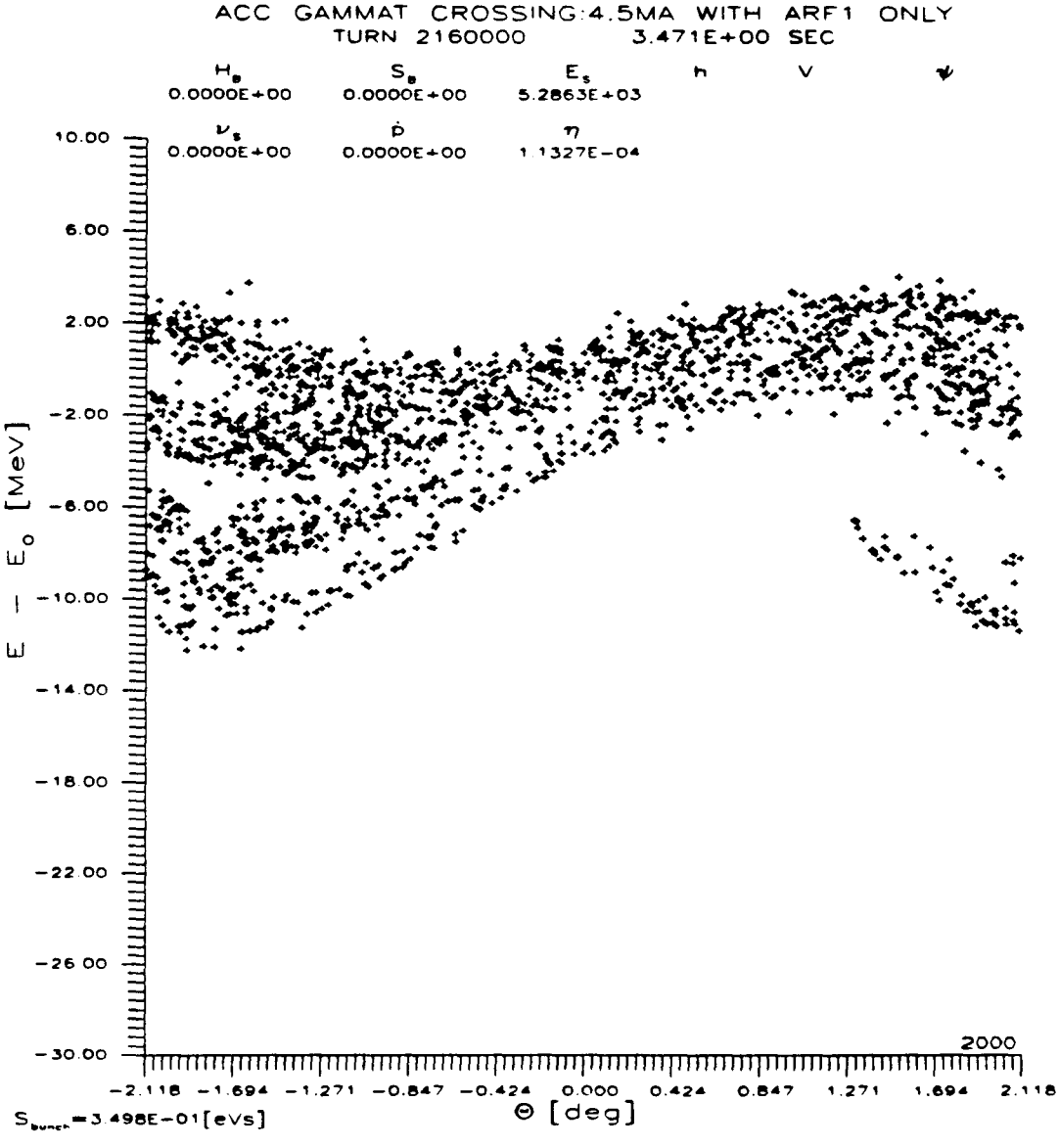

(c) Phase space distribution at $\eta = 1.1 \times 10^{-4}$.

Figure 7.4. (continued)

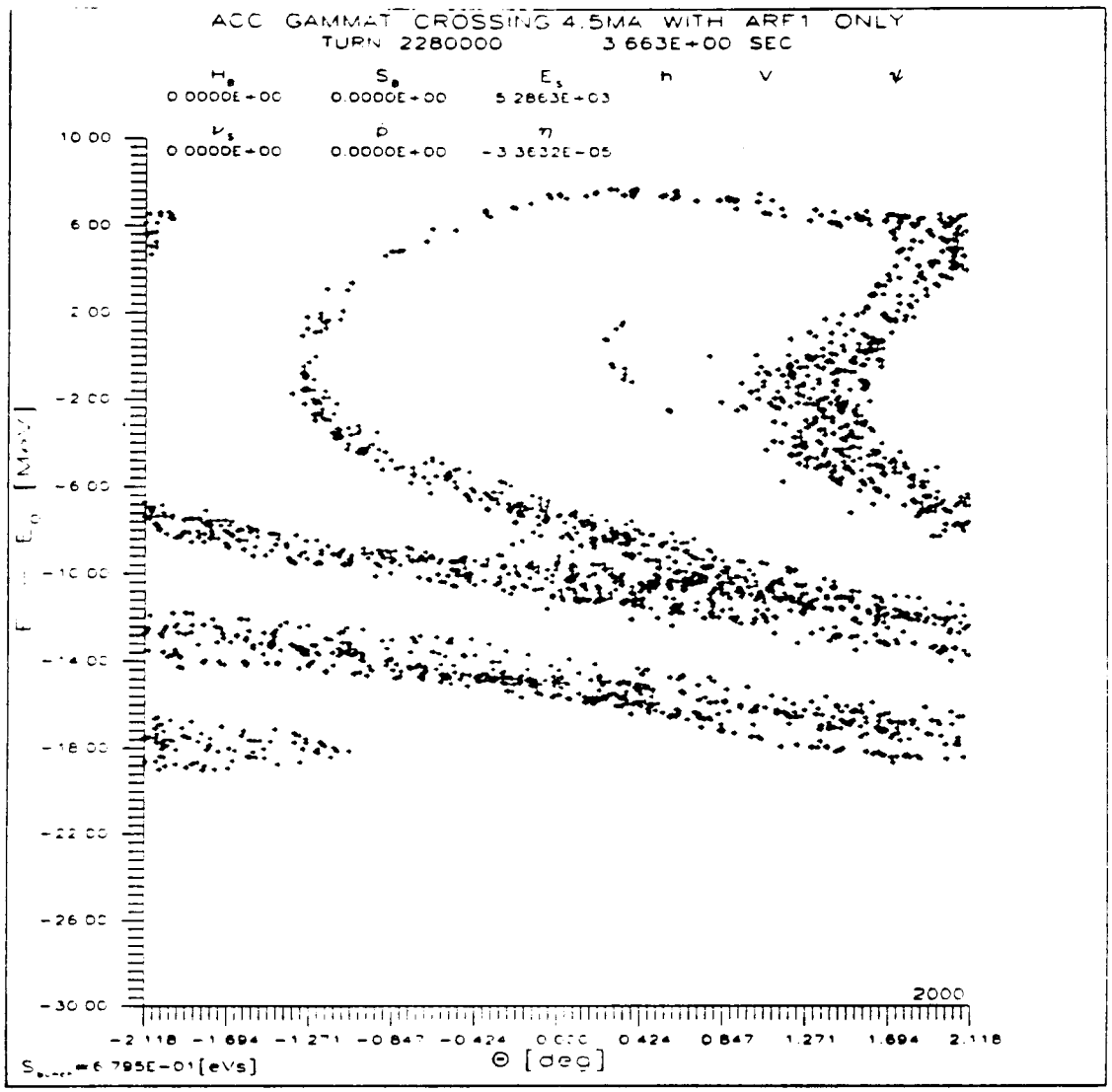

(d) Phase space distribution at $\eta = -3.4 \times 10^{-5}$.

Figure 7.4. (continued)

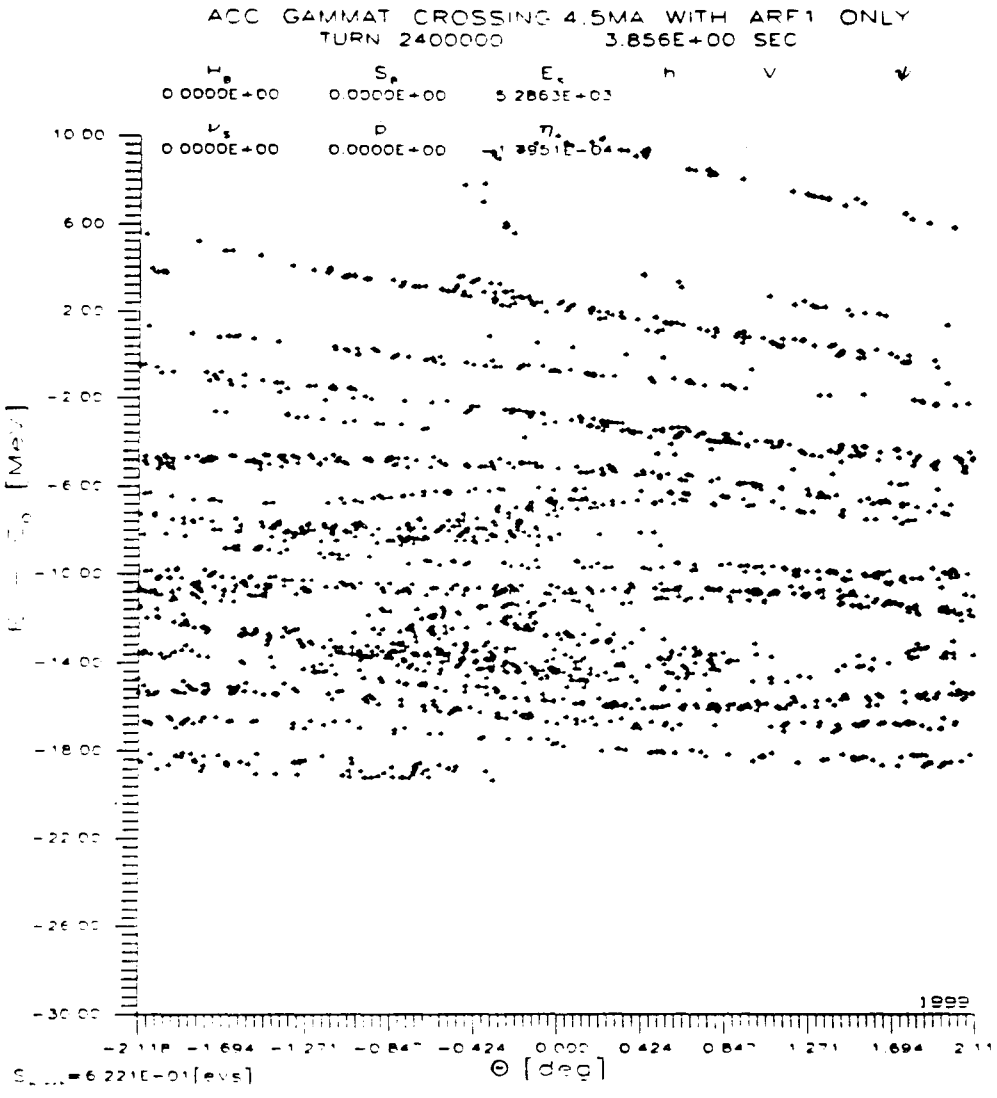

(a) Phase space distribution.

Figure 7.5. Phase Space and Energy Distribution at $\eta = -1.8 \times 10^{-4}$.

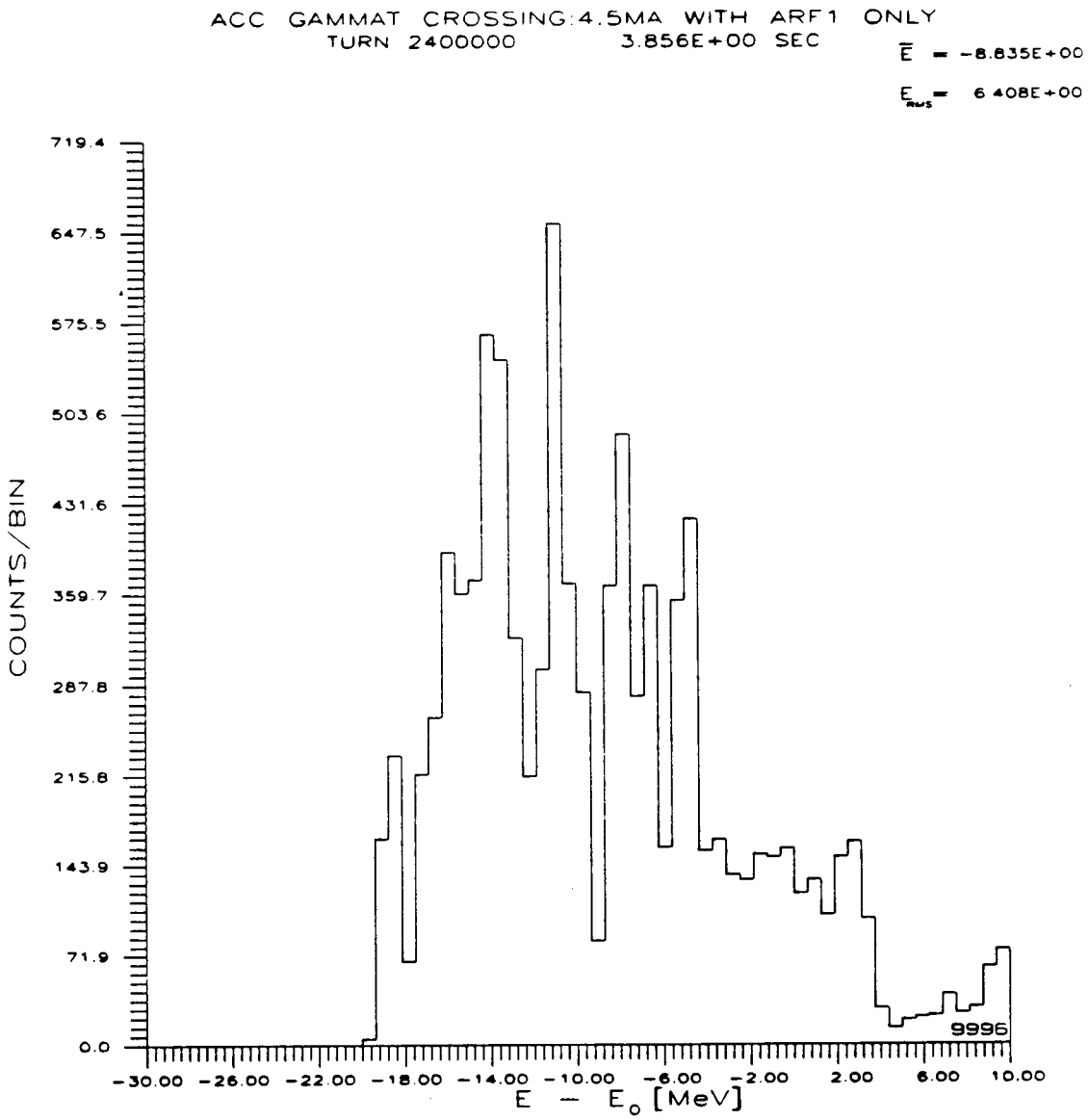

(b) Energy distribution.

Figure 7.5. (continued)

Figure 7.6 shows the Fourier component of the beam spectrum at 53 MHz as a function of time in transition crossing. The sharp peak appears when transition is crossed. The rise time of this Fourier component is obtained by converting data from the linear scale to the logarithmic scale and doing the linear least-square fitting to the rising edge. The fitting takes 194 points and its result gives a rise time of 36.4 milliseconds. This agrees very well with the measurement.

The average energy of the beam in the transition crossing process is plotted in figure 7.7. It can be seen from the figure that the major beam energy loss happens when transition is crossed, and the value is approximately 8 MeV. Both the measured and simulated beam rms energy spread are plotted in figure 7.8. The measurement result has already been shown in figure 6.11. The simulated rms energy spread should be smaller than the measured value since the simulation is done for a continuous crossing process whereas to measure the beam energy spread, γ_t is raised step by step. In addition, the measured energy spread has about 40% of its uncertainty coming from the η measurement. It can be seen that the simulation agrees with the measurement.

The effect of space charge in the crossing process has also been simulated. The conclusion is that adding space charge does not make a significant difference in the beam parameters such as the average energy and rms energy spread of the beam. Figure 7.9 shows the Fourier component as a function of time as the transition is crossed. The rise time obtained is 32.3 milliseconds with 207 points used in the fitting.

Another simulation is done taking into account the dependence of path length on momentum. The first order non-linear coefficient α_1 in equation (7.4) is set to be

$$\alpha_1 \approx -2\alpha_0 \tag{7.5}$$

in the crossing process. This choice results in about the same transition energy for all particles of different momenta. It can be seen in figure 7.10 that the occurence of the sharp rise of the coherent structure occurs is delayed in time. This is caused

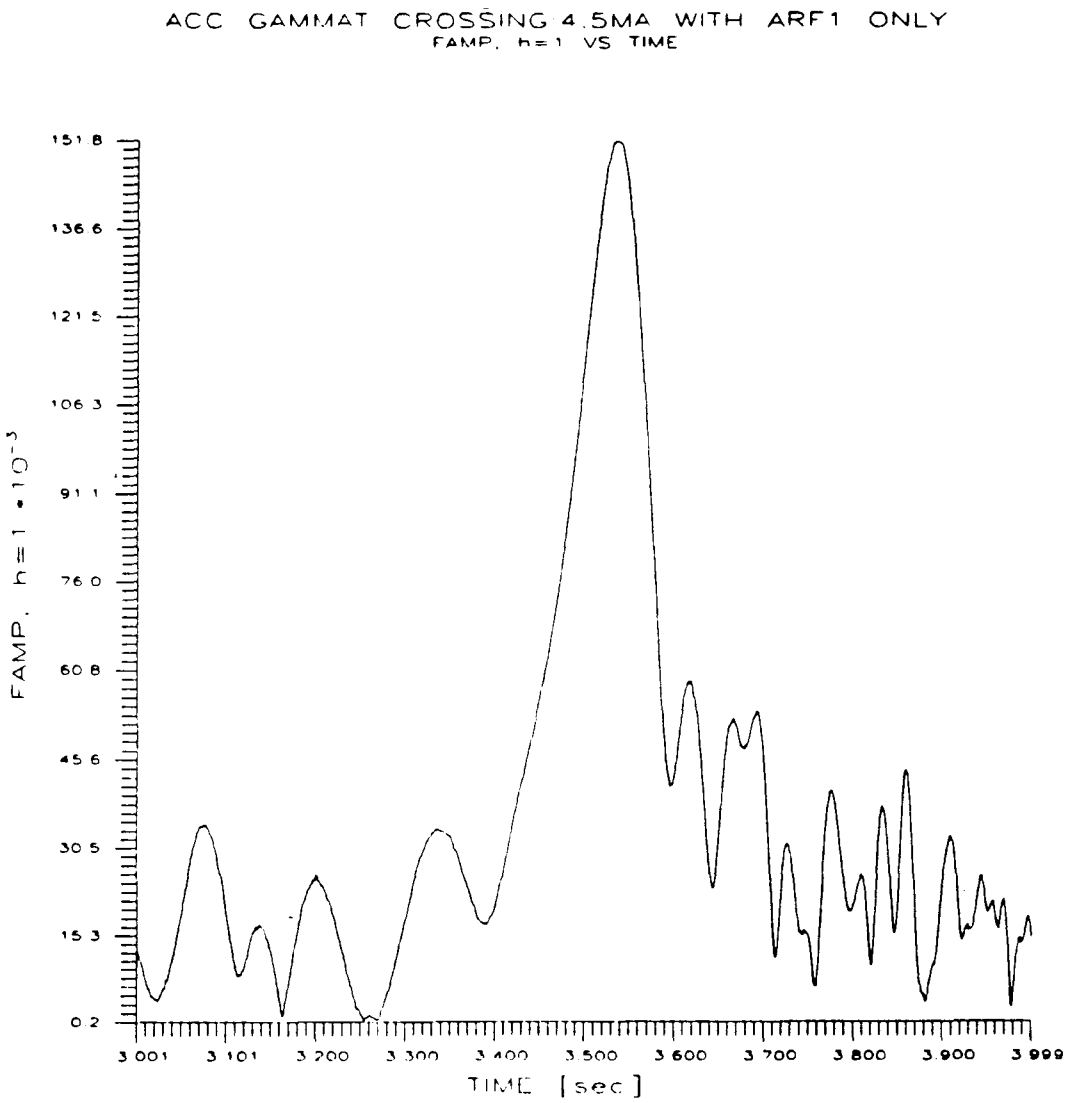

Figure 7.6. The First Fourier Component of the Beam Current as a Function of Time in Transition Crossing. The transition is crossed at the time 3.6 seconds. Since the simulation is done in 1/85 of the ring, this first harmonic appears at 53 MHz.

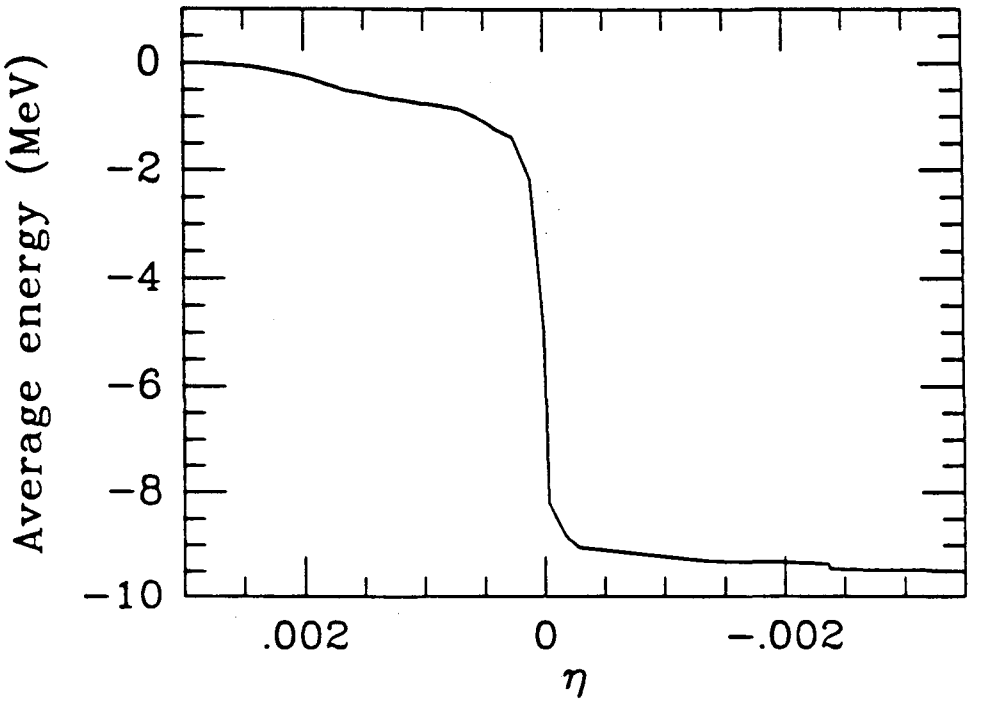

Figure 7.7. Simulated Beam Average Energy as a Function of η. The values are relative to the initial average energy.

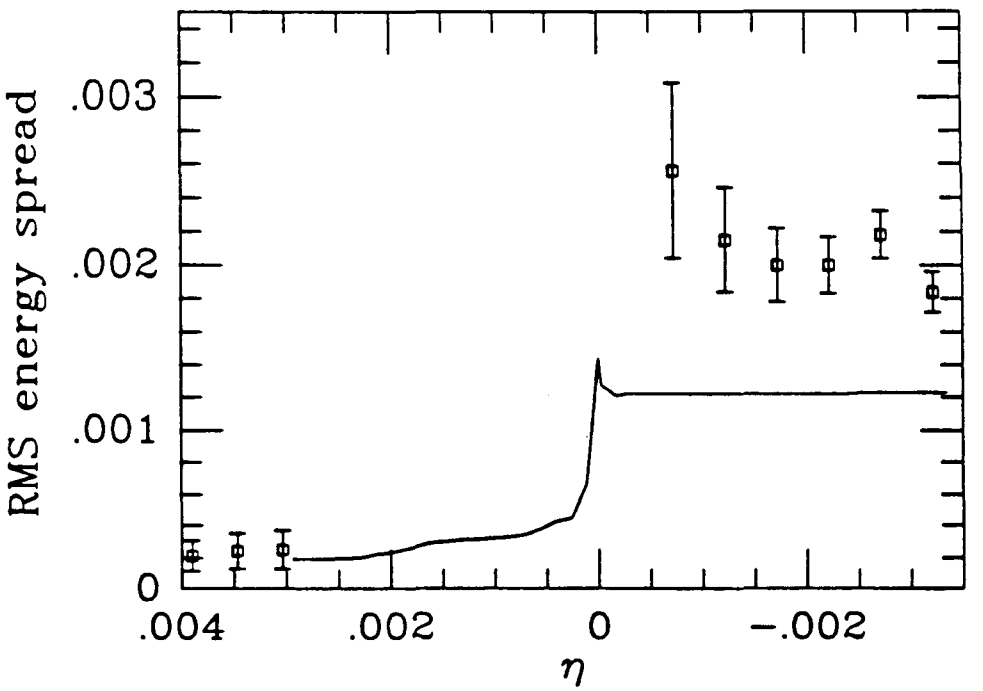

Figure 7.8. Measured and Simulated Beam rms Energy Spread as a Function of η. The measured values are represented with data points, which are the same as in figure 6.11. The solid line represents the simulated result.

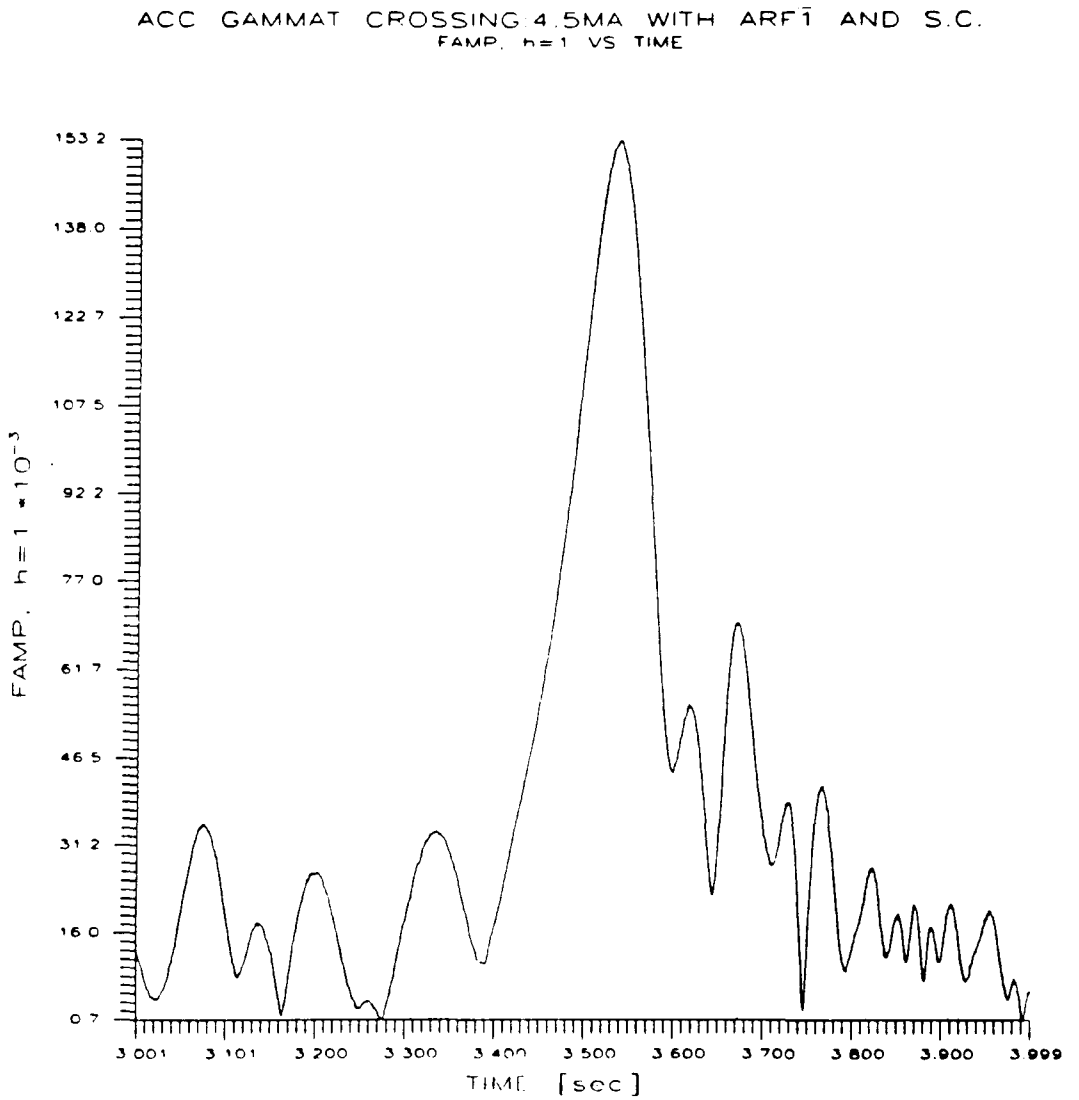

Figure 7.9. The Fourier Component in Transition Crossing with Space Charge Added. Transition is crossed at the time instant of 3.6 seconds.

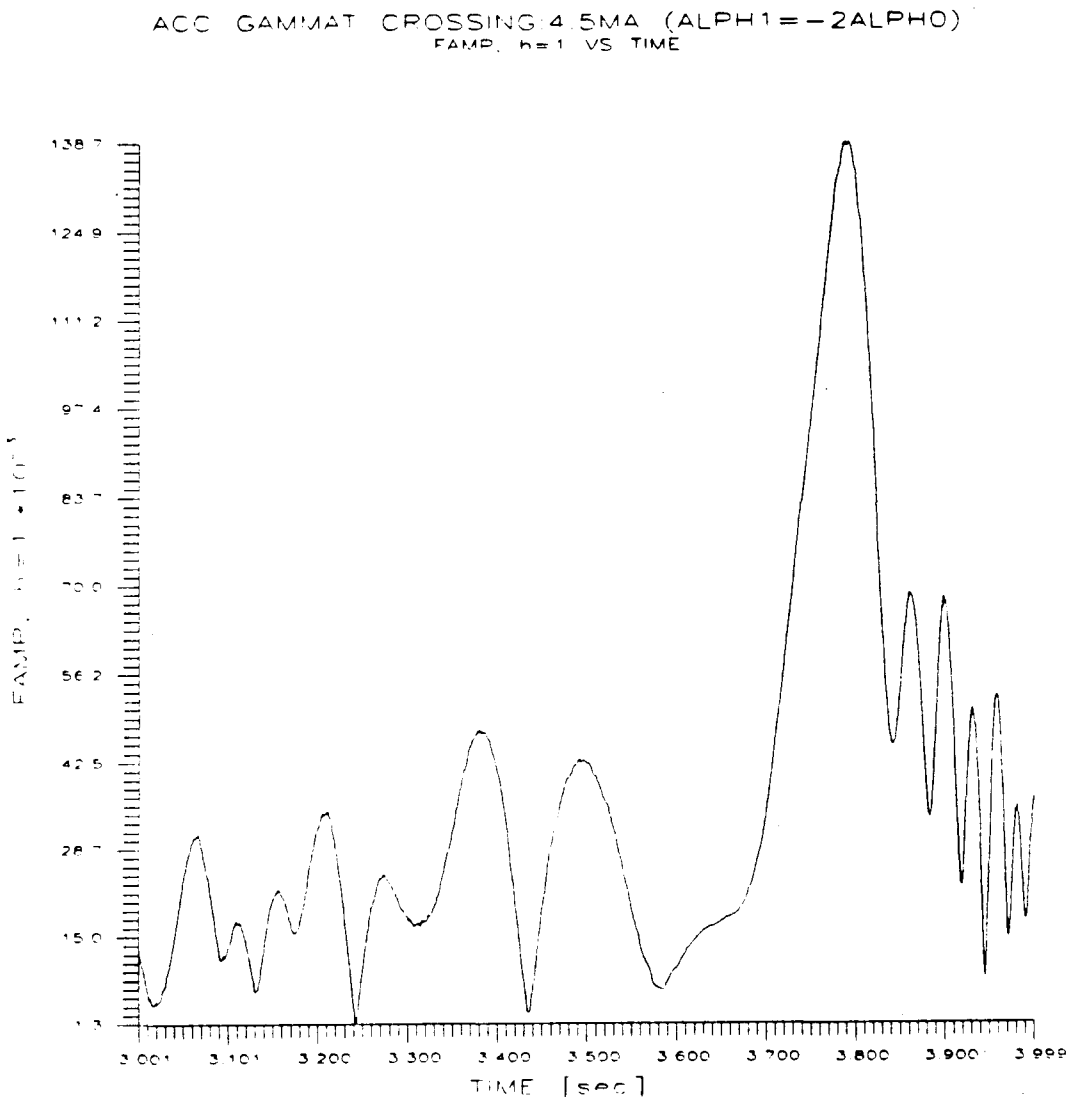

Figure 7.10. The Fourier component in Transition Crossing with $\alpha_1 \approx -2\alpha_0$.

by the delay of the transition crossing time. The rise time is found to be 31 milliseconds with 161 points used in the fit.

To summarize the above, the simulation gives the details of the phase space motion of the beam particles in the transition crossing, which leads to a better understanding of the process. In addition, it satisfactorily reproduces the beam parameters in the crossing process, which confirms the measurements.

CHAPTER VIII

CONCLUSIONS

This thesis contains three relatively separate subjects: the E760 deceleration, the Accumulator impedance measurement, and the longitudinal instability study in the process of the Accumulator transition crossing. Before E760 deceleration started, transition crossing had been expected to cause serious disruption to the beam. With the deceleration method described in section 4.2 the Accumulator transition crossing was made successful for beam intensities up to 10 mA. Nonetheless, the longitudinal coherent instability was still a dominant factor which damaged the beam quality in the crossing process. The instability study in the transition region was very important for enhancing the efficiency of transition crossing with a large beam.

Knowledge of the longitudinal impedance of the Accumulator is necessary for transition studies. Chapter 5 discusses the beam-based measurements of the Accumulator longitudinal impedance. The measurements do not agree with previous estimates. So far there has not been any published measurement result of the longitudinal impedance using this method.

One difficulty in the instability study near transition is that the momentum spread of the beam cannot be measured precisely by measuring its frequency spread from the Schottky signal. This is because of uncertainties in both the frequency spread and η measurements. As a consequence, the measurement results of the average energy and energy spread of the beam can only be compared roughly with the simulation results. However, the measurements provide enough evidence for identifying the major source of the longitudinal instability in transition crossing.

Measurements in the transition region show that the beam-induced voltage in the ARF1 cavities results in the major energy loss and energy spread blow up of a beam in the crossing process. As can be seen in both chapters 6 and 7, this has been confirmed by the computer simulation and has been proved in a later

experiment of transition crossing with ARF1 shorted. All these measurements are done with beams of a few milliamperes. If necessary, similar technique will be used in the future to find other impedances that may cause problems at higher intensities.

REFERENCES

[1] Tevatron 1 Design Report, Fermilab, September 1984.

[2] J. Peoples, "Prospects for $\bar{p}p$ Experiments in the Tev I Accumulator", Low Energy Antimatter, World Scientific Publishing Co., 1986, pp. 144-166.

[3] V. Bharadwaj *et al.*, "A Proposal to Investigate the Formation of Charmonium States Using the Pbar Accumulator Ring", Fermilab Proposal Number 760, March 1985.

[4] S.L. Glashow, "Partial-Symmetries of Weak Interactions", Nucl. Phys., vol. 22, 1961, pp. 579-588.

[5] S. Weinberg, "A Model of Leptons", Phys. Rev. Lett., vol. 19, 1967, pp. 1264-1266.

[6] A. Salam, Elementary Particle Theory, ed. N. Swartholm, Almquist and Wiksell, Stockholm, 1968, p. 367.

[7] H. Fritzsch and M. Gell-Mann, "Current Algebra: Quarks and What Else?", Proceedings of XVI International Conference on High Energy Physics, ed. J.D. Jackson and A. Roberts, vol. 2, Chicago, 1972, pp. 135-165.

[8] H. Fritzsch, M. Gell-Mann and H. Leutwyler, "Advantages of the Color Octet Gluon Picture", Phys. Lett., vol. 47B, 1973, pp. 365-368.

[9] H.D. Politzer, "Reliable Perturbative Results for Strong Interactions?", Phys. Rev. Lett., vol. 30, 1973, pp. 1346-1349.

[10] D.J. Gross and F. Wilczek, "Asymptotically Free Gauge Theories, I", Phys. Rev. D, series 3, vol. 8, 1973, pp. 3633-3652.

[11] S. Weinberg, "Non-Abelian Gauge Theories of the Strong Interactions", Phys. Rev. Lett., vol. 31, 1973, pp. 494-497.

[12] C. Quigg and J.L. Rosner, "Quantum Mechanics with Applications to Quarkonium", Phys. Rep. vol. 56, No. 4, 1979, pp. 167-235.

[13] A. Martin, "A Fit of Upsilon and Charmonium Spectra", Phys. Lett., vol. 93B, 1980, pp. 338-342.

[14] A. Martin, "A Simultaneous Fit of $b\bar{b}$, $c\bar{c}$, $s\bar{s}$ (bcs Pairs) and $c\bar{s}$ Spectra", Phys. Lett., vol. 100B, 1981, pp. 511-514.

[15] A. Khare, "Can Upsilon and Charmonium Spectra Really be Fitted by a Common Potential $A + Br^{\alpha}$?", Phys. Lett., Vol. 98B, 1981, pp. 385-387.

[16] Particle Data Group, "Review of Particle Properties", Phys. Lett., vol. 170B, April 1986.

[17] C. Baglin *et al.*, "Charmonium Spectroscopy at the ISR using an Antiproton Beam and a Hydrogen Gas Jet Target", EP Internal Report, 85-01, CERN, January 1985.

[18] M. Sands, "The Physics of Electron Storage Rings: An Introduction", SLAC-121, November 1970.

[19] D.A. Edwards and M.J. Syphers, "An Introduction to the Physics of Particle Accelerators", AIP Conference Proceedings, No. 184, 1989, pp. 2-189.

[20] E. Courant and H. Snyder, "Theory of the Alternating-Gradient Synchrotron", Annuals of Physics, Vol. 3, 1958, pp. 1-48.

[21] K.G. Steffen, High Energy Beam Optics, John Wiley & Sons, Inc., 1965.

[22] D.W. Kerst and R. Serber, "Electronic Orbits in the Induction Accelerator", Phys. Rev., Vol. 60, 1941, pp. 53-58.

[23] K.L. Brown, "A 2nd-Order Magnetic-Optical Achromat", IEEE Trans. Nucl. Sci., vol. NS-26, June 1979, pp. 3490-3492.

[24] C. Bovet *et al.*, "A Selection of Formulae and Data Useful for the Design of A. G. Synchrotrons", CERN/MPS-SI/Int. DL/70/4, 23 April 1970

[25] E. Ciapala, "Stacking and Phase Displacement Acceleration", General Accelerator Physics, vol. 1, CERN Accelerator School Proceedings, CERN 85-19, 27 November 1985, pp. 195-225.

[26] D. Möhl *et al.*, "Physics and Technique of Stochastic Cooling", Phys. Rep. vol. 58, No. 2, 1980, pp. 73-119.

[27] R.H. Siemann, "Bunched Beam Diagnostics", AIP Conference Proceedings No. 184, 1989, pp. 430-471.

[28] J.E. Griffin, "A Numerical Example of an RF Accelerating System", AIP Conference Proceedings No. 87, 1982, pp. 564-582.

[29] J.E. Griffin, "RF Cavity Primer for Cyclic Proton Accelerator", Fermilab Internal Note TM-1519, April 1988.

[30] P.B. Wilson, "High Energy Electron Linacs: Application to Storage Ring RF Systems and Linear Colliders", AIP Conference Proceedings No. 87, 1982, pp. 450-582.

[31] R. Pasquinelli, Fermilab Internal $\bar{p}$ Note 478 (unpublished).

[32] D.W. Peterson *et al.*, "An Improved 1.26MHz System for the Fermilab Antiproton Accumulator", Proceedings of the 1989 IEEE Particle Accelerator Conference, March 20-23, 1989, Chicago, pp. 237-239.

[33] T. Bagwell *et al.*, "Antiproton Source Beam Position System", Fermilab Internal Note TM-1254, May 1984.

[34] G. Lambertson, "Dynamic Devices-Pickups and Kickers", AIP Conference Proceedings No. 153, 1987, pp. 1414-1442.

[35] J. Petter *et al.*, "New 4-8 GHz Core Cooling Pickups and Kickers for the Fermilab Accumulator", Proceedings of the 1989 IEEE Particle Accelerator Conference, March 20-23, 1989, Chicago, pp. 648-650.

[36] R. Webber, "Longitudinal Emittance An Introduction to the Concept and Survey of Measurement Techniques Including Design of a Wall Current Monitor", Fermilab Internal Note TM-1655, March 1990.

[37] D. Bogert, "The Fermilab Accelerator Control System", Nuclear Instruments and Methods in Physics Research, Vol. A247, 1986, pp. 8-24.

[38] V. Bharadwaj *et al.*, "Operation of the Fermilab Accumulator for Medium Energy Proton-Antiproton Physics", Proceedings of the 2nd EUROPEAN PARTICLE ACCELERATOR CONFERENCE, June 12-16, 1990, pp. 617-619.

[39] T. Armstrong *et al.*, "Charmonium Spectroscopy in the Fermilab $\bar{p}$ Accumulator Ring", to be published in Phys. Rev. D.

[40] M. Church *et al.*, "Energy and Energy Width Measurement in the FNAL Antiproton Accumulator", to be published in Proceedings of the 1991 IEEE Particle Accelerator Conference, May 6-9, 1991, San Francisco.

[41] A.W. Chao, "Coherent Instabilities of a Relativistic Bunched Beam", AIP Conference Proceedings No. 105, 1983, pp. 353-523.

[42] A. Hofmann, "Single-Beam Collective Phenomena – Longitudinal", Theoritical Aspects of the Behaviour of Beams in Accelerators and Storage Rings, CERN 77-13, 19 July 1977, p. 152.

[43] H.G. Hereward, "The Elementary Theory of Landau Damping", CERN 65-20, Proton Synchrotron Machine Division, May 28, 1965.

[44] E. Keil and W. Schnell, CERN Report ISR-TH-RF/69-48, 1969.

[45] J. Marriner *et al.*, "Stability Criterion and Wall Impedances for the Antiproton Accumulator", Fermilab Internal $\bar{p}$ Note 422.

[46] R.H. Siemann, "Computer Models of Instabilities in Electron Storage Rings", AIP Conference Proceedings No. 127, 1985, pp. 368-442.

[47] G. Jackson *et al.*, "Results from Longitudinal Impedance Measurements in the Fermilab Tevatron", to be published in Proceedings of the 1991 IEEE Particle Accelerator Conference, May 6-9, 1991, San Francisco.

[48] S. Stahl and J.M. Maclachlan, "User's Guide to ESME v. 7.1", Fermilab Internal Note TM-1650, February 26, 1990.

[49] J.M. Maclachlan, "Fundamentals of Particle Tracking for the Longitudinal Projection of Beam Phase Space in Synchrotrons", Fermilab Internal Note FN-481, April 15, 1988.

[50] J.M. Maclachlan, "Longitudinal Phase Space Tracking With Space Charge and Wall Coupling Impedance", Fermilab Internal Note FN-446, February 1987.